Pollutant dispersion in wall-bounded turbulent flows
an experimental assessment

Eisma, Jerke

DOI
10.4233/uuid:205f36da-9d4b-4c28-a326-864b27cb857d

Publication date
2017

Document Version
Final published version

Citation (APA)
Eisma, J. (2017). *Pollutant dispersion in wall-bounded turbulent flows: an experimental assessment*. [Dissertation (TU Delft), Delft University of Technology]. https://doi.org/10.4233/uuid:205f36da-9d4b-4c28-a326-864b27cb857d

POLLUTANT DISPERSION IN WALL-BOUNDED TURBULENT FLOWS

An Experimental Assessment

PROEFSCHRIFT

ter verkrijging van de graad van doctor
aan de Technische Universiteit Delft,
op gezag van de Rector Magnificus prof. ir. K.C.A.M. Luyben,
voorzitter van het College voor Promoties,
in het openbaar te verdedigen op vrijdag 10 februari 2017 om 12:30 uur

door

Heerke Eelke EISMA
Ingenieur Lucht- en Ruimtevaart
Technische Universiteit Delft
geboren te Wouterswoude, Nederland.

Dit proefschrift is goedgekeurd door de
Promotor: Prof. dr. ir. J. Westerweel
Copromotor: Dr. ir. G.E. Elsinga

Samenstelling promotiecommissie:

Rector Magnificus,	voorzitter
Prof. dr. ir. J. Westerweel,	Technische Universiteit Delft
Dr. ir. G.E. Elsinga,	Technische Universiteit Delft
Onafhankelijke leden:	
Prof. dr. F. Scarano	Technische Universiteit Delft
Prof. dr. ir. W. Uijttewaal	Technische Universiteit Delft
Prof. dr. M.C. Krol	Wageningen University & Research
Prof. dr. ir. B. Ganapathisubramani	University of Southampton
Prof. dr. ir. J. van Beeck	Von Kármán Institute

This research is supported by the Dutch Technology Foundation STW, which is part of the Netherlands Organisation for Scientific Research (NWO) and partly funded by the Ministry of Economic Affairs (project number 11989).

Nederlandse Organisatie voor Wetenschappelijk Onderzoek

Cover: Instantaneous concentration field over urban roughness (Chapter 4)
Printed by: GildePrint - Enschede

ISBN 978-94-6233-527-1
An electronic version of this dissertation is available at
http://repository.tudelft.nl/.

CONTENTS

SUMMARY

A growing number of citizens, that increasingly lives in large urban areas, are exposed to high concentrations of polluting and harmful species. The large impact on public health requires appropriate measures to improve the air quality. Therefore, accurate models to predict dispersion of pollutants in urban environments are necessary. Nevertheless, the current dispersion models are often unable to accurately predict pollutant concentrations in urban areas. The complex turbulent flow around individual buildings and streets makes it difficult to obtain accurate pollutant concentration levels from the (often) statistical dispersion models.

The aim of this thesis is to contribute to the understanding of urban flow and pollutant dispersion mechanisms. First of all, the characteristics of internal shear layers in a boundary layer at laboratory scale are researched. Stereoscopic particle image velocimetry (PIV) measurements show the presence of thin shear layers that separate large scale uniform momentum zones. A conditional sampling approach reveals that these internal layers depict similar characteristics compared to a layer that separates turbulent flow from non-turbulent flow. A first order jump model is derived for these internal layers, with which growth rates can be estimated. The results indicate that the average internal shear layers move only slowly, i.e. on the order of the average boundary layer growth rate, while the wall-normal velocity of these layers increases away from the wall. As a result, large scale zones only grow slowly.

The influence of these large scale structures on the dispersion of a passive scalar is investigated by means of a simultaneous tomographic PIV and laser-induced fluorescence (LIF) experiment. Based on the probability density functions of the instantaneous realization of the velocity and scalar concentration, several uniform zones can be identified in the velocity field and the concentration field. In at least 75% of the snapshots multiple zones can be identified. Concentrations zones are on average slightly bigger compared to momentum zones. Conditional statistics around the edges of both zones clearly show that these edges work as barriers to scalar transport.

The second part of this thesis contains the results of velocity and passive scalar concentration measurements over an idealized urban geometry that is submerged in a scaled version of the atmospheric boundary layer. Specifically, research is done on a roughness transition that is usually found at the edge of urban areas, where the roughness changes from rural terrain (low roughness) to urban areas (high roughness). The buildings in this geometry are represented as cubes or bars. Furthermore, a highway is modelled as a uniform line source, and the vehicle emissions are modelled as a passive scalar that neither interacts with itself, nor influences the flow field. Simultaneous stereoscopic PIV and LIF measurements allow to study the influence of flow structures on dispersion processes. First of all, the influence of the urban geometry is researched. The aspect ratio (length l versus width w ratio) of the buildings is systematically varied over a range of $1 < l/w < \infty$. The results are compared with 'large-eddy simulation' (LES) results. Independently, both methods predict the same velocity and concentration statistics to within a few percent. Small differences can be explained based on the ac-

curacy of both methods. In all investigated geometries, the ventilation of the first three streets after the roughness transition is dominated by the advective concentration flux, while turbulence in all cases acts to remove pollutants out of the streets. A joint probability density function of the streamwise velocity fluctuations and the wall-normal concentration flux at roof level indicates that low-momentum fluid is responsible for street canyon ventilation. Based on a linear stochastic estimation, an average flow structure is obtained, which is associated with street ventilation. This structure reveals a large scale low-momentum region that spans multiple streets. Furthermore the height of this structure increases with increasing aspect ratio. In accordance with existing literature, no clear Reynolds number dependence is observed for the chosen geometry over the range $h^+ = u_\tau h/\nu = 209 - 598$.

Finally, the effect of a sound barrier on pollutant concentrations and dispersion mechanisms is researched. The noise barrier, modelled as a 2D fence and located in between the pollutant source and the urban roughness, results in a very distinct shear layer that marks the start of a new internal boundary layer. This internal boundary layer grows in case of a higher fence. As a result of this increased boundary layer height, the concentration behind the fence decreases compared to the case without the sound barrier. A quadrant analysis shows that both 'sweeps' and 'ejections' are important for street canyon ventilation. A simplified mixing length model is created. The most important parameters for such a model are the roughness geometry and the development of the internal boundary layer. Besides this, the concentration field in the fully-developed region can be parametrized solely based upon the properties of this newly formed internal boundary layer.

The results in this thesis show that combined PIV and LIF measurements are suitable methods to study pollutant dispersion in urban areas. Combined with LES simulations they offer the ability to perform accurate dispersion research. Nevertheless, the use of these experimental techniques is likely to be limited to the academic field only, as it is impractical to perform these type of experiments to the great variety in practical situations. Therefore, fast derived models remain important for dispersion research in more practical situations, i.e. for instance in the calculation of yearly average concentration levels. Based on the results in this thesis, several perspectives are given for new or improved models that can be used to effectively model pollutant dispersion in urban environments.

SAMENVATTING

Een groeiend aantal burgers, die in toenemende mate in grote stedelijke omgevingen woont, worden blootgesteld aan hoge concentraties vervuilende en schadelijke stoffen. De impact op de bevolkingsgezondheid is dusdanig groot dat het van belang is geschikte maatregelen te nemen die de luchtkwaliteit te verbeteren. Het is daarom van belang om verspreiding van fijnstof in stedelijke omgevingen adequaat te voorspellen. Desondanks zijn de huidige verspreidingsmodellen vaak niet in staat om de concentraties van fijnstof in urbane omgevingen accuraat te voorspellen. De complexe turbulente stroming om individuele gebouwen en straten bemoeilijkt het om uit de (veelal) statistische verspreidingsmodellen correcte fijnstof concentraties te voorspellen.

Het doel van deze thesis is om bij te dragen aan kennis op het gebied van urbane stromingen en verspreidingsmechanismen. Allereerst worden de eigenschappen van interne schuiflagen (shear layers) in een grenslaag op laboratoriumschaal onderzocht. Stereoscopische particle image velocimetry (PIV) metingen laten dunne lagen zien in een grenslaag die grootschalige uniforme impuls zones scheiden. Een conditioneel statistische aanpak over deze lagen laat zien dat deze lagen soortgelijke karakteristieken vertonen als de laag die een turbulente stroming separeert van een niet-turbulente stroming. Een eerste orde 'jump' model is afgeleidt voor de interne lagen, waarmee groeisnelheden voor interne lagen kunnen worden afgeleidt. Hieruit blijkt dat een gemiddelde interne laag slechts langzaam van de wand af beweegt, i.e. in de orde van de gemiddelde grenslaaggroei, terwijl de wand-normale snelheid toeneemt verder van de wand af. Dit heeft als gevolg dat grootschalige zones in een grenslaag slechts langzaam groeien.

De invloed van deze grootschalige structuren op de verspreiding van een passieve scalair is onderzocht door middel van een simultaan tomografisch PIV en laser-induced fluorescence (LIF) experiment. Op basis van kansdichtheidsfuncties van instantane realisaties van snelheid en concentratie zijn duidelijk meerdere uniforme zones te onderscheiden in het snelheidsveld en in het concentratieveld. Beide zones overlappen voor een groot gedeelte. In het overgrote deel van de samples zijn meerdere zones te onderscheiden, waarbij concentraties zones gemiddeld iets groter zijn dan impuls zones. Conditionele statistieken over de randen van beide soorten zones laat duidelijk zien dat de randen functioneren als barriëres voor scalair transport.

Het tweede deel van dit proefschrift bevat de resultaten van snelheids- en concentratie metingen gedaan over een geïdealiseerde stedelijke omgeving in een geschaalde versie van de atmosferische grenslaag. Specifiek is hier gekeken naar een ruwheidstransitie die vaak aan de rand van stedelijke omgevingen wordt gevonden, waarbij de oppervlaktestructuur verandert van landelijk terrein (met een lage ruwheid) naar stedelijk gebied (hoge ruwheid). De gebouwen in deze geometrie worden voorgesteld door kubusjes en staven. Daarnaast is een snelweg gemodelleerd als een uniforme lijnbron, en de uitstoot van verkeer wordt gemodelleerd als passieve deeltjes die niet reageren met elkaar en ook de stroming niet beïnvloeden. Simultane stereoscopische PIV en LIF metingen maken het mogelijk om de invloed van stromingsstructuren op

verspreidingsprocessen te bestuderen. Allereerst is in dit gedeelte de invloed van de gebouwgeometrie bekeken. De vormverhouding (lengte l versus de breedte w verhouding) van de gebouwen is systematisch gevarieerd over het bereik $1 < l/w < \infty$. De resultaten zijn vergeleken met 'large-eddy simulation' (LES) resultaten. Onafhankelijk van elkaar laten de experimenten en de simulaties vrijwel dezelfde snelheids- en concentratiestatistieken zien. Kleine verschillen kunnen worden uitgelegd aan de hand van de nauwkeurigheid van beide methodes. In alle onderzochte geometrieën blijkt dat de ventilatie van de eerste drie straten na de ruwheidstransitie gedomineerd wordt door de advectieve concentratieflux, terwijl turbulentie er in alle gevallen voor zorgt dat fijnstof de straat uit getransporteerd wordt. Een gecombineerde kansdichtheidfunctie van de stroomwaartse snelheidsfluctuaties en de wand-normale concentratieflux op dakniveau laat zien dat lage impuls stroming verantwoordelijk is voor straat ventilatie. Op basis van een lineaire stochastische benadering is een gemiddelde stromingsstructuur afgeleid die verantwoordelijk is voor deze straat ventilatie. Het resultaat laat een grootschalige lage impuls structuur zien die meerdere straten beslaat. Verder groeit de hoogte met een toenemende vormverhouding. In overeenstemming met resultaten uit de literatuur blijkt ook hier dat de resultaten voor de gekozen geometrie geen duidelijke Reynolds getal afhankelijkheid laten zien over de range van $h^+ = u_\tau h/\nu = 209 - 598$.

Als laatste is het effect van een geluidsscherm op fijnstof concentraties en verspreidingsmechanismen onderzocht. De geluidswal, gemodelleerd als een 2d scherm, zorgt voor een sterke schuiflaag die het begin markeert van een nieuwe interne grenslaag. Deze interne grenslaag wordt hoger naarmate het scherm hoger wordt. Door deze toegenomen grenslaaghoogte neemt de concentratie achter de geluidswal af ten opzichte van de casus zonder geluidswal. Een kwadranten analyse toont aan dat 'sweeps' en 'ejections' belangrijk zijn voor straat ventilatie. Een eenvoudig mengweg-lengte model is opgesteld waarbij het belangrijk is om de ruwheidsgeometrie en de ontwikkeling van de interne grenslaag mee te nemen. Daarnaast kan het concentratieveld in het volledig ontwikkelde gebied geparametriseert worden met op basis van de eigenschappen van de nieuw gevormde interne grenslaag.

De resultaten van dit proefschrift laten zien dat gecombineerde PIV en LIF metingen goede methodes zijn om dispersie in urbane omgevingen te bestuderen. Gecombineerd met nauwkeurige LES simulaties bieden ze de mogelijkheid om nauwkeurig verspreidingsonderzoek te doen. Desondanks zal het gebruik van dit soort experimenten in veel gevallen beperkt blijven tot het onderzoeksveld, aangezien het onuitvoerbaar is om dit type experimenten uit te voeren bij de grote variëteit van praktische situaties. Daarom blijven afgeleide modellen van groot belang voor dispersiemodellering in meer praktische situaties, bijvoorbeeld in het berekenen van jaarlijkse gemiddelde concentraties. Aan de hand van de resultaten in dit proefschrift worden verschillende perspectieven geboden voor nieuwe of aangepaste modellen waarmee verspreiding in urbane omgevingen effectief gemodelleerd kan worden.

NOMENCLATURE

ACRONYMS

ABL	atmospheric boundary layer
AR	aspect ratio
BRF	basic reference frame
DALES	Dutch Atmospheric Large-Eddy Simulation
DNS	direct numerical simulation
EL	elongation
IBL	internal boundary layer
JPDF	joint probability density function
LES	large-eddy simulation
LIF	laser induced fluorescence
LSE	linear stochastic estimation
LSM	large-scale motion
PDF	probability density function
PIV	particle image velocimetry
ppp	particles per pixel
Rh-B	Rhodamine B
Rh-WT	Rhodamine WT
RMS	root mean square
RR	rigid-body rotation
RT	roughness transition
SGS	subgrid-scale
SH	shear
TBL	turbulent boundary layer
T/NT	turbulent/non-turbulent
TPIV	tomographic particle image velocimetry
UBL	urban boundary layer
UCZ	uniform concentration zones
UMZ	uniform momentum zone
WHO	World Health Organization

LIST OF SYMBOLS

Latin Symobls

Symbol	Description	Units
A	region below T/NT and internal shear layers	-
A_f	total frontal area	m^2
A_p	total area covered with obstacles	m^2
A_t	total area from top	m^2
A_{UMZ}	area occupied by UMZ	m^2
A_{UCZ}	area occupied by UCZ	m^2
B	jump region of T/NT and internal shear layers	-
B_n	LIF background image	-
C	region above T/NT and internal shear layers (Chapter 2)	-
c	non dimensional passive scalar concentration (Chapter 3)	[-]
c^*	concentration	kg/m^3
c_f	friction coefficient	-
c_s	source concentration	kg/m^3
d	zero-plane displacement height (log-law fit)	m
D	mass diffusivity	m^2/s
D_I	linear dimension of the interrogation window	m
E	mean inward velocity over interface	m/s
E_b	boundary entrainment velocity	m/s
E_f	velocity of the interface relative to the local mean flow	m/s
F	fluorescence	-
$f_\#$	aperture number	-
f	focal length	m
f_s	scanning frequency	1/s
H	shape factor (δ^*/θ)	-
h	obstacle height	m
h^+	Reynolds number based on h and u_τ	-
I	excitation intensity	W/m^2
I_{sat}	saturation intensity	W/m^2
I_0	constant excitation intensity	W/m^2
I_n	uncorrected LIF image	-
K	acceleration parameter ($\nu/U_\infty^2 dU_\infty/dx$)	-
k	wave number	1/m

L	integral length scale	m
l	spanwise obstacle length	m
l_c	canopy length scale	m
l_i	length scale proportional to δ_i	m
l_m	mixing length	m
L_x	streamwise length of the line source	m
L_y	spanwise length of the line source	m
L_z	height of the settling chamber of the line source	m
L_x, L_y, L_z	computational domain dimensions in x, y, and z	m
$L1$, $L2$	first/second laser pulse	-
$\mathcal{L}_{c,y}$, $\mathcal{L}_{u,y}$	wallnormal height of UCZ/UMZ	m
$\mathcal{L}_x$, $\mathcal{L}_z$	length scales of low momentum regions in x and z	m
N_{UCZ}, N_{UMZ}	number of UCZ/UMZ	-
n	powerlaw exponent (Chapter 2)	-
n	frame index	-
m	frame index for LIF images	-
P	laser power	W
P	probability	-
p	pressure	Pa
Q	second invariant of ∇u	$1/\mathrm{s}^2$
$Q1$-$Q4$	quadrants of JPDF	-
R^2	coefficient of determination	-
Re	Reynolds number based on U_∞ and h	-
Re_θ	Reynolds number based on momentum thickness	-
Re_δ	Reynolds number based on boundary layer thickness	-
T	time scale (h/U_h)	m
Re_τ	friction Reynolds number	-
t_f	fly back time of scanning mirror	s
Sc	Schmidt number	-
Sc_{sgs}	SGS Schmidt number	-
Δt	time separation between double frame images	s
u_τ	friction velocity	m/s
$\nabla \mathbf{u}$	velocity gradient tensor	1/s
$\Delta \langle U \rangle$	jump of conditional streamwise velocity over the interface	m/s
U_∞	freestream velocity	m/s
U_c	local convection velocity at $\overline{\delta}_{int}$ (Chapter 2)	m/s
U_h	mean undisturbed velocity at obstacle height	m/s

U_i	dye injection velocity	m/s
u_i	mean streamwise velocity at half the IBL depth $u_i(x) = \overline{u}(x, z = 1/2\delta_i)$	m/s
X_c	streamwise shift of TPIV frames	m
(x, y, z)	streamwise, wall-normal, spanwise coordinates (Chapter 2,3),	m
	streamwise, spanwise, wall-normal coordinates (Chapter 4)	m
x^*	streamwise distance traveled of internal shear layers	m
y^*	wall-normal distance traveled of internal shear layers	m
y_1, y_2	wall-normal location of bottom/top of T/NT interface and internal shear layers	m
y_i	interface location	m

Greek Symobls

Symbol	Description	Units
α	power-law exponent	-
α	efficiency prefactor LIF setup	-
α	constant in mixing length model	-
β	angle between PIV cameras and light sheet normal	$^\circ$
γ	LIF pulse to pulse correction factor	-
γ_1	gradient in $\langle U \rangle_{(y-y_i)<y_1}$	1/m
γ_2	gradient in $\langle U \rangle_{(y-y_i)>y_2}$	1/m
γ_3	gradient in $\langle V \rangle_{(y-y_i)>y_2}$	1/m
γ_4	gradient in $\langle \tilde{u}\tilde{v} \rangle_{(y-y_i)<y_1}$	1/m
γ_5	gradient in $\langle \tilde{u}\tilde{v} \rangle_{(y-y_i)>y_2}$	1/m
δ_i	internal boundary layer depth	m
δ_v	viscous length scale (ν/u_τ)	m
δ_w	interface thickness	m
δ_{99}	boundary layer depth defined by $\bar{u}(y = \delta_{99}) = 0.99U_\infty$	m
δ_{int}	T/NT interface position	m
δ_{Kleb}	boundary layer depth as defined by Klebanoff [53]	m
δ^*	displacement thickness	m
ϵ	integration distance below/above interface (Chapter 2)	m
ϵ	extinction coefficient fluorescent dye	m
ζ	quality parameter for vector field divergence	-
η	Kolmogorov length scale	m
θ	momentum thickness	m

κ	von Kármán constant	-
Λ	length of dominant flow structure	m
λ	obstacle area density	-
λ_B	Batchelor length scale	m
λ_f	frontal area density	-
λ_p	plan area density	-
λ_T	Taylor micro-scale	m
ν	kinematic viscosity	m^2/s
ν_{sgs}	SGS viscosity	m^2/s
ν_T	turbulent viscosity	m^2/s
Π, Π_c,Π_u	measures for overlap between UMZ and UCZ	-
τ_{ij}	SGS stress tensor	-
σ	gaussian filter width	m
ϕ_s	source volume flow rate	m^3/s
Ω_z	out-of-plane vorticity	$1/s$

Operator symbols

Symbol	Description	Units
$\overline{(..)}$	temporal average, i.e. 'mean'	-
$(..)'$	fluctuating component	-
$\langle..\rangle$	conditional average (Chapter 2,3)	-
$\langle..\rangle$	spatial average (Chapter 4)	-
$\widetilde{(..)}$	quantity expressed in BRF (Chapter 2,3)	-
$\widetilde{(..)}$	LES filtering operation (Chapter 4)	-
$\overline{(..)^e}$	conditional average from LSE	-

Superscripts

Symbol	Description	Units
$(..)^+$	quantity normalized with viscous length scale δ_v	-

1 INTRODUCTION

1.1 BACKGROUND

THE PROBLEM OF URBAN AIR POLLUTION

Almost everyone is familiar with pictures from unbearably polluted cities with smog concentration that are well above permitted levels. Nearly every week there is a news story related to the problem of urban air pollution. Health studies show that the impact of urban air pollution on the public health should not be underestimated. The problem of air pollution is probably as old as humanity. The ancient city of Rome also suffered from this problem according to the Roman philosopher Seneca, who wrote in AD 61: *As soon as I had escaped the heavy air of Rome and the stench of its smoky chimneys, which when stirred poured forth whatever pestilent vapours and soot they held enclosed, I felt a change in my disposition*. The wood fires to cook food and the coal-fired central heating systems generated a significant amount of air pollution. However, the problem took serious proportions during the industrial revolution. Large coal-fired factories in densely populated urban areas exposed a huge amount of citizens to significant concentrations of hazardous and toxic exhaust gases. Even nowadays, this problem is still relevant as the World Health Organization (WHO) estimated that more than 80% of the people living in urban enviroments are exposed for a prolonged time to unhealthy air that exceeds the allowed pollutant concentration levels [1].

The topic of urban air pollution is clearly of great societal interest. The health effects associated with air pollution are severe: acute cardiovascular and respiratory diseases, lung cancer, chronic cardiovascular diseases, asthma, COPD, and infant mortality [2]. In 2014, the WHO announced that 7 million annual deaths can directly be linked to air pollution [3]. The increasing awareness of these detrimental health effects enforced several governments to take measures. In the late 90s, the European Union established limit values and alert thresholds for several harmful species in the atmosphere to prevent or reduce the harmful effects on human health and the environment [4]. The Dutch government turned these guidelines into practice by starting up the program *Nationaal Samenwerkingsprogramma Luchtkwaliteit*. This program is ment to take appropriate measures at both national and regional level to enhance the air quality in The Netherlands [5]. Examples of the measures taken by the Dutch government include the promotion of cleaner cars, and accelerating the development of sustainable energy rescources like wind, water and solar power.

Despite the fact that a certain amount of progress has been made (in particularly the western world), urban air pollution remains a significant problem, and it will remain so for the coming few decades as the energy consumption and the demand for fossil fuels keep growing. The aforementioned problems motivate to a large extent the contents of this thesis.

CURRENT MODELLING APPROACHES

To take appropriate and effective measures, it is of prime importance to know how pollutant dispersion occurs in urban environments. Modelling of pollutant dispersion processes in urban environments is often done by employing Gaussian plume models [6]. This is a (strongly idealized) analytical solution to the turbulent convection-diffusion equation, i.e. a homogeneous, steady-state flow and a steady-state point source are assumed. It further assumes that the concentration of a continuous source is proportional to the emission rate, inversely proportional to the wind speed and that the time averaged horizontal and vertical pollutant concentrations are well described by a Gaussian shaped profile [7]. Due to its simplicity and its low computational cost this Gaussian plume model remains the favourite choice for many dispersion toolboxes. These models are especially suited to simulate an eleveated point or line source, i.e. a high rise chimney, in open terrain. For instance, the *Nieuw Nationaal Model* [8] which is the current Dutch dispersion model is completely based upon this Gaussian plume model. Despite its popularity, there are a number of serious drawbacks related to this model. First of all, mean wind profiles and turbulence profiles are assumed to be homogeneous (at least) in horizontal direction; an assumption that certainly fails in actual atmospheric flows over urban canopies. Secondly, it is good to realize that this model is inappropriate at low wind velocities, in which diffusion dominates over convection. Furthermore, Gaussian plume models are more suited to provide long-term averages compared to instantaneous pollutant concentration predictions. This might become important in an emergency, for instance in case of an accidental hazardous release of toxic materials in urban areas [9]. Finally, the pollutant concentrations close to the emission source are difficult to predict, with increasing uncertainty for emission sources close to the wall in complex urban environments [8].

There are a number of studies that propose dispersion models for more general urban conditions; see Vardoulakis *et al.* [7] for an overview on these models. Usually these models are based on the local geometry of streets or buildings, and empirical relations [10–12]. For instance, Soulhac *et al.* [11] proposes the SIRANE model, which essentially decomposes the domain in a canopy part and the overlying atmosphere. The canopy part consists of a series of box models, which are used for each street canyon and street intersection. Between each of these elements, exchange coefficient and air fluxes are defined. Furthermore, dispersion in the overhead atmosphere is governed by a modified Gaussian plume model.

The main reason to employ (semi) empirical models is the inherent difficulty in predicting flow in urban geometries, where each building induces a complex flow pattern. Especially at the neighborhood scale (100-1000 meter), dispersion is controlled by a complex interaction of turbulent mixing and mean flow transport through the streets [13]. Hence, parameterization of this type of situations remains a challenge. A recently

developed analytical model for the boundary layer flow over rectangular-prism roughness elements is given by Yang *et al.* [14]. Though a promising approach, the analytical model is only accurate when the location of flow separation can be easily predicted, which poses a limitation to the applicability of this model to (more complex) real life situations.

From the previous observations it is clear that there is a need for understanding dispersion characteristics in urban environments. One way of gathering this knowledge is to perform full-scale measurements in existing cities [15–18]. However, a serious drawback of this approach is the fact that the results obtained in such studies are limited to that specific geometry. The reason is that topological dispersion, i.e. dispersion related to the geometrical layout, plays a major role in urban dispersion processes [13]. Furthermore, it is difficult to assess the influence of a single parameter (e.g. wind direction) as all atmospheric variables continuously vary in time. Finally, the resolution of these measurements is usually limited to a few measurement points only.

Therefore, in this thesis dispersion processes are studied in a laboratory setup with the aid of optical measurements techniques like *particle image velocimetry* (PIV) and *laser induced fluorescence* (LIF). These methods provide whole field measurements of two or three velocity components (PIV) or the scalar concentration field (LIF). This approach enables us to systematically vary a single parameter and assess its effect on dispersion.

STRUCTURE OF TURBULENT FLOWS

Turbulence is characterized by highly chaotic and disorderly motions, with a strong spatial and temporal variation. Understanding the motions and physics of turbulence is interesting from various perspectives. For instance, ships and airliners use up to half of their fuel consumption to overcome the drag that is associated with turbulent boundary layers (TBL). On the other hand, mixing and heat transfer processes are significantly enhanced by the presence of turbulence [19]. Also dispersion in the lower part of the atmospheric boundary layer (ABL) and the urban boundary layer (UBL) [20] is greatly influenced by turbulence.

Despite their chaotic character, wall-bounded turbulent flows demonstrate a certain degree of coherency, i.e instantaneous velocity fields exhibit organized motions [19]. A coherent structure may loosely be defined as an organized motion that is persistent in time and space, and that contributes significantly to transport of heat, mass and momentum [21]. A recent overview of different coherent structures in wall-bounded turbulence is given by Marusic *et al.* [21]. An example of such a structure is the uniform momentum zone (UMZ) in a turbulent boundary layer, which was first reported by Meinhart and Adrian [22]. These large-scale zones appear in instantaneous snapshots of the flow as distinct peaks in the probability density function (PDF) of the streamwise velocity. While the interior of these zones are relatively quiescent regions, the edges of these zones are populated by thin layers of high shear. Research by Morris *et al.* [23] showed that these uniform momentum zones also exist in the atmospheric surface layer at a much higher Reynolds number. Furthermore, Michioka *et al.* [24] showed that large-scale low-momentum zones passing over a street canyon reveal a large overlap with patches of high concentration of a passive scalar at that location, which were

released at street level. Hence, street canyon ventilation is significantly enhanced when a low-momentum region passes over.

1.2 AIM OF THE THESIS

The overarching goal of this thesis is to understand urban dispersion with the aim to improve dispersion modelling in urban environments. This thesis adds to this research area by first of all studying the dispersion of a passive scalar in a TBL. The TBL can be viewed as made up of UMZs and shear layers, where UMZs are relative quiescent regions bounded by dynamically active shear layers (see previous paragraph). One of the key issues is to detect and quantify the characteristics of these internal shear layers. These results are used to deduce growth rates of the large scale zones that are bounded by them. Secondly, the influence of large scale uniform momentum zones and the accompanying shear layers on the dispersion of a passive scalar is studied. Specifically it will be shown that next to UMZs also so-called uniform concentration zones are present in the TBL. However, it is presently unclear how significant these UMZs are in passive scalar transport.

The second goal of this thesis is to study the transport of pollutants around an idealized urban geometry in a scaled version of the atmospheric boundary layer. Whereas the majority of the atmospheric dispersion studies focus on so-called 'fully-developed' conditions, relatively little is known about pollutant dispersion when the urban flow experiences a sudden roughness transition, e.g. the transition from rural to urban terrain. The objectives of this study are to set-up a well-validated data set for flow and pollutant dispersion over a roughness transition. Furthermore, the research questions of this second part are:

- What is the influence of varying the spanwise length scale of the roughness on a rural-to-urban transition in terms of velocity statistics, internal boundary layer depth and pollutant dispersion?
- What are the dominant pollutant removal mechanisms from street canyons and how do these change in the transition region?
- What is the influence of the Reynolds number on the flow statistics and pollutant dispersion mechanisms?
- What is the influence of a fence on the flow and concentration characteristics in the urban canopy after a roughness transition?

Finally, the results of this research are used to propose an updated mixing-length model [25] for high density urban canopies in case of a roughness transition.

1.3 OUTLINE OF THE THESIS

This thesis consists of four remaining separate chapters, which can broadly be divided into two parts. Chapters 2-3 provide results on the fundamental aspects of coherent structures in TBLs (Chapter 2) and their relation to passive scalar transport (Chapter

3). The second part, i.e. Chapter 4, discusses the dispersion of a passive scalar in an idealized urban geometry that is submerged in a scaled atmospheric boundary layer.

Chapter 2 comprises the characteristics of the T/NT interface and internal shear layers. Conditional statistics are used to quantify the entrainment velocities of these layers, which are interpreted as growth rates for large scale regions. The approach is validated by performing the same conditional analysis around the T/NT interface, for which a theoretical prediction is available.

A simultaneous scanning tomographic particle image velocimetry (TPIV) and LIF measurement on a TBL is described in detail in Chapter 3. Attention is paid to the accuracy assessment of the combined velocity and concentration fields. These results are then used to elucidate the link between the dispersion of a passive scalar and the presence of large scale organized structures, i.e. uniform momentum zones, that are present in a TBL [22]. More specifically, it is shown that the concentration fields exhibit so-called uniform concentration zones (UCZ), which depict a significant geometrical overlap with the UMZs. Conditional analysis is performed around the edges of these UMZs and UCZs indicating that both are characterized by distinct jumps in either velocity (UMZ) or concentration (UCZ) statistics.

The dispersion of a passive scalar in an idealized urban geometry is studied in Chapter 4. Instead of studying pollutant dispersion under so-called 'fully-developed' urban roughness conditions, this chapter deals with pollutant dispersion in case of a roughness transition, i.e. the transition from rural to urban terrain. The simultaneous PIV/LIF measurements are compared with results from large-eddy simulations (LES). First of all, the influence of the aspect ratio of the buildings on the velocity- and concentration statistics is shown. Furthermore, the dominant pollutant removal mechanisms are identified, and the way they change in the transition region is described. Secondly, the influence of the Reynolds number on the velocity and concentration statistics is discussed. Finally, the effect of a fence upstream from the urban geometry is discussed. The mixing length formulation for sparse urban canopies [25], is extended to take into account the blockage effect in dense urban canopies. Additionally, the concentration field following a roughness transition is parametrized by scaling it with the internal boundary layer (IBL) depth and the bulk velocity inside the IBL.

Finally, Chapter 5 summarizes the conclusions of this thesis as a whole, along with an outlook for further research in the area of pollutant dispersion.

2

INTERFACES AND INTERNAL LAYERS IN A TURBULENT BOUNDARY LAYER

2.1 INTRODUCTION

In many fluid flows, such as jets, wakes and boundary layers, the turbulent flow is enclosed by an irrotational non-turbulent flow domain. The pioneering work of Corssin and Kistler [27] has shown that there exists a thin layer that separates the turbulent from the non-turbulent flow, with strong jumps in vorticity and/or velocity across these layers. Previous research has recognized the significance of these interfaces on the overall dynamics of the turbulent flow [27–35]. Knowledge on physical mechanisms occurring at these interfaces is especially important as a number of processes take place at or in close vicinity of the interface, e.g. it governs the overall growth of the turbulent flow region as entrainment of non-turbulent fluid into the turbulent flow occurs across this interface. Previous research on the turbulent/ non-turbulent (T/NT) interface has focussed on the definition of the interface and on the physical mechanism of entrainment at the interface. The usual way to detect interfaces is using threshold based methods [36], giving rise to some arbitrariness in the exact definition of the interface. However, the consensus is that there exists a T/NT interface that is bounded by a viscous superlayer that separates the different flow regions [36, 37]. Furthermore, entrainment over the T/NT interface has been researched for several unbounded flows [29, 31, 33, 34], where it has been shown that the entrainment process at the T/NT interface is mainly dominated by a small scale process ('nibbling'). Chauhan *et al.* [38] has shown that entrainment over the T/NT interface in a turbulent boundary layer (TBL) is characterized by small scale 'nibbling' whereas large scales present at the interface convolute the interface. As the large scales govern the overall entrainment, the small scale motions turn non-turbulent fluid by viscous diffusion into a turbulent state. The characteristics of the T/NT interface in a TBL has been studied before by Ishihara *et al.* [39] by direc numerical simulation (DNS). A sharp drop in conditional two-point correlations were observed indicating that the T/NT interface acts as a barrier to external non-turbulent fluctuations.

Thin layers, as described by Corssin and Kistler [27], however are not only found in the region that separate the turbulent flow from the non-turbulent region, but also between layers of different turbulent intensities [28, 40]. Recently, internal layers with similar characteristics as a T/NT interface within homogeneous isotropic turbulence

This chapter is published as: J. Eisma, J. Westerweel, G. Ooms, and G. E. Elsinga, "Interfaces and internal layers in a turbulent boundary layer," *Phys. Fluids*, vol. 27, no. 055103, 2015

were reported by Ishihara *et al.* [30, 32]. According to Robinson [41] (and references therein), internal shear layers have been observed throughout TBLs as well, even in the outer region of the flow. For instance, Blackwelder and Kovasznay [42] showed that significant shear layers were observed upstream of large scale motions based on space-time correlations of hotwire data in a TBL. Meinhart and Adrian [22, their Figure 2] and Adrian *et al.* [43, their Figure 17] visually observed internal thin shear layers in a TBL that separated large scale regions with nearly uniform momentum. These large scale regions were also observed by others [44], who found that these structures persist over long streamwise distances. The dynamical significance of these large scale structures has been elucidated in recent years with the evolution of new experimental measurement techniques [21]. It was found that these large scale regions are statistically relevant by carrying a significant amount of kinetic energy and have an important contribution to the Reynolds shear stresses while only occupying a small portion of the total flow volume [45, 46]. Not only instantaneous observations have been made of these internal shear layers. Linear stochastic estimation by Christensen and Adrian [47, their Figure 4] and Hambleton *et al.* [45, their Figure 6] show clearly structures separating two large-scale flow regions. Moreover, it turns out that layered structures were found to be characteristic of the mean structure associated with the principal strain in different turbulent flows by Elsinga and Marusic [48], which therefore can be considered to be typical for turbulent flow fields. Wei *et al.* [49] have shown that the flow around the shear layers in a TBL exhibit a scaling related to the macro scales in a TBL. This indicates that the shear layer is closely related to large scales present in the flow. Although the relevance of these interfaces and internal layers on the overall dynamics of the flow has been suggested for unbounded turbulent flows by several authors [28, 33], only minor attention has been paid to the characteristics of these internal layers present in wall bounded turbulent flows.

In this chapter we examine the characteristics of the T/NT interface and internal layers that are observed in the instantaneous flow fields in experimental data of a turbulent boundary layer. In our present work we define internal layers as regions of high shear. It should be noted that internal layers are not solely characterized by regions of intense shear; there may also be internal layers without significant shear [28]. Internal layers and the T/NT interface are shown to have similar characteristics and can be described by the same theoretical framework. By quantifying the entrainment over the bounding shear layers, growth rates of the associated large scale regions can be estimated, which is analogous to the overall TBL growth by the entrainment across the T/NT interface. This sheds new light on the growth mechanisms of large scale structures in a TBL, which are bounded by these layers.

The work in this chapter is arranged as follows: section 2.2 describes the experimental details of the experiment including the global boundary layer properties. Section 2.3 describes the different detection criteria that are employed for the T/NT interface and the internal layers. Section 2.4 describes the model that is employed to derive the boundary entrainment velocity for internal shear layers as well as the external T/NT interface. In section 2.5 the conditional sampled profiles around these layers are discussed and the boundary entrainment velocity derived from these statistics is shown. Section 2.6 discusses the implications of the previous sections in relation to previous obtained results. Finally, section 2.7 summarizes and draws final conclusions.

2.2 EXPERIMENTAL SETUP

The experiment is performed in the water tunnel at the Laboratory for Aero- and Hydrodynamics at the Delft University of Technology. It has a test section with a length of 5 m and a cross-section of $0.6 \times 0.6\,\mathrm{m}^2$. Boundary layer measurements were done at one of the side walls, approximately 3.5 m downstream of a boundary layer trip, at a free-stream velocity of $U_\infty = 0.73\,\mathrm{m/s}$. At this location the boundary layer thickness was $\delta_{99} = 74\,\mathrm{mm}$, where δ_{99} is the wall distance where the velocity has reached 99% of the free-stream value. The corresponding momentum and displacement thickness are $\theta = 8.7\,\mathrm{mm}$ and $\delta^* = 11.3\,\mathrm{mm}$, resulting in a shape factor $H = 1.31$, which is a typical value for a zero-pressure gradient TBL. The Reynolds number based on the momentum thickness is $\mathrm{Re}_\theta = 6578$. Finally, the friction velocity u_τ was derived from a Clauser plot technique ($u_\tau = 26.5\,\mathrm{mm/s}$). The main properties of the boundary layer are summarized in Table 2.1.

For the stereoscopic PIV measurements the flow is seeded with 10 μm buoyant neutral tracer particles (Sphericell). A streamwise-wall-normal plane is illuminated with a twin-cavity double pulsed Nd:YAG laser (Spectra-Physics Quanta Ray). The thickness of this light sheet was 1 mm. The particle images were recorded using two high resolution CCD cameras with a 4872×3248 pixel format (Image LX 16M, LaVision) which were equipped with a Micro-Nikkor F105 mm objective operating at an aperture number $f_\# = 8$. The resulting field of view was $1.35\delta_{99}$ in streamwise direction and $1.87\delta_{99}$ in wall-normal direction. Calibration, data acquisition and post-processing was performed with a commercial software package (Davis 8.1, LaVision). The PIV images are interrogated with a multi-pass interrogation technique, where the final interrogation windows have a size of 24×24 pixels with 75% overlap, corresponding to a spatial resolution based on the window size D_I^+ of 19.9 viscous wall units ($D_I^+ = D_I/\delta_v$). Here, D_I is the linear dimension of the interrogation window and δ_v is the viscous length scale defined as $\delta_v = \nu/u_\tau$ with ν the kinematic viscosity. The resolution is approximately 3-4 times the Kolmogorov length scale in the outer layer [50], hence the current measurement can be regarded as fully resolved. Individual spurious vectors are detected using a median test [51] and replaced by linear interpolation. In total 1824 in-plane instantaneous velocity fields were captured at a frame rate of 0.77 Hz to obtain sufficiently converged first and second order statistics.

The velocity profile in inner scaling is shown in Figure 2.1a. Reliable instantaneous data could be obtained for distances of 25 or more viscous wall units from the wall. Good agreement with data from literature is observed in the outer layer of the TBL. The outer regions of the root mean square (RMS) profiles shown in Figure 2.1b have been corrected for the PIV measurement noise. An estimate of the noise contribution to the RMS values was obtained from the method described by Poelma *et al.* [52]. It should be noted that Klebanoff [53] adopts a different definition for the boundary layer thickness. Based on the intermittency curves (not shown here) it is estimated that this is approximately given as $\delta_{Kleb} \approx 1.3\delta_{99}$; this has been accounted for in Figure 2.1b. However, Figure 2.1b still shows that the RMS profiles are slightly higher in the free stream compared to reference data from Klebanoff [53]. This may be attributed to the higher freestream turbulence intensity in the facility as well as to the uncertainty in determining the boundary layer thickness δ_{99}. The value for the free-stream turbulence intensity

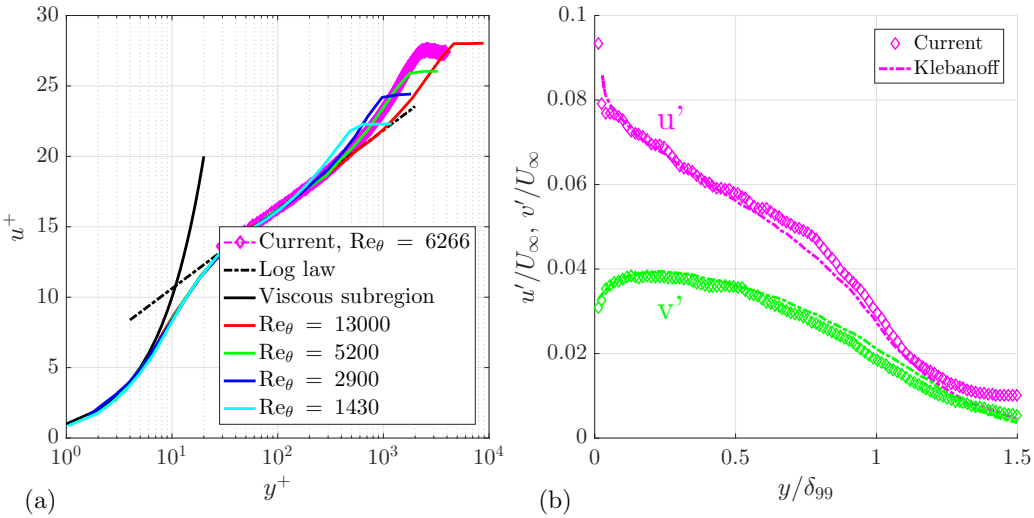

Figure 2.1: (a) The velocity profile in inner scaling compared with data from DeGraaff and Eaton [56]. (b) The RMS profiles of the streamwise and wall-normal components of the velocity compared with data from Klebanoff [53].

is found to be below 1% of U_∞. This is slightly higher compared to the turbulence intensity as reported by Schröder *et al.* [54] who performed PIV measurements in the same facility. Finally, the current measurements are subject to a very small favourable pressure gradient. Independent pitot measurements indicate that the acceleration parameter, $K = 2 \cdot 10^{-8}$. As shown by Joshi *et al.* [55], effects on the turbulence structure in a boundary layer become noticable at $K = 10^{-6}$. Hence, the pressure gradient will have a negligible influence on the results discussed here.

Table 2.1: Summary of the boundary layer properties.

U_∞	0.73 m/s	θ	8.7 mm	Re_τ	2053
δ_{99}	74 mm	u_τ	26.5 mm/s	$H = \delta^*/\theta$	1.31
δ^*	11.3 mm	Re_θ	6578	c_f	$2.7 \cdot 10^{-3}$

2.3 LAYER DETECTION AND GEOMETRICAL CHARACTERISTICS

2.3.1 T/NT INTERFACE

The T/NT interface is detected using a method that relies on the out-of-plane vorticity Ω_z, which is found to be the dominant component at the interface [57]. Gaussian smoothing, characterized by a filter width of $\sigma \approx 10y^+$, of the velocity field is performed after which the available velocity gradients are calculated using a second order least squares difference scheme [58]. Care is taken to ensure that the filter width is smaller than the Taylor micro-scale $\lambda_T \approx 180y^+$, to prevent affecting the relevant flow

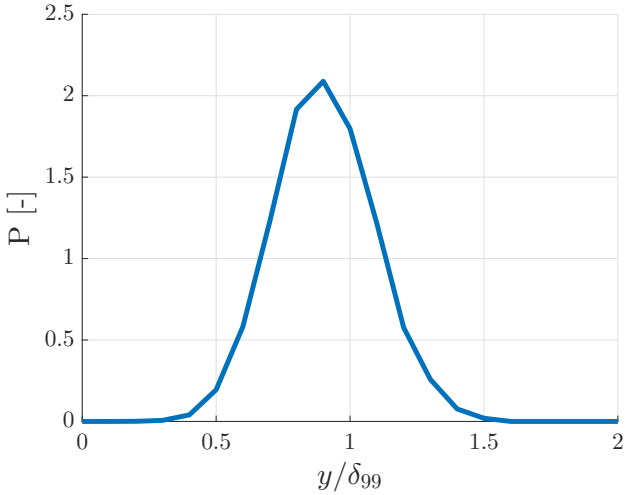

Figure 2.2: Probability density function of the location of the interface y_i. The average interface location is found at $y_i = 0.9\delta_{99}$. .

scales. Subsequent conditional sampling is performed on the raw unfiltered velocity fields. This approach is justified because the thickness of the interfaces δ_w is commonly regarded to be of the order of λ_T for flows with a mean shear [33]. Detection of the T/NT interface was performed using the vorticity method as proposed by Holzner *et al.* [34], which proves to be effective in detecting the T/NT interface. A noise level for the instantaneous vorticity is estimated by taking the RMS values of Ω_z in the non-turbulent part of the flow (i.e. $y/\delta_{99} \geq 1.5$), which is approximately $2.7s^{-1}$. A threshold of three times this level effectively separates the irrotational non-turbulent region from the turbulent region. The T/NT interface is then defined as the set of outermost points that exceed this threshold. The average interface position is found to be at $\overline{\delta}_{int} \approx 0.9\delta_{99}$ (see Figure 2.2), which is somewhat higher than the result of Corssin and Kistler [27] who found $\overline{\delta}_{int} \approx 0.80\delta_{99}$.

2.3.2 INTERNAL LAYERS

In order to detect the internal layers the triple decomposition method as proposed by Kolář [59] is applied. This decomposition was originally introduced to provide a more robust description of vortices in turbulent flows. However, the method can also be used to detect shear layers [60]. The velocity gradient tensor $\nabla\mathbf{u}$ is decomposed into three parts:

$$\nabla\mathbf{u} = (\nabla\mathbf{u})_{RR} + (\nabla\mathbf{u})_{SH} + (\nabla\mathbf{u})_{EL}, \tag{2.1}$$

where RR, SH and EL denote the rigid-body rotation, shear, and elongation components of the velocity gradient tensor respectively. This decomposition only applies to an appropriate reference frame, the so-called basic reference frame (BRF). In order to derive the shear component $(\nabla\mathbf{u})_{SH}$ in Equation 2.1, the following steps are performed. First, the 2D velocity gradient tensor $\nabla\mathbf{u}$ and the strain rate tensor (i.e. the symmetric

part of $\nabla\mathbf{u}$) are computed. Secondly, the eigenvectors of the strain rate tensor are found resulting in the principal axes. Third, $\nabla\mathbf{u}$ is expressed in the BRF with orthogonal axes that are rotated 45° with respect to the principal axes of the strain rate tensor (denoted as $\nabla\tilde{\mathbf{u}}$). Then, $(\nabla\tilde{\mathbf{u}})_{SH}$ is computed with:

$$(\nabla\tilde{\mathbf{u}})_{SH} = \begin{bmatrix} 0 & \frac{\partial\tilde{u}}{\partial\tilde{y}} - \mathrm{sgn}\left(\frac{\partial\tilde{u}}{\partial\tilde{y}}\right)\cdot\min\left(\left|\frac{\partial\tilde{u}}{\partial\tilde{y}}\right|,\left|\frac{\partial\tilde{v}}{\partial\tilde{x}}\right|\right) \\ \frac{\partial\tilde{v}}{\partial\tilde{x}} - \mathrm{sgn}\left(\frac{\partial\tilde{v}}{\partial\tilde{x}}\right)\cdot\min\left(\left|\frac{\partial\tilde{u}}{\partial\tilde{y}}\right|,\left|\frac{\partial\tilde{v}}{\partial\tilde{x}}\right|\right) & 0 \end{bmatrix}, \tag{2.2}$$

The vorticity associated with the shear component of the velocity gradient tensor is calculated as $\omega_{SH} = (\nabla\tilde{\mathbf{u}})_{SH,21} - (\nabla\tilde{\mathbf{u}})_{SH,12}$, i.e. the element on the second row/first column minus the element on the first row/second column. An example of an instantaneous ω_{SH} distribution is presented in Figure 2.3. Shear layers are visible which separate large scale regions with nearly uniform velocity, similar to observations by Meinhart and Adrian [22]. The shear layer like structure that is present inside the rectangle (indicated in Figure 2.3a) can directly be related to an instantaneous jump in the streamwise velocity component (Figure 2.3b). To distinguish between surrounding flow and intense shear layers a composite threshold criterion is used. First of all, the ω_{SH} noise level is estimated as before in the non-turbulent part of the flow. Three times this level effectively separates noise from actual shear layers. However, close to the wall the average shear is significantly higher compared to the outer region. Hence, in the near wall region a threshold is set based on the mean shear vorticity $\overline{\omega_{SH}}$ to detect internal layers closer to the wall. The highest value of either is found to be a suitable criteria to detect internal layers throughout the boundary layer.

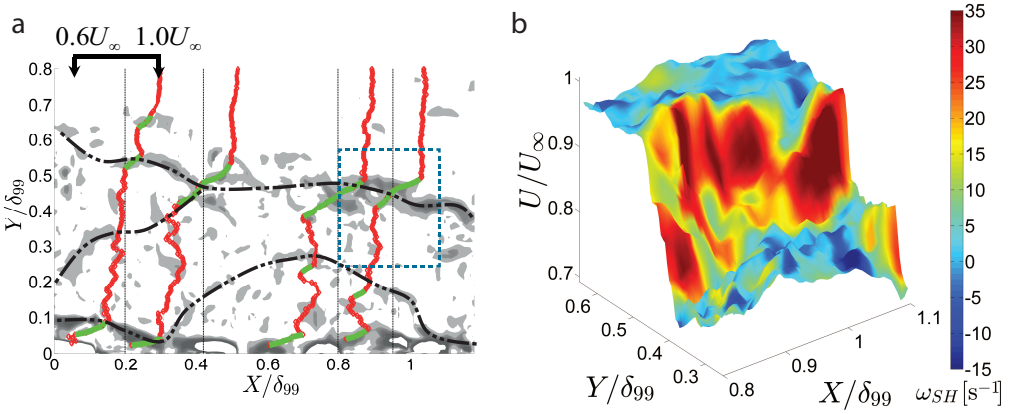

Figure 2.3: (a) An instantaneous realization of the shear component of the vorticity ω_{SH}, indicated with gray contours. The dashed dotted lines indicate the edges of uniform momentum zones determined from visual inspection of the velocity field. Streamwise velocity profiles are plotted to show the instantaneous jump across a shear layer. Regions of high velocity gradients are indicated with green dots. (b) Surface plot of the streamwise velocity field around the shear layer inside the rectangle in (a). For visualization purposes this image has been Gaussian filtered to suppress noise, characterized by a standard deviation $\sigma/\delta_{99} = 0.003$

.

Next the geometrical characteristics of the internal layers are quantified. It should be noted that all of the areas above a certain threshold, shown in Figure 2.3a, are regarded as internal layers. This eliminates the possibility of deliberately favouring certain layers, thereby distorting the statistics. Of course, this comes at the cost of slightly biased statistics. A probability density function (PDF) of the centroidal location is shown in Figure 2.4a, together with the intermittency function obtained from the position of the T/NT interface. The occurrence of internal layers closely follows the intermittency profile, suggesting internal layers are distributed uniformly throughout the turbulent region of the flow. This behavior also indicates why the conditional profiles shown later in section 2.5 in the outer region of the TBL do not appear to be converged. The number of detected internal layers is insufficient to obtain converged statistics in that part. The orientation with respect to the wall and the major axis length versus the minor axis of the internal layers are determined by fitting an ellipse with the same area moment of inertia as the detected layer, see Figure 2.4b,c. It turns out that the average orientation of 12° closely resembles the angle that Adrian *et al.* [43] report for the angle of hairpin packets. This underlines once more that the effect of the pressure gradient in the current measurements is negligible as one of the first observable consequences of a favourable pressure gradient is to decrease the inclination of structures observed based on two-point correlations for u' [55]. Moreover, the angle of the shear layers remains relatively constant over the height of the boundary layer (not shown here). Finally the PDF of the major/minor axis of the internal layers shows that the detected regions of high shear are elongated i.e. layer-like structures, as their aspect ratio is on average 3.6.

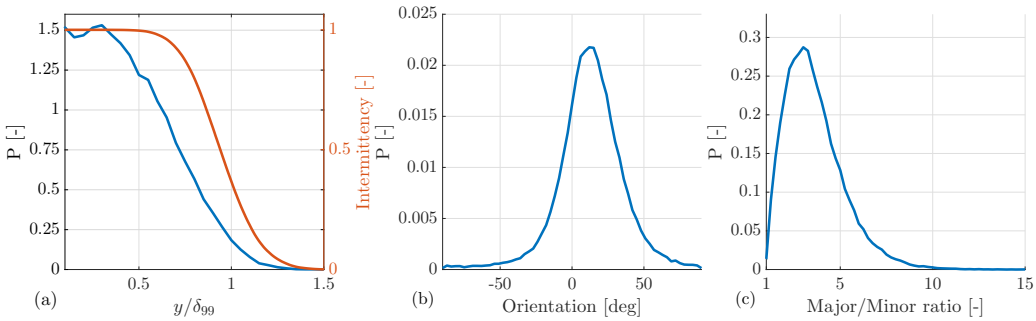

Figure 2.4: (a) PDF of the centroidal location of the internal layes over the height of the TBL. The red curve depicts the intermittency curve determined from the T/NT interface. (b) PDF of the orientation of the internal layers with respect to the wall, present throughout the TBL. (c) PDF of the ratio between the major- and the minor axis length of internal layers present throughout the TBL.

2.4 BOUNDARY ENTRAINMENT VELOCITY AND MODEL DESCRIPTION

A short description of the model used to determine the boundary entrainment velocity (E_b) is given in this section. The boundary entrainment velocity is defined here as the velocity with which the interface convects away from the wall, when following the interface in space (in a Lagrangian sense). Our approach corresponds with the definition of the boundary entrainment velocity as given by Westerweel *et al.* [29] and Turner [61].

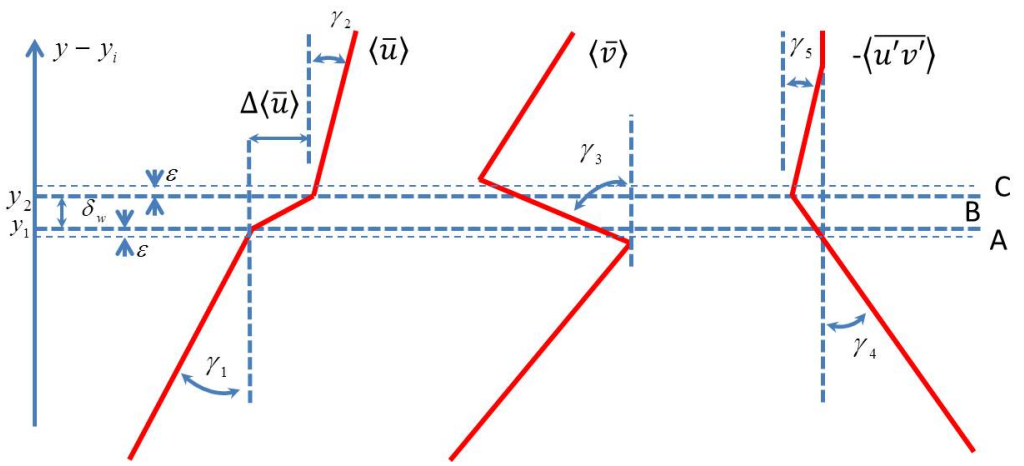

Figure 2.5: Schematic description of the model. The average interface location is located between $y_1 - y_2$. The jump in streamwise velocity occurs over a finite region δ_w. The three integration regions are given by the letters A-C

The last reference clearly points out the different usages of the term entrainment velocity. A clear distinction should be made between the velocity with which the interface spreads outward, i.e. the boundary entrainment velocity E_b, the rate at which external fluid flows into the turbulent flow across a boundary (E) and the outward velocity of the interface relative to the local mean flow (E_f). For instance in case of a turbulent jet, Turner [61] predicted that the outward velocity at the edge of the jet, measured in a fixed coordinate system will be: $E_b = -2E$. This was experimentally confirmed by Westerweel *et al.* [29] by employing the super-layer jump condition. In order to derive the boundary entrainment velocity for the T/NT interface and the internal shear layers a first order jump model is presently applied. This model is based on the work by VanZanten *et al.* [62] and Pino *et al.* [63] who used it to determine the growth rate of convective boundary layers. In a similar fashion the spatial growth rate can be calculated for a neutral convective boundary layer as will be shown here. The reason not to choose a zeroth order jump model as proposed by Lilly [64] is because his model assumes $\langle\overline{u}\rangle$ to be discontinous over an inversion, which is certainly not applicable when inspecting the conditional profiles (i.e. $\Delta\langle\overline{u}\rangle$ occurs over a small but finite region δ_w). In the current work the situation as sketched in Figure 2.5 is considered. Consider the idealized profiles for the conditional streamwise velocity $\langle\overline{u}\rangle$, the conditional wall-normal velocity $\langle\overline{v}\rangle$ and the conditional Reynolds shear stresses $\left\langle\overline{u'v'}\right\rangle$ as given in Figure 2.5. The lowercase u' and v' denote the fluctuating velocity components with respect to the mean velocities $\overline{u}$ and $\overline{v}$. In this model the jump in streamwise velocity $\Delta\langle\overline{u}\rangle$ occurs over a finite region δ_w (i.e. between $y_1 - y_2$). Furthermore, on both sides of the interface the conditional streamwise and Reynolds stress profiles show approximately constant gradients denoted by respectively $\gamma_{1,2}, \gamma_{4,5}$. Finally, the conditional wall-normal velocity has a constant gradient in the jump region γ_3.

The profiles shown in Figure 2.5 are entered into the conditional mean x-momentum equation, which in absence of viscous effects and pressure gradient effects reads:

$$\frac{\partial \langle \overline{u} \rangle}{\partial t} = - \langle \overline{v} \rangle \frac{\partial \langle \overline{u} \rangle}{\partial y} - \frac{\partial \left\langle \overline{u'v'} \right\rangle}{\partial y} \tag{2.3}$$

The pressure gradient is neglected as independent pitot measurements indicate a negligible small acceleration parameter. In order to derive the growth rate of both internal layers and the T/NT interface, Equation 2.3 is integrated over three regions:

1. In a small region below the interface, between $(y_1 - \epsilon)$ and y_1. Where ϵ has a small but finite value.
2. Over the jump region, between y_1 and y_2
3. In a small region above the interface, between y_2 and $(y_2 + \epsilon)$

By substitution of the results obtained from region A and C into the equation obtained from region B the boundary entrainment velocity is derived as:

$$E_b = \frac{1}{\Delta \langle \overline{u} \rangle - \frac{\delta_w}{2}(\gamma_1 + \gamma_2)} \left[-\frac{\delta_w}{2} \left(\gamma_1 \langle \overline{v} \rangle_{y_1} + \gamma_2 \langle \overline{v} \rangle_{y_2} + \gamma_4 + \gamma_5 - \gamma_3 \Delta \langle \overline{u} \rangle \right) - \left\langle \overline{u'v'} \right\rangle_{y_1} + \left\langle \overline{u'v'} \right\rangle_{y_2} + \Delta \langle \overline{u} \rangle \langle \overline{v} \rangle_{y_1} \right] \tag{2.4}$$

The complete derivation of Equation 2.4 can be found in Appendix A.

2.5 CONDITIONAL SAMPLING

2.5.1 T/NT INTERFACE

Conditional sampling is performed at fixed wall-normal distances with respect to the location of the interface. This conditional sampling technique is described in detail in Bisset *et al.* [57]. The conditional profiles of the streamwise velocity, wall-normal velocity, Reynolds shear stress and the out-of-plane vorticity Ω_z are shown in Figure 2.6, each normalized with appropriate large scale parameters. First of all, the conditional streamwise velocity profile indicates a distinct jump over the T/NT interface of approximately $0.04U_\infty$. In the turbulent region below the interface this profile exhibits a constant gradient which is consistent with the approximately constant value for Ω_z in this region. Secondly, on the non-turbulent side of the interface there is still a finite gradient in the conditional streamwise velocity. This behavior is probably due to the presence of irrotational fluctuations in the non-turbulent part of the flow [27, 65]. Furthermore, the conditional out-of-plane vorticity in the non-turbulent part quickly drops to zero, as shown in Figure 2.6c. This confirms once more that the correct T/NT has been detected. The vorticity strongly peaks inside the T/NT interface and it reaches approximately a constant value on the turbulent side of the interface. This behavior is consistent with the observations from jets [29] and TBL [38]. From Figure 2.6b it is observed that the gradient in the conditional wall-normal velocity profile is negative over the interface. This

wall-normal compression behavior implies that out-of-plane vorticity stretching occurs over this interface in order to maintain a sharp interface. Overall it should be noted that the profiles shown in Figure 2.6 appear to be consistent with the model proposed in Figure 2.5.

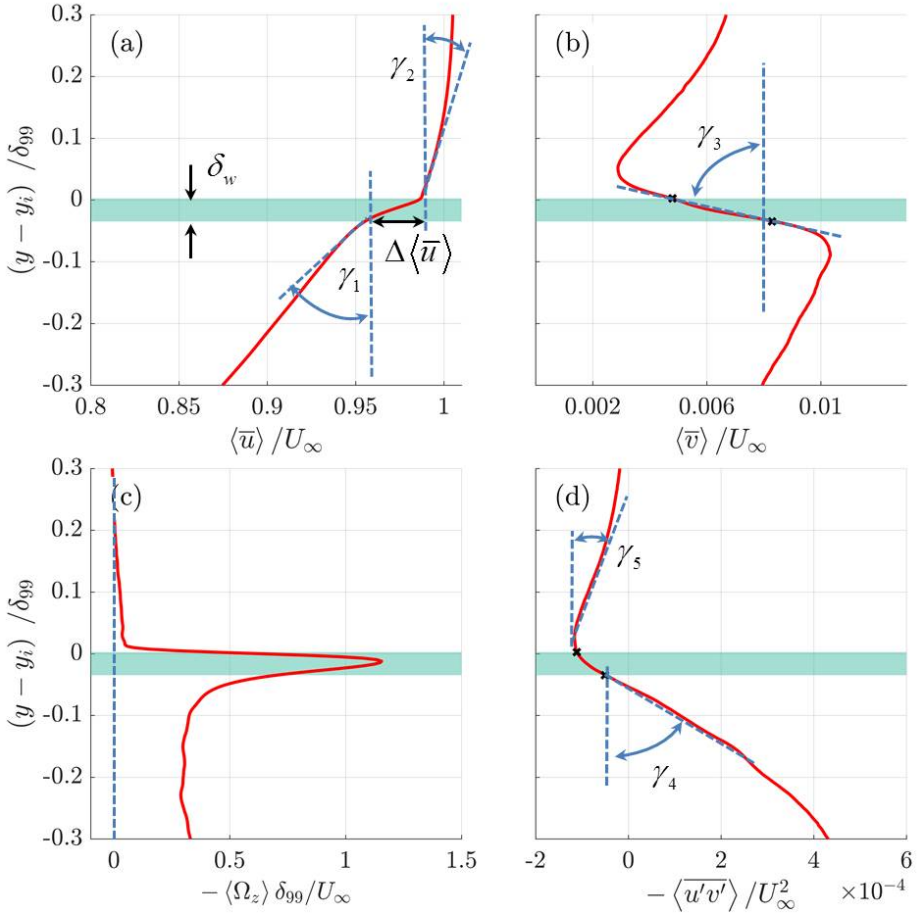

Figure 2.6: (a) Conditionally sampled velocity profile $\langle\overline{u}\rangle$ over the T/NT interface.(b) Conditional $\langle\overline{v}\rangle$. (c) Conditional out-of-plane vorticity $\langle\Omega_z\rangle$. (d) Conditional sampled Reynolds shear stress profiles $\left\langle\overline{u'v'}\right\rangle$. The green patch indicates the jump region. The relevant gradients are indicated by $\gamma_1 - \gamma_5$. The values for $V_{y_1}, V_{y_2}, \left\langle\overline{u'v'}\right\rangle_{y_2}$ and $\left\langle\overline{u'v'}\right\rangle_{y_1}$ are indicated by black dots. Positive y-axis points in the same direction as the wall-normal axis.

In order to derive the entrainment velocity of the T/NT interface, the first order jump model as described in section 2.4 is employed. First of all the edges of the T/NT interface are determined from the linear fits made to the velocity profile in Figure 2.6a on both the turbulent side (lower part) and the non turbulent side (upper part). For the current research the intersections between these fits are regarded as the edges of the T/NT interface, this yields a jump in streamwise velocity $\Delta\langle\overline{u}\rangle = 0.04U_\infty$ and a thickness over which this jump occurs of $\delta_w = 0.035\delta_{99}$. δ_w is an important geometric

attribute, it describes the characteristic "thickness" of mixing layer eddies that exchange momentum between zones of uniform momentum. The different gradients, depicted in Figure 2.5, that are required to calculate E_b are indicated in Figure 2.6. The values for the wall-normal and the Reynolds shear stress at top and bottom side of the interface are indicated by black dots. Combining these results and substituting this into Equation 2.4 produces a boundary entrainment velocity $E_b = 0.0109U_\infty$.

A second validation strategy adopting a different approach is employed to calculate the boundary layer growth rate, using a method as described by White [66]. Basically, von Kármán's momentum law $\left(c_f = 2\frac{d\theta}{dx}\right)$ and a power-law approximation to the friction number $\left(c_f \approx 0.02Re_\delta^{-1/6}\right)$ are combined together with a $1/5^{th}$ power law approximation of the TBL velocity profile. A fit to the mean velocity profile of the TBL (not shown here) justifies a $1/n^{th}$ power law approximation to the mean velocity profile, where $1/n = 0.1931 \pm 0.002$. Therefore, the $1/5^{th}$ power law approximation (with a difference of less than 2%) was applied to predict the global boundary layer growth. This yields a first order differential equation that can be solved by separation of variables. The spatial growth rate is thus estimated as:

$$\frac{d\delta}{dx} \approx 0.14\frac{6}{7}\left(\frac{\nu}{U_\infty x}\right)^{\frac{1}{5}} \approx 0.0142, \tag{2.5}$$

where x is taken as the distance behind the trip wire (i.e. $x = 3.5$m). The average T/NT interface position is observed at $\langle\delta_{int}\rangle \approx 0.90\delta_{99}$. Hence, the spatial growth rate of the T/NT interface is approximated by: $\frac{d\delta_{int}}{dx} \approx \frac{\delta_{int}}{\delta_{99}}\frac{d\delta}{dx} \approx 0.0128$. From the conditional streamwise velocity profile in Figure 2.6a it is observed that the local convection velocity at the mean interface location is $U_c \approx 0.97U_\infty$. Hence the boundary entrainment velocity can be approximated by:

$$E_b \approx U_c\frac{d\delta_{int}}{dx} \approx 0.0124U_\infty \tag{2.6}$$

Given the above assumptions and the finite measurement precision the difference between Equation 2.6 and the results obtained from the first order jump model fall within acceptable limits. Comparing the result given in Equation 2.6 and the results obtained from the first order jump model, it turns out that both are in close agreement (i.e. $\approx 12\%$ difference). Hence, the analysis near the T/NT interface could be directly related to the large scale features of the boundary layer growth rate.

2.5.2 INTERNAL LAYERS

Conditional sampling is also performed on the internal layers. The resulting profiles of the streamwise velocity, wall-normal velocity and the Reynolds shear stress are given in Figure 2.7. Comparing the conditional streamwise velocity profiles for the T/NT interface (Figure 2.6) and the internal shear layers (Figure 2.7) it is clear that both display qualitatively similar behavior. This supports the notion that the shear layers inside the TBL are in essence similar to the external T/NT interface in the current framework of the integral momentum balance approach. It should be noted however that this observation does not imply that both the T/NT interface and the internal shear layers are

identical in the small scale details which have been lost in the conditional averaging process. The jump in conditional streamwise velocity shown in Figure 2.7a indicates a strong increase towards the wall, whereas an approximately constant velocity jump is obtained far away from the wall ($y/\delta_{99} > 0.5$). Furthermore, $\frac{\partial\langle\overline{u}\rangle}{\partial y}$ on the bottom side of the internal layers increases much more rapidly compared to the top side. As such, the flux of momentum through the interface increases closer to the wall. From Figure 2.7b it is clear that $\frac{\partial\langle\overline{v}\rangle}{\partial y}$ is negative over the internal layers similar to the external T/NT interface, indicative of vorticity stretching happens within these internal layers. It should be noted that the Reynolds shear stress profiles in the outer region of the TBL do not appear to be converged (Figure 2.7c). As is evident from Figure 2.4a it is due to the small number of layers found at that location.

Closer to the wall the conditional Reynolds shear stress profiles $\left\langle\overline{u'v'}\right\rangle$, shown in Figure 2.7c, depict a distinct jump over the layer, which increases when approaching the wall. On the top side of the layers (i.e. $(y-y_i)/\delta_{99} > 0$), the shear stress profiles steadily decrease towards zero. It should be noted that in contrast to the T/NT interface, the shear stresses over the internal layers never reaches positive values. On the bottom side of the shear layers (i.e. $(y-y_i)/\delta_{99} < 0$) near wall peaks in Reynolds shear stress are observed (i.e. for layers below $y/\delta_{99} = 0.5$).

The velocity jump across the internal layers is quantified in Figure 2.8a. As mentioned before an approximately constant value is observed for $y/\delta_{99} > 0.5$ (Figure 2.8a). The jump thickness is observed to scale with the local Taylor microscale (Figure 2.8b, $\delta_w \approx 0.4\lambda_T$), which is in accordance with the scaling of the T/NT interface thickness [33, 36].

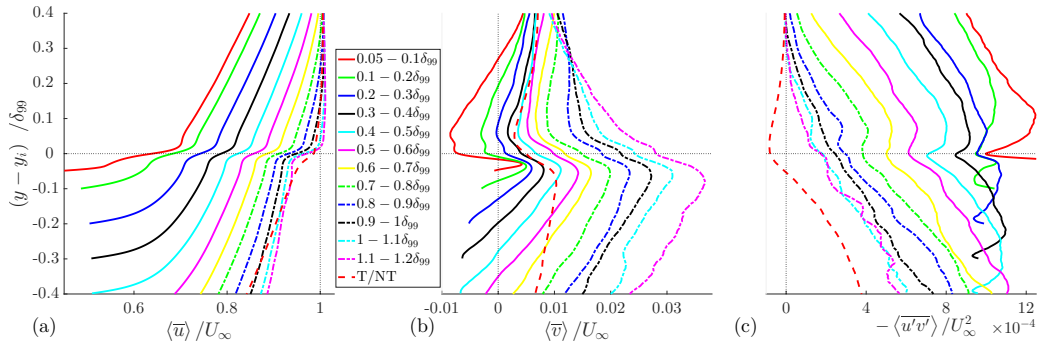

Figure 2.7: (a) Conditionally sampled streamwise velocity profiles over internal shear layers. (b) Conditional wall-normal velocity profiles. (c) Conditionally sampled Reynolds shear stress profiles. Positive y-axis points in the same direction as the wall-normal axis. Shear layers are binned according to their centroidal location in the boundary layer with a binsize of $0.1\delta_{99}$.

As a next step, the model approach as shown in Figure 2.5 is applied to the internal layers to obtain E_b for each internal layer from Equation 2.4. The result is presented in Figure 2.9. A standard bootstrapping method is applied to derive the confidence interval. The first point above the wall indicates a large confidence interval due to the large gradients that are present. It turns out that the internal shear layers move faster away from the wall as y/δ_{99} increases. The conceptual picture that emerges from this graph is that one may have a TBL with multiple shear layers where the outermost layers move

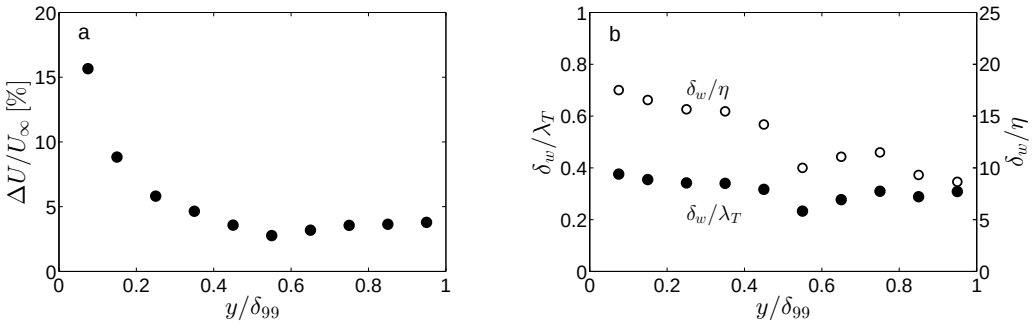

Figure 2.8: (a) The streamwise velocity jump $\Delta \langle \overline{u} \rangle$ normalized with U_∞ as function of the wall normal distance. (b) Layer thickness estimated from the streamwise velocity jump of the internal layers normalized with the local λ_T and with the local Kolmogorov length scale η.

at a velocity faster than the innermost layers. It may well be that shear layers accelerate when moving up into the boundary layer and then eventually become the new T/NT interface as the old interface further from the wall dissipates and disappears. It should be noted that this concept only holds for the average shear layers, as instantaneously there still might be coalescence between different shear layers. Note that the entrainment velocities of the internal layers present in the outer layer (i.e. at $y/\delta_{99} = 0.8 - 0.9$) are approximately twice as high as the boundary layer growth rate calculated before. Hence, internal shear layers have the tendency to run into the non-turbulent region faster than the overall growth of the boundary layer. Comparing the internal shear layer entrainment velocity E_b with the wall normal velocity profile $\overline{v}$ obtained from DNS data [67], it is observed that the shear layers are not moving with the average wall-normal velocity. In fact, the entrainment velocity of the internal shear layers E_b is larger than V. This indicates that the layers are dynamically significant [28] and there is actual mass transport across the layers.

2.6 DISCUSSION

As suggested in Figure 2.3, shear layers separate large scale regions of approximately uniform momentum. This has been observed before by Meinhart and Adrian [22], Adrian *et al.* [43], Christensen and Adrian [47], Hambleton *et al.* [45], and Wei *et al.* [49]. From the analysis performed in section 2.5 we derived the entrainment velocities of conditionally averaged shear layers. This process can be regarded as analogous to the overall boundary layer entrainment by the T/NT interface, which governs the growth of the TBL. A first suggestion that presents itself is that the entrainment velocities of the shear layers may be indicative for the growth rate of the uniform momentum zones that they bound. This is supported by the observation that the angle of the internal shear layers is found to be 12°, which corresponds to the typical angle of hairpin packets [43]. From Figure 2.9 it is clear that the conditionally averaged shear layers in the region $y/\delta_{99} > 0.5$ move at velocities on the order of the average boundary layer growth rate, shown as the red/green dot. We therefore conjecture that large scale regions on average grow slowly, i.e. with the same order of magnitude as the average boundary layer

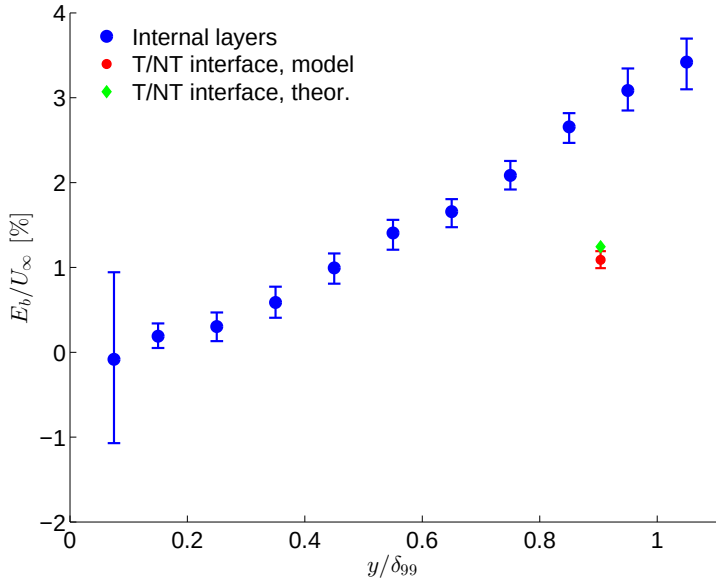

Figure 2.9: The boundary entrainment velocity E_b of the internal shear layers (blue dots) normalized with U_∞ as function of the wall normal distance. The errorbar indicates the 95% confidence interval obtained from a standard bootstrapping method. The red dot indicates E_b of the T/NT interface obtained from the first-order jump model, whereas the green dot indicates the E_b for the T/NT interface obtained from Equation 2.6

growth rate. Furthermore, it is worth mentioning that the boundary entrainment velocity of the average shear layer at $y/\delta_{99} = 0.2$ ($E_b \approx 0.003U_\infty$) shows a correspondence with the work of Elsinga *et al.* [68], who found the average wall-normal convection velocity of spanwise vortices to be $0.006U_e \pm 0.002U_e$. Assuming these vortices populate the shear layers, this correspondence with the motion of instantaneous vortex structures supports the present conditional averaging approach. Furthermore, the recent work by Zheng and Longmire [69] showed that 77% of the observed low momentum regions remained coherent over a significant long streamwise distance ($> 9\delta_{99}$). Similar results have been obtained by Dennis and Nickels [70]. As such, the layers accompanying these large scale motions will also be persistent over long streamwise distances. A simple analysis using Figures 2.9 and 2.1a is carried out in order to estimate where the average shear layer at a height $y/\delta_{99} = 0.95$ may have originated from. First the movement of the shear layer is evaluated in the wall-normal direction based on its entrainment velocity (Figure 2.9), yielding its y-position with time $y^*(t)$ between $y = 0$ and $y = 0.95\delta_{99}$. At the same time the layer also travels a distance x^* in the streamwise direction, which is obtained by integrating the mean velocity profile over $y^*(t)$. Based on this calculation it turns out that this average layer originated from the wall approximately $50\delta_{99}$ upstream. As we measured $40\delta_{99}$ downstream of the boundary layer trip, this cannot be the case. Therefore, we conjecture that shear layers may be generated not only at the wall but also via distinct (yet unknown) mechanisms away from the wall. This concept challenges the idea of for instance Head and Bandyopadhyay [71]. Based on their vi-

sualization study they proposed that hairpin structures are generated at the wall and rapidly grow into the outer region of the turbulent boundary layer.

2.7 SUMMARY AND CONCLUSIONS

In this chapter, the characteristics of the T/NT interface and the internal layers have been quantified experimentally in a turbulent boundary layer. Layered structures have been observed before in statistical analysis of different turbulent flows [47, 48]. However, the current results confirm the existence of such layered structures in instantaneous flow fields. Conditional sampling is used to determine the quantitative properties of these layers. Compelling evidence is given that the internal layers and the external T/NT interface show qualitatively the same behavior in terms of the conditional velocity profiles. A first order jump model is applied in order to estimate the entrainment velocities of the interface and internal layers. By this approach a correct prediction of the overall boundary layer growth could be obtained. Furthermore, conditional averaged internal layers move slowly in close vicinity of the wall, whereas their entrainment velocity is of the order of the boundary layer growth rate in the outer part of the TBL. The internal layers are believed to bound the large scale motions in the flow. Therefore, the current results strongly suggest that these large scale motions only grow slowly, i.e. on the order of the boundary layer growth rate.

3

THE ROLE OF UNIFORM MOMENTUM ZONES IN THE DISPERSION OF A PASSIVE SCALAR

3.1 INTRODUCTION

Dispersion of pollutants commonly occurs around urban environments that are submerged in a turbulent flow. The worldwide increase of urban areas and the increasing energy consumption give rise to more pollutant emission sources near populated areas. Consequently, there is a need to generate reliable models for urban air pollution. In turn, this requires proper understanding of the mechanisms of pollutant dispersion in turbulent environments. Despite the fact that turbulence is characterized by highly chaotic and disordered motions, recent research has shown that large scale coherent structures are existing in turbulent flows. An example of such a coherent structure is the uniform momentum zone (UMZ) as observed by Meinhart and Adrian [22]; see also Chapter 2. These UMZs are also observed in atmospheric boundary layers (ABL) at much higher Reynolds numbers [23, 44, 73].

Recent work suggests that these large scale motions (LSM) strongly influence the dispersion of air pollution in urban areas that are immersed in ABLs [74, 75]. For instance, Michioka and Sato [74] showed that instantaneous large-scale low momentum regions passing over idealized street canyons largely overlap with regions of high pollutant concentrations, indicating the importance of these LSMs for pollutant dispersion processes in urban environments. This is supported by the results obtained by Perret and Savory [75], who showed that the coupling or decoupling of the flow within the canyon and the flow is strongly influenced by these LSMs.

In this chapter we perform a combined time resolved scanning *tomographic particle image velocimetry* (TPIV), and *laser induced fluorescence* (LIF) experiment on a TBL to elucidate the role of UMZs, and the shear layers that separate these UMZs on the dispersion of a passive scalar. A scanning-TPIV approach [76, 77] allows for a high spatial resolution within a thick volume, by reducing the number of ghost particles in the separate reconstructed volumes. Recently, tomographic LIF was introduced by Halls *et al.* [78]. Here however, volumetric LIF is achieved by scanning thin light sheets through the measurement volume. Combining PIV and LIF measurements provides the opportunity to quantify turbulent transport [79]. For instance, Westerweel *et al.* [29] used the combined PIF/LIF technique to study turbulent entrainment at the turbulent/non-turbulent

This chapter is an extended version of: J. Eisma, J. Westerweel, and G. E. Elsinga, "Simultaneous scanning tomo-PIV and LIF in a turbulent boundary layer: The role of internal shear layers in the dispersion of a passive scalar," in *11th Int. Symp. Part. Image Velocim.*, Santa Barbara, 2015, pp. 1–10

interface of a jet. A more sophisticated approach was used by Hishida and Sakakibara [80], who employed a two-color planar LIF measurement combined with planar PIV, which enabled them to study the mechanism of turbulent heat transfer of an impinging jet on a heated plate.

The present experiment considers the dispersion of a passive scalar from a point source in a TBL. Specifically, the objectives of this study are to explore the properties of uniform momentum zones and uniform concentration zones [22, 73] in terms of occurrence, geometrical characteristics (e.g. size), and conditional statistics around the edges of these zones. The conditional statistics show that both uniform momentum zones (UMZ) and uniform concentration zones (UCZ) are distinct zones separated by regions of increased shear [26], which basically act as barriers to concentration fluxes. Furthermore, the geometrical overlap between UCZs and UMZs is identified [81], indicating the relevance of UMZs to passive scalar dispersion.

This chapter is organized as follows. First of all the experimental setup is discussed in Section 3.2.1. Basic velocity and passive scalar concentration statistics are given in Section 3.2.2. Details of the TPIV reconstruction and an assessment of the measurement accuracy are given in Section 3.2.3. The filtering, calibration, and reconstruction procedure regarding the LIF images are given in Section 3.2.4. An extensive discussion on the characteristics of UCZs and UMZs is given in Section 3.3. Finally, conclusions are drawn in Section 3.4.

3.2 MATERIALS AND METHODS

3.2.1 EXPERIMENTAL SETUP

The experiment was performed in the same water tunnel facility that was used for the measurements described in Chapter 2. The boundary layer under consideration developed over one of the side walls of the test section. Measurements were performed approximately 3.5 m downstream of the boundary layer trip (a spanwise zig-zag tape). The passive scalar (a dye) was injected as a point source at the wall, nearly 750 mm upstream of the measurement volume, corresponding to $18\delta_{99}$, where δ_{99} is the wall normal distance where the velocity reaches 99% of the free-stream velocity $U_\infty = 0.74$ m/s. The spanwise location of the source was approximately halfway the tunnel depth (see Figure 3.1). The dye was injected with a syringe pump (Hamilton ML500) at half the free-stream velocity $U_i = 0.5U_\infty$

In order to measure the flow velocity and the scalar concentration simultaneously, a scanning tomographic PIV system was combined with scanning LIF. An image and a sketch of the setup are given in Figure 3.1, indicating the different components. Four high-speed CMOS cameras (Dimax, PCO) are used for tomographic PIV. Two cameras were equipped with $f = 200$ mm objectives, whereas the others were equipped with $f =$ 105 mm objectives, all operating at $f_\# = 11$. Additionally, all PIV cameras were equipped with Scheimpflug adapters to allow for large viewing angles while keeping the particle images in focus. The top two PIV cameras were positioned at a nominal angle of $\beta = 30^\circ$ with respect to the normal of the light sheet, whereas the both side viewing PIV cameras were looking at a nominal angle of $\beta = 45^\circ$ with respect to the normal. In order to

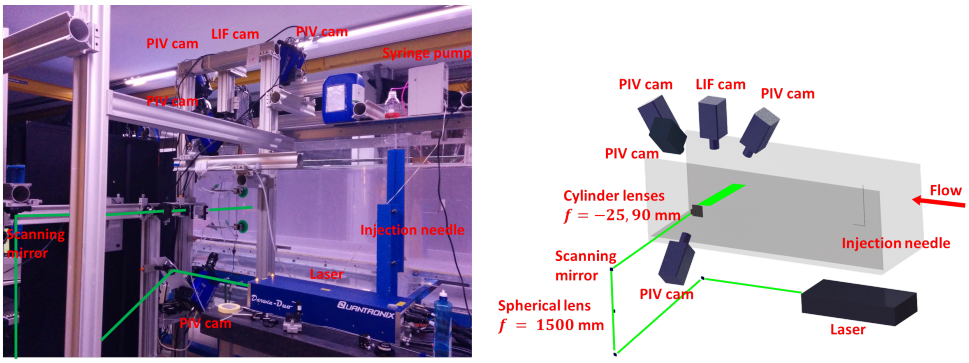

Figure 3.1: (left) Overview of the experimental setup indicating the different components: Four PCO Dimax PIV cameras, a Photron Fastcam LIF camera, a highspeed ND:YLF laser, the syringe pump and the injection needle. The solid green line indicates the path of the laser beam/sheet. (right) An additional sketch of the setup indicates the same components.

minimize astigmatic aberrations, water-filled prisms were employed for all PIV cameras. LIF is performed using a single high-speed camera (Fastcam, Photron) equipped with a $f = 105$ mm objective at $f_\# = 8$. Illumination was provided using a 50 mJ double pulsed Nd:YLF laser (Darwin Duo 80M, Quantronix) with a frequency-doubled light wavelength of 527 nm.

A long focal length spherical lens ($f = 1500$ mm) was employed in order to focus the laser beam into a narrow beam. Subsequently, two cylindrical lenses with focal lengths of -25 and 90 mm, respectively, were used to create a 90 mm wide collimated light sheet with a thickness of about 1.4 mm. The light sheet spans the streamwise (x) and the wall-nomal (y) directions of the TBL, while the scanning is performed in the spanwise direction (z). The use of a collimated beam was mainly motivated by the fact that the stripe removal filter (see Section 3.2.4) performs optimal when possible striations in the LIF images were oriented either horizontally or vertically along either pixel rows or pixel columns. Scanning of the measurement volume was performed using a galvanometer (6210H, Cambridge Technology) with a small 5 mm diameter mirror. The scanning protocol was generated via a custom written LabView script, resembling a staircase like sawtooth wave; see Figure 3.2.

Each scan, consisting of five subvolumes, is followed by a fly back time t_f (less than 130 μs). The scanning mirror is located 1660 mm away from the measurement location. As the width of the scanned volume is at most 12 mm, the maximum deflection of the mirror is limited well below 1 degree. Hence, the different sheets within the measurement volume can be regarded as parallel, similar to Casey *et al.* [77]. The galvanometer was synchronized with the camera and laser setup via the Highspeed controller (LaVision GmbH). The second trigger pulse of the laser is used with a delay of 10 μs to trigger the mirror to proceed to the next position. The scanning motion was found to be quite stable over a dataset (see Section 3.2.3). The overall measurement volume consists of five thin laser sheets of 1.4 mm thickness each, with an overlap of approximately 30%. A scanning frequency f_s of 640 Hz results in a recording frequency of the full measurement volume of 128 Hz.

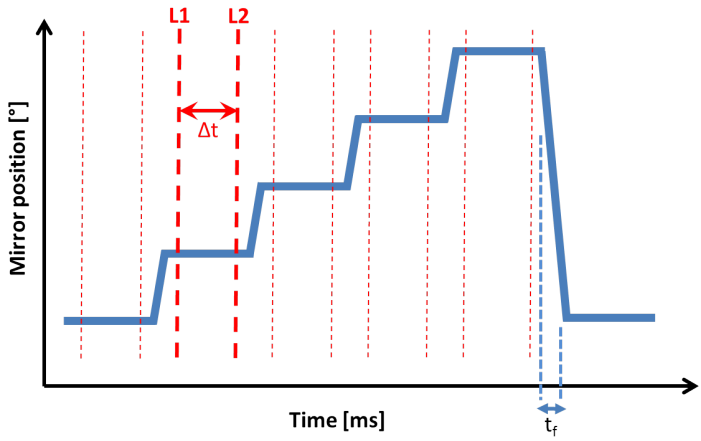

Figure 3.2: Timing sequence showing the mirror position with the laser pulses indicated by the dashed vertical red lines. The first and second laser pulse are indicated by L1 and L2 respectively, the time separation between the pulses by Δt and the fly back time by t_f.

The flow is seeded with 10 μm diameter tracer particles (Sphericell) that are nearly neutrally buoyant. The seeding density in the TPIV images is around 0.025 particles per pixel (ppp), corresponding to an equivalent source density of approximately $0.05 - 0.075$ [82]. Rhodamine B (Rh-B) was selected as the dye, because the current laser, operating at a wavelength of 527 nm, is suitable for excitation of this dye. Separation of the PIV and LIF signals is obtained by employing lowpass filters (PIV cameras) and a highpass filter (LIF camera). Calibration of the distorted LIF and PIV images was performed using a 3D calibration plate (Type 11, LaVision). The mapping of the distorted images was done using 3rd order polynomials in x- and y-direction, whereas linear interpolation is used in the z-direction. Self-calibration, as proposed by Wieneke [83], was performed to enhance the accuracy of the particle reconstruction. After several refinements, the remaining disparities were typically on the order of $0.1 - 0.2$ pixels. Data acquisition and processing was performed with a commercial software package (Davis 8.2, LaVision). Image pre-processing was applied on the PIV images in order to eliminate the effect of background noise. First, a sliding minimum filter, with a filter length of 6 pixels in both directions was applied, to remove background noise. The filter length was slightly larger than the average particle image diameter of $2 - 3$ pixels, to avoid eliminating real particles. Second, a local average filter was employed with a filter length of 150 pixels, to eliminate the reflections in the near-wall region. Finally, a Gaussian smoothing filter with a kernel size of 3×3 pixels was used. As a next step, the particle volumes were reconstructed from the PIV images using five iterations of the Fast-MART algorithm [84]. The particle volumes were 3D cross-correlated using an iterative multi-grid scheme reaching a final interrogation box size of 32^3 voxels. This yields a spatial resolution of about 1.1 mm, corresponding 34 wall units in each direction. The resulting field of view is $1.50\delta_{99}$, $1.65\delta_{99}$, and $0.15\delta_{99}$ in streamwise, wall normal and spanwise direction respectively. Velocity and concentration gradients were obtained by

employing a second-order spatial regression filter [85] with a filter size of 1.5 times the dimension of the interrogation box in each direction.

Care was taken to ensure that the concentration in the LIF images is sufficiently low for the fluid to be optically thin, resulting in no attenuation along light rays. In that case the analysis of the LIF signal can be simplified significantly [86], avoiding a pixel wise correction procedure. For further details on the theoretical background and the practical implementation of the LIF technique, the reader is referred to Section 4.4.4. In order to convert the local light intensity to a local dye concentration a calibration procedure was performed. For this purpose, a small container with a known uniform concentration is positioned inside the measurement domain, after which images were recorded. This procedure was repeated for a few different known concentrations, resulting in a calibration curve for each pixel. Linear interpolation was employed to obtain the dye concentration from intensities at each pixel location. After calibration small negative concentrations were present in the free-stream region of the flow (see Figure 3.8 and 3.11), which is a result of the finite accuracy of the LIF calibration. In order to remove these negative concentrations, the mean value of the concentration in the free-stream part of the flow is set to zero by subtracting it from the from the concentration field, thereby eliminating most of the negative concentration values in this part of the flow.

3.2.2 BOUNDARY LAYER STATISTICS

For the general characterization of the TBL, the top two PIV cameras shown in Figure 3.1 were used to obtain stereoscopic PIV (SPIV) data at a sampling rate of 40 Hz. A total of 5522 samples were used to obtain the boundary layer statistics. The results were used to compute the mean velocity profile as well as the RMS profiles of the velocity fluctuations across the boundary layer. Furthermore, a comparison is made with the boundary layer statistics obtained from the TPIV measurements. At the measurement location the boundary layer thickness is $\delta_{99} = 38$ mm. The resulting momentum and displacement thicknesses are $\theta = 4.0$ mm and $\delta^* = 5.2$ mm, respectively. This results in a shape factor $H = 1.32$, which is a typical value for a zero-pressure gradient TBL [56]. The Reynolds number based on the momentum thickness is $\mathrm{Re}_\theta = 3050$, which is well above the transitional regime [87]. The wall-friction velocity ($u_\tau = 31$ mm/s) was determined based on the Clauser plot technique [88]. The main properties of the TBL are summarized in Table 3.1. The velocity profiles in inner scaling as well as the RMS profiles in outer scaling are shown in Figure 3.3. On top of these results, also the profiles from the TPIV datasets are shown. First of all, there is a good overlap between the stereo PIV data and the TPIV data, i.e. the difference in mean velocity profiles is less than 3%. Furthermore, a difference between both PIV datasets and the reference data from DeGraaff and Eaton [56] is less typically less than 2% in the mean velocity profiles. Figure 3.3a indicates the presence of a slightly favourable pressure gradient, as the wake is slightly suppressed compared to the reference data. Independent pitot tube measurements by Eisma *et al.* [26] show that this pressure gradient is small, i.e. the acceleration parameter ($K = \nu/U_\infty^2 dU_\infty/dx$) is on the order of $\mathcal{O}\left(10^{-8}\right)$, and this implies that this pressure gradient has a negligible influence on the results presented here [55]. The turbulence intensities are presented in Figure 3.3b. The RMS values for u are around 4% higher in the region up to $y/\delta_{99} = 0.75$ for both TPIV data and SPIV data

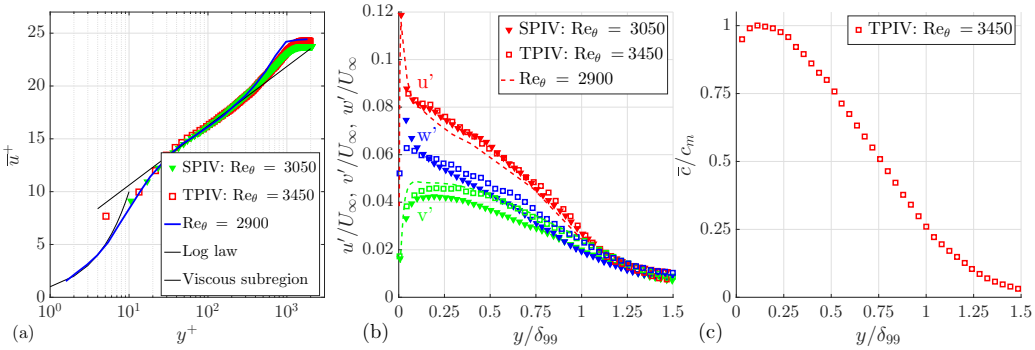

Figure 3.3: (a) The velocity profile in inner scaling. (b) The RMS profiles of the fluctuations of the three velocity components compared with data from DeGraaff and Eaton [56]. (c) Mean concentration profile across the boundary layer. The maximum concentration c_m is used for normalization of the concentration statistics.

when compared to DeGraaff and Eaton [56], while in the same region the RMS values for v are underestimated by 3% in the TPIV data and by 14% in the SPIV data compared with data from DeGraaff and Eaton [56]. A higher turbulence level in the free-stream ($y/\delta_{99} > 1$) is present in comparison to Schröder *et al.* [89] who reported free-stream turbulence levels below 0.5% for the same flow facility. Similar to Poelma *et al.* [52], the noise level in the free-stream region is estimated based on the autocorrelation of the velocity components. At $y/\delta_{99} = 1.2$ the noise level in the SPIV data is $0.0024U_\infty$, $0.0027U_\infty$, and $0.0078U_\infty$ for u, v, and w respectively. Hence, the real turbulence levels are below 1% of the free-stream velocity.

Finally, the mean scalar concentration $\overline{c}$ profile across the boundary layer is shown in Figure 3.3c. The maximum concentration is found around $y/\delta_{99} = 0.11$. Please note that the region in close vicinity ($y/\delta_{99} < 0.1$) of the wall should be taken with care due to reflections from the wall. The concentration approaches zero in the free-stream part of the flow, as expected. The maximum value of the mean concentration profile $c_m = 0.074$ mg/L is used to normalize concentration statistics in Section 3.3.

Table 3.1: Summary of the boundary layer properties.

U_∞	0.74 m/s	θ	4.0 mm	Re_τ	1235
δ_{99}	38.1 mm	u_τ	31 mm/s	$H = \delta^*/\theta$	1.32
δ^*	5.2 mm	Re_θ	3050	c_f	3.4×10^{-3}

3.2.3 RECONSTRUCTION AND QUALITY ASSESSMENT OF THE TPIV VOLUMES

Reconstruction of TPIV Volumes

First we assess the quality of the reconstructed particle subvolumes. Figure 3.4a presents the light intensity profile in the depth direction (z) averaged over the two in-plane direc-

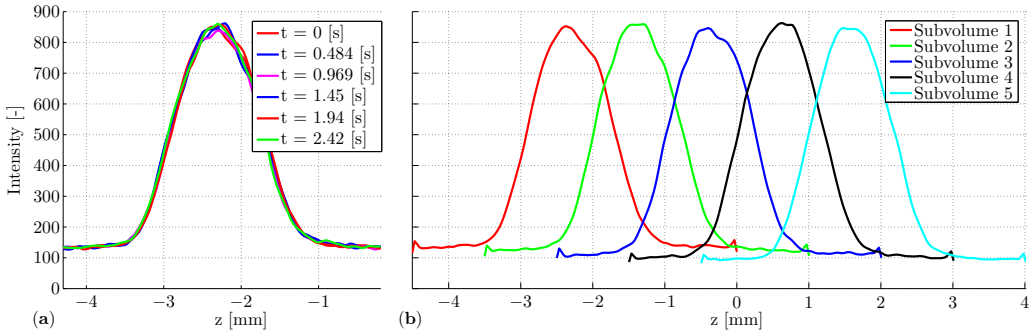

Figure 3.4: (a) The intensity profiles of the first frame in the measurement volume at different time instances in the dataset. (b) The intensity profiles of consecutive subvolumes composing a single measurement volume.

tions (x and y). The different profiles correspond to the same subvolume in subsequent scans of the full measurement volume. The results show that the scanning mirror is accurate, that is, the light sheet is returned to the same position after a full scan. There is virtually no jitter, i.e. the center of gravity of the displayed curves in Figure 3.4a varies by less than 1%. Furthermore, the resulting intensity distribution indicates a laser sheet thickness of about 1.4 mm, where the laser sheet thickness is defined as the full width at half the maximum intensity. The noise level in the reconstruction is estimated from the reconstructed intensity outside the light sheet, which is about 17% of the peak average intensity inside the light sheet. This is considered to be a low noise level [84]. Figure 3.4b shows a graph of the intensity profiles of adjacent subvolumes that together make up the complete measurement volume.

The volume cross-correlation analysis of each reconstructed subvolume provided the instantaneous velocity distribution within that subvolume. The thin sliced vector subvolumes were then stitched together in order to obtain a single vector volume. Due to the finite scanning frequency (i.e. $f_s = 640$ Hz), the flow structures are convected downstream between consecutive subvolumes. In case of a measurement volume consisting of five subvolumes the shift between the first and the last recorded subvolume in the outer region of the flow is on the order of 4.6 mm (or 150 viscous wall unit). This corresponds to five interrogation windows, which is regarded to be non-negligible. A complicating factor is the presence of a strong velocity gradient near the wall. Hence, the shift depends on the height within the boundary layer. To compensate for this inhomogeneous shift the subvolumes within the volume are shifted with respect to the third subvolume as:

$$x_c = x - u(y)\frac{n}{f_s}, \tag{3.1}$$

where $u(y)$ is the spatially averaged streamwise velocity profile in wall normal direction obtained in an instantaneous realization of the third subvolume, and n is -2, -1, 0, 1 and 2 for subvolumes $1-5$ respectively. The first two subvolumes (1, 2) are shifted forward in time, hence space, whereas the last two subvolumes (4, 5) are shifted backward in space. The shifted velocity volumes are then interpolated onto a single grid using a

cubic spline interpolation method, which approximates the velocity distribution at the time of the third frame ($n = 0$).

Quality Assessment

In order to assess the quality of the stitched velocity volumes, a joint probability density function (JPDF) of the velocity gradients $-\partial u/\partial x$, and $(\partial v/\partial y + \partial w/\partial z)$ is shown in Figure 3.5a. From mass conservation it follows that the data in Figure 3.5a should be along the red diagonal line, indicating the divergence free condition. The length of the distribution along the diagonal line indicates the range of measured velocity gradients, while the width of the distribution is indicative for the noise level. The JPDF shows that the data is aligned with the diagonal, indicating that no systematic errors are present in the stitched vector volumes. The correlation coefficient between the two components $-\partial u/\partial y$ and $\partial v/\partial y + \partial w/\partial z$ is 0.84 (at $y/\delta_{99} = 0.3$), which is comparable to the results found by Jodai and Elsinga [90] for TPIV in the near-wall region of a TBL. Correlation coefficients of 0.96 can be achieved for scanning TPIV measurements as shown by Casey *et al.* [77]. The slightly smaller value found here is probably due to the relatively low seeding density of 0.025 ppp in the current images, and the stitching procedure that increases the divergence error. This is also observed from the contours shown in Figure 3.5a, which have a smaller aspect ratio compared to the data shown by Jodai and Elsinga [90], indicative for a larger divergence error in the present results. The present RMS divergence error is $7.9\,\mathrm{s}^{-1}$. This error is found to be acceptable as it is less than 20% of the threshold used to identify the shear layers in Figure 3.7. Despite this slightly higher divergence error, the influence on the observations in the current chapter is believed to be small as none of the structure detection presented in Section 3.3 is based on the velocity gradients.

Furthermore, two probability density functions (PDF) are calculated. Figure 3.5b shows the PDFs of the quantity $\nabla \cdot U$ normalized with the 2-norm of the velocity gradient tensor similar to Casey *et al.* [77]. The PDFs have been obtained in the outer layer of the TBL, i.e. between $0.3 < y/\delta_{99} < 0.4$. The mean value turns out to be approximately zero, whereas the RMS value is 0.27. This is consistent with values reported by Casey *et al.* [77] (and references therein). Typical values are found in the range of 0.07 [77] up to 0.3 [91]. Following Zhang *et al.* [92], Figure 3.5c indicates the parameter ζ which is given by:

$$\zeta = \frac{(\nabla \cdot U)^2}{\mathrm{trace}\,(\nabla U \cdot \nabla U)} \tag{3.2}$$

This parameter captures the deviation of the divergence of the velocity field with respect to the divergence free condition ($\zeta = 0$). For the current case, a mean value $\zeta = 0.21$ is found, which is in the same range as Casey *et al.* [77] found for a scanning tomographic PIV experiment on a turbulent jet ($\zeta = 0.09 - 0.36$), and channel flow experiments with holographic PIV ($\zeta = 0.07 - 0.74$) by Zhang *et al.* [92].

Based on these three indicators it is shown that the divergence of the velocity field is regarded to be within acceptable limits.

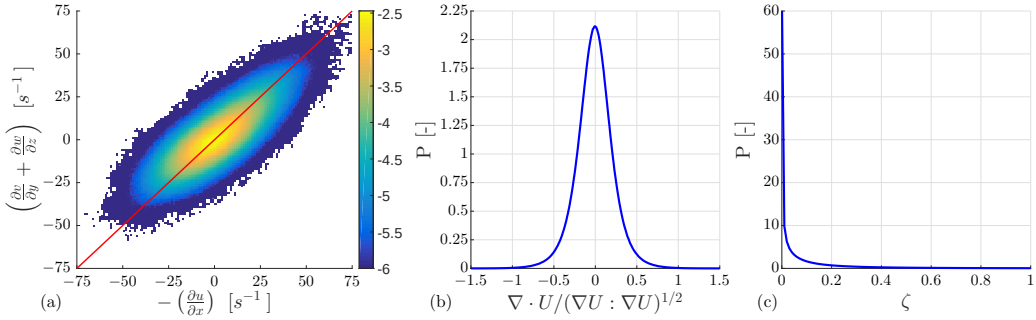

Figure 3.5: (a) JPDF of $-\partial u/\partial x$ and $\partial v/\partial y + \partial w/\partial z$. The contours are in log scale. (b) PDF of the divergence of the vector field U normalized with the 2-norm of the velocity gradient tensor. (c) PDF of the divergence error ζ as defined by Zhang *et al.* [92].

3.2.4 RECONSTRUCTION OF THE LIF VOLUMES

The raw LIF images are processed in a number of steps. The first step is to map the LIF data onto the correct spanwise location. The spanwise location of the LIF image is determined from the intensity profiles of the reconstructed intensity volumes from the PIV images (see Figure 3.4b). The spanwise location of the peak in the mean intensity is taken as the position where the LIF image is positioned. Next, a background image is subtracted from the LIF images, eliminating the uniform background that is present in the images. Second, due to scratches and other imperfections in the light sheet, the raw LIF images show the presence of striations or stripes. Following Krug *et al.* [93] these stripes are effectively removed by employing a combined Fourier/wavelet filter approach developed by Münch *et al.* [94]. Occasionally the scattered light by the particles passes the high pass filter of the LIF images [93]. In order to eliminate the contributions of those particles, a median filter is applied with kernel size of 9×9 pixels, which proves to be an effective filter to remove this type of noise. A sample image of an unfiltered field and the filtered versions is given in Figure 3.6. Similarly as for the PIV subvolumes, the average streamwise velocity profile determined in the third PIV subvolume is used to properly shift the LIF images. However, an additional shift is required to position the LIF images at the same time instance at which the velocity fields are obtained, i.e. halfway between the double-exposure LIF images that were simultaneous recorded with the double frame PIV images. Hence the total shift for the LIF images reads:

$$x_c = x - u(y)\left(\frac{n}{f_s} + m\Delta t\right) \tag{3.3}$$

where $f_s = 640$ Hz is the scanning frequency, n is -2, -1, 0, 1 and 2 for subvolumes $1-5$ respectively, $\Delta t = 780\,\mu$s is the time separation between the exposures, and m is $-1/2{,}1/2$ for the first and second frame respectively. Instead of using one of the two LIF images, the average of both images after the shift correction is used to obtain the LIF realization at the same time instance as the velocity fields. This yields the most accurate representation of the LIF image at the time instance at which the PIV results are obtained.

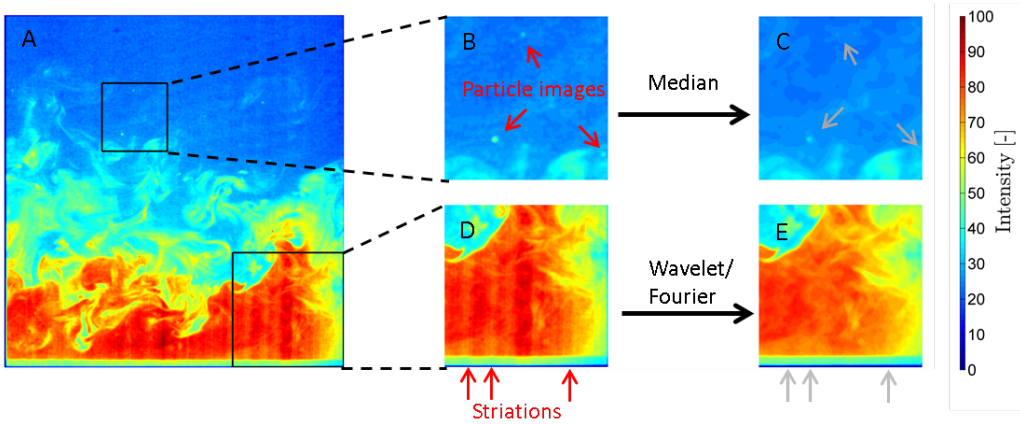

Figure 3.6: An example of a raw concentration field (a), (b) and (c) show the detail of (a) before and after applying the median filter. (d) and (e) show the detail of (a) before and after employing the combined wavelet-Fourier filtering approach. Particles and striations are indicated with red arrows in (b) and (d), whereas the same locations are indicated with gray arrows in (c) and (e).

3.2.5 SHEAR LAYER DETECTION

For completeness this section discusses briefly the method by which shear layers are detected. For more details the reader is referred to Section 2.3.2 and Maciel *et al.* [60]. The shear layers that separate the uniform momentum zones reported by Meinhart and Adrian [22] are detected using a triple decomposition method as proposed by Kolár [59]. Originally, this method was developed in order to provide a better description of vortices in turbulent flows, i.e. vortices that are not contaminated by shear. The key of this method is to split the velocity gradient tensor ∇u into three different parts:

$$\nabla u = (\nabla u)_{RR} + (\nabla u)_{SH} + (\nabla u)_{EL}\,, \tag{3.4}$$

where RR, SH, and EL denote the rigid-body rotation, shear and elongation parts of the velocity gradient tensor. This decomposition only holds in a suitable reference frame, the so called basic reference frame (BRF). For detecting cross-sections of vortices in a 2D plane there exists a closed form solution to find this BRF. However, as far as the authors are aware, no closed form solution exists for the 3D case. Kolár [59] provides an extensive procedure to find this BRF in the 3D case, which is a very computationally intensive operation. Hence, currently shear layers are detected in the 2D slices in the streamwise-wall-normal plane of the measurement volume. In order to delineate regions of high shear from measurement noise and background shear, a threshold is used based on vorticity ω_{SH} related to the shear component of the velocity gradient tensor $(\nabla \tilde{u})_{SH}$:

$$\omega_{SH} = (\nabla \tilde{u})_{SH,21} - (\nabla \tilde{u})_{SH,12} \tag{3.5}$$

An example of a combined PIV/LIF volume with the detected shear layers and vortices (based on the Q-criterion) is shown in Figure 3.7.

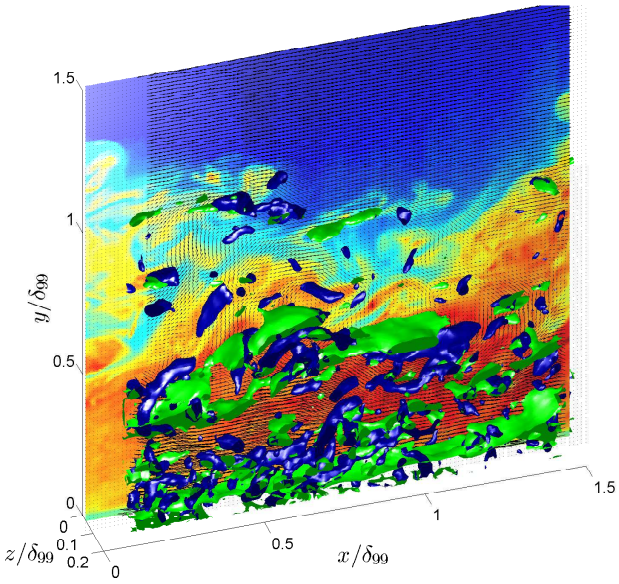

Figure 3.7: An example of a combined TPIV/LIF volume. Iso-surfaces of ω_{SH} according to Equation 3.5 are shown in green ($\omega_{SH} = 2.8U_\infty/\delta_{99}$), whereas vortical structures are shown by the blue iso-surfaces of constant $Q = 0.95U_\infty^2/\delta_{99}^2$). A contourplot of the concentration is shown in the (x,y) plane. On top of the LIF slice, inplane velocity vectors (u, v) are plotted viewed in a frame-of-reference convecting at $U_c = 0.9U_\infty$.

3.3 UNIFORM MOMENTUM AND UNIFORM CONCENTRATION ZONES IN A TBL

Meinhart and Adrian [22] and Adrian *et al.* [43] delineated different uniform momentum zones (UMZ) in a TBL based on snapshots of the velocity fields. By subtracting a constant reference velocity from the streamwise velocity component in instantaneous flow fields, large scale zones with approximately uniform momentum became visible. It turns out that these zones are separated by thin layers that contain high shear ($\partial u/\partial y$), i.e. a significant jump in velocity across the edges of these zones is observed. As a result, these zones appear as distinct peaks in the PDFs of the streamwise velocity component, within a given snapshot. Three snapshots of the present dataset are shown in Figures 3.8-3.10. The contourplots of streamwise velocity clearly depict the aforementioned UMZs, which also appear as distinct peaks in the PDFs of the streamwise velocity (Figures 3.8c-3.10c). Note that these peaks are not a result of the so-called pixel-locking effect as the particle displacement range is between 0 and 18 pixels, and no tendency is found towards integer displacements (not shown). Furthermore, regions of high ω_{SH} are found at the edges of these zones, fully in line with Eisma *et al.* [26] and Adrian *et al.* [43]. The velocity profiles at the different streamwise locations clearly show the presence of a jump when crossing a region of high shear.

The PDF of the concentration also depicts distinct peaks (Figures 3.8d-3.10d). Instead of being uniformly mixed throughout the boundary layer, the passive scalar is organized in distinct uniform concentration zones (UCZ). Visual inspection of the concen-

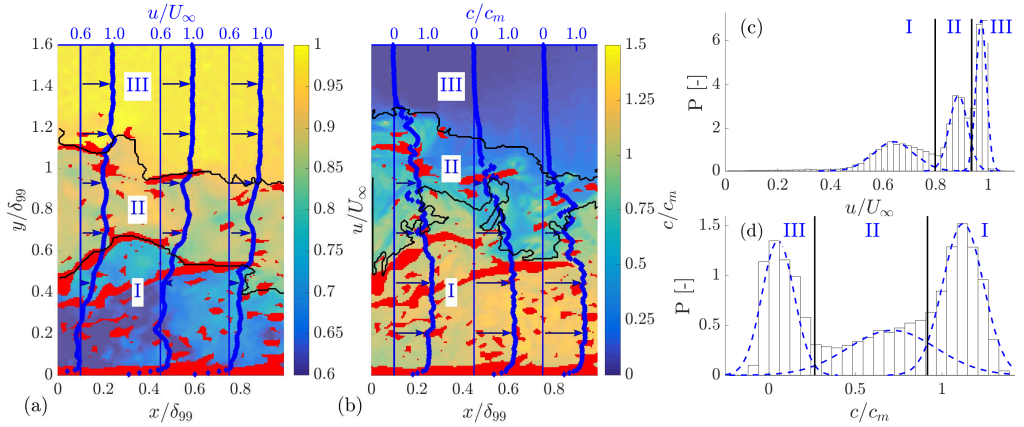

Figure 3.8: (a) An instantaneous contourplot of the streamwise velocity. (b) snapshot of the concentration. Red isocontours show regions where ω_{SH} is larger than five times the noise level. On top of the contour plots the streamwise velocity and concentration profiles over the boundary layer height are plotted at $x/\delta_{99} = 0.1$, 0.45, and 0.75 respectively. The black contour lines give the edges of the detected zones based on the PDFs of streamwise velocity (c) or the concentration (d). Additionally, the dashed blue lines in (c,d) depict the fitted Gaussian curves to local peaks in the PDFs, while the black lines indicate the theshold values used to detect the edges of the different zones shown in (a,b). This snapshot corresponds to the snapshot shown in Figure 3.7.

tration PDFs reveals strong support for the presence of these UCZs. However, the edges of the UCZs in the corresponding contourplots in Figures 3.8-3.10b appear to be more contorted compared to the edges of the UMZ. The overlap between the edges of UCZs and region high shear is less apparent. The edges of the UCZs appear slightly above the regions of high shear, i.e. they are at larger wall-normal distance. Furthermore, the concentration reaches an approximately constant value in the zones near the wall, while the concentration profiles of the UCZs in the outer region appear more irregular, i.e. larger concentration fluctuations are visible. This behaviour is ascribed to an increased level of turbulent mixing in the near-wall region.

Statistical analysis reveals that in at least 75% of the snapshots more than two concentration zones can be identified inside the TBL, i.e. the free-stream region excluded. The overlap between the different zones in concentration and streamwise velocity in the sample shown on the top row in Figure 3.8a,b reveals that the zones in the streamwise velocity and the concentration roughly overlap, i.e. 70% of the uniform concentration zone II resides in the uniform momentum zone II. Similarly, concentration zones I overlaps fully with the momentum zone I. Zones III in this example corresponds to the free-stream in which the streamwise velocit and scalar concentration are nearly constant as expected. These results suggest a connection between UMZs and UCZs, which is examined below.

3.3.1 OVERLAP OF UNIFORM ZONES

Visual inspection of the contour plots of the instantaneous streamwise velocity u and the scalar concentration c, as shown in Figures 3.8-3.10, reveals a clear overlap between

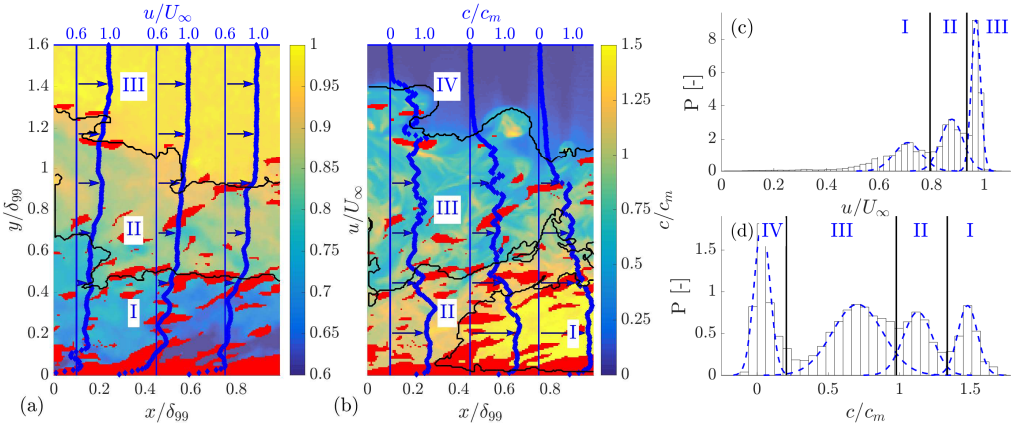

Figure 3.9: For caption see Figure 3.8

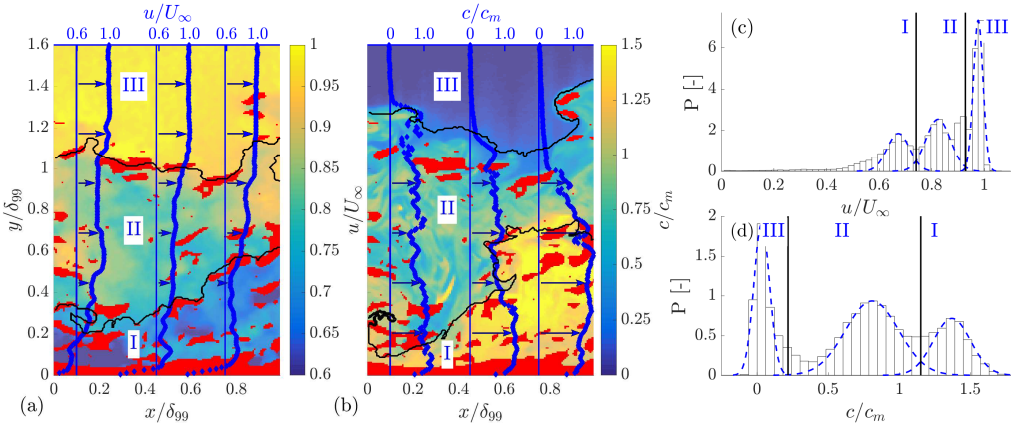

Figure 3.10: For caption see Figure 3.8

UCZs and UMZs. To further quantify this overlap a zone detection algorithm is developed, which extracts the different zones. These zones are associated with local maxima in the instantaneous PDF of u and c. First of all, the PDFs of u and c are determined for each snapshot, in which 50 bins are used for both velocity and concentration fields to ensure a sufficient number of vectors in each bin [95]. The streamwise extent of the analysis domain is taken as δ_{99} [43]. As mentioned by Silva *et al.* [95] this is a reasonable choice as a longer streamwise domain would inevitably smear out local maxima in the PDF. As a second step the highest peak in the PDF is detected. Next, a Gaussian curve is fitted to this peak (see red curves in Figure 3.11a,c) and the contribution of this peak is subtracted from the original PDF. Then, the next peak is found and the previous fitting and subtraction procedure is repeated. This step is repeated ten times. Threshold values, which are used to detect edges of the different zones, are then determined by the intersection between the fitted Gaussian curves (see black dashed lines in Figure 3.11a,c). Furthermore, a merging procedure is employed to remove zones that occupy only a small area in space. For robustness, the minimum area of a zone is set to $0.05\delta_{99}^2$. Zones smaller than this threshold are removed from the list of detected zones and the contour levels between the different zones are re-determined as described before. This results in a smaller number of detected zones. Only these larger zones away from the wall are of interest here. Finally, small patches of a different zone inside another one are removed from the zones. Examples of the detected zones based on the PDFs and the resulting contours after the described procedure has been applied is given in Figures 3.8-3.11.

The overlap between the different zones is quantified based on three different criteria. First of all, Figure 3.12a shows the PDF of the non-dimensional overlap parameter Π between UCZs and UMZs. The overlap Π is calculated as the total shared area of the respective UCZ (A_{UCZ}) and UMZ (A_{UMZ}) (i.e. the intersection of both areas) divided by the total area that the UCZ and UMZ occupy (i.e. the union of both zones). This is written as:

$$\Pi = \frac{A_{\mathrm{UMZ}} \cap A_{\mathrm{UCZ}}}{A_{\mathrm{UMZ}} \cup A_{\mathrm{UCZ}}} \tag{3.6}$$

The other two overlap indicators are given by Π_u and Π_c which are defined as:

$$\Pi_u = \frac{A_{\mathrm{UMZ}} \cap A_{\mathrm{UCZ}}}{A_{\mathrm{UMZ}}} \tag{3.7}$$

$$\Pi_c = \frac{A_{\mathrm{UMZ}} \cap A_{\mathrm{UCZ}}}{A_{\mathrm{UCZ}}}, \tag{3.8}$$

where Π_u and Π_c represent the overlap with either a UMZ or a UCZ instead of the total area that both UMZ and UCZ occupy. To eliminate the zones that do not overlap (e.g. a near wall UCZ with the free-stream UMZ), in each snapshot only the UCZs and UMZs that most likely belong to each other (i.e. the ones that maximally overlap) are taken into account in the overlap statistics. Furthermore, the statistics are calculated for the cases including or excluding the free-stream region. The overlap Π shown in Figure 3.12a indicates a mean overlap of about 0.42 (no free-stream) up to 0.49 (with free-stream). To test the significance of these results, the procedure is performed on

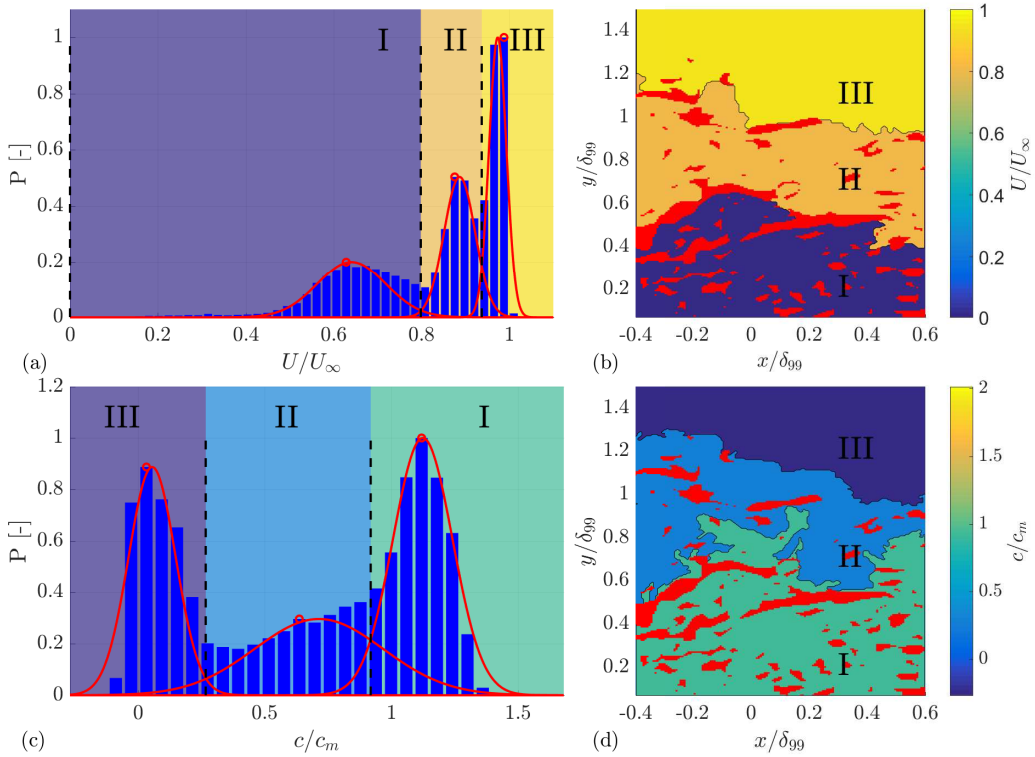

Figure 3.11: (a) and (c) show the PDFs for the streamwise velocity and the concentration of the combined TPIV/LIF volume as shown in Figure 9. The black dashed lines in (a,c) indicate the position of the intersections of the different Gaussian fits, delineating different uniform momentum/concentration zones. (b) and (d) show the contour plots for streamwise velocity and concentration respectively, coloured by the modal concentration/velocity as indicated by the red circles in (a,c). Regions of high shear are shown by the red patches in (b,d)

randomly distributed data, i.e. no systematic connection between the UCZs and UMZs. For both UMZs and UCZs, 1D profiles are generated in which the number of zones and the height distribution are randomly drawn from a uniform distribution. Here it is assumed that this 1D situation is representative of the 2D case. The number of zones is allowed to randomly vary between 1 and 6, while this amount of zones is distributed with a random length distribution between 0 and 1. This procedure is repeated 1×10^5 times, which results in a mean overlap of this randomly distributed data of 0.44. Note that the overlap Π increases to 0.65 for the free-stream regions in velocity and concentration, indicating that the edge of the TBL largely corresponds with the edge of the free-stream concentration zone. Hence, despite the fact that the qualitative observation from the previous section indicates a substantial overlap, it does not seem to be relevant in a statistical average sense. However, it should be taken into mind that actually there is no specific reason to expect such a significant overlap, as the degree of overlap is dependent upon time history of the scalar concentration field, i.e. the passive scalar is introduced at a specific location that is not necessarily related to the location where also the UMZs are formed. These results are in contrast with the suggestions of Vanderwel and Tavoularis [81], who conjectured that in a TBL the overlapping UCZs and UMZs are more likely to occur compared to uniform shear flow, as the tracer was released close to the wall, i.e. the location at which UMZs are formed [81]. This explanation is based on the idea that UMZs are generated at the location of the dye injection. Eisma *et al.* [26] provides evidence for the relatively slow growth of shear layers that bound these UMZs. Therefore, we conjecture that it is unlikely that the observed overlap between UCZs and UMZs stems from fact that UMZs are generated at the location of the dye injection.

The overlap parameters Π_u and Π_c (shown in Figure 3.12b-c) provide additional information on whether (on average) UMZs encapsulate UCZs or vice versa. A high value for Π_u and a low value for Π_c shows that UMZs on average encapsulate one (or more) UCZs, whereas a low value for Π_u and a high value for Π_c indicates the opposite. The mean value for both overlap parameters is found as $\overline{\Pi}_u = 0.84$ and $\overline{\Pi}_c = 0.51$. Hence, UCZs are on average (slightly) bigger than UMZs and typically encapsulate one or more UMZs. Both PDFs that include the free-stream region in Figure 3.12b, c show a peak near 0.9, which is a result of the high overlap in free-stream region (see Figure 3.12d).

3.3.2 GEOMETRICAL CHARACTERISTICS OF ZONES

This section presents the geometrical characteristics of the zones detected by employing the zone extraction algorithm described in the previous section. Figure 3.13 shows the PDF of the number of zones detected in each snapshot. Note that the free-stream region is excluded from the analysis. The average number of zones in the real measurements is 2.3 for the UMZs and 2.2 for the UCZs. This is consistent with the value of 2.3 that Silva *et al.* [95] found at a similar Reynolds number.

In more than 85% of all detected UMZs the streamwise extent is larger than the streamwise extent of the field of view, in line with the observations from Adrian *et al.* [43], while 85% of the UCZs have a streamwise extent larger than $0.95\delta_{99}$. The distribu-

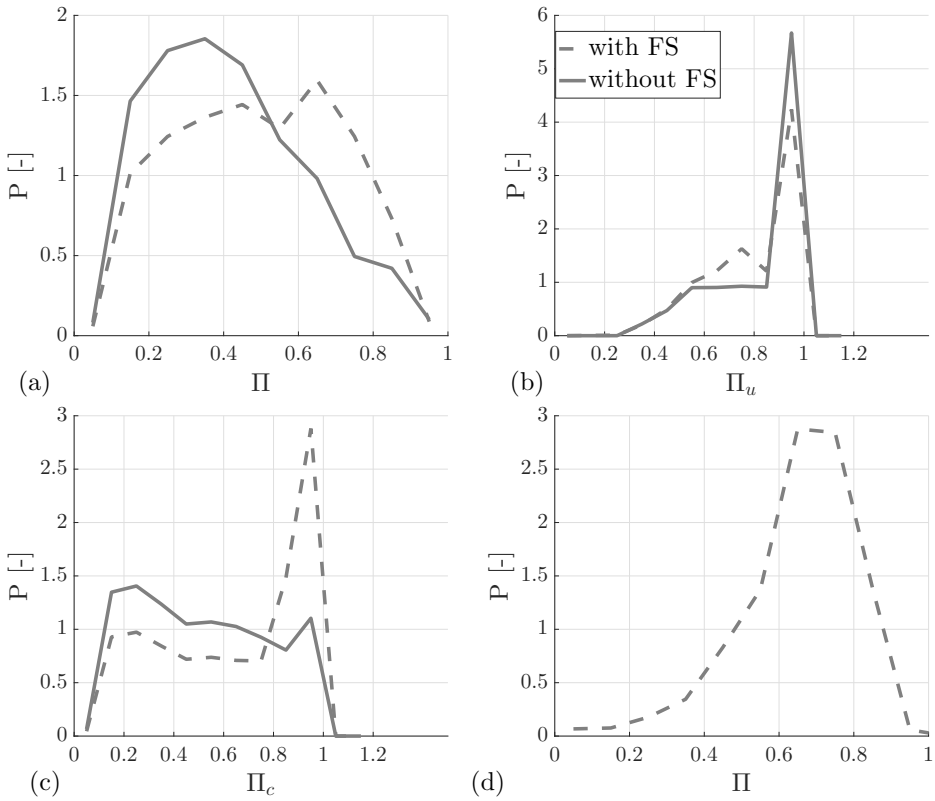

Figure 3.12: PDF of the overlap parameter Π defined in Equation 3.6 (a), Π_u defined in Equation 3.7 (b), Π_c defined in Equation 3.8 (c), and Π for the free-stream regions in u and c (d). The dashed lines show the results for the analysis with the free-stream region included whereas the solid lines depict the results without the free-stream region included.

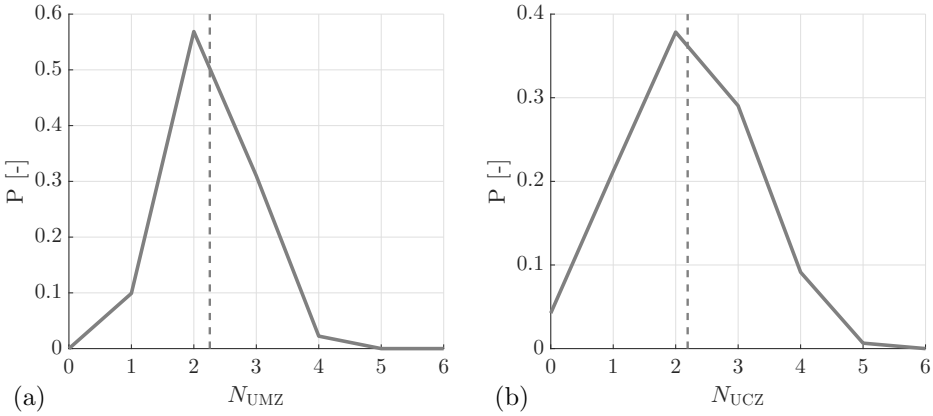

Figure 3.13: PDF of the number of UMZ (a) and UCZ (b).

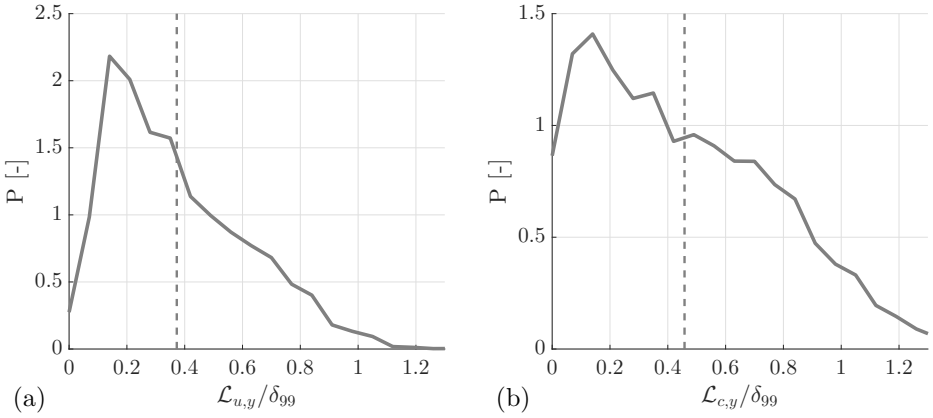

Figure 3.14: PDF of the height of UMZ (a) and UCZ (b).

tion of the wall-normal height of the zones is shown in Figure 3.14. The mean height of UMZs ($\mathcal{L}_{u,y}$) and UCZs ($\mathcal{L}_{c,y}$) is calculated to be 0.37 and 0.46 respectively.

3.3.3 CONDITIONAL STATISTICS OVER THE EDGES OF UNIFORM ZONES

As suggested by several authors [26, 43, 95], the edges of UMZs are occupied by regions of high shear. To verify this qualitative observation, we perform conditional sampling at fixed wall-normal distances with respect to the location of the edges of UMZs and UCZs. The conditional sampling technique is described in detail in Bisset *et al.* [57]. As shown in the previous section, there is no clear evidence for a significant overlap of the UMZs and the UCZs in the statistical average sense. This behaviour is likely to show up in the conditional statistics as a smearing of the mean conditional statistics. Nevertheless, the conditional wall-normal scalar concentration flux $\langle vc \rangle$ is expected to be more distinct over the interface, even in case of this non-perfect overlapping. This behaviour is schematically explained in Figure 3.15. At time t a shear layer is present

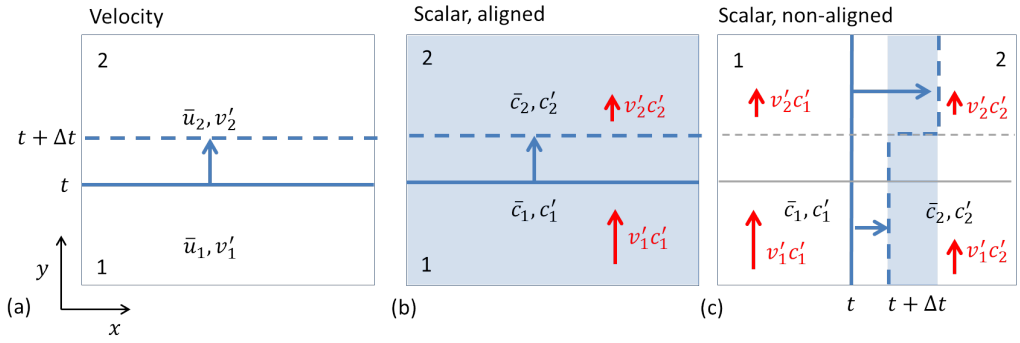

Figure 3.15: Sketch of a control volume around the edge of a UMZ at two different time instances (t, $t + \Delta t$). (a) Control volume depicting two velocity regions 1,2 with different mean $\overline{u}$ velocities and turbulence intensities u' separated by a moving interface (solid/dashed blue lines). (b) Control volume depicting two scalar concentration fields 1,2 with mean concentration $\bar{c}$ and concentration fluctuations c' separated by a moving interface (solid/dashed blue lines); (b) A perfect alignment with velocity interface, (c) non-aligned case. The shaded area in (b) and (c) indicates the region that contributes to the jump in $\langle c \rangle$.

that separates the velocity regions 1 and 2, each having a different mean velocity $\overline{u}(y)$, turbulence intensity, and with a jump in u at the interface. As a result of the momentum flux into the interface it will move from time t (indicated by solid line) a different position at time $t + \Delta t$ (indicated by dashed line) [29]. Similarly, the control volume for c at time t and $t + \Delta t$ is given in Figure 3.15b,c. For clarity, the two cases are considered: (1) the concentration interface is aligned with the velocity interface (Figure 3.15b), (2) no alignment with the velocity interface (Figure 3.15c). Conditional statistics over the shear layer in wall-normal direction y and averaged in streamwise direction x will clearly depict a jump in the conditional streamwise velocity profile $\langle \overline{u} \rangle$ (see also Chapter 2). Furthermore, in case of a perfect alignment of the interfaces (Figure 3.15b), also a clear jump in $\langle c \rangle$ will be visible. However, the situation sketched in Figure 3.15c results in a weak jump in the conditional scalar concentration profile. The reason is that only part of the streamwise domain (the shaded area) in Figure 3.15b adds to the jump in $\langle c \rangle$, as $\langle c \rangle$ is constant in wall-normal direction in the rest of the domain. Nevertheless, the $\langle v'c' \rangle$ is still expected to show a jump as v' still varies in wall-normal direction, independent of the orientation of concentration interface, as indicated by the red arrows in Figure 3.15b,c.

First, the conditional statistics around the edges of UMZs are described. The edges of the zones are binned according to the contour level that separates the different zones (see Figure 3.11a-b). A bin-width of $0.1U_\infty$ is used for this purpose. Figure 3.16 presents the conditional profiles of the streamwise velocity (a), magnitude of the vorticity vector (b), magnitude of the shear vorticity according to Equation 3.5 (c), scalar concentration (d), the wall-normal gradient of the scalar concentration (e), and the wall-normal concentration flux. Note that regions overlapping with the wall are excluded from Figure 3.16.

Figure 3.16a shows a finite jump in streamwise velocity present near the edges of the UMZs. The magnitude of the jump of the $0.9 - 1U_\infty$ curve, is about 5% of U_∞ that

corresponds to the jump magnitude found for the turbulent/non-turbulent interface in a TBL [26, 39]. This jump increases in height for zones closer to the wall, i.e. zones with a lower contour level. This behaviour is consistent with the results presented on the conditional statistics of regions of high shear inside a TBL as observed in Eisma *et al.* [26] (see also Chapter 2).

Both the magnitude of the vorticity and the shear vorticity (Figure 3.16b,c) show a peak at the location of the UMZ edge, increasing in magnitude for edges of lower streamwise velocity. This implies that indeed the edges of UMZs are occupied by regions of high shear, in agreement with the qualitative observations in TBLs by Eisma *et al.* [26], Adrian *et al.* [43], and Silva *et al.* [95].

The conditional concentration profiles are shown in Figure 3.16d. Because the UMZs do not overlap perfectly with the UCZs, the jump in concentration is not clearly observed. However, the wall-normal gradient $(\partial c/\partial y)^2$, representative of the dissipation of scalar concentration fluctuations, (Figure 3.16e), indicates a moderate peak near the edges of UMZs, indicative for a high scalar dissipation at the UMZ edges. Furthermore the total flux vc over the edges of UMZs is shown in Figure 3.16f. A clear jump is present in the conditional profile of vc indicating that wall-normal transport is prohibited by the presence of shear layers that occupy the edges of the UMZs. Therefore, pollutants remain largely inside a UMZ. This observation bears resemblance to the results obtained by Michioka *et al.* [24]. Large scale low momentum regions above an urban canopy were found to largely overlap with regions of high concentration. The large overlap in several instantaneous realizations suggested that pollutants were kept inside these regions, without significant pollutant transport to other flow regions, similar to the present observations on UMZs.

Conditional sampling was also performed around the edges of UCZs. Figure 3.17 depicts the conditional profiles around the edges of these UCZs for the same quantities as shown in Figure 3.16. First of all, smoothing of the conditional velocity statistics is observed as a result of the non-perfect overlapping between UCZs and UMZs. In contrast to the edges of UMZs, no distinct jump is observed in the streamwise velocity (Figure 3.17a). Additionally no peak in vorticity magnitude (Figure 3.17b) is present, though the shear vorticity shows the presence of a moderate peak on the lower side of the UCZ edge (Figure 3.17c). UCZs are distinct zones which are characterized by distinct jumps in scalar concentrations across their boundaries (Figure 3.17d). Furthermore, a significant peak is observed in $(\partial c/\partial y)^2$ (Figure 3.17e), which indicates that most of the scalar dissipation occurs at the edges of the UCZs. Finally, Figure 3.17f shows that the scalar flux significantly decreases over the edge of a UCZ, even changing sign for the higher contour levels. This behaviour indicates that the scalar concentration flux is directed into the shear layer on both sides of the edge. As observed before by Eisma *et al.* [26], this is indicative for vortex stretching that occurs in the vortices that populate the edges of these zones. Instead of being transported vertically across the shear layer the passive scalar is transported into the spanwise direction along the edge of a UMZ/UCZ, and as such the passive scalar largely remains inside a uniform zone.

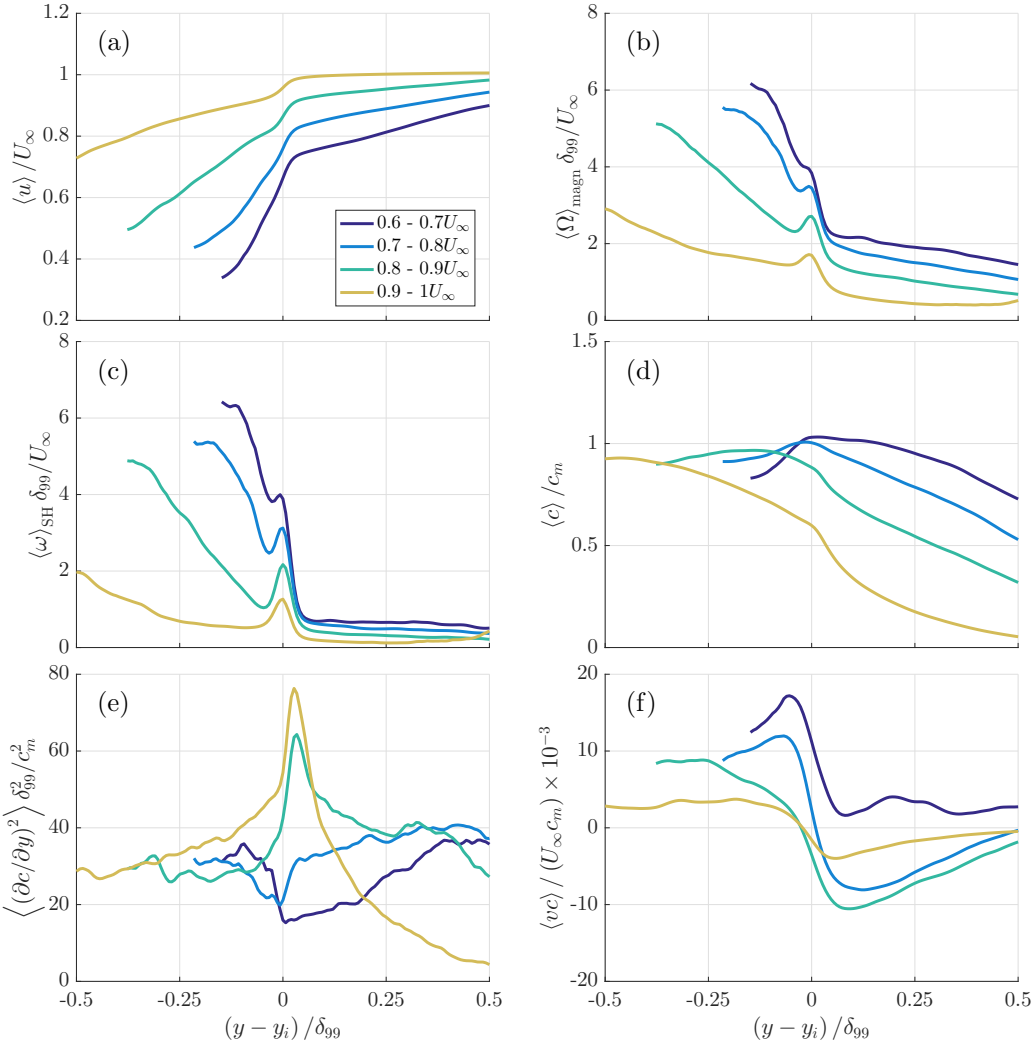

Figure 3.16: Conditionally sampled profiles across the edges of UMZs. (a) Streamwise velocity $\langle U \rangle$, (b) Vorticity magnitude $\langle \Omega \rangle_{\text{magn}}$, (c) Shear vorticity $\langle \omega_{SH} \rangle$ according to Maciel *et al.* [60], (d) Scalar concentration $\langle c \rangle$, (e) Wall-normal scalar concentration gradient $\left\langle (\partial c / \partial y)^2 \right\rangle$ representative of the dissipation of scalar concentration fluctuations, (f) Wall-normal concentration flux $\langle vc \rangle$.

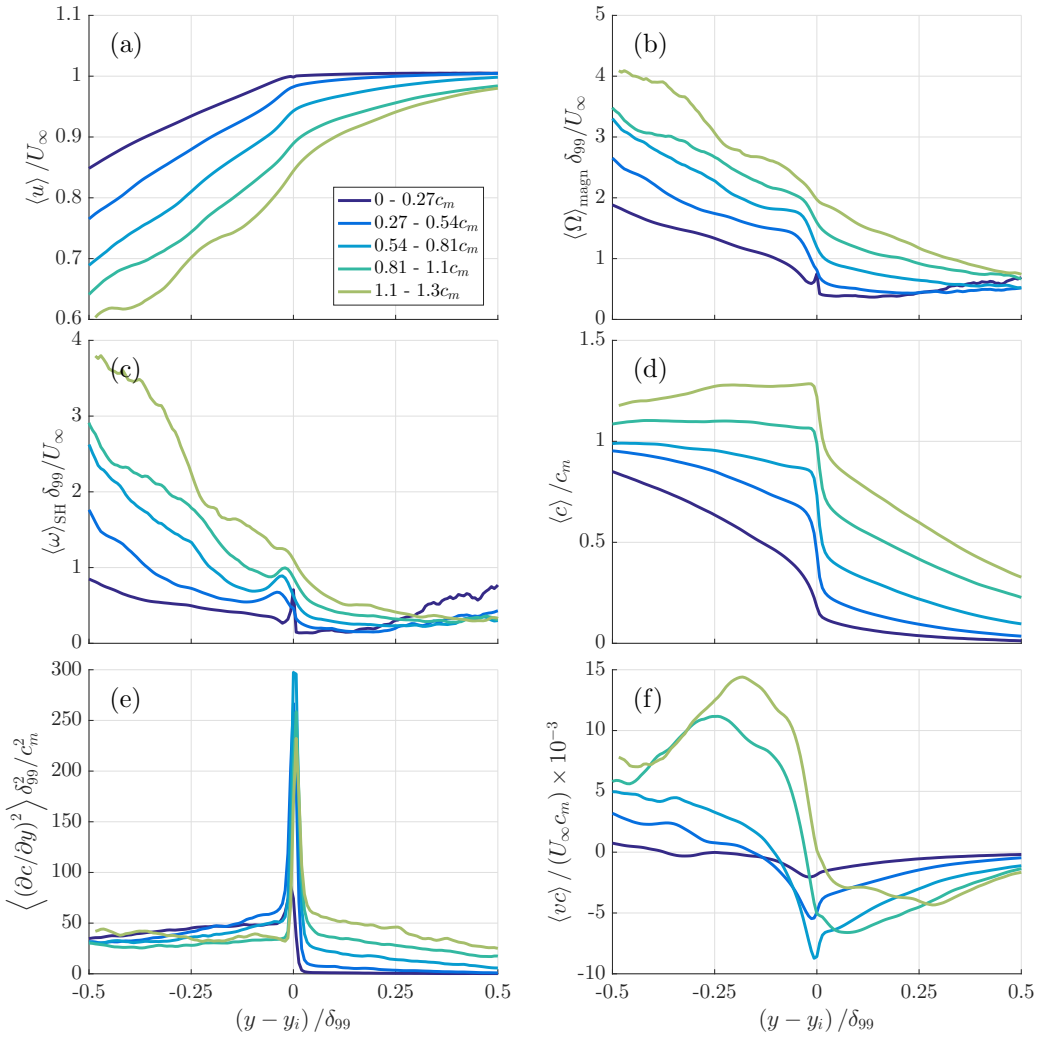

Figure 3.17: Conditionally sampled profiles across the edges of UCZs. (a) Streamwise velocity $\langle U \rangle$, (b) Vorticity magnitude $\langle \Omega \rangle_{\text{magn}}$, (c) Shear vorticity $\langle \omega_{SH} \rangle$ according to Maciel *et al.* [60], (d) Scalar concentration $\langle c \rangle$, (e) Dissipation of scalar concentration fluctuations $\left\langle (\partial c / \partial y)^2 \right\rangle$, (f) Wall-normal concentration flux $\langle vc \rangle$.

3.4 CONCLUSIONS

In this chapter a combined scanning TPIV and LIF measurement is described. The scanning procedure is found to be robust, i.e. no significant drift in light sheet position is observed during the measurement. An inhomogeneous shift of the velocity and the scalar concentration over the height of the measurement volume is used to correct for convection during the volume scan. PDFs of the divergence indicate no systematic error in the velocity gradients evaluated from these reconstructed volumes.

Analysis of the PDFs of instantaneous velocity fields reveals the presence of UMZs [22]. The PDF of instantaneous concentration fields shows the presence of distinct UCZs. These UCZs are observed in more than 75% of the snapshots. An automated zone extraction algorithm was developed, which allowed to quantify the overlap between the UMZs and the UCZs statistically. The overlapping parameters, as defined in Equations 3.6-3.8, indicate a significant overlap between the UMZs and UCZs. Furthermore, UCZs turn out to be slightly larger compared to UMZs, and consequently UCZs typically span multiple UMZs. The detected UMZs and UCZs are zones with a large streamwise extent, with the vast majority spanning the complete analysis domain, i.e. their length is larger than δ_{99}.

Conditional statistics around the edges of UMZs indicates that the edges of these zones are characterized as regions of high vorticity and shear. However, due to the non-perfect overlapping of UMZs and UCZs no distinct scalar jump is observed around the edges of UMZs. Conditional statistics around the edges of UCZs also suffers from this non-perfect overlap, resulting in no distinct peak in vorticity magnitude or shear vorticity. Conditional statistics around UCZs and UMZs both show that the wall-normal concentration flux vc is significantly reduced, demonstrating that shear layers at the edges of these uniform zones reduce concentration transport across the layers.

4

DISPERSION OF A PASSIVE SCALAR IN AN IDEALIZED URBAN GEOMETRY

4.1 INTRODUCTION

Because there is a worldwide increase of urban population, more pollutant emission sources, such as from power generation, households and traffic, are present near populated areas. As a consequence, the demand for accurate urban air quality predictions is rising, which requires proper understanding of the dispersion of pollutants in urban environments. Investigations of the urban boundary layer are often done for fully-developed flow over areas with uniform properties. For example Cheng and Castro [98] performed experiments on turbulent boundary layers where the complete bottom wall of the wind tunnel was covered with cubical roughness elements, which represented the flow over an urban area. In multiple numerical simulation studies the fully-developed character of the flow is implicitly assumed by employing periodic boundary conditions in the horizontal directions (e.g., [24, 99, 100]). However, in reality the surface roughness changes, e.g. from rural to urban regions, which means the boundary layer has to adapt to this roughness transition. There are only a few recent numerical studies on turbulent flow over an explicitly resolved roughness transition [101, 102], where mostly cubical roughness elements or riblets are considered. In addition, experimental investigations with results up to the roughness elements are scarce, and when a roughness transition is considered it is often done to find out when the boundary layer retains an equilibrium state, without investigating pollutant dispersion [103].

In order to obtain insight in pollutant dispersion mechanisms, Michioka *et al.* [24] performed large-eddy simulations (LES) on fully-developed flow over an array of obstacles with various aspect ratios l/h, where l is the spanwise obstacle length and h is the obstacle height. They conclude that for fully-developed conditions the turbulent pollutant flux is the main contributor to street canyon ventilation, although the ratio of the turbulent to the advective pollutant flux does change slightly for different aspect ratios [104]. Tomas *et al.* [104] show that up to $14h$ downstream of a rural-to-urban roughness transition the advective pollutant flux remains significant. Furthermore, Michioka *et al.* [105] and Michioka *et al.* [24] conclude that street canyon ventilation mostly takes place when low momentum regions pass over the canyon, and they suggest that these regions

Part of this chapter is published in: J. M. Tomas, H. Eisma, M. J. B. M. Pourquie, G. E. Elsinga, H. J. J. Jonker, and J. Westerweel, "Pollutant Dispersion in Boundary Layers Exposed to Rural-to-Urban Transitions : Varying the Spanwise Length Scale of the Roughness," *Boundary-Layer Meteorol.*, vol. submitted, 2016 and H. E. Eisma, J. M. Tomas, M. B. J. M. Pourquie, G. E. Elsinga, H. J. J. Jonker, and J. Westerweel, "Effects of a 2D fence on Pollutant Dispersion in Boundary Layers Exposed to Rural-to-Urban Transitions," *(in Prep.*,

are of small scale compared to the the coherent structures in the outer region and are generated close to the top of the canopy.

Currently, there are only few experimental investigations on urban geometries in which concentration fields and velocity fields are measured simultaneously, such that these dispersion mechanisms can be investigated [106]. To the authors knowledge there is no such experimental data available for regions containing multiple street canyons that allow a study on the streamwise development. Therefore, in the current study both LES and experimental measurements were performed to investigate pollutant dispersion mechanisms after a rural-to-urban roughness transition in neutrally buoyant conditions. The set-up is similar to Tomas *et al.* [107], where the urban canopy consists of cubical obstacles in an in-line arrangement. In addition, in the current study various urban canopies are considered by varying the spanwise aspect ratio of the obstacles and by positioning a fence with different heights upstream of the urban canopy. The experiments were done in the water tunnel at the Laboratory for Aero- and Hydrodynamics at the Delft University of Technology using simultaneous stereoscopic particle image velocimetry (PIV) and laser-induced fluorescence (LIF) techniques in order to investigate instantaneous pollutant dispersion mechanisms. The objectives of the study are (1) to set up a well-validated data-set for flow and pollutant dispersion and (2) to answer the following questions:

- What is the influence of the aspect ratio l/h on flow over a rural-to-urban transition, in terms of velocity statistics, internal boundary-layer depth and pollutant dispersion?
- What is the influence of the Reynolds number based on obstacle height h^+ on the velocity and pollutant dispersion statistics?
- What is the influence of a fence with different heights mounted upstream of the urban canopy on the flow and dispersion characteristics above/inside the urban canopy?
- What are the dominant mechanisms of pollutant removal from street canyons and how do these mechanisms change in the transition region for the different variables given above?

This chapter is organized as follows. First of all, the considered cases in the current setup are discussed in section 4.2. Second, a short overview of the numerical setup is given in Section 4.3. Third, Section 4.4 discusses the experimental setup that is used, including an extensive discussion on the processing of the LIF images. The results on the comparison between the LES and the experimental results regarding the aspect ratio variation is discussed in Section 4.5. The effect of the Reynolds number is discussed in Section 4.6. The influence of a fence on the mean flow field and the pollutant removal mechanisms is discussed in detail in Section 4.7. Finally, a summary of the most important conclusions from this chapter are given in Section 4.8.

4.2 CONSIDERED CASES

In both the experiments and the simulations a smooth wall turbulent boundary layer is generated that approaches an urban roughness geometry consisting of an array of

obstacles. The Reynolds number of the approaching flow, $\mathrm{Re}_\tau = u_\tau \delta_{99}/\nu$, based on the friction velocity $u_\tau = \sqrt{\nu \partial u/\partial z}$ and the boundary-layer depth δ_{99}, is around 2.0×10^3 for the lowest Reynolds number case considered. Additionally, in the experiments the Reynolds number Re_τ is varied between 2.4×10^3 and 5.7×10^3. Figure 4.1a shows the top view and the side view of both the experimental set-up (black lines) and the domain used in the LES (blue lines). The coordinate axes are as follows: x denotes the streamwise direction, y the spanwise direction and z is in the wall-normal direction. Please note that we do adopt a different coordinate system in this chapter compared to the previous chapters. The location $x = 0$ corresponds to the upstream walls of the first row of obstacles, while the plane $y = 0$ lies in the middle of the domain at the symmetry plane of the obstacles. A uniform street layout of obstacles placed in an in-line arrangement is considered to capture the basic characteristics of urban areas. The first parameter that is varied is the obstacle aspect ratio l/h; aspect ratios of 1, 2, 3.5, 5, 8 and ∞ are simulated by LES, while aspect ratios of 1, 5 and 8 are investigated in the experiments. The urban model in the experiments was made from Plexiglas blocks with cross-sectional dimensions of $2.0 \times 2.0\,\mathrm{cm}^2$ and lengths of 2.0, 10.0, and 16.0 cm for the different aspect ratio cases. Figure 4.1b shows the top view of the different cases, which are indicated by AR1, AR2, AR3.5, AR5, AR8 and 2D. The second parameter that is changed is the addition of a fence $1h$ upstream of the first row of obstacles (not shown), i.e. just in between the line source and the first row of obstacles. The fence height in the experiments is varied between $0h$ and $1.5h$, whereas in the LES the $0h$ case and the $1h$ case is simulated. The different fence cases are indicated by C00, C05, C10, and C15.

For each aspect ratio case two 'streets' are shown in Figure 4.1b that consist of an obstacle row and a 'street canyon'. In all cases the width of the obstacles as well as the width of all street canyons is equal to h. Consequently, the plan area density $\lambda_\mathrm{p} = A_\mathrm{p}/A_\mathrm{t}$ is equal to the frontal area density $\lambda_\mathrm{f} = A_\mathrm{f}/A_\mathrm{t}$, where A_t is the total area viewed from the top, A_p is the total area covered with obstacles and A_f is the total frontal area of the obstacles. $\lambda = \lambda_\mathrm{f} = \lambda_\mathrm{p}$ is between 0.25 (AR1) and 0.5 (2D) and all cases are in the skimming flow regime [108]. In addition, a line source of passive tracer is placed in front of the urban environment to simulate an emission from a highway as is often found near urban regions. Its location is $2h$ upstream of the first row of obstacles. In the experiments the tracer is released from the ground surface, while in the simulations the source is located at $z/h = 0.2$.

4.3 NUMERICAL SETUP

The set-up of the LES is the same as in Tomas *et al.* [107] except that in the current study only neutrally buoyant conditions are considered and that several obstacle aspect ratios and the addition of a fence are studied. Here, the main characteristics of the simulations are given, while further details can be found in Tomas *et al.* [107].

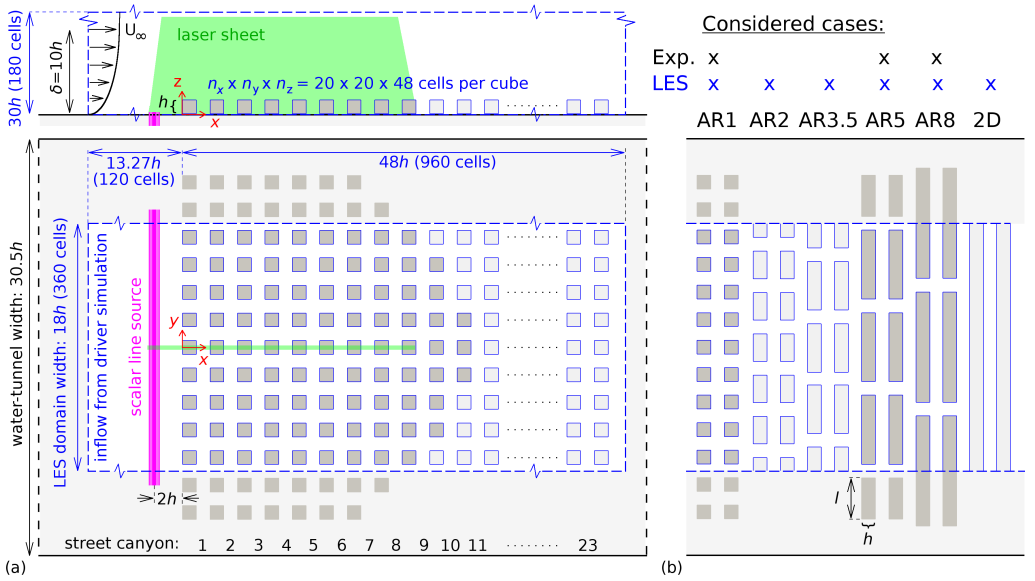

Figure 4.1: A schematic overview of the experimental and numerical set-up (a) and an overview of the cases that are considered in the experiments and in the simulations (b). The experimental set-up is shown by black lines and dark grey obstacles, while the numerical domain is shown by blue lines and light grey obstacles. The green line represents the laser sheet.

4.3.1 GOVERNING EQUATIONS AND NUMERICAL METHOD

The filtered continuity equation and the filtered Navier-Stokes equations for incompressible flow are

$$\frac{\partial \widetilde{u_i}}{\partial x_i} = 0, \tag{4.1}$$

$$\frac{\partial \widetilde{u_i}}{\partial t} = -\frac{\partial}{\partial x_j}\left(\widetilde{u_i}\widetilde{u_j}\right) - \frac{\partial}{\partial x_i}\left(\frac{\widetilde{p} + \tau_{kk}/3}{\rho}\right) + \nu\frac{\partial^2 \widetilde{u_i}}{\partial x_j^2} + \frac{\partial}{\partial x_j}\left(2\nu_{sgs}S_{ij}\right), \tag{4.2}$$

$$\frac{\partial \widetilde{c^*}}{\partial t} = -\frac{\partial}{\partial x_j}\left(\widetilde{c^*}\widetilde{u_j}\right) + \frac{\nu}{\mathrm{Sc}}\frac{\partial^2 \widetilde{\varphi}}{\partial x_j^2} + \frac{\partial}{\partial x_j}\left(\frac{\nu_{sgs}}{\mathrm{Sc}_{sgs}}\frac{\partial \widetilde{c^*}}{\partial x_j}\right) + \mathcal{S}, \tag{4.3}$$

where $\widetilde{(..)}$ denotes filtered quantities, $\left(\widetilde{p} + \tau_{kk}/3\right)/\rho$ is the modified pressure, τ_{kk} is the trace of the subgrid-scale (SGS) stress tensor, ν is the fluid kinematic viscosity, ν_{sgs} is the SGS viscosity, Sc_{sgs} is the SGS Schmidt number, $S_{ij} = \frac{1}{2}\left(\frac{\partial \widetilde{u_i}}{\partial x_j} + \frac{\partial \widetilde{u_j}}{\partial x_i}\right)$ is the rate of strain tensor and $\mathcal{S}$ is a source term. The eddy-viscosity SGS model, $\tau_{ij}/\rho = \widetilde{u_i u_j} - \widetilde{u_i}\widetilde{u_j} = -2\nu_{sgs}S_{ij}$, where τ is the SGS stress tensor, is already incorporated in Equation 4.2 and Equation 4.3. Equation 4.3 describes the transport equation for the pollutant concentration c^*. Hereafter the $\widetilde{(..)}$ symbol is omitted for clarity, while the $\overline{(..)}$ symbol represents temporal averaging, and the $\langle..\rangle$ symbol represents spatial averaging. Furthermore, fluctuating quantities are represented by $(..)'$.

The code developed for this study is based on the Dutch Atmospheric Large-Eddy Simulation (DALES) code [109], where the main modifications are the addition of an immersed boundary method [110], the implementation of inflow/outflow boundary conditions and the application of the eddy-viscosity SGS model of Vreman [111]. This model has the advantage over the standard Smagorinsky-Lilly model [112, 113] that no wall-damping is required to reduce the SGS viscosity near walls. The equations of motion are solved using second-order central differencing for the spatial derivatives and an explicit third-order Runge-Kutta method for time integration. For the scalar concentration field the second-order κ scheme is used to ensure monotonicity [114]. The simulations are wall-resolved, so no use is made of wall functions. The Schmidt number Sc was 0.71, and Sc_{sgs} was set to 0.9, equal to the turbulent Prandtl number found in the major part of the turbulent boundary layer in direct numerical simulation (DNS) studies by Jonker *et al.* [115]. The code has been used previously to simulate turbulent flow over a surface-mounted fence, showing good agreement with experimental data [104, 116].

4.3.2 DOMAIN AND BOUNDARY CONDITIONS

Figure 4.1 shows the LES domain in blue together with the applied number of grid cells in each direction. At the ground and the obstacle walls no-slip conditions were applied. The velocity and the concentration fields were assumed to be periodic in the spanwise direction. Furthermore, the smooth-wall turbulent boundary layer imposed at the inlet was generated in a separate 'driver' simulation using the rescaling method proposed by Lund *et al.* [117]. At the outlet a convective outflow boundary conditions was applied for both velocity and concentration. Furthermore, at the top wall free-slip conditions were assumed for the horizontal velocity components. In addition, a small vertical outflow velocity was applied that corresponds to the outflow velocity used in the driver simulation to achieve a zero pressure-gradient boundary layer. The computational grid, boundary conditions, as well as the inflow turbulent boundary layer are the same as for the neutrally buoyant case described by Tomas *et al.* [107], in which further details are given.

4.3.3 STATISTICS

The simulations with a turbulent inflow started from a statistically steady solution generated with a steady mean inflow profile. A constant timestep of $0.0156T$ was used, where $T = h/U_h$. The simulations ran for at least $780T$ before statistics were computed, which was long enough to assure a steady state. Statistics were computed for a duration of at least $780T$ with a sampling interval of $0.31T$ resulting in converged results. This duration corresponds to approximately 125 uncorrelated samples in the experiment. The simulations were well-resolved, such that the average subgrid stress $\overline{-2\nu_{sgs}S_{13}}$ did not exceed 6% of the total Reynolds stress, as shown by Tomas *et al.* [107]. Therefore, only the resolved statistics are shown in the subsequent sections.

4.4 EXPERIMENTAL SETUP

In this section an overview of the different components of the experimental setup and their characteristics are given. The method of generating an appropriate approach flow boundary layer is discussed. Furthermore, the line source design and its lateral homogeneity are discussed. Next, the PIV and LIF setup are discussed. The theoretical background, the calibration, and the correction procedure are discussed in detail to show the validity of the concentration measurements.

4.4.1 APPROACH FLOW BOUNDARY LAYER

The characteristics of the approaching flow boundary layer affect the flow development over obstacles [118, 119]. Therefore, in this section a comparison is given of the approaching flow boundary layer in the experiments and in the simulations. The experiment was performed in the same water tunnel facility that was used in Chapter 2 and 3. A false floor, with dimensions 4.5×0.6 m^2, is mounted 0.17 m above the bottom wall to limit the influence of remaining flow disturbances emanating from the contraction upstream of the measurement section, as well as to allow the placement of the scalar line source. An artificially thickened smooth wall boundary layer is generated with spires. To generate a scaled atmospheric boundary layer (ABL) there are several methods available in literature, as for example spires [120, 121], an active grid [105, 122], or a naturally developing ABL over surface mounted roughness [123, 124]. Due to the relatively short length of the test section of the water tunnel the third option is not feasible. The flexibility of an active grid is quite appealing, however from a production/development perspective quite elaborate as it requires a significant amount of time before such an active grid is developed and build. The use of spires has been a very attractive way of generating a properly scaled ABL in windtunnels with a relatively short length. Counihan [121] proposed the use of a combination of spires, barriers and surface mounted roughness elements, with which he was able to obtain properly scaled versions of ABLs. Cook [123] refined this method by considering different types and arrangments of roughness elements. Another simple but powerful approach is provided by Irwin [120] who proposes an easy design method for spires and subsequent roughness elements to simulate an ABL for different types of terrain. As the 3D shape of the Counihan vortex generators is more complicated to produce, the Irwin method is chosen to generate a scaled ABL. A schematic overview of the experimental setup is given in Figure 4.2.

The spires are mounted 0.5 m downstream of the sharp leading edge of the ground plate. An additional fence with a height of 2.0 cm is placed 12 cm upstream of the spires in order to generate an additional momentum deficit at the start of the boundary layer development. As input parameters for the design of these spires the boundary layer thickness $\delta_{99} = 200$ mm and the exponent of the power-law velocity profile $\alpha = 0.1$ (corresponding to smooth terrain) are used. The power-law profile is defined as:

$$U/U_\infty = (z/\delta_{99})^\alpha \tag{4.4}$$

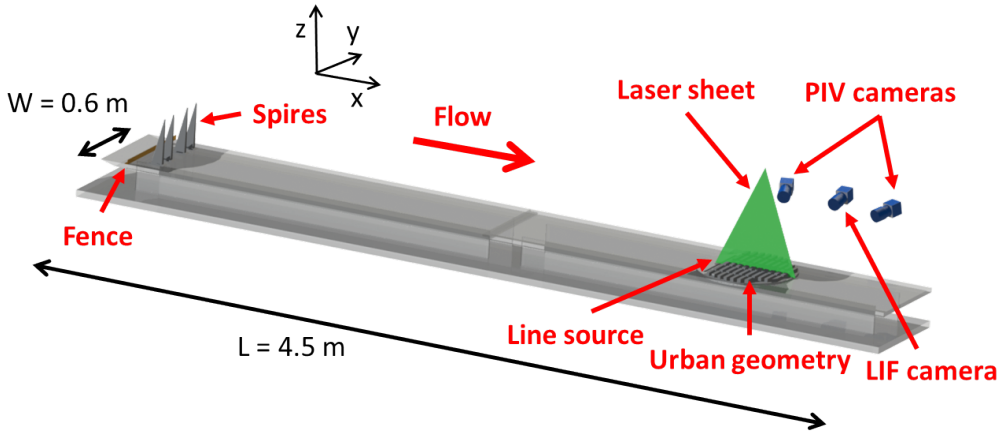

Figure 4.2: Schematic overview of the experimental setup indicating the different components

As flat terrain is considered as the upstream fetch, no additional roughness elements are mounted downstream of the spires. The resulting design of the spires including the dimensions is summarized in Figure 4.3.

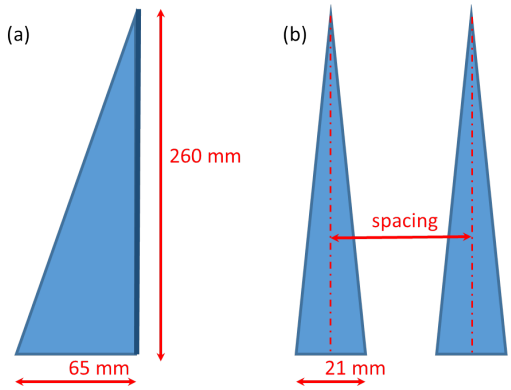

Figure 4.3: Sketch of the spire layout. (a) Side view. (b) Front view

The boundary layer characteristics at the model location (approximately 3.9 m downstream of the spires) are characterized by a planar PIV setup in both the streamwise - wall-normal plane as well as the streamwise - spanwise plane (at $z/\delta_{99} \approx 0.25$), where the latter was used to characterize the spanwise uniformity of the boundary layer. In order to optimize the boundary layer characteristics at the measurement location (i.e. the velocity profile, Reynolds stress distribution and the spanwise flow uniformity), the number of spires and the spanwise spacing of the spires were varied (see Figure 4.3). It is found that a standard uniform spacing implicitly assumed by Irwin [120] generates a significant inhomogeneity in the mean streamwise velocity $\overline{u}$ in spanwise direction y of about 16%, see Figure 4.4. By adopting a non-uniform spacing this inhomogeneity reduces to 7.5%, which is regarded to be acceptable for the present investigation. After a few iterations the optimum configuration consists of four spires that are non-uniformly positioned in spanwise direction, i.e. the first and fourth spire are positioned at 105 mm

from the side-walls, while the second and third spire are positioned 110 mm away from the first or fourth spire respectively.

Figure 4.6 depicts the velocity profile, the profiles of the root mean square (RMS) of the velocity fluctuations and the mean Reynolds stress distribution in the wall-normal direction for the experiments and the LES. These profiles are normalized with the velocity at obstacle height. $U_h \equiv \overline{u}|_{z=h}$, which proved to be the best scaling for the rural-to-urban flows discussed in the subsequent sections. Nevertheless, it should be kept in mind that this velocity scale is not the preferred choice to scale the undisturbed velocity profiles, as U_h is not the relevant velocity scale for the velocity statistics in a turbulent boundary layer. Furthermore, small changes in the location at which U_h is determined has a considerable effect upon the scaled velocity statistics. Finally, Figure 4.5 shows the velocity profile in inner scaling compared with reference data from Osterlund [125].

Despite the different ways of generating the approaching boundary layer there is a satisfactory agreement between the results of the two methods; a good match is found for the mean velocity profile in the range $0 \leq z/h \leq 3$ (Figure 4.6a). In the LES a zero pressure-gradient boundary layer was generated, while in the experiment a slightly favourable pressure gradient was present due to the boundary-layer growth and the constant cross-sectional area of the tunnel. With the normalization with U_h this difference is reflected in a lower streamwise velocity in the outer region (above $z/h = 3$) of the experimental boundary layer (see Figure 4.6a). Moreover, it is reflected as a suppressed wake in the velocity profile in inner scaling in Figure 4.5. Furthermore, Figure 4.5 indicates a small dimple in the wake region of the current experimental result, which is attributed to the design and arrangement of the spires. Note, that the LES in Figure 4.5 depict a slightly suppressed log layer. This manifests itself as a mismatch in the outer layer of the mean streamwise velocity as shown in Figure 4.6a.

As observed in Figure 4.6b the profiles of u_{RMS} and w_{RMS} are similar in shape when comparing the experimental data with the LES simulations. The main differences are attributed to the difference in predicted and measured U_h (see Table 4.1), i.e. the lower U_h in the LES causes the scaled velocity fluctuations to be larger than in the experiments. In addition, the slightly favourable pressure gradient reduces the velocity fluctuations in the experimental boundary layer [55], thereby reducing the turbulence level. This is also reflected in the shape parameter H, defined as the ratio of the displacement thickness δ^* to the momentum thickness θ, which is found to be 12% higher in the experimental data. Furthermore, a reduction is observed in the mean Reynolds stress in the experiments in the region $2 \leq z/h \leq 5$, see Figure 4.6c. This is most likely attributed to the design and the arrangement of the spires. Nevertheless, as will be shown in the subsequent sections, the differences in characteristics of the approaching flow do not cause significant discrepancies in the development of the flow over the urban canopy.

The Reynolds number (Re) based on U_∞ and h is around 5.0×10^3 for the numerical simulations. In the experiments it ranges between 5.4×10^3 and 16.4×10^3, which is in the regime where Reynolds number effects are small when flow over sharp-edged obstacles is considered [98]. In addition, the wall-friction Reynolds number (h^+), based on u_τ and h, is around 200 (LES) and between 200 and 600 in the experiments, which is in the fully rough regime [126]. A summary of the relevant boundary-layer properties for both the experiments and the simulations can be found in Table 4.1.

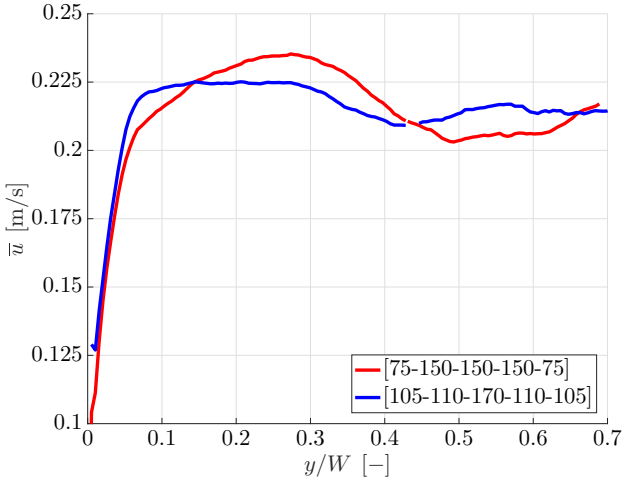

Figure 4.4: Spanwise uniformity of the streamwise velocity $\overline{u}$ at $z/h \approx 0.25$ for $\mathrm{Re}_\theta = 5876$, The red curve corresponds to the case where the spacing S between the spires is 150 mm, and the spires next to the wall are at a distance $S/2$ away from the wall. The blue curve shows the spanwise variation of $\overline{u}$ for optimal spacing. The numbers given in the legend correspond to the spacing between the spires in millimeter or the spacing between the wall and a spire (first and last number in legend entry).

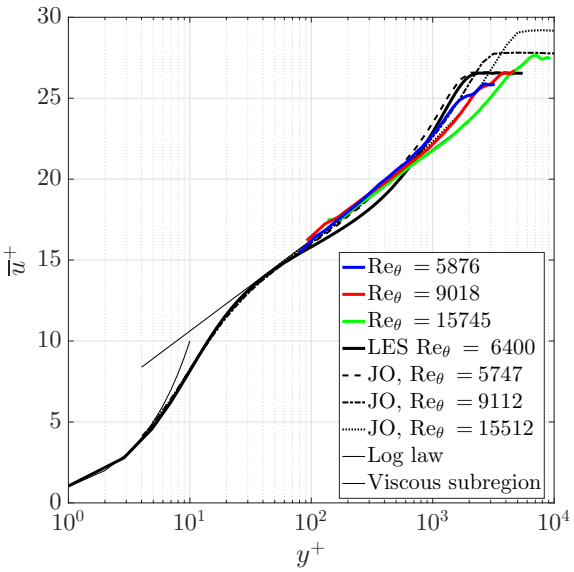

Figure 4.5: Velocity profile in inner scaling compared with data from Osterlund [125] (indicated by JO).

4.4.2 UNIFORM LINE SOURCE

The fluorescent dye is injected upstream of the first row of obstacles by a uniform line source, modelling the vehicle exhaust on a highway. A design of a line source in a wind tunnel environment is presented by Meroney *et al.* [127]. To correctly represent vehicle

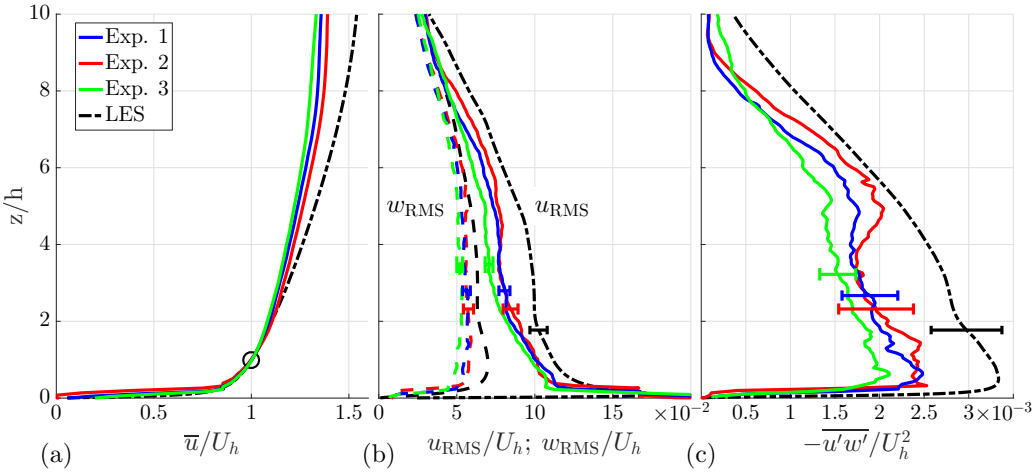

Figure 4.6: Properties of the approach flow boundary layer; mean streamwise velocity $\overline{u}$ (a), RMS of the velocity components (b) and Reynolds stress $-\overline{u'w'}$ (c). The circle in (a) indicates the reference velocity at obstacle height $U_h = \overline{u}|_{z=h}$. The errorbars in (b) and (c) represent the statistical mean $\pm$ the standard error of the mean.

Table 4.1: Summary of the properties of the approaching boundary layer; δ^* is the displacement thickness, θ is the momentum thickness, and H is the shape factor.

	$\frac{\delta_{99}}{h}$	$\frac{\theta}{h}$	$\frac{\delta^*}{h}$	H $\left(\frac{\delta^*}{\theta}\right)$	$\frac{U_\infty}{U_h}$	$\frac{u_\tau}{U_h}$	Re_τ $\left(\frac{u_\tau \delta_{99}}{\nu}\right)$	h^+ $\left(\frac{u_\tau h}{\nu}\right)$	Re $\left(\frac{U_\infty h}{\nu}\right)$
Exp. 1	11.43	1.09	1.65	1.52	0.70	0.055	2.4×10^3	209	5.4×10^3
Exp. 2	11.35	1.10	1.62	1.47	0.72	0.052	3.5×10^3	307	8.2×10^3
Exp. 3	9.59	0.96	1.35	1.41	0.75	0.049	5.7×10^3	598	16.4×10^3
LES	10.3	1.28	1.78	1.39	1.56	0.059	2.0×10^3	194	5.0×10^3

exhaust, the line source is required to have low vertical momentum as the exhaust of vehicles is predominantly directed horizontally. Furthermore, it is important to achieve a sufficiently high pressure drop over the line source. This causes the injection to be insensitive to local turbulent pressure fluctuations. The current design of this uniform line source is inspired based on the work of Doorne [128], who uses a porous metal plate to generate a uniform injection. In contrast to the trials by Meroney *et al.* [127] in air, the pressure drop over such a porous plate in water is sufficiently high to generate homogeneous dye injection.

A picture of the line source indicating the different components is given in Figure 4.7. The line source basically consists of a homogeneous porous metal plate with dimensions 1.0×40.0 cm ($L_x \times L_y$) on top of a small settling chamber with cross-sectional dimensions 1.0×2.0 cm ($L_x \times L_z$). The porous metal plate is mounted flush with the ground plate (see Figure 4.2). The permeability of the plate is specified by the manufacturer (Pall Corporation) as 23.2×10^{-12} m^2.

A uniform injection is critically dependent upon the pressure distribution in the settling chamber below the porous plate and the homogeneity of the porous plate. To achieve a homogenous pressure distribution below the porous plate, the dye is injected at nine discrete points below the porous plate (see Figure 4.7). The hoses connnecting the injection points to the syringe pump system are all of equal length, thereby ensuring that the pressure drop is equal over each hose. Doorne [128] suggested to inject the dye parallel to the porous plate thereby avoiding stagnation points on the porous plate. However, due to geometric constraints this is not feasible in the current setup and the dye is injected at nine discrete points in the bottom plate of the settling chamber (i.e. perpendicular to the porous plate). After a number of design modfications, kitchen sponge is added in the settling chamber, which breaks up the jets that are present at each injection point and thereby homogenizes the output profile. The lateral homogeneity is assessed in more detail below.Based upon visual inspection this yields a sufficient degree of lateral homogeneity of the line source.

A 4-axle syringe pump system (neMESYS, Cetoni GmbH) controlled by the neMESYS user interface is used to inject a concentrated solution of Rh-WT ($C = 10\,\mathrm{mg/L}$) at a continuous volume flow rate between 3 and 5 ml/s. At the current volume flow rates, the average vertical injection velocity is about 0.75 mm/s or $0.3\%U_\infty$, which is considered to be nearly momentum free.

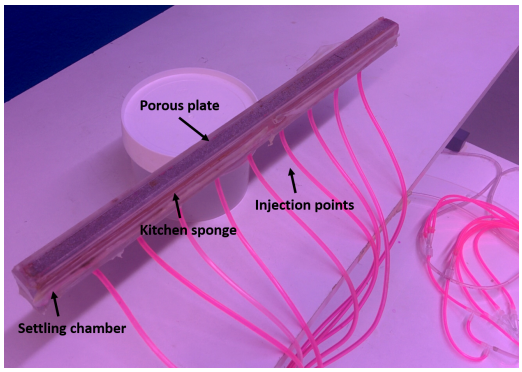

Figure 4.7: Picture of the line source indicating the different components.

The spanwise homogeneity of the line source is evaluated by measuring the spanwise concentration distribution with an LIF setup. The line source is mounted in ground plate of the experimental setup without the urban model present. Next, a collimated laser sheet is generated parallel to the line source at different downstream positions. A camera viewing from above is employed to record the spanwise intensity distribution. The spanwise profiles behind the line source are shown in Figure 4.8. The spanwise inhomogeneity close to the line source is considerable. More downstream the mixing due to turbulence decreases the inhomogeneity. Note that no buildings are present in this setup, which otherwise would significantly decrease the spanwise inhomogeneity downstream direction as a result of turbulent mixing due to the presence of the buildings.

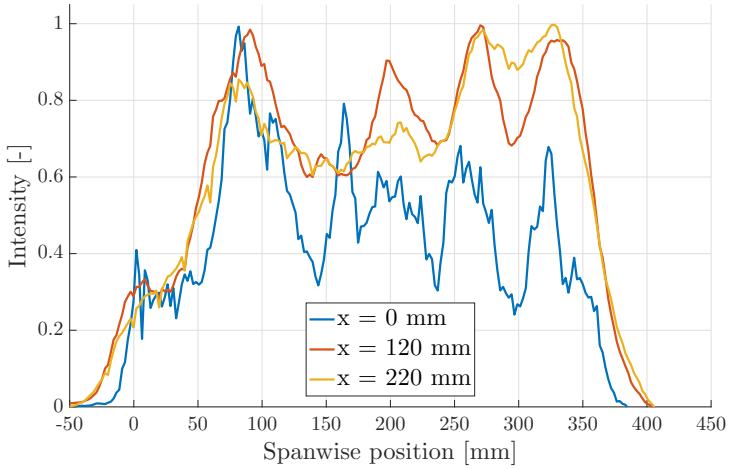

Figure 4.8: Intensity profiles of line source at different streamwise distances behind the source

4.4.3 PIV SETUP

To perform simultaneous velocity and concentration measurements above and partly inside the canopy, a stereoscopic PIV set-up was combined with a planar LIF set-up, as shown in Figure 4.2. For the stereoscopic PIV measurements, the flow was seeded with 10 μm buoyant-neutral tracer particles (Sphericell). The $y = 0$ plane was illuminated with a twin-cavity double pulsed Nd:YAG laser (Spectra-Physics Quanta Ray), resulting in a field of view of approximately $430 \times 250\,\mathrm{mm}^2$ ($x \times z$). Dedicated optics were used to form a thin laser sheet with an estimated thickness of approximately 1 mm. The particle images were recorded using two high resolution CCD cameras with a 4872×3248 pixel format (Image LX 16M, LaVision). Both PIV cameras are equipped with Micro-Nikkor F105mm objectives operating at an aperture number $f_\# = 8$. Additionally, both cameras were equipped with Scheimpflug adapters to allow for large viewing angles while keeping the particle images in focus [129]. The total separation angle between the PIV cameras was set to 56°. To enable measurements partly inside the canopy, both cameras had a small vertical inclination of about 10°.

Data acquisition was performed using the commercial software package Davis 8.3. Additionally, Davis 8.3 was used to calibrate and process the PIV data. The calibration and the self calibration procedure as proposed by Wieneke [83] was employed to remove the perspective deformation in stereoscopic viewing and obtain the viewing angles. The PIV images were interrogated with a multi-pass interrogation technique, where the final interrogation windows had a size of 24×24 pixels, corresponding to a spatial resolution of 0.1h, with 75% overlap between the neighboring windows. The fraction of spurious vectors was found to be less than 2%. These were reliably detected using a median test and replaced by linear interpolation [51]. Each dataset consisted of at least 1,500 instantaneous velocity/concentration fields acquired at a temporal resolution of 1.44 Hz. This low acquisition frequency ensured that subsequent samples could be considered as statistically uncorrelated. As a result, reliable and accurate first and second order statistics could be obtained.

4.4.4 LIF SETUP, CALIBRATION AND CORRECTION PROCEDURE

A third camera (Image LX 16M, LaVision) was added to perform the planar LIF measurements. This camera was also equipped with a Micro-Nikkor F105mm objective operating at an aperture number $f_{\#} = 2.8$. A lower aperture number was chosen to collect a larger amount of fluorescent signal. To provide a better view into the canopy this camera had a slight vertical inclination of just 10 degrees, which did not require a Scheimpflug adapter. In order to separate the simultaneous measurements of velocity and concentration, shortpass filters (PIV cameras) and a longpass filter (LIF camera) were employed. Note that both the PIV cameras and the LIF camera were operated in double frame mode. However, the LIF results presented in this chapter are only based upon the first frame of each snapshot as the second laser pulse turned out to be too unstable in time, i.e. the profile of laser beam changed its shape significantly during the course of an experiment, which would decrease the accuracy of the reconstructed concentration fields. As a result, there is a small mismatch between the concentration field and the velocity data due to convection, which is typically on the order of 4 pixel displacement. This is regarded to be small as the shift is well below the size of a PIV interrogation area. The effective spatial resolution of the concentration fields was $0.004h$. In order to evaluate the concentration fluxes, the velocity field obtained by the PIV measurements was interpolated onto the high resolution LIF grid through bicubic interpolation.

Theoretical Background

A short theoretical background on the working principles of LIF is given in this section in order to show how the raw intensity images are converted to concentration images. In conjunction, also the important criteria for valid LIF measurements are discussed. Planar LIF is a popular and powerful technique to measure concentrations in aqueous environments. The origins of this technique possibly go back to the time that Osbourne Reynolds started his famous visualization experiments by injecting a dye into a round pipe to visualize the laminar to turbulent transition [130]. As noted by Crimaldi [86] it took over a century before this visualization technique was extended to a more quantitative measurement technique. Without going into great detail, the basics of LIF are explained in this section. The fundamental relation that underlies the LIF theory is given by the fact that the local fluorescence F, the local dye concentration c^* and the local excitation intensity I are related as:

$$F \propto \frac{I}{1 + I/I_{sat}} c^*, \tag{4.5}$$

where I_{sat} is the saturation intensity of the specific chosen dye. As long as $I \ll I_{sat}$ the excitation is weak and Equation 4.5 is linear to a good approximation. Melton and Lipp [131] estimated the I_{sat} of Rh-WT to be in the order $10^{10}\,\mathrm{W/m^2}$. For the current experiments, a pulsed ND:YAG laser is employed (400 mJ/pulse), resulting in peak intensities to be of the order $8 \times 10^{10}\,\mathrm{W/m^2}$, which is in the same range the saturation intensity limit of Rh-WT. However, Melton and Lipp [131] pointed out that reliable measurements can be obtained by operating under so-called optical thin conditions. Under that condition, Equation 4.5 is still valid, while F is found to remain linear in c^*. The term 'optically thin' originates from the analysis of the Beer-Lambert law. This

law states that a light ray with intensity I passing trough a medium with thickness dr, extinction coefficient ϵ and concentration c^* experiences an intensity change dI as:

$$\frac{\mathrm{d}I}{I} = -\epsilon c^* dr \tag{4.6}$$

A light ray traveling over a distance $\mathrm{d}z = z_0 - z_1$through a medium with spatially varying concentration $C(x,z)$, then experiences an intensity change equal to:

$$I(x,z) = I_0(x,z)e^{-\epsilon \int_{z_0}^{z_1} c^*(x,z)\mathrm{d}z} \tag{4.7}$$

As long as $\epsilon \int_{z_0}^{z_1} c^*(x,z)\mathrm{d}z \ll 1$, attenuation of the laser sheet intensity due the presence of the dye can be neglected (i.e. $I(z_1) \approx I(z_0)$) and the system is called optically thin [86]. In case attenuation would become significant, the integral given in Equation 4.7 needs to be evaluated for each end every pixel. Therefore, many researches have performed their experiments under these conditions, circumventing such a tedious pixel-by-pixel integration procedure [93, 131, 132]. Note that I_0 is still dependent upon x and z as the laser sheet intensity changes because the laser sheet is radially expanding and there is an intensity profile in streamwise direction. The next section shows that the calibration curves are linear (see Figure 4.10), indicating that the current experiments are indeed performed under these optical thin conditions. In accordance with Krug *et al.* [93], the imaged fluorescence intensity I_F for each pixel can be written as:

$$I_F(i,j) = \alpha(i,j)I(x,z)c^*(x,z), \tag{4.8}$$

where $\alpha(i,j)$ is an efficiency prefactor that comprises for instance the fraction of received fluorescence or the quantum efficiency of the dye, $c^*(x,z)$ denotes the local concentration imaged onto pixel (i,j) and $I(x,z)$ is the local laser light intensity as given by Equation 4.7. Substituting Equation 4.7 into Equation 4.8 by assuming optical thin conditions yields:

$$I_F(i,j) = \alpha(i,j)I_0(x,z)c^*(x,z) \tag{4.9}$$

Equation 4.9 is the basis to determine a calibration curve for each pixel in the measurement domain. Equation 4.9 is evaluated at different known concentration levels by positioning a container with a known uniform concentration in the field of view. The value of the coefficient $\alpha(i,j)I_0(x,z)$ is then obtained by a linear least squares fit for each individual pixel.

Dye Selection and Schmidt Number Effects

The fluorescent dye used in the experiments is Rhodamine WT (Rh-WT). The main reason to select this dye is that the present laser is able to excite Rh-WT [131].This dye has spectral characteristics similar to the more commonly used Rhodamine B (Rh-B), however it is much less toxic [86]. Although Rh-WT is a temperature sensitive fluorescent tracer [133], the effect of temperature variations is found to be negligible, because the water temperature varies less than 1°C over the course of a measurement day. The Schmidt number ($\mathrm{Sc} = \nu/D$, where ν is the kinematic viscosity and D is the mass diffusivity) of Rh-WT in the experiments is estimated to be about 2,500. However, the finite thickness of the laser sheet and the camera resolution both act as a low pass filter,

resulting a in lower 'effective'Schmidt number Sc_{eff}. In order to provide an estimate for this effective Schmidt number, the Schmidt number can also be written as the ratio between the Kolmogorov length scale η and the Batchelor length scale λ_B as [134]:

$$Sc = \left(\frac{\eta}{\lambda_B}\right)^2 \tag{4.10}$$

When looking at the spatial spectrum of the concentration fluctuations, Obukhov [135] and Corrsin [136] showed that for wavenumbers $1/L < k < 1/\eta$ (where L is the integral length scale) the scalar spectrum obeys a $-5/3$ power scaling in accordance with the classical Kolmogorov-Richardson cascade. However, for large Schmidt numbers, as presently the case, the Batchelor scale is much smaller than the Kolmogorov length scale and another scaling regime in the range $1/\eta < k \leq 1/\lambda_B$ is observed, the so called viscous-convective range. Batchelor [137] hypothesized that the spectrum in this wavenumber range obeys a -1 scaling law. Amongst many others Donzis *et al.* [134] show evidence of this -1 power scaling in DNS. Figure 4.9 shows the spectrum of the scalar concentration fluctuations in the present AR5 case at a friction Reynolds number of about 2.4×10^3. The data is taken at $z/h = 2$ near the downstream edge of the measurement domain ($15.5 < x/h < 17$). Figure 4.9 indicates clearly the two different scaling regimes. The relatively low Reynolds number results in a small range of wave numbers over which the the $-5/3$ scaling law is observed, as pointed out previously by Warhaft [138]. Additionally, the strong inhomogeneity of the concentration field in streamwise direction further suppresses the appearance of the $-5/3$ part in the spectrum.

Returning back to Equation 4.10, an effective Schmidt number can now be obtained. First of all, η is estimated from the non-dimensional wavenumber kh at which the -1 scaling law starts (i.e. $\eta \approx 0.75$ mm). Second, an effective Batchelor scale is obtained by determining the highest wave number that can be resolved, i.e. $\lambda_B \approx 0.17$ mm. This results in an effective Schmidt number of $Sc \approx 20$. Additionally, Equation 4.10 is used to provide an estimate for the real Batchelor scale as $\lambda_B = 1/50\eta \approx 0.015$ mm, where $Sc = 2500$ and $\eta = 0.75$ mm was used. This is well below the current resolution of the LIF camera. Therefore, the low resolution of the camera reduces the Schmidt number considerably.

Calibration Procedure

The calibration of the LIF images, i.e. the conversion of raw intensity images to concentration fields according to Equation 4.9, is performed by positioning a small Plexiglas container (with a size of $45.0 \times 12.0 \times 4.0$ cm) in the measurement domain. This container is filled with different known uniform concentrations. Then the calibration procedure is as follows. First, 10 liter of tap water is degassed in a vacuum chamber, to remove most of the dissolved air from the water. This greatly limits the presence of unwanted air bubbles in the calibration container, which will otherwise spoil the calibration images. This water is then circulated through the plexiglass container by means of a circulation pump. The reason to circulate the calibration fluid is to avoid any unwanted photobleaching effects, that will become noticable once the same Rhodamine molecules are excited too often with a high power laser (as discussed later). A second motivation

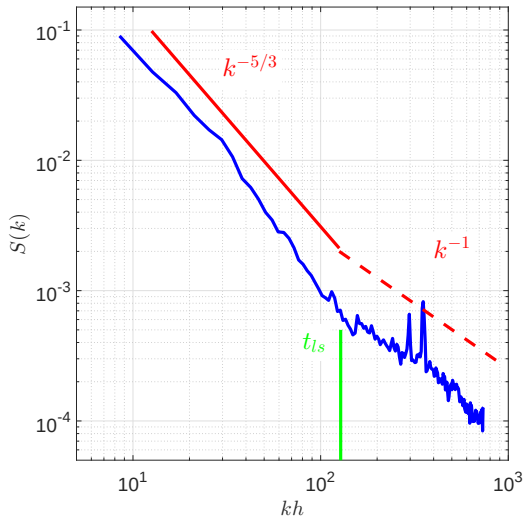

Figure 4.9: Spectrum of the scalar concentration fluctuation determined at $z/h = 2$ averaged in horizontal direction at over a streamwise distance of $1.5h$. The data is taken from the AR5 dataset at a friction Reynolds number of 2.4×10^3. Additionally, the thickness of the light sheet is indicated by the green line.

is the fact that there is no need to touch the container during the calibration process while increasing the concentration in the container. This lowers the risk of changing the laser sheet shape and position during the calibration phase. A syringe pump (Hamilton ML500) is used to add 0.25 ml of a concentrated Rh-WT solution (1 g/L) in between each calibration step. As a result, the concentration in the plexiglass container is varied in seven step between 0 and 150 μg/L. This range of concentrations covers most of the instantaneous concentrations that are observed in the actual experiments. After adding this concentrated Rh-WT solution to the calibration setup, we wait approximately two minutes to ensure a homogeneous mixed calibration fluid, after which 50 calibration images are recorded. As suggested by Krug *et al.* [93] the effects of PIV seeding on the concentration images cannot be neglected. A different opinion is given by Vanderwel and Tavoularis [132] who basically assume this effect to be negligible. In the current experiments it is found that the effect of particles on the LIF measurements becomes noticeable once the particle concentration is far above typical seeding levels encountered in the actual experiments. Still, in the current experiments seeding particles are introduced into the calibration container before starting the calibration procedure and there is no need to perform an additional attenuation correction as proposed by Krug *et al.* [93]. Seeding is added in small steps until a seeding concentration is reached which is comparable with seeding levels found in the actual experiments. The additional benefit of the circulating flow in the calibration container is that it ensures that the particles remain homogeneously distributed within the calibration container during the course of the calibration procedure.

The result of this procedure is a calibration curve for each pixel in the measurement domain. After subtraction of the zero-concentration image, a least squares fit is performed for each and every pixel to obtain a pixel-wise calibration relation between the

concentration and intensity according to Equation 4.9. A few examples of such calibration curves are shown in Figure 4.10. The calculated R^2 value of this least squares fit is on average 0.9985 for the calibration curves, indicating that these least squares approximation fits the data.

As mentioned before, the current experiments are performed under optical thin conditions. This means that there exists a linear relationship between the measured intensity and the concentration. This behavior is nicely reflected in the calibration curve. Even at the highest concentrations, the calibration curves are linear [139]. Furthermore, it is noticed that almost the complete dynamic range of the camera is used, i.e. 4095 gray scales in case of the 12-bit camera, which is beneficial in terms of the signal to noise ratio of the signal [86], i.e. the measured concentrations have an intensity that is much higher than the dark image response of the camera.

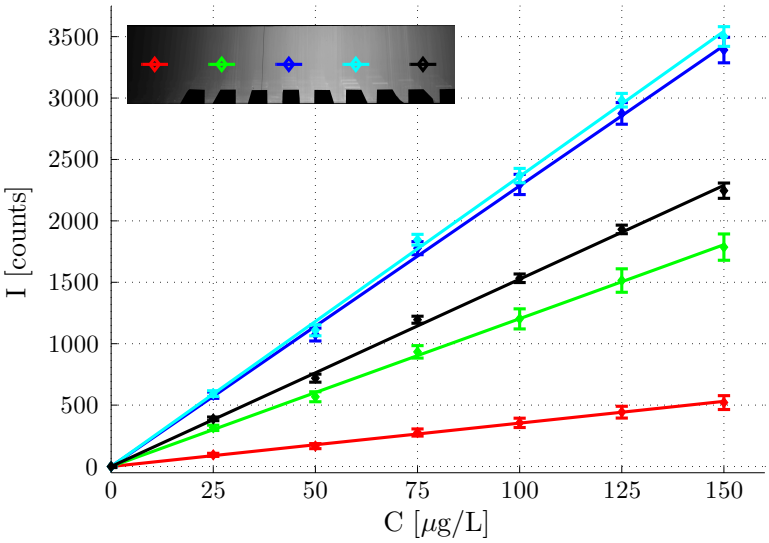

Figure 4.10: Calibration curves for different pixels inside the field of view. Values at each concentration are obtained by averaging over 50 images. The errorbars indicate the standard deviation of the signal. The solid lines indicate the linear least squares fit through the measurement points. The R^2 value of these fit is on average 0.9985. The inset shows the plexiglas calibration container and the locations at which the displayed calibration curves are taken.

Background Subtraction and Pulse-to-Pulse Variation

Before the raw images are converted to a concentration, first of all the raw digital images are rescaled (with a factor γ) to compensate for the pulse to pulse variations that are inherently present in the laser beam of a Nd:YAG laser. It is found that the standard deviation of this fluctuation is about 3% of the mean intensity, which is comparable with previous results by Vanderwel and Tavoularis [132]. In addition, a proper background is subtracted. Because the water tunnel is a recirculating flow facility, the background concentration slowly builds up during an experiment. To account for this change in background concentration, the background image $B_n(i, j)$ is a linear interpolated im-

age obtained from background images taken before and after each experiment. The instantaneous concentration $c_n^*(i,j)$ of snapshot n is obtained by:

$$c_n^*(i,j) = \gamma \frac{I_F(i,j) - B_n(i,j)}{\alpha(i,j) I_0(x,z)}, \tag{4.11}$$

where the coefficient $\alpha(i,j)I_0(x,z)$ is determined from the calibration procedure as described before.

On the Validity of the LIF Measurements

As a result of the used laser, several problems are likely to occur; e.g. photo bleaching and dye saturation [86]. To prevent photobleaching effects, the calibration fluid is circulated during the calibration phase. During the experiments, photo bleaching is not a problem as the dye passes the laser beam only once. Figure 4.11 shows the intensity variation in time. The first average is taken in a small area in the background part (red square and line), which is the area in which non-circulating fluid is present. The second averaging area is taken inside the calibration container, in which the calibration fluid is circulated (blue square and line). The solid lines represent the least squares fit to the data. It is clear that the non-circulating fluid is subject to more pronounced photobleaching effects compared to the circulating fluid inside the calibration container, reflected in a larger drop-off of the least squares fit.

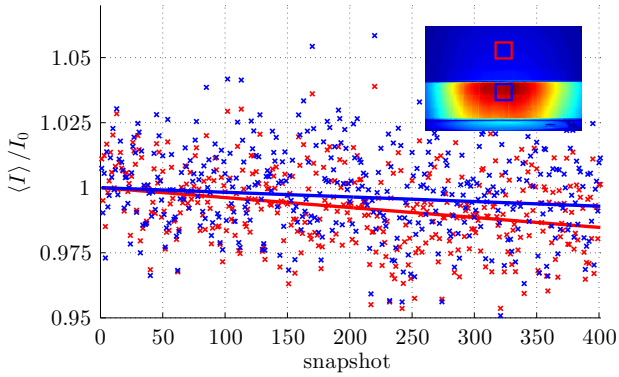

Figure 4.11: Photobleaching effects over the course of a dataset. Averages in the non-circulating background (red) and in the circulating calibration container (blue) are shown, normalized by the intensity value of the first snapshot (from least squares fit). The average intensity in each sample is given by crosses and the solid lines correspond with the least squares fit to the data. The inset shows the calibration tank and the areas over which average intensities are determined.

Next to photobleaching effects, also dye saturation might become a problem because of the high peak intensities of the laser [86]. To test for this behavior, the laser power is systematically varied at a known uniform concentration. The laser power is measured using a laser power meter (Ophir 30A-P-SH). The result of this experiment is shown in Figure 4.12. Up to $P \approx 2.5$ W the fluorescence is approximately linear with the incident laser power, indicating no dye saturation effects. However, the last measurement point indicates a significant higher fluorescence intensity compared to the expected value from the linear trend upto 2.5 W.

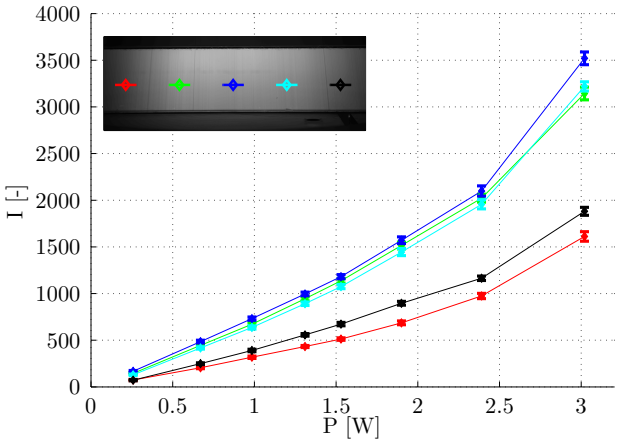

Figure 4.12: Fluorescence intensity versus laser power. The errorbars indicate the standard deviation of the signal. The inset shows the calibration container and the locations at which the displayed curves are taken.

4.5 RESULTS: VARYING THE SPANWISE LENGTH SCALE OF THE ROUGHNESS

4.5.1 THE FLOW OVER THE URBAN CANOPY

In this section the acquired rural-to-urban flow fields are compared for the first eight streets in the $y = 0$ plane, see Figure 4.1. All velocity statistics are normalized with the undisturbed velocity at obstacle height U_h. A snapshot of the spanwise velocity component is shown in Figure 4.13 for case AR5 comparing the experiment and the simulation. The results show similar large turbulent structures arising from the top of the obstacles, that grow in downstream direction and that have a larger magnitude than the velocity fluctuations in the approaching flow. Figure 4.14 visualizes the effect of the roughness transition on the mean flow. It shows the contour plots of the mean streamwise velocity component $\overline{u}$ as well as the mean vertical velocity component $\overline{w}$ for case AR5. As the results were averaged over a duration of the order of $10^3 T$, the statistics were converged to within a few percent. The differences in $\overline{u}$ and $\overline{w}$ between the simulations and the experiments are mostly smaller, indicating that the agreement is very good. The only significant difference is the size of the mean recirculation areas at the top of the first three rows of obstacles. The LES predicts a negative vertical velocity close to the downstream walls of the first two street canyons, while in the experiment the flow is solely directed out of the street canyons. This difference can be caused by a limitation of the employed methods; especially at the top of the first obstacle the PIV/LIF results should be interpreted with care, because due to high spatial gradients of the velocity and reflections from the obstacle, the PIV results in this region are prone to errors. In this region, too, the numerical errors in the LES can be expected to be largest due to the high velocity near the singularity at the obstacle corners and the large change in velocity gradients. However, these differences could also be purely physical, since the slightly different turbulence characteristics in the approaching flow (see Section 4.4.1)

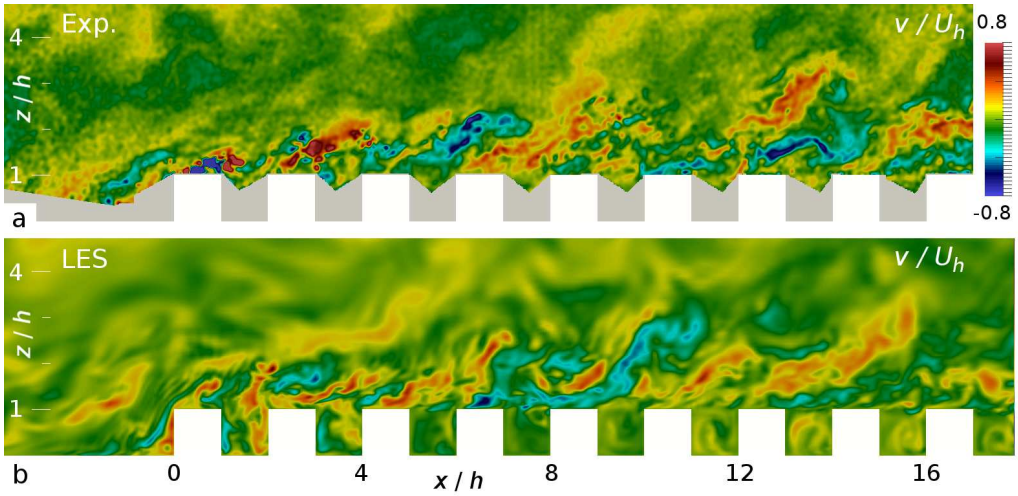

Figure 4.13: Contours of instantaneous spanwise velocity component v/U_h in the midplane of case AR5; (a) experiment and (b) simulation. Areas that could not be illuminated or seen in the experiments have been masked in grey and the obstacles are shown in white.

can influence the development of the shear layer emanating from the first obstacle [118, 119]. Nevertheless, downstream of the third row the results of the two methods are nearly indistinguishable.

Figure 4.15 shows the mean Reynolds stresses $\overline{u'u'}$ and $-\overline{u'w'}$ for the same case. The strong shear layer emanating from the upstream corner of the first obstacle generates large turbulent fluctuations resulting in a peak in $\overline{u'u'}$ above the first obstacle and a peak in $-\overline{u'w'}$ above the first street canyon. The flow appears to be also strongly affected by the presence of the second obstacle, above which another peak in $\overline{u'u'}$ is present, while a peak in $-\overline{u'w'}$ is located above the second street canyon. The intensity of the turbulent plume decreases in downstream direction, while weaker plumes of $-\overline{u'w'}$ are produced by the shear layers above the street canyons. Just as for $\overline{u}$ and $\overline{w}$ there are some discrepancies between the experiments and the simulations above the first three obstacle rows due to the aforementioned reasons.

The contour plots in Figure 4.14 and Figure 4.15 give an overview of the flow and can be used for a qualitative comparison of the two methods. Figure 4.16 allows for a quantitative comparison of cases AR1, AR2, AR5, AR8 and 2D, by showing the vertical profiles of the mean streamwise velocity component $0.5h$ in front of the first obstacle row and in the middle of each subsequent street canyon. The LES data are shown by continuous lines, while, if available, the experimental data are shown by dashed lines. In all cases backflow occurs inside the canopy, while above the canopy an internal boundary layer developed, shown in Figure 4.16 by open symbols for the experiment and by solid symbols for the LES. The internal boundary layer depth δ_i is found by subtracting the smooth-wall inlet velocity profile from the mean velocity field for the roughness transition: $\Delta\langle\bar{u}\rangle = \langle\bar{u}\rangle_{RT} - \langle\bar{u}\rangle_{inlet}$. δ_i is defined as the height at which the vertical gradient of $\Delta\langle\bar{u}\rangle$ reaches zero. The threshold $|d\Delta\langle\bar{u}\rangle/dz| < 0.005U_h/h$ is used to determine this location. In all cases the flow profiles in the street canyon changes

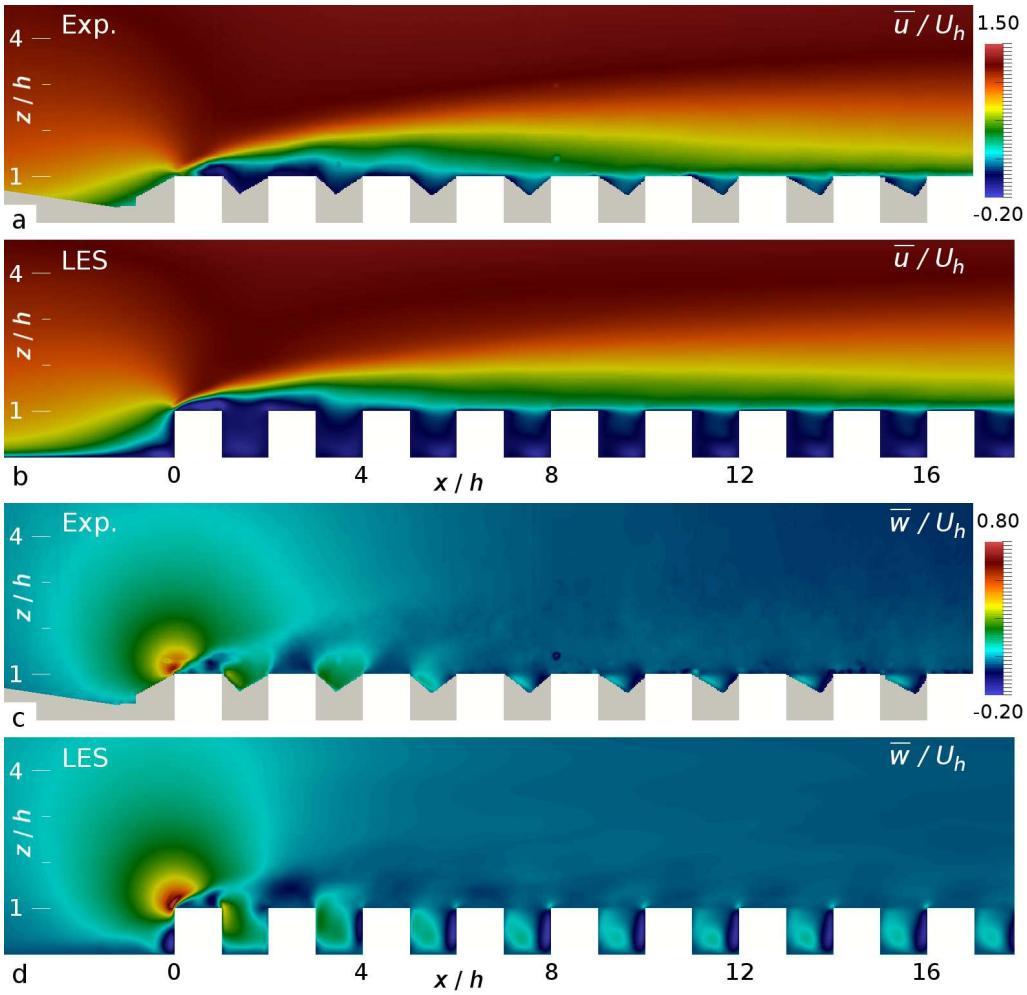

Figure 4.14: Contours of mean streamwise velocity component $\overline{u}/U_h$ (a, b) and mean vertical velocity component $\overline{w}/U_h$ (c, d) in the midplane of case AR5; experiment (a, c) and simulation (b, d). Areas that could not be illuminated or seen in the experiments have been masked in grey and the obstacles are shown in white.

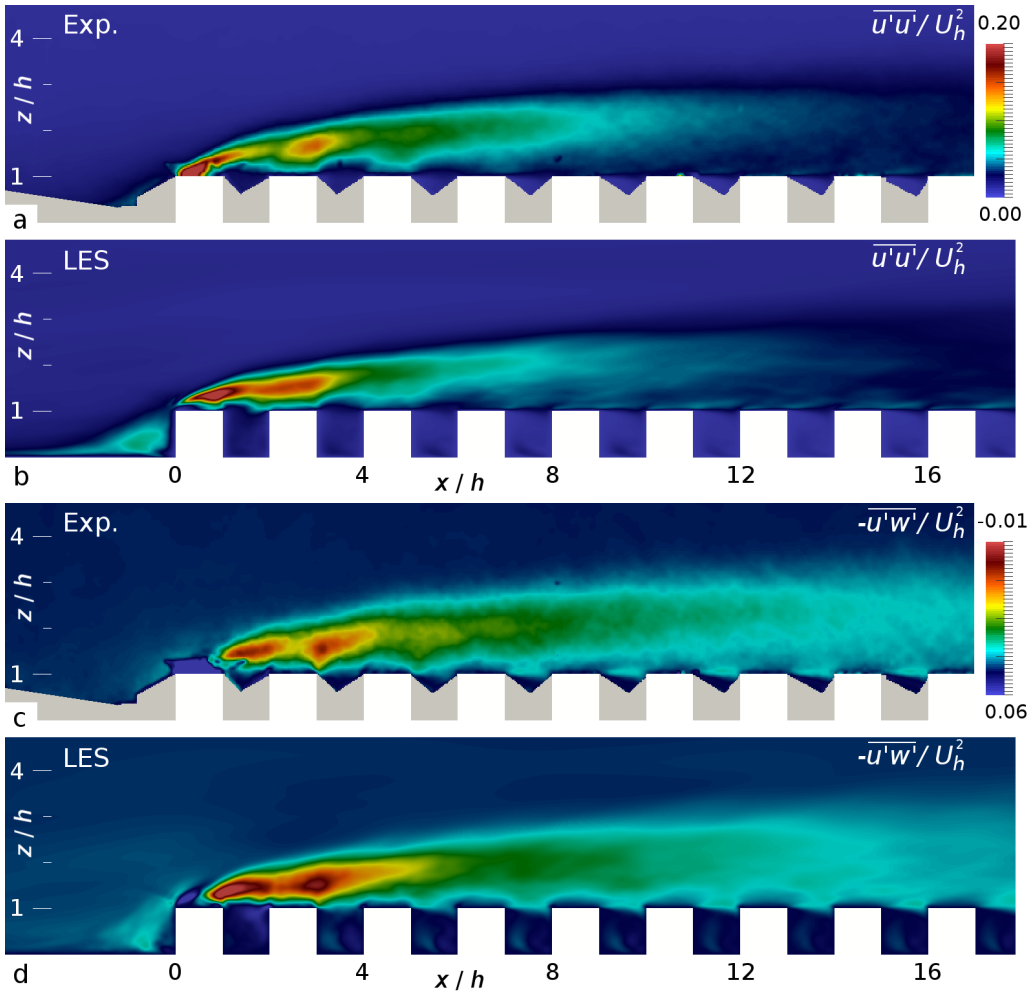

Figure 4.15: Contours of $\overline{u'u'}/U_h^2$ (a, b) and $\overline{u'w'}/U_h^2$ (c, d) in the midplane of case AR5; experiment (a, c) and simulation (b, d). Areas that could not be illuminated or seen in the experiments have been masked in grey and the obstacles are shown in white.

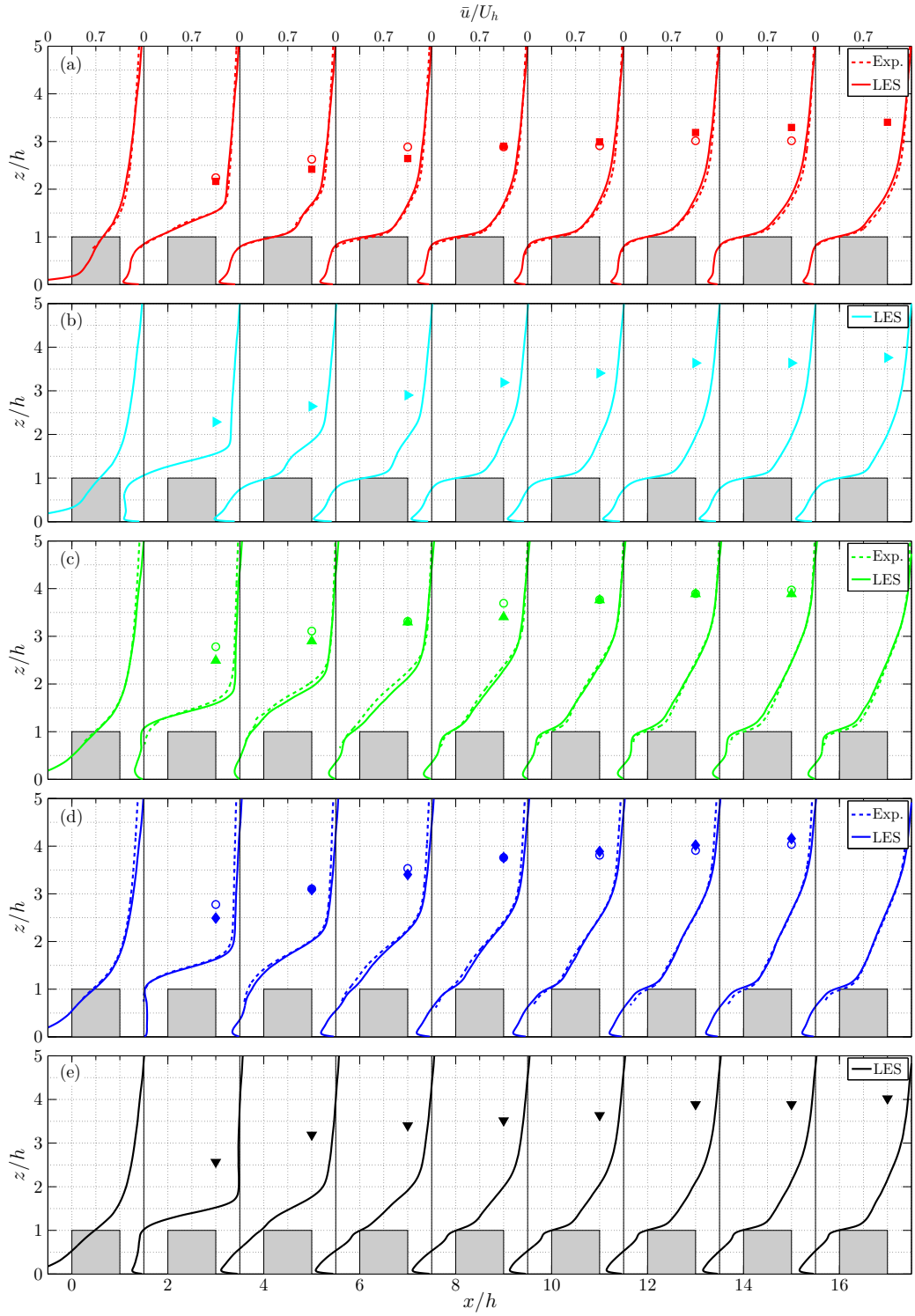

Figure 4.16: Profiles of mean streamwise velocity component $\overline{u}/U_h$ in the middle of each street canyon for cases AR1 (a), AR2 (b), AR5 (c), AR8 (d) and 2D (e). The internal boundary-layer depth, δ_i, is shown by solid markers for the LES and by open markers for the experiment (if available).

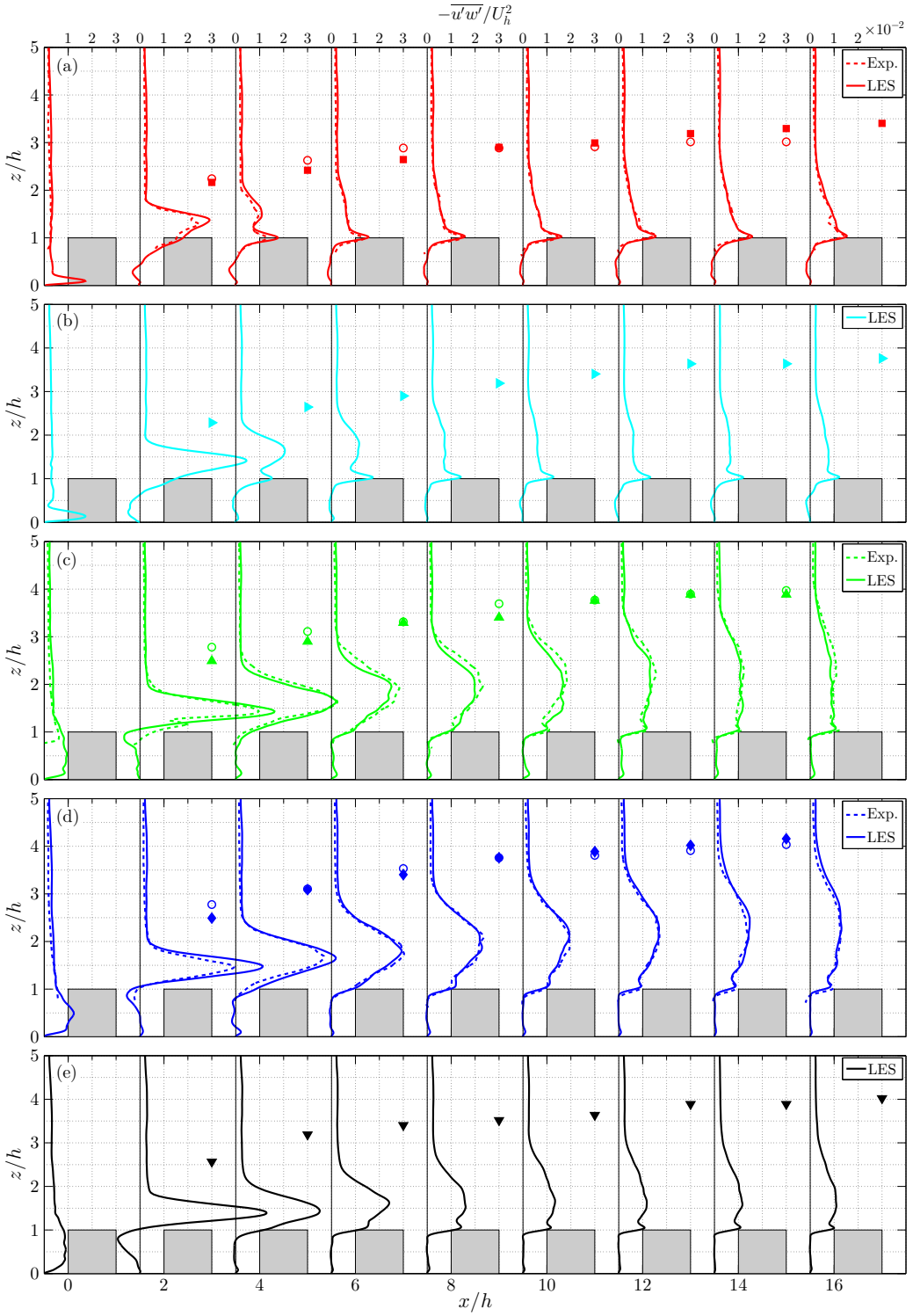

Figure 4.17: Profiles of mean Reynolds stress $-\overline{u'w'}/U_h^2$ in the middle of each street canyon for cases AR1 (a), AR2 (b), AR5 (c), AR8 (d) and 2D (e). The internal boundary-layer depth, δ_i, is shown by solid markers for the LES and by open markers for the experiment (if available).

significantly over the first three to four rows of obstacles while only minor changes are observed from street canyon 4 onwards. For case AR1, and especialy case AR2, $\overline{u}$ is mostly negative at this location in the street canyon, while for cases AR5, AR8 and 2D a 'canyon vortex' arises that is most apparent in case 2D. Figure 4.17 shows the profiles of the mean Reynolds stress $-\overline{u'w'}$ at the same locations. The differences between the LES and the experiments are minor with the maximum differences occurring in the region with large gradients just above the canopy in the first street canyon. In this region the finite resolution of the PIV acts as a lowpass filter, which results in an underestimation of the peak value of the Reynolds stresses. The fraction of resolved Reynolds stresses can be estimated from the ratio between the PIV resolution and the length scale Λ of the dominating flow structures [140]. Λ is estimated using the distance required for the streamwise two-point correlation of u to decrease to 0.5. Above the first street canyon in case AR8 (Figure 4.17d) Λ is $0.3h$, resulting in approximately 83% of the Reynolds stress being resolved at that location.

With increasing aspect ratio l/h the blockage of the incoming flow increases, which results in an increase of the peak in $-\overline{u'w'}$ behind the first row of obstacles. Further downstream this peak diffuses and eventually the largest value of $-\overline{u'w'}$ occurs near the top of the canopy, where the rooftop shear layers are the largest sources of turbulence production. In view of blockage of the flow case AR8 approximates the 2D case, which is reflected in a similar peak in $-\overline{u'w'}$ behind the first row. Furthermore, since the Reynolds stress induced by the first row of obstacles is more than ten times larger than the Reynolds stress in the approaching flow boundary layer, the influence of the slight difference in approaching flow characteristics between experiments and simulations is marginal. However, in the eighth street canyon the depth of the region with increased Reynolds stress is larger for case AR8 than case 2D. This is because the three-dimensional roughness arrays (all cases other than 2D) induce a secondary flow that causes the internal boundary layer to grow more rapidly in case AR8 than in case 2D. This behavior is shown in Figure 4.18. There is a satisfactory agreement between the simulations and the experiments. Initially, δ_i grows more rapidly for larger aspect ratios, suggesting that δ_i increases with increasing blockage. However, δ_i does not solely depend on the blockage of the flow. This is indicated by the fact that δ_i is slightly larger for case AR8 than for case 2D, while the blockage of the flow is less. Hence, there the three-dimensional nature of the roughness results in secondary flows that also affect the internal boundary layer growth.

4.5.2 POLLUTANT DISPERSION

Pollutant dispersion is investigated by considering concentrations of a passive tracer released from a line source $2h$ upstream of the urban canopy. The concentrations c^*, retrieved both from measurements and from simulations, are non-dimensionalized using the reference velocity U_h, obstacle height h, source width L_y, source concentration c_s and source volume flow rate ϕ_s (see Section 4.4.2):

$$c = \frac{c^* U_h h L_y}{c_s \phi_s} \tag{4.12}$$

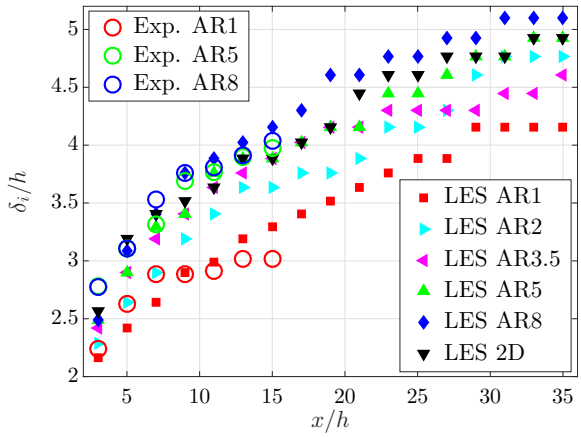

Figure 4.18: Internal boundary-layer depth δ_i at different streamwise locations. LES results are given by the solid symbols, while the open symbols represent the experimental results.

Figure 4.19 shows the contours of c for case AR5 corresponding to the instantaneous velocity field shown in Figure 4.13. The experimental results exhibit more distinctive layers than the simulations due to the larger Schmidt number (Sc). Nevertheless, there is a high degree of similarity when the larger structures are considered. This is reflected in a turbulent Schmidt number of 1.21 in the experiments and 0.77 in the LES, which was estimated by deriving the turbulent viscosity and the turbulent diffusivity using the Boussinesq approximation.

Mean Concentration Fields

Figure 4.20a-d shows the vertical distribution of mean concentration starting $0.5h$ upstream of the first row of obstacles and in the middle of each subsequent street canyon for cases AR1, AR5, AR8 and 2D. The LES data are shown by continuous lines, while, if available, the experimental results are shown by the dashed lines. The internal boundary-layer depth δ_i is plotted by solid markers for the LES and by open markers for the experiment. Clearly, the vertical profiles for $\overline{c}$ are largely controlled by δ_i as high concentrations remain inside the internal boundary layer. The most pronounced differences between the numerical and experimental results are observed inside and just above the street canyons (i.e. $z/h < 1.5$), where the experiments indicate a significantly higher concentration. Additional tests revealed that the line source was slightly non-uniform in spanwise direction with a higher than average flow rate at the location of the measurement plane. Nevertheless, the flow rate through the line source was kept constant in time. The influence of the spanwise non-uniformity decreases in downstream direction as turbulence decreases this lateral inhomogeneity, leading to a closer match between the two methods further downstream. This behaviour is also reflected in Figure 4.20e, where the average street canyon concentration is shown. Since the street canyon is only partially visible in the experimental results, the average street canyon concentration is determined only in the upper part of the street canyon. From the LES results it is concluded that this is a good approximation, as the street canyon concentration is quite

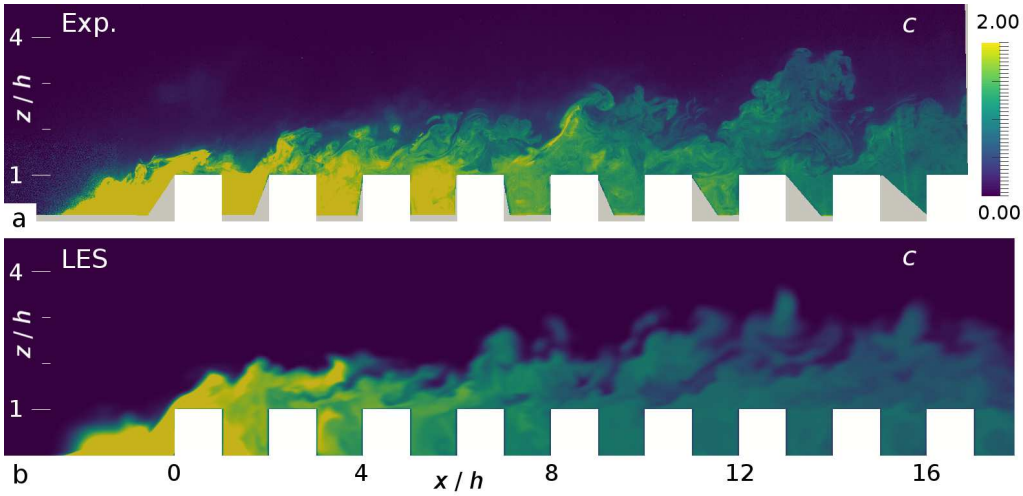

Figure 4.19: Contours of instantaneous concentration c (defined in Equation 4.12) in the midplane of case AR5; (a) experiment and (b) simulation. The snapshots correspond to the velocity fields shown in Figure 4.13. Areas that could not be illuminated or seen in the experiments have been masked in grey and the obstacles are shown in white.

uniform (especially in the more downstream street canyons). Considering the different aspect ratios it is clear that cases AR5, AR8 and 2D predict qualitatively similar behaviour: the maximum average concentration occurs in the first street and the average concentration decreases slowly in subsequent streets. Different behaviour is found in the AR1 case, where the street canyon concentration is lower in the first street and subsequently reaches its maximum in the third street canyon. This is because for case AR1 a large part of the concentration is advected with high velocity through the streamwise streets, thereby passing the first two street canyons. As the flow velocity has decreased after two streets, the concentration in the wakes of the cubes increases.

Pollutant Dispersion Mechanisms

The geometry of the urban canopy has an influence on the dispersion of pollutants [13]; e.g. in the currently considered geometries pollutants can travel with the mean flow through streamwise streets or above the urban canopy. Sometimes pollutants get trapped inside the wakes of the obstacles and since the considered cases are in the skimming flow regime these wakes form street canyon flows. Pollutants leave the street canyons mostly through the top of the canopy either by being advected with the mean flow or by turbulent velocity fluctuations. Therefore, the average total pollutant flux in the midplane of each street canyon can be separated into an advective and a turbulent contribution:

$$\overbrace{\langle \overline{wc} \rangle_{z=h}}^{\text{total}} = \overbrace{\langle \overline{wc} \rangle_{z=h}}^{\text{advection}} + \overbrace{\langle \overline{w'c'} \rangle_{z=h}}^{\text{turbulence}} \tag{4.13}$$

where $\langle .. \rangle|_{z=h}$ represent the average over the region $(0.05 < x'/h < 0.95, 0.95 < z/h < 1.05)$, with $x' = 0$ corresponding to the location of the upstream wall of the street

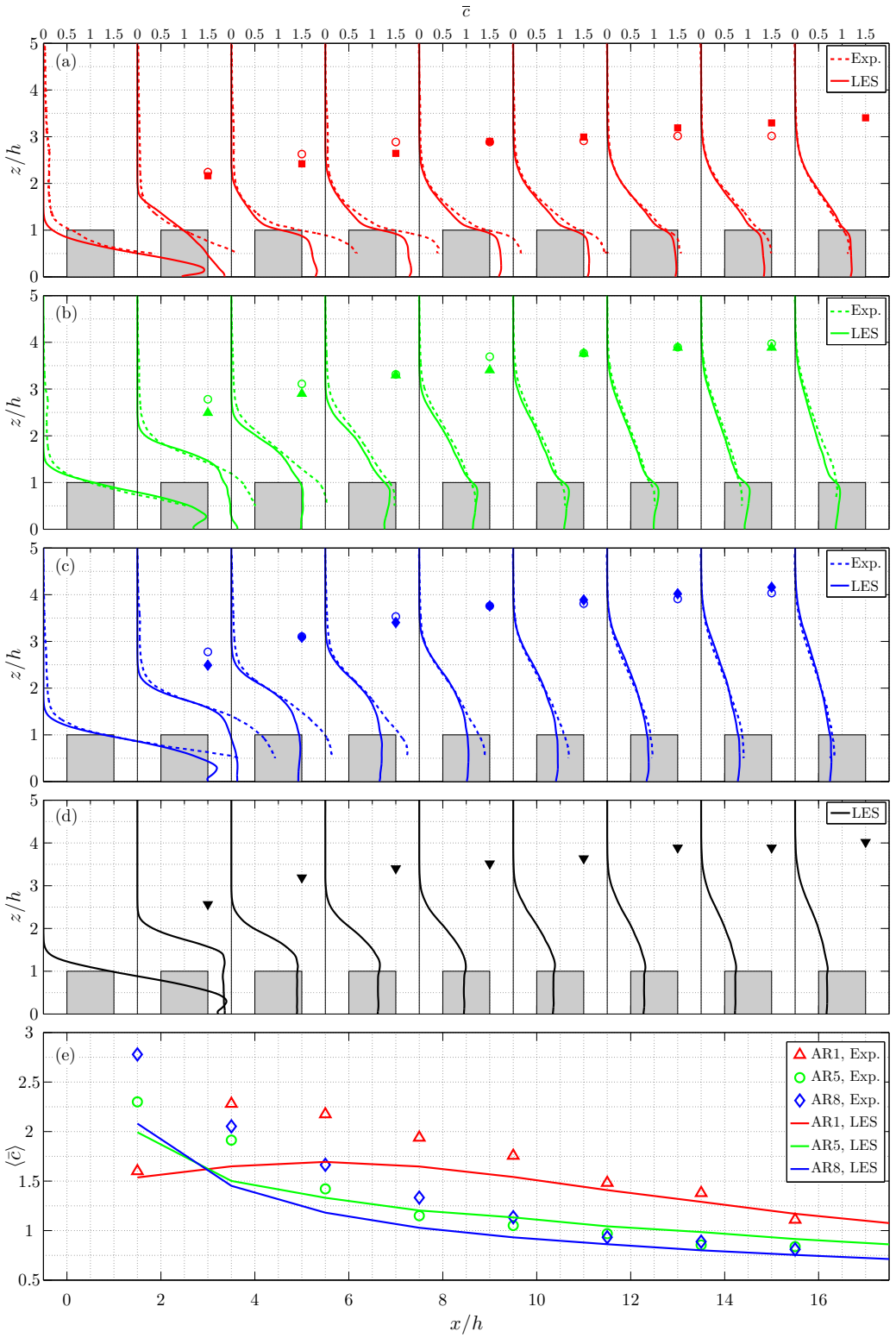

Figure 4.20: Profiles of mean concentration $\overline{c}$ in the middle of each street canyon for cases AR1 (a), AR5 (b), AR8 (c), 2D (d) and spatially-averaged street canyon concentration $\langle\overline{c}\rangle$ (e). In Figures 4.20a-d the internal boundary-layer depth, δ_i, is shown by solid markers for the LES and by open markers for the experiment (if available).

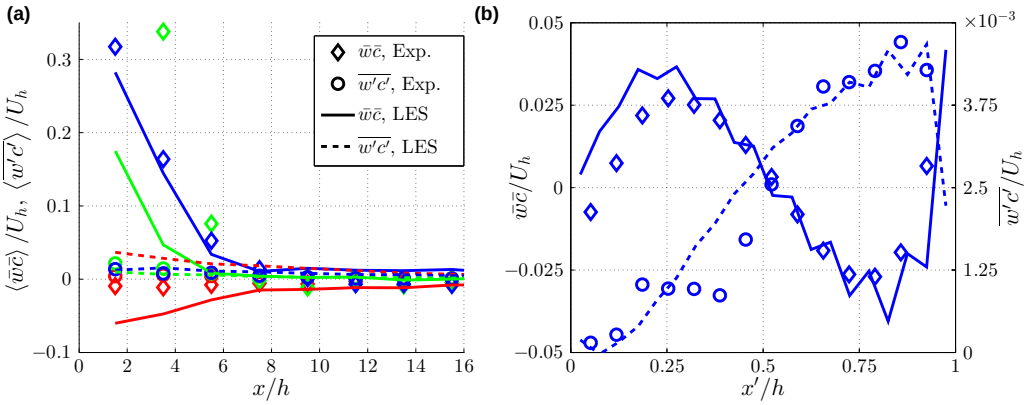

Figure 4.21: Streamwise variation of the advective and turbulent pollutant fluxes for different aspect ratios (a) and spatial variation of advective and turbulent pollutant fluxes for the 5th street of case AR8 (b). Red, green and blue lines/symbols correspond to case AR1, AR5 and AR8, respectively; $x' = 0$ corresponds to the upstream street canyon wall.

canyon. Figure 4.21a shows the streamwise development of both contributions. Clearly, in the first three streets the advective pollutant flux is significant. Remarkably, case AR1 shows a negative advective pollutant flux both in the experiment and in the LES, in contrast to the spanwise-averaged result (as in Tomas *et al.* [107]). This indicates that the three-dimensionality of the flow causes the advective pollutant flux in the midplane of the obstacles to be opposite to the spanwise-averaged result, which is positive because the mean spanwise-averaged vertical velocity is positive. Furthermore, the experimental and LES results for the average advective flux are approximately the same, except for case AR5, where the experimental results show a much larger average advective flux from the first three street canyons. This is mostly related to the difference in vertical velocity at these locations (as was discussed in Section 4.5.1 and shown in Figure 4.14) and partly due to the larger mean concentration. Furthermore, Figure 4.21b shows the spatial distribution of $\overline{w}\,\overline{c}$ and $\overline{w'c'}$ at the top of street 5 of case AR8. The shapes of these profiles are similar from street 4 and onwards. The agreement between the experiment and the LES is good; for the simulation $\overline{w}\,\overline{c}$ shows wiggles that are characteristic for simulations of flow near sharp obstacle corners when using central-differencing for the advection terms in the momentum equations. However, the local values of $\overline{w}$ are relatively small and the agreement with the experiment is satisfactory. It is found that, similar to Michioka *et al.* [24], $\overline{w'c'}$ is always positive at the top of the canopy, i.e. turbulence always acts to remove pollutants from the street canyons.

To investigate under which conditions pollutants are ventilated from street canyons, the joint probability density function (JPDF) of streamwise velocity fluctuation u' and instantaneous vertical pollutant flux wc was computed in each street in the region $(0.05 < x'/h < 0.95, 0.95 < z/h < 1.05)$, where $x' = 0$ represents the location of the upstream wall of the street canyon. The shape of the JPDF does not vary significantly inside this region. Therefore, the JPDF is averaged over this region and shown for street 6 for cases AR1, AR5, AR8 and 2D in Figure 4.22, where the JPDF has been multiplied with the associated value of wc to visualize the contribution to the total average pollutant flux

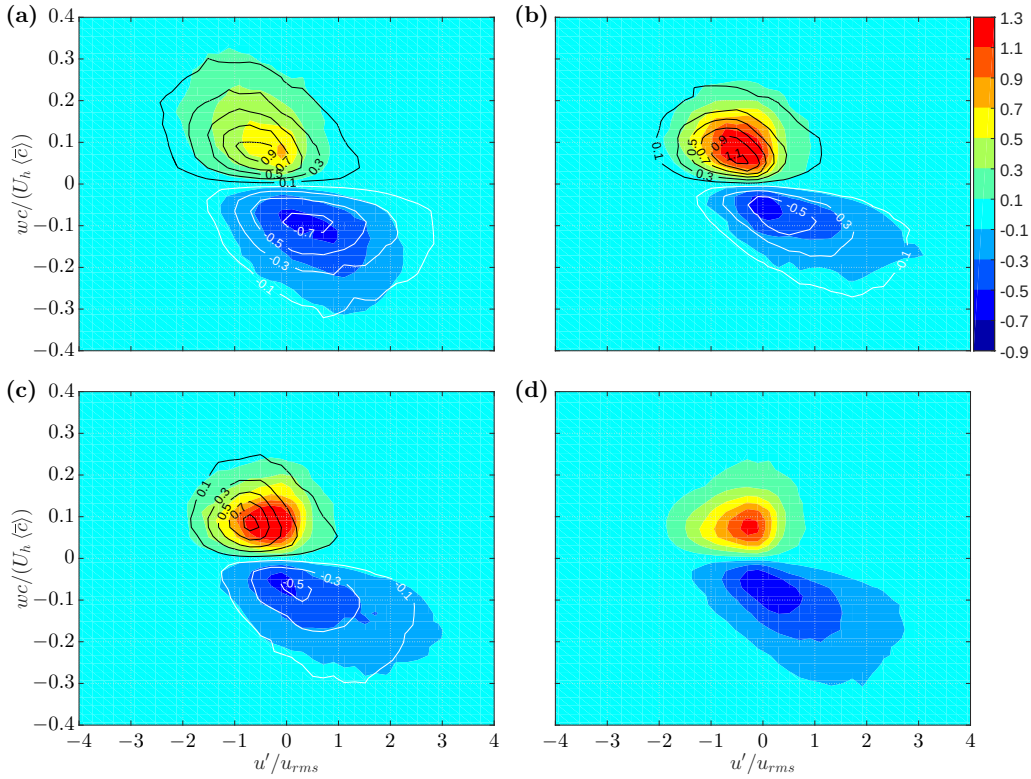

Figure 4.22: Joint probability density function (JPDF) of streamwise velocity fluctuation u' and instantaneous vertical pollutant flux wc multiplied with the associated value of wc; the results are averaged over the region $(0.05 < x'/h < 0.95, 0.95 < z/h < 1.05)$ for street 6; (a) AR1 (b) AR5 (c) AR8 (d) 2D; the line contours show the experimental results and the coloured contours show the LES results.

$\overline{wc}$. For all cases the pollutant flux wc is mainly negative when $u' > 0$, i.e. pollutants enter the street canyon from above, while for $u' < 0$ the pollutant flux wc can be either positive or negative. It is found that after three streets the JPDFs have the same shape as shown in Figure 4.22, which suggests the dominating mechanism responsible for pollutant removal has developed after three streets. Accordingly, in (periodic) simulations of fully-developed flow over street canyons qualitatively similar JPDFs are found [24]. From the results presented here it can be concluded that ventilation of street canyons is associated with low momentum regions passing the street canyons.

The Average Fluctuating Velocity Field for Street Canyon Ventilation

Apart from the knowledge that low momentum regions are responsible for street canyon ventilation, details about the associated flow structure are unknown. Reynolds and Castro [141] and Michioka *et al.* [142] investigated the occurrence of sweeps and ejections in the urban canopy by computing two-point correlations of u. However, the direct correlation between street canyon ventilation and the flow was not made. Here, use is made of linear stochastic estimation (LSE) [143] to approximate the conditional mean velocity

fluctuation for the event of a pollutant flux $\langle wc \rangle_e$ out of the street canyon: $\overline{u_i'(\boldsymbol{x})|\langle wc \rangle_e}$, where $\boldsymbol{x} = (x, y, z)$ and $\langle .. \rangle$ represents the spatial average over the region ($0.05 < x'/h < 0.95, 0.95 < z/h < 1.05$) in the midplane of the obstacles. Analogously to Christensen and Adrian [47] this conditional mean is approximated by:

$$\overline{u_i'^{\,e}} = \overline{u_i'(\boldsymbol{x})|\langle wc \rangle_e} \approx \frac{\overline{\langle wc \rangle u_i'(\boldsymbol{x})}}{\overline{\langle wc \rangle^2}} \langle wc \rangle_e \tag{4.14}$$

which shows that the mean fluctuating velocity field associated with a given value of $\langle wc \rangle_e$ can be reconstructed using unconditional two-point correlation data. LSE is more practical than the conventional conditional-averaging procedure, because all available samples are used in reconstructing the conditional fluctuating velocity field, so that less samples are required for converged results. As the amplitude of $\overline{u_i'^{\,e}}$ depends (linearly) on the chosen magnitude of $\langle wc \rangle_e$ a realistic event value is chosen to compare with. Figure 4.22 shows that the event of $\langle wc \rangle_e = 0.1 U_h \langle \overline{c} \rangle$ occurs frequently in all considered cases. Therefore, this will be the event for which the considered roughness geometries are compared.

Figure 4.23 shows for cases AR1 and AR8 the vector field of the fluctuating velocity $\overline{u_i'^{\,e}}$ together with contours of $\overline{u'^{\,e}}$ obtained using Equation 4.14. The experimental data is shown for street 6, but from street 5 and onwards the structure does not change significantly. Therefore, for the LES the data has been averaged over streets 6 to 21 for statistical convergence. As expected from the JPDFs, low momentum flow is indeed present above the canopy. The agreement between the results from the experiment and the LES is good; in the proximity of the top of the street canyon the contours are very similar, while the contours further away have a slightly different shape. Nevertheless, both methods predict a flow structure of greater length and height for case AR8 than for case AR1. To indicate the influence of the aspect ratio on the size of these regions the streamwise length scale $\mathcal{L}_x$ and the vertical length scale $\mathcal{L}_z$ of the contour $\overline{u'^{\,e}} = -0.04 U_h$ are plotted in Figure 4.24, where $\mathcal{L}_x$ is the length of the contour just above the canopy and $\mathcal{L}_z$ is the maximum height of the contour above the canopy. Using a different value for the contourlevel did not show significantly different behaviour. Figure 4.24 indicates that increasing the aspect ratio mostly affects $\mathcal{L}_z$, which increases linearly. The relative increase is significant, which is evident from Figure 4.23. Surprisingly, $\mathcal{L}_z$ is lower for the 2D case. The results for the streamwise length scale $\mathcal{L}_x$ (Figure 4.24a) do not show a clear trend, because there is less agreement between the experimental and numerical results, and because the relative differences in $\mathcal{L}_x$ are smaller than for $\mathcal{L}_z$.

Although the contours of $\overline{u'^{\,e}}$ in Figure 4.23 indicate that the correlation of $\overline{u_i'^{\,e}}$ with $\langle wc \rangle_e$ decreases significantly when considering locations inside the street canyon, $\overline{w'^{\,e}}$ inside the street canyon does correlate with $\langle wc \rangle_e$ (as is evident from the length of the vectors). From the simulations $\overline{u_i'^{\,e}}$ can also be retrieved in the horizontal plane inside the urban canopy, which is shown in Figure 4.25 for the plane $z/h = 0.5$. Cases AR1 and AR2 clearly show a horizontal inflow from the adjacent streamwise streets and even from the neighbouring street canyons to balance the outflow at the top the street canyon. For these cases the vertical velocity fluctuation even extends around the obstacle. In the other cases (AR3.5, AR5, AR8 and 2D) outflux in the middle of the top of the street canyon is balanced by inflow within the region of the street canyon itself,

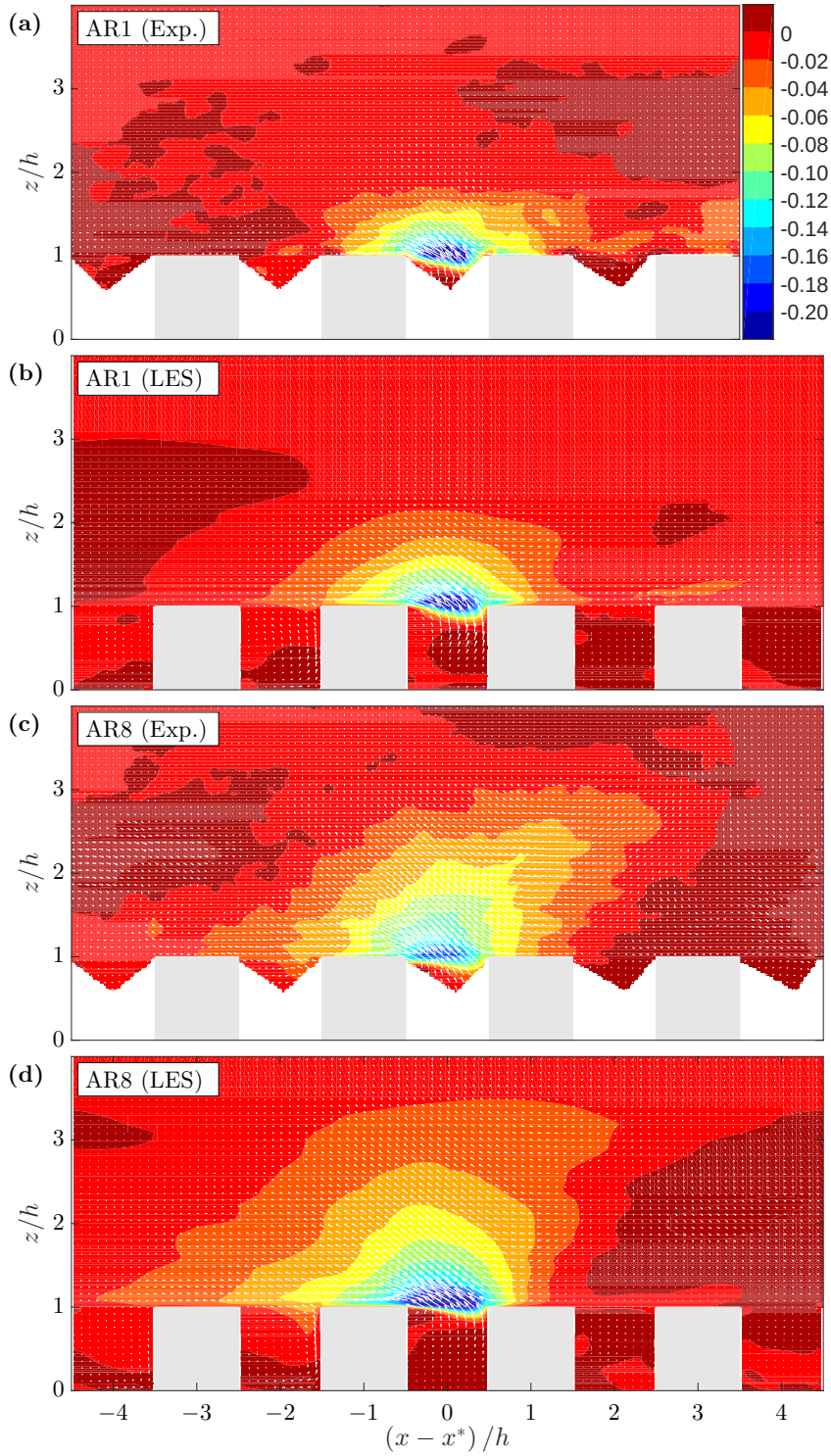

Figure 4.23: Mean fluctuating velocity field $\overline{u_i'^{\,e}}$ associated with $\langle wc \rangle_e = 0.1 U_h \langle \bar{c} \rangle$ from linear stochastic estimation for case AR1 (a, b) and case AR8 (b, c). Contours of $\overline{u'^{\,e}}/U_h$ are shown together with the vector field $(\overline{u'^{\,e}}, \overline{w'^{\,e}})$ in the $y = 0$ plane for the experiments in street 6 (a, c), while for the LES the average result of street 6 to street 21 is shown (b, d). The average streamwise location of the event is indicated by x^*.

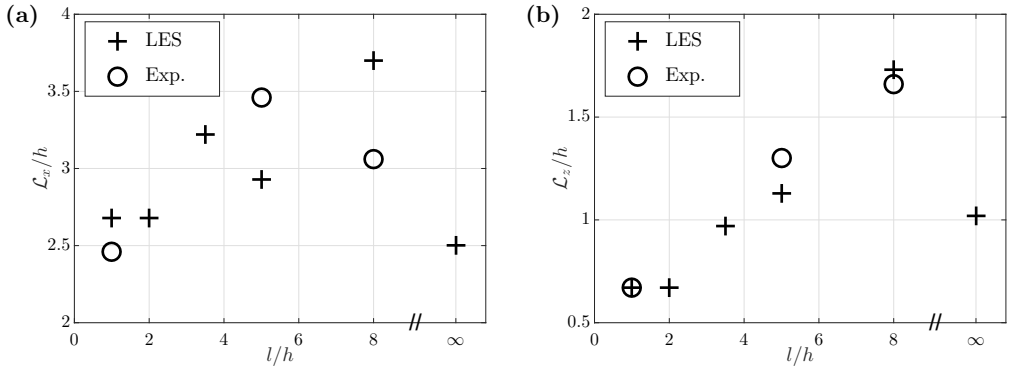

Figure 4.24: Length scales of the contour $\overline{u'^e} = -0.04U_h$ in the plane $y = 0$ for different aspect ratios l/h; (a) streamwise length just above the canopy $\mathcal{L}_x$ and (b) maximum height above the obstacles $\mathcal{L}_z$.

such that the velocity fluctuation field looks similar for cases AR3.5 to 2D. The contours of $\overline{w'^e}$ indicate that in all cases the event influences the flow in one or two upstream street canyons.

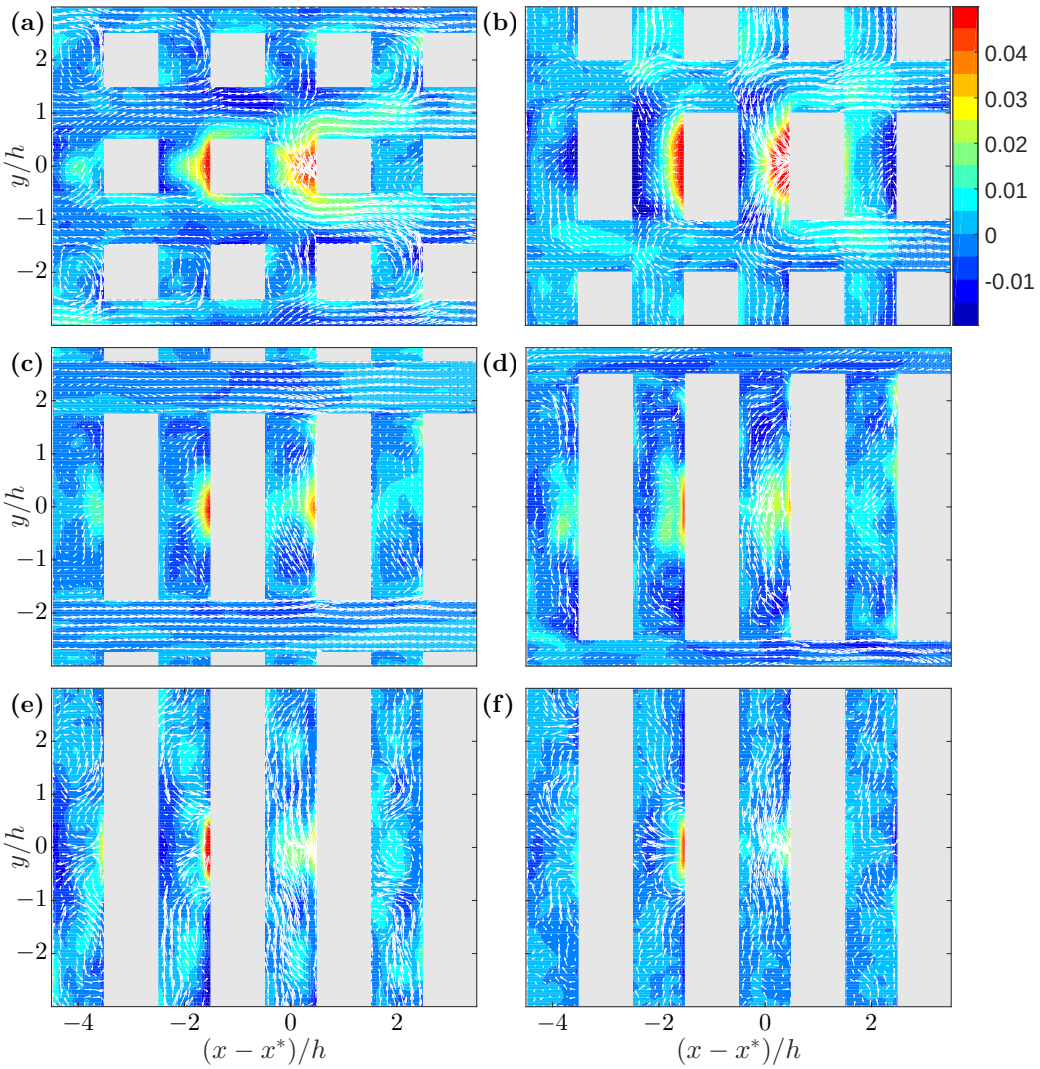

Figure 4.25: Mean fluctuating velocity field $\overline{u_i'^{\mathrm{e}}}/U_h$ associated with $\langle wc \rangle_{\mathrm{e}} = 0.1 U_h \langle \bar{c} \rangle$ from linear stochastic estimation for cases AR1 (a), AR2 (b), AR3.5 (c), AR5 (d), AR8 (e) and 2D (f). Contours of $\overline{w'^{\mathrm{e}}}/U_h$ are shown together with the vector field $(\overline{u'^{\mathrm{e}}}, \overline{w'^{\mathrm{e}}})$ in the $z/h = 0.5$ plane. The average result of street 6 to street 21 is shown, while use is made of symmetry. The average streamwise location of the event is indicated by x^*.

4.6 RESULTS: EFFECT OF VARYING REYNOLDS NUMBER

This section presents the results of the flow over an urban canopy at different Reynolds numbers for the AR1 case. The Reynolds number used in this section is the roughness Reynolds number $h^+ = u_\tau h/\nu$, that varies between 200 and approximately 600 (see Table 4.1). As noted by Castro [118], the Reynolds number dependence in the current range, also denoted as the fully rough regime, is weak. The goal of this section is to verify this Reynolds number dependency and to see to what extent the results presented in Section 4.5 (e.g. JPDFs and LSEs) are influenced by a change in Reynolds number.

4.6.1 THE FLOW OVER THE URBAN CANOPY

Similar to the previous section, the streamwise velocity profiles $\bar{u}/U_h$ are shown in Figure 4.26a, starting $0.5h$ in front of the first row and subsequently in the middle of each street canyon. For reference, also the LES results of AR1 are depicted by the dashed lines. Please note that in this section and the next section the LES results are plotted as dashed lines and the experimental results as solid lines, contrary to the convention in Section 4.5. As noted before, the agreement between the LES and the lowest Reynolds number (red curve) is good. Similar agreement is observed when considering the higher Reynolds number cases. Small differences are observed especially in the outer region ($z/h \geq 2$). With increasing Reynolds number the profiles start to deviate. This is because of small differences in the approach flow boundary layer as discussed in Section 4.4.1. Figure 4.26b shows the Reynolds stress profiles $-\overline{u'w'}$ at the same locations as in Figure 4.26a. The characteristic peak near the top of each obstacle after street 3 is captured well in each different Reynolds number case. The main differences in the Reynolds stress profiles are found in street 1, where for the two highest Reynolds number cases, the peak amplitude around $z/h \approx 1.5$ is reduced with respect to the LES results at $\mathrm{Re}_\tau = 194$. This is most likely due to the relative course resolution of the PIV results. As before in Section 4.5.1, the fraction of resolved Reynolds stresses is estimated from the ratio between the PIV resolution and the length scale Λ of the dominating flow structures [140]. Λ is estimated using the distance required for the streamwise two-point correlation of u to decrease to 0.5. For the current Reynolds numbers considered the resolved parts of the Reynolds stresses is approximately 93%, 75% and 66% for $h^+ = 209$, $h^+ = 307$ and $h^+ = 598$ respectively. Despite these differences between the different Reynolds numbers, it can safely be concluded that the Reynolds number dependence on the mean flow fields and the Reynolds shear stresses is weak and the turbulence in the internal boundary layer is dominated by the flow around these sharp edged obstacles, see also Castro [118], Raupach *et al.* [126], and Snyder and Castro [144].

4.6.2 POLLUTANT DISPERSION

Mean Concentration Fields

The mean concentration profiles starting $0.5h$ in front of the first row of obstacles and subsequently in the middle of each canyon for different Reynolds numbers is shown in Figure 4.27. The LES results for AR1 are also plotted for reference. Furthermore,

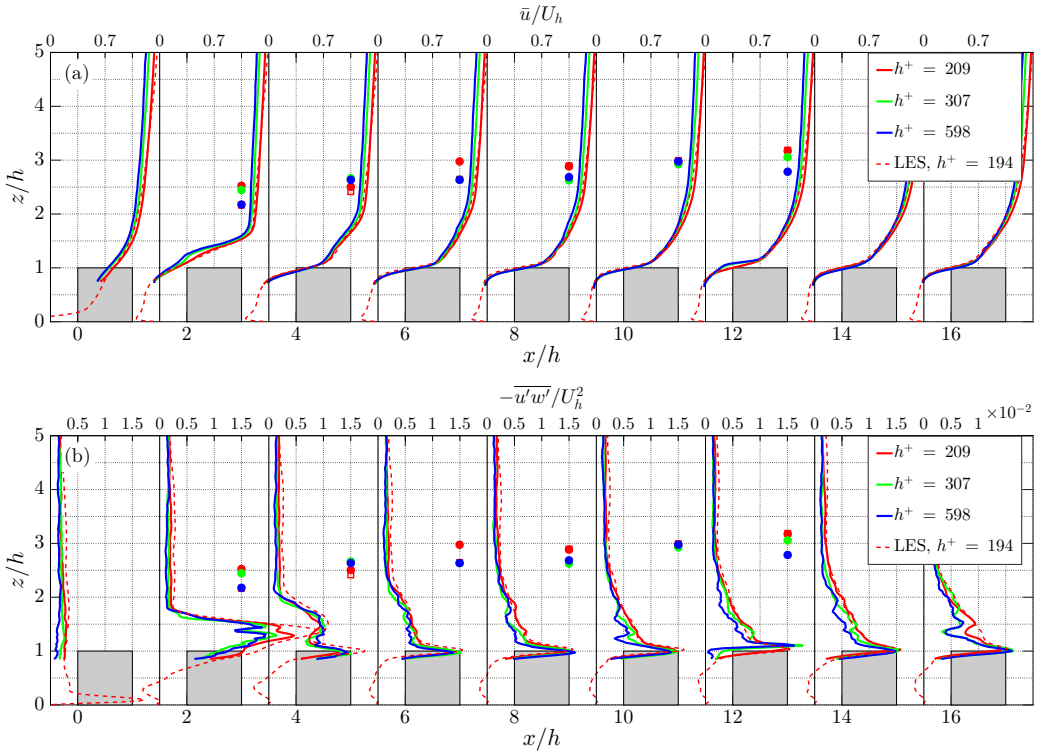

Figure 4.26: (a) Profiles of mean streamwise velocity component $\overline{u}/U_h$, (b) mean Reynolds stress $-\overline{u'w'}/U_h^2$ in the middle of each street canyon for the different Reynolds numbers. The internal boundary layer depth, δ_i, is shown by open markers for the LES and by filled markers for the experiment.

the internal boundary layer δ_i is plotted by open markers for the LES results and by filled markers for the LES results. The profiles are non-dimensionalized using Equation 4.12. Figure 4.27 indicates that the largest differences between the experiments and the simulations are found in and just above the canopy ($0.5 \leq z/h \leq 2$) for the first five streets. An exception to this observation is the $h^+ = 307$ case, which continues to predict substantially higher concentrations even in the more downstream street canyons. It is probable that these differences in the first few streets are linked to the inhomogeneity of the line source. Finally, no clear Reynolds number dependence is present in the mean concentration field.

Turbulent and Advective Fluxes

Pollutant removal from the street canyons occurs mainly via the top of the street canyon. This pollutant flux is separated into two contributions: an advective and a turbulent contribution. Figure 4.28 shows the advective and turbulent contribution to the total pollutant flux according to Equation 4.13. In contrast to the larger aspect ratios as shown in Figure 4.21, the advective part of the pollutant flux acts to introduce the pollutants into the street canyon in the AR1 case. This behavior is observed for all Reynolds numbers. Note however that a certain amount of scatter is present in the advective part of

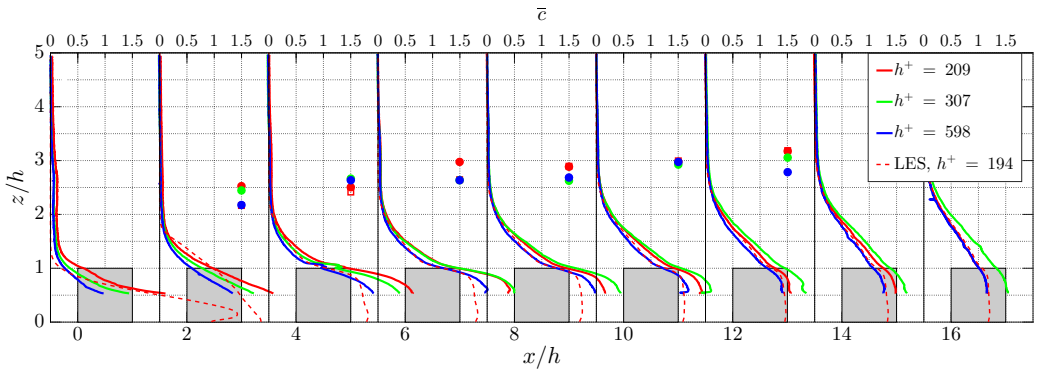

Figure 4.27: Profiles of mean concentration $\overline{c}$ in the middle of each street canyon for the different Reynolds numbers. The internal boundary layer depth, δ_i, is shown by open markers for the LES and by filled markers for the experiment.

the total pollutant flux, which is likely a result of the finite experimental accuracy. In accordance with previously observed behavior of the turbulent flux (see Figure 4.21), turbulence always acts to remove pollutants from the street canyon, irrespective of the Reynolds number.

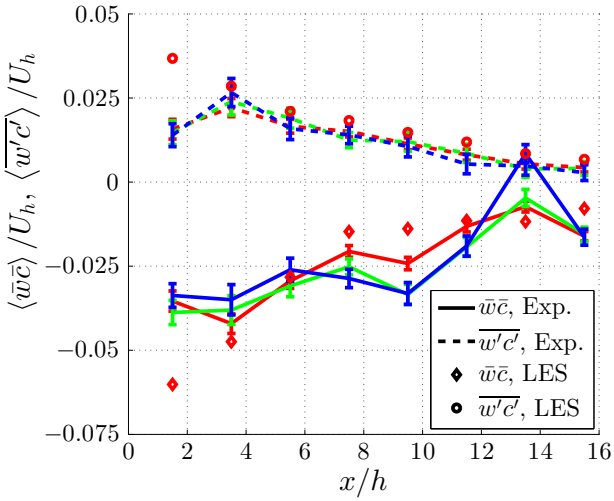

Figure 4.28: Streamwise variation of the advective and turbulent fluxes for different Reynolds numbers; $h^+ = 209$ (red), $h^+ = 307$ (green) and $h^+ = 598$ (blue). The errorbars represent the statistical mean $\pm$ the standard error of the mean.

Pollutant Removal Mechanisms

The JPDF of the streamwise velocity fluctuations u' and the instantaneous vertical pollutant flux wc multiplied with the associated value of wc is computed for street six in the region ($0.05 < x'/h < 0.95$, $0.95 < z/h < 1.05$), where $x' = 0$ denotes the upstream wall

of street canyon six (see Figure 4.29). Low momentum fluid ($u' < 0$) is responsible for pollutant removal from the street canyon (i.e. similar to Michioka *et al.* [24]), irrespective of the Reynolds numbers shown here.

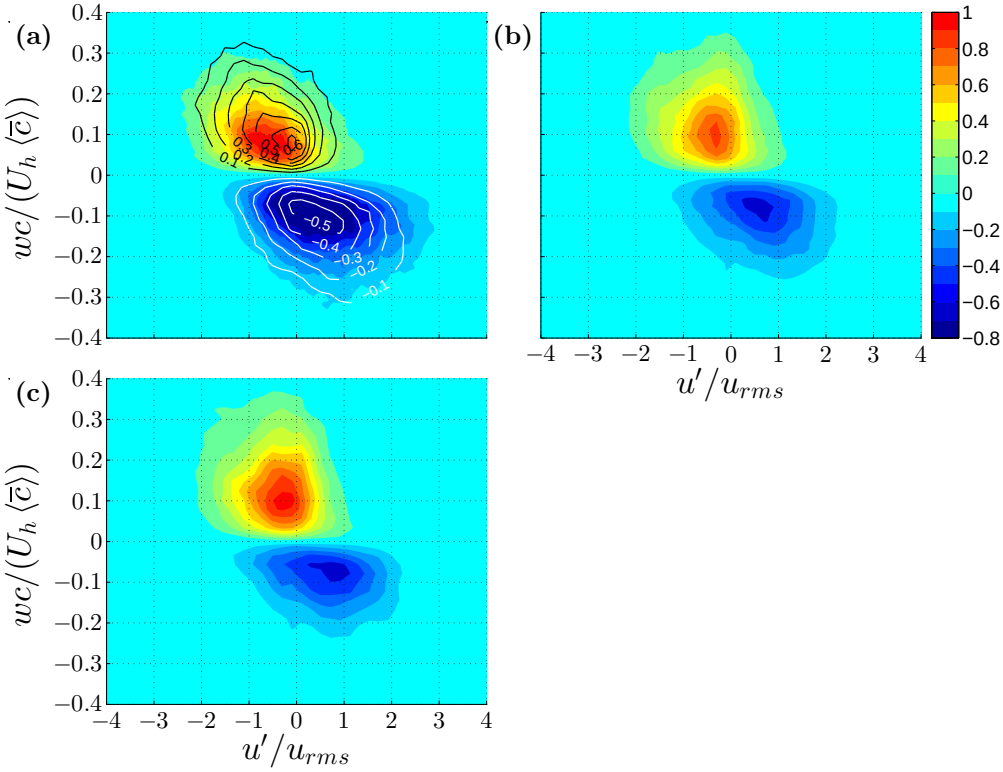

Figure 4.29: Joint probability density function (JPDF) of streamwise velocity fluctuation u' and instantaneous vertical pollutant flux wc multiplied with the associated value of wc; the results are averaged over the region $(0.05 < x'/h < 0.95, 0.95 < z/h < 1.05)$ for street 6; (a) $h^+ = 209$ (b) $h^+ = 307$ (c) $h^+ = 598$; the line contours show the LES results (if available) and the colored contours show the experimental results.

The average fluctuating velocity field obtained by LSE according to Equation 4.14 is shown for the different Reynolds numbers in Figure 4.30. The event used here is $\langle wc\rangle_e = 0.1U_h\langle\bar{c}\rangle$. Both $h^+ = 209$ and $h^+ = 307$ yield almost identical contour shapes representing a 'blob' shape, while the $h^+ = 598$ case reveals a more ramp like structure, similar to LSE results in boundary layer research [47]. Additionally, the streamwise and wall-normal length scale of the $\overline{u'^e} = -0.04U_h$ contour decrease slightly with increasing Reynolds number.

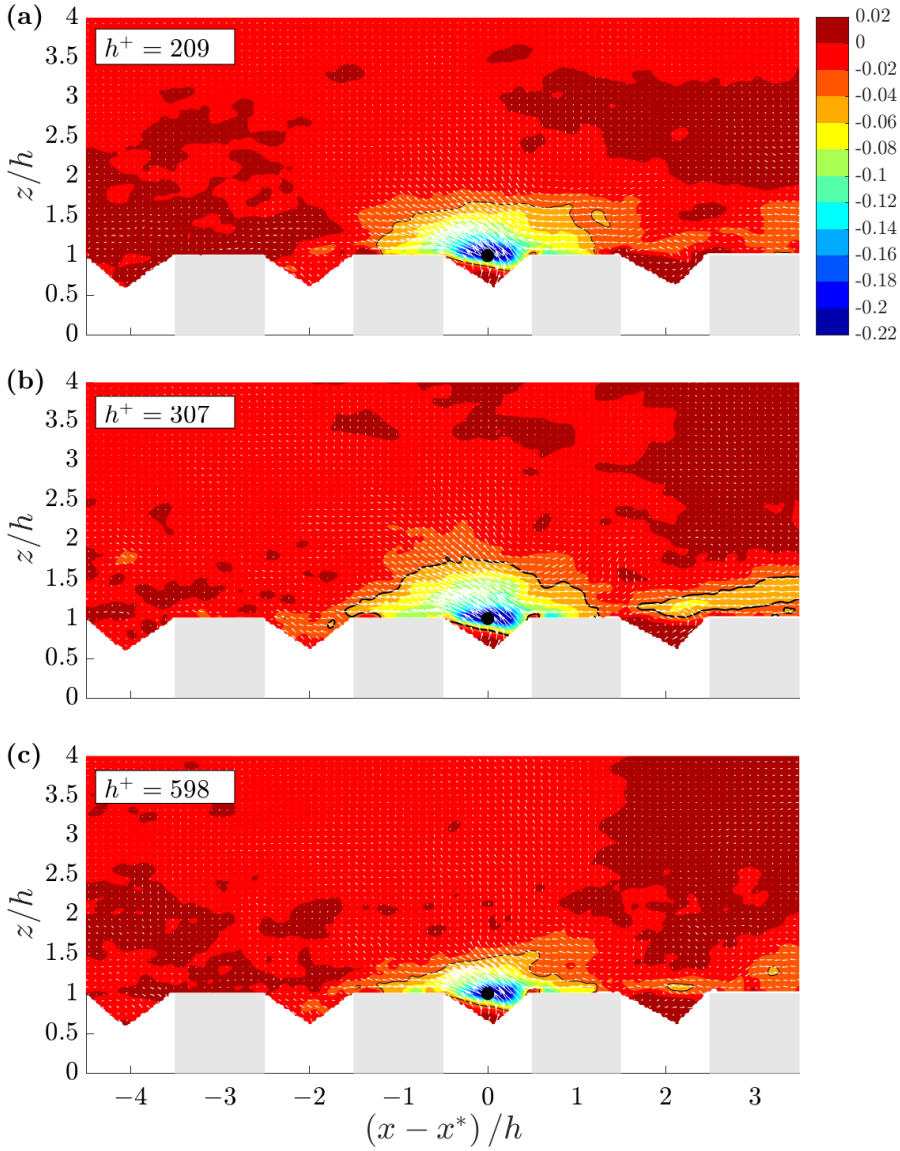

Figure 4.30: Mean fluctuating velocity field $\overline{u_i'^{\mathrm{e}}}$ associated with $\langle wc \rangle_{\mathrm{e}} = 0.1 U_h \langle \bar{c} \rangle$ from linear stochastic estimation for case $h^+ = 209$ (a), $h^+ = 307$ (b) and $h^+ = 598$ (c). Contours of $\overline{u'^{\mathrm{e}}}/U_h$ are shown together with the vector field $(\overline{u'^{\mathrm{e}}}, \overline{w'^{\mathrm{e}}})$ in the $y = 0$ plane for in street 6. The solid black line indicates the contour $\overline{u'^{e}} = -0.04 U_h$, while the filled black dot indicates the reference location.

4.7 RESULTS: INFLUENCE OF A FENCE

This section presents the results of the fence geometry. The fence in this case was an L-shaped aluminum profile with a thickness of $0.1h$ and with subsequent heights of $0.5h$, $1h$, and $1.5h$ denoted by C05, C10, and C15, respectively. Additionally, the no-fence case is also included and denoted as C00. The fence was mounted $1h$ upstream of, and parallel to, the first row of obstacles (see Figure 4.1). The experiments are done at the intermediate Reynolds number, i.e. $h^+ = 307$.

This case is of particular practical relevance as it resembles the case in which a sound-barrier would be placed in between a roadway and an urban area. This urban setting is frequently encountered in The Netherlands. Surface-mounted fences have been a research topic for quite some time. Castro [118] presents an experimental study of the wake of a two-dimensional obstacle submerged in a thick rough-wall boundary layer. His work is related to the experimental and theoretical work done by Counihan *et al.* [145], who provided a theoretical model for the velocity and turbulent statistics downstream of a surface mounted fence. Recently, Tomas *et al.* [104] studied the influence of a single 2D fence on the flow characteristics and pollutant dispersion subject to neutral and stable boundary layers. They found that thermal stratification has a noticeable effect upon the concentration far downstream of the obstacle. However, there is no data, either numerical or experimental, available on the specific combination of a 2D roughness element, i.e. a fence, adjacent to 3D urban roughness elements. The structure of this section is similar to that of the the previous two sections. First of all, the mean flow fields for the different cases are shown in Section 4.7.1. Second, a quadrant analysis to elucidate the structure of the turbulent flow field is shown in Section 4.7.2. Mean concentration fields and pollutant dispersion mechanisms are discussed in detail in Section 4.7.3. Finally, an updated mixing length model and a scaling of the mean concentration field are presented in Section 4.7.4.

4.7.1 THE FLOW OVER THE URBAN CANOPY

The rural-to-urban flow fields (including the fence) are compared for the first eight streets in the $y = 0$ plane, see Figure 4.31. All velocity statistics are normalized with the undisturbed velocity at obstacle height U_h. A snapshot of the spanwise velocity component v is shown in Figure 4.31 for both the experiment and the simulation. Both snapshots indicate clearly the presence of large turbulent structures that are shed from the fence and the roughness elements. These structures grow in size in the downstream direction. Note that the magnitude of the velocity fluctuations associated with these structures is significantly higher compared to the velocity fluctuations in the approaching flow.

In order to make a quantitative comparison between different cases, the mean streamwise velocity profiles for the cases C00, C05, C10, and C15 are shown in Figure 4.32. Wall-normal profiles are determined, starting $0.5h$ behind the fence and subsequently in the middle of each street canyon. Additionally, the internal boundary layer depth is shown for the experiments (filled symbols) and the LES (open symbols, if available). The internal boundary layer depth δ_i is found by subtracting the smooth-wall inlet velocity profile from the street mean velocity profiles in the roughness transition region

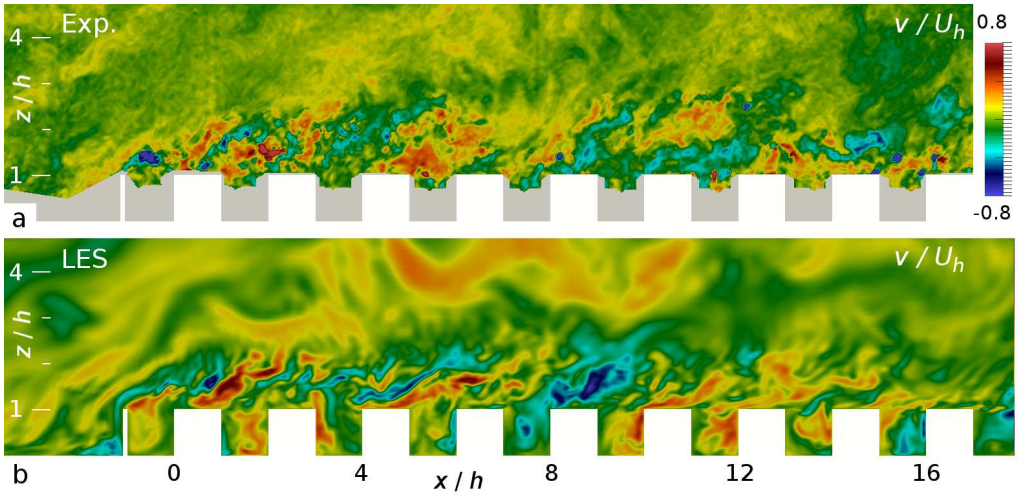

Figure 4.31: Contours of instantaneous spanwise velocity component v/U_h in the midplane of case $1h$; (a) experiment and (b) simulation. Areas that could not be illuminated or seen in the experiments have been masked in grey and the obstacles are shown in white.

as: $\Delta\langle\bar{u}\rangle = \langle\bar{u}\rangle_{\mathrm{RT}} - \langle\bar{u}\rangle_{\mathrm{inlet}}$. δ_i is defined as the height at which the vertical gradient of $\Delta\langle\bar{u}\rangle$ approaches zero. A threshold of three times the RMS value of $|\mathrm{d}\Delta\langle\bar{u}\rangle/\mathrm{d}z|$ outside the canopy region is used to determine this location.

In Figure 4.32a the C00 cases are re-plotted. These results are the same as presented before in Figure 4.16a. In this section, Exp. 1 and Exp. 2 refer to the different Reynolds number cases as shown Table 4.1, corresponding to Reynolds numbers of $h^+ = 209$, and $h^+ = 307$ respectively. There is a close agreement between the LES results and the experimental results at the lower Reynolds number (C00 Exp. 1), as noted before in Section 4.5. Additionally, the higher Reynolds number case $h^+ = 307$ (C00, Exp. 2) also closely matches the other two curves. The main difference can be found in the outer region of the flow ($z/h > \delta_i$). This small difference is attributed to the difference in approaching flow conditions, as observed in Figure 4.6a. Nevertheless, it is concluded that the Reynolds number dependence is weak, which was also concluded from an experimental study by Raupach *et al.* [126] (see also Section 4.6). The profiles of the streamwise velocity components change noticeable over the first three rows of obstacles, while further downstream only minor changes are observed. The downstream influence of the $0.5h$ fence on the mean streamwise velocity profiles is only limited as the differences between the C05 case and the C00 case are typically below 3%.

With increasing fence height, the downstream influence of the fence increases. Both the C10 case (Figure 4.32c) and the C15 case (Figure 4.32d) introduce a very sharp and distinct shear layer just behind the fence, i.e. at $x/h = -0.5h$. Further downstream, this shear layer increases in thickness. From Figure 4.32c it is clear that the shear layer generated in the C10 case smears out and the velocity profile shows similar behaviour as the C00 case by the eighth street, i.e. the effect of the fence dampens out further downstream. The LES results of the C10 case indicate a slightly higher streamwise velocity above the first few street canyons (Figure 4.32c). This is attributed to the dif-

ference in blockage in both methods, as the height of the LES domain ($30h$) is smaller compared to that of the experiments ($40h$). The C15 case (Figure 4.32d) indicates the presence of a larger recirculation region that starts just downstream the fence and extends downstream up to $x/h \approx 12$, inducing backflow at the top of several obstacles. Although this back flow gradually decreases in magnitude downstream, by the eighth street there is still a considerable difference in flow structure between C00 and C15. Finally, it is clearly visible that increasing the fence height significantly increases the internal boundary layer height.

Figure 4.33 shows the profiles of the mean Reynolds stress $-\overline{u'w'}$ at the same locations. Figure 4.33a shows that the experimental results at the different Reynolds numbers, i.e. Exp. 1 and Exp. 2, indicate a lower value of the peak in Reynolds stress than the LES, while the location of this peak is similar to the peak location observed in the LES results. This suggests that, as a result of the finite PIV resolution, the Reynolds stress in the experiments is likely underestimated. An estimate for the fraction of resolved Reynolds stress to the total Reynolds stress is made by considering the ratio between the PIV resolution and the length scale Λ of the dominant flow structure [140]. Similar to Tomas *et al.* [96], the length scale of the dominant flow structure is calculated from the two-point correlation of u. Following this procedure, the resolved part of the Reynolds stress in Figure 4.33a is approximately 75% and 83% of the total for Exp. 1 and Exp. 2, respectively. The magnitude of the Reynolds stress in Fig 4.33c is smaller in the experiments compared to the LES results, while the shape of the profile is similar. This is a direct consequence of the presence of the fence, which introduces a length scale that is even smaller compared to the no fence case, i.e. in the experiments only 55% of the Reynolds stress is resolved in the peak above the first street canyon ($x/h = 1.5$). With increasing fence height the peak in $-\overline{u'w'}$ increases. In the downstream direction this peak widens and decreases in amplitude. For the fence heights up to $1h$, most of the turbulence in street 8 is produced by the rooftop shear layers, except for the C15 case, in which the peak emanating from the fence still dominates.

4.7.2 THE STRUCTURE OF THE URBAN CANOPY FLOW

One way of characterizing the structure of the turbulent flow field is to study the quadrants of the joint probability density function (JPDF) of u' and w' (see Wallace [146]). The four quadrants of this JPDF are defined as:

$$\begin{aligned} &\text{Q1} : u' > 0,\ w' > 0 \\ &\text{Q2} : u' < 0,\ w' > 0 \\ &\text{Q3} : u' < 0,\ w' < 0 \\ &\text{Q4} : u' > 0,\ w' < 0, \end{aligned} \tag{4.15}$$

where Q1 events refer to outward interactions, Q2 events are known as ejections that transport low-momentum fluid upwards, Q3 events are the inward interactions and Q4 events are referred to as sweeps that carry high momentum fluid towards the wall. Due to its simplicity, it remains a very powerful tool in the analysis of turbulent flow fields. For instance, Lu and Willmarth [147] provided the first results on the contribution of the different quadrants to the Reynolds shear stress $\overline{u'w'}$ in a turbulent boundary layer.

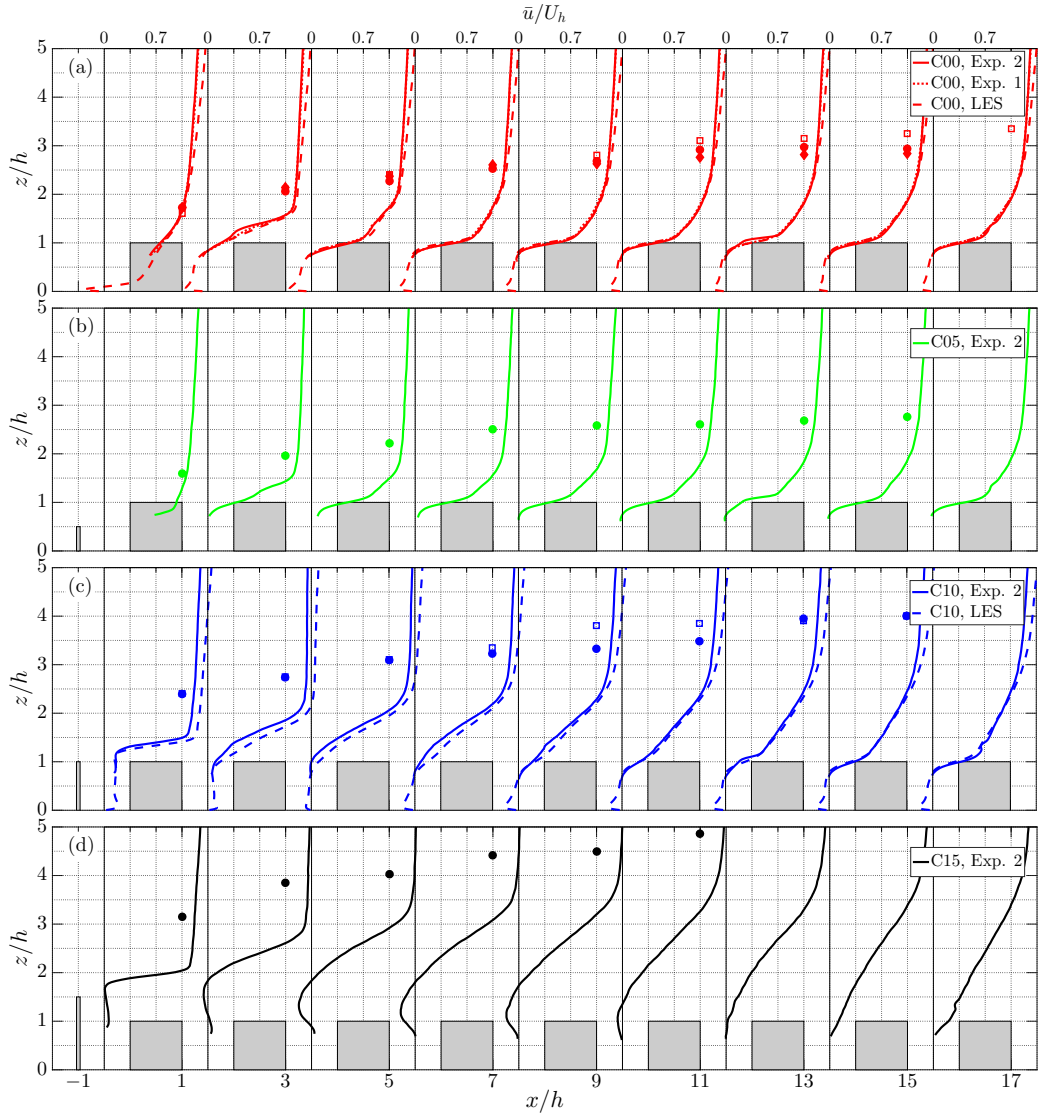

Figure 4.32: Profiles of mean streamwise velocity component $\overline{u}/U_h$ in the middle of each street canyon for cases C00 (a), C05 (b), C10 (c), and C15 (d). Additionally for $0h$ (a) the profiles of $\overline{u}/U_h$ for $h^+ = 209$ case in the experiments is shown as the dotted line. The internal boundary-layer depth, δ_i, is shown by solid markers for the experiments and by open markers for the LES (if available).

They found that ejections are the largest contributors to $\overline{u'w'}$ throughout the boundary layer depth, closely followed by sweeps. Reynolds and Castro [141] provided a quadrant analysis of the flow over a staggered array of cubes in fully-developed conditions. In contrast to smooth-wall turbulent boundary layers, sweeps are prevailing at obstacle height while ejections become the dominant contributor to $\overline{u'w'}$ in the outer region of the flow.

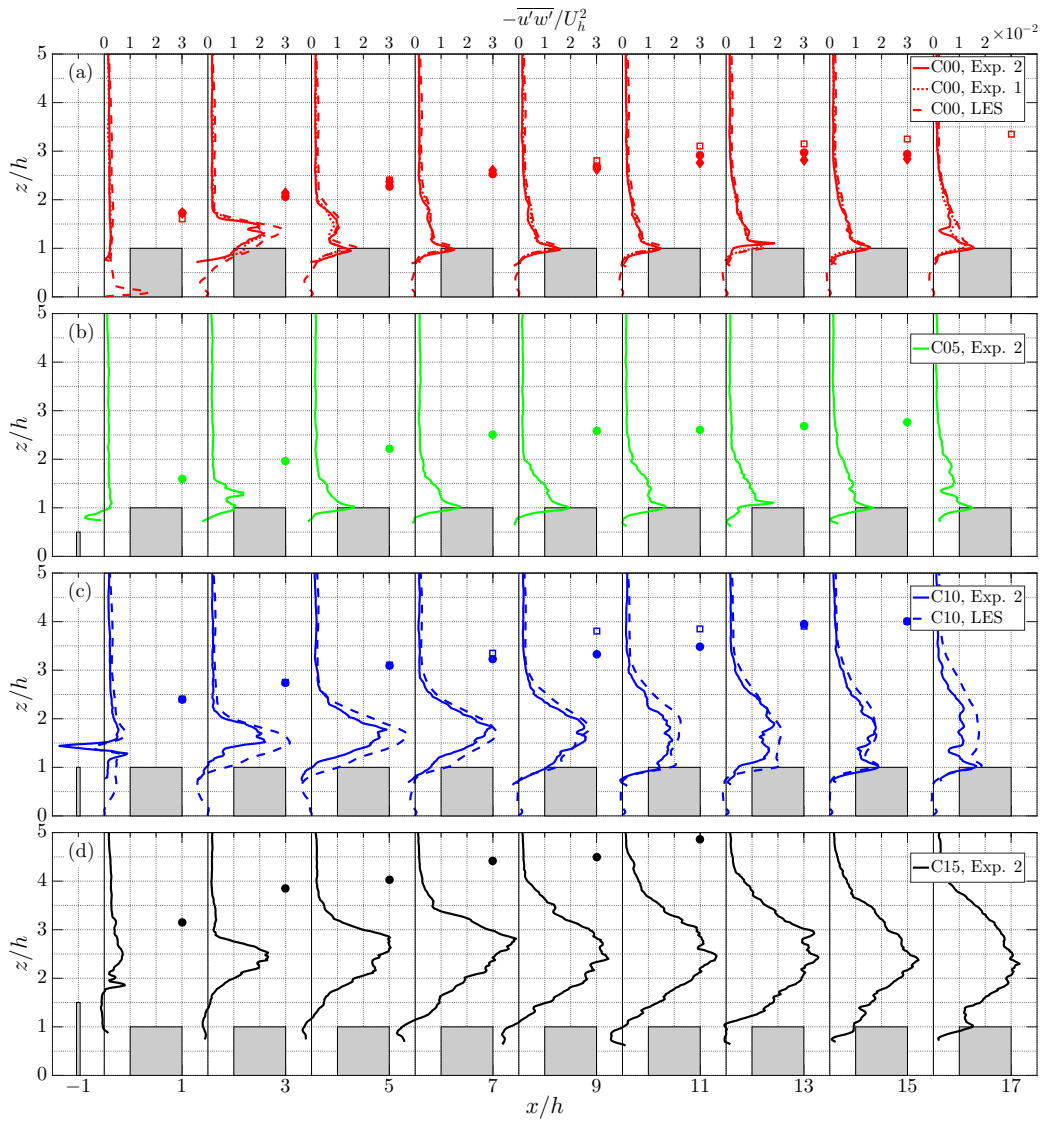

Figure 4.33: Profiles of mean Reynolds stress $\overline{u'w'}/U_h^2$ in the middle of each street canyon for cases C00 (a), C05 (b), C10 (c), and C15 (d). Additionally for the C00 case (a) the profiles of $\overline{u}/U_h$ at $h^+ = 209$ in the experiments is shown as the dotted line. The internal boundary-layer depth, δ_i, is shown by solid markers for the experiments and by open markers for the LES (if available).

In Figure 4.34 the vertical distribution of the occurrence of the different quadrants at several streamwise locations is shown for C00 and C10. Additionally, at the same streamwise locations, the contribution of the different quadrants to the Reynolds stress is quantified for the same cases (see Figure 4.35). The profiles are spatially averaged over the full canyon width. Additionally, the internal boundary-layer depth δ_i is plotted by the solid black markers. The effect of sweeps and ejections on the scalar pollutant flux will be discussed later in Section 4.7.3.2.

First we consider the Coo case (Figure 4.34a and Figure 4.35a). The profiles for the different quadrants depict only a limited streamwise development, i.e. from $x/h = 7.5$ onward minor changes are observed. For $1 < z/h < \delta_i/h$, both sweeps and ejections are the dominant flow features. The occurrence of Q1 and Q3 remains approximately constant with height from the wall for all streamwise locations. Inside the canopy, both Q1 and Q3 become important, indicating that the flow in that region is close to isotropic. Above the canopy ($1 < z/h < \delta_i/h$), $\overline{u'w'}$ is dominated by strong ejections, closely followed by frequently occurring (but weaker) sweeps, similar to the observations in a turbulent boundary layer [147]. However, this is in contrast to fully-developed flow over a staggered array of cubes [141, 148], where sweeps were found to dominate the region just above the canopy, i.e. $1 < z/h < 1.25$.

Secondly, the C10 case is presented in Figure 4.34b and Figure 4.35b. Similar to the Coo case, inside the canopy region ($z/h < 0.9$) the turbulence is close to isotropic for the last three streets shown in Figure 4.34b. Downstream of the fence the profiles at $x/h = 3.5$ indicate isotropic conditions near roof level ($z/h = 1$). Further downstream a strong shear layer is present at roof level (see also Figure 4.35b), increasing the level of anisotropy.

There is a clear crossover point between the dominance of sweeps and ejections around $z/h = 1.5$ (Figure 4.34b) for the streamwise locations $x/h = 5.5 - 13.5$. Note that this crossover point is slightly higher compared to the value of $z/h = 1.25$ found by Coceal *et al.* [149]. In contrast to the Coo case, strong sweeps dominate $\overline{u'w'}$ in the region $1 < z/h < 1.5$ [149]. Krogstad *et al.* [150] hypothesized for 2D roughness elements that this behaviour is a result of low-momentum fluid being trapped between the roughness elements, thereby reducing the influence of ejections on $\overline{u'w'}$. As a result of the fence in the C10 case, the flow velocity along streamwise streets is greatly reduced compared to the Coo case. Hence, low-momentum fluid is kept inside the canyons and ejections contribute less to $\overline{u'w'}$. This behaviour is only observed for the first six street canyons in the C10 case. The profiles at $x/h = 15.5$ are similar in shape as the Coo case (Figure 4.34), i.e. sweeps become more important in the region $1 < z/h < 1.5$.

The IBL ($1 < z/h < \delta_i/h$) that develops over the roughness elements resemblances a smooth-wall boundary layer. The frequency of occurence of sweeps increases with height while the strength of the sweeps decreases. At the same time, less frequently occurring ejections are found to dominate the Reynolds shear stress in those parts of the flow. This behaviour is characteristic for a smooth-wall turbulent boundary layer [147]. This also confirms the observations by Krogstadt and Antonia [151] and Reynolds and Castro [141] in the outer region of rough-wall boundary layers.

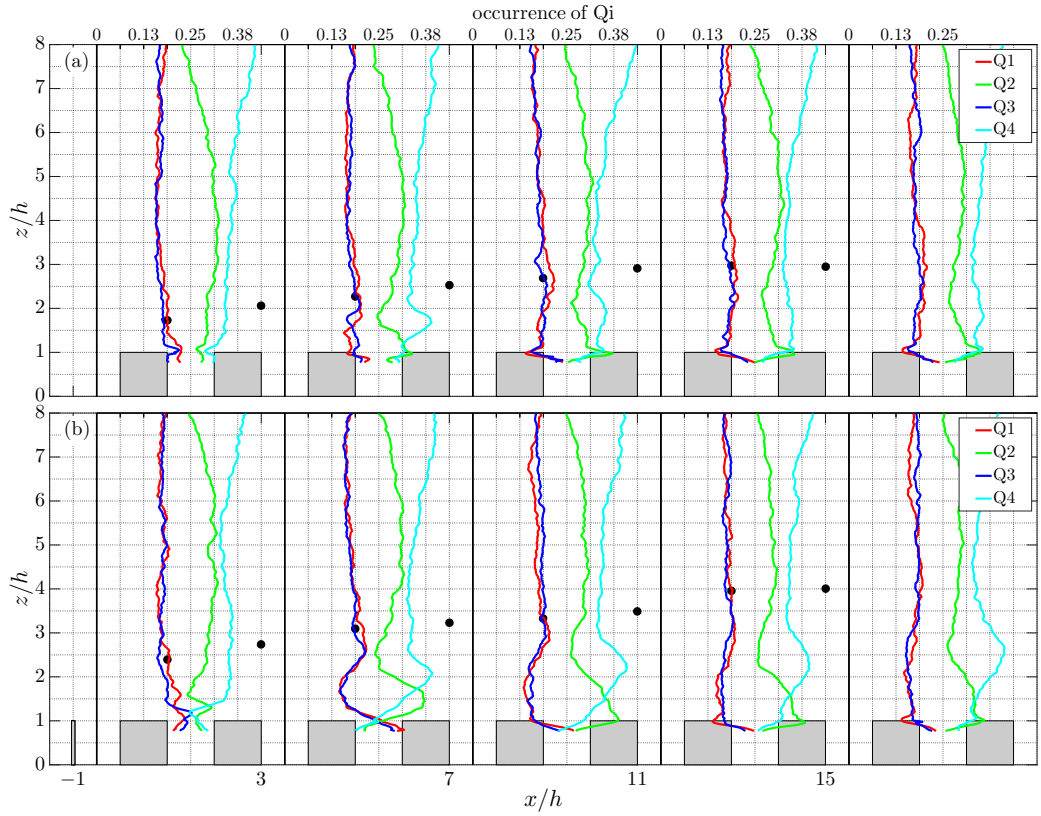

Figure 4.34: Profiles of the occurence of the different quadrants Q_i in the middle of the street canyon for C00 (a) and C10 (b). The internal boundary layer depth δ_i is shown by the solid markers.

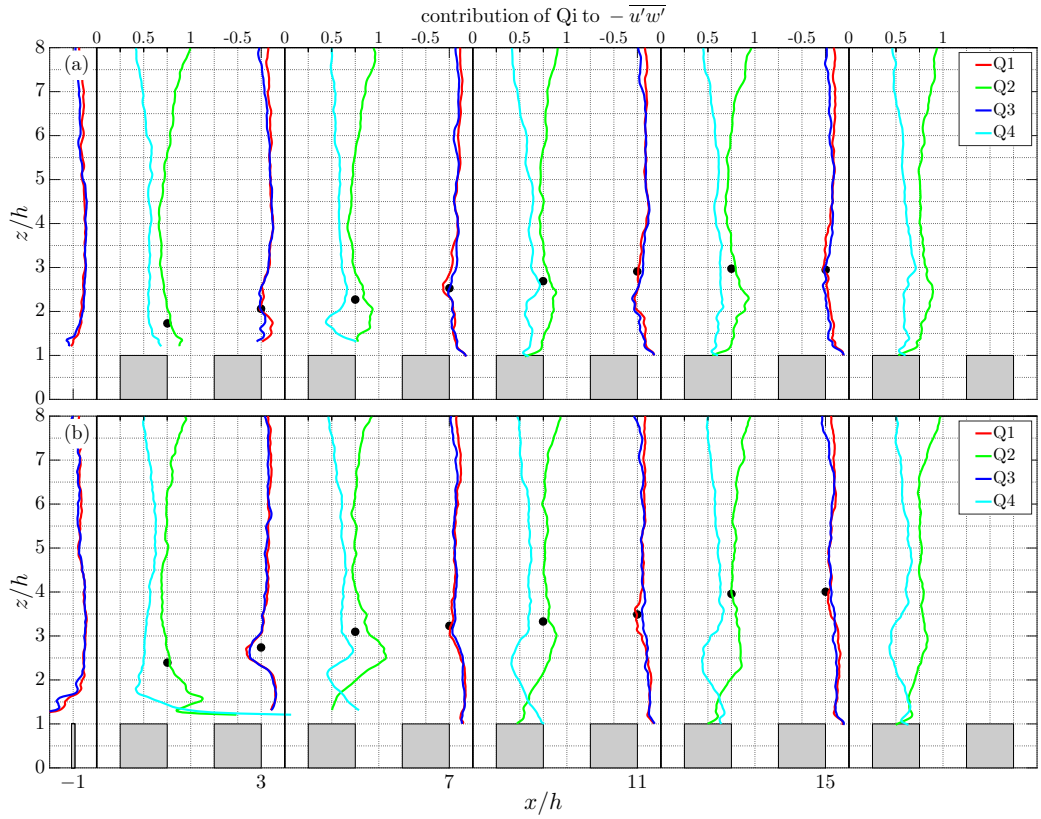

Figure 4.35: Profiles of the contribution of the different quadrants Q_i to the mean Reynolds stress $\overline{u'w'}$ normalized with the total Reynolds stress in the middle of the street canyon for C00 (a) and C10 (b). The internal boundary layer depth δ_i is shown by the solid markers.

4.7.3 POLLUTANT DISPERSION

This section discusses the influence of a fence on the pollutant dispersion behaviour. All concentrations statistics shown in this section are non-dimensionalized according to Equation 4.12. Two snapshots of the concentration fields of the Coo case for both experiments and simulations case are shown in Figure 4.36. Both snapshots display the strongly intermittent character of the concentration field. Slender plumes of high concentration are visible just above the top of the fence. This behaviour is related to the fact that the line source is positioned close to the fence, i.e. the distance between the fence and the source is $1h$ (see Figure 4.1). On average a separation bubble is present just upstream of the fence [104]. Therefore, we conjecture that the presence/absence of this separation bubble in instantaneous snapshots, as determined by the upstream turbulence, is responsible for the strong intermittent behavior of the concentration field. The Schmidt number in the experiments was significantly higher compared to that used in the simulations. However, the turbulent Schmidt number was of the same order of magnitude (see also Section 4.5), which is also indicated by a high degree of similarity in the large structures observed in Figure 4.36.

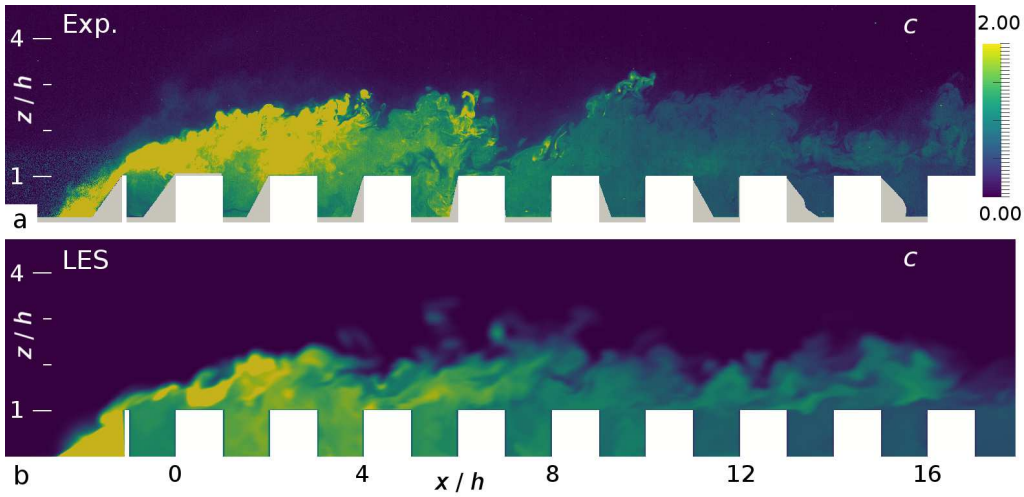

Figure 4.36: Contours of instantaneous concentration c (defined in Equation 4.12) in the midplane of case AR5; (a) experiment and (b) simulation. The snapshots correspond to the velocity fields shown in Figure 4.31. Areas that could not be illuminated or seen in the experiments have been masked in grey and the obstacles are shown in white.

4.7.3.1 *Mean Concentration Fields*

Figure 4.37 shows the vertical distribution of the mean concentration starting $0.5h$ upstream of the first row of obstacles and subsequently in the middle of each street canyon for cases Coo, C05, C10, and C15. The experimental data is shown by the continuous lines, while, if available, the LES data are shown by the dashed lines. The internal boundary layer depth δ_i is indicated by the solid markers for the experiment and by the open markers for the LES. Note that in the second street canyon ($x/h = 3.5$) no

experimental data for Exp. 2 is shown in the region $0.975 < z/h < 1.13$ because of a small (dust) particle in the calibration tank rendered the LIF calibration inaccurate at that location.

From the C00 case, it is evident that the Reynolds number effect is small in the considered Reynolds number range. The two experimental data sets at $h^+ = 209$ and $h^+ = 307$ are nearly on top of each other in the region $z/h > 1$, while minor differences are found inside the canopy region. The most pronounced differences between the experiments and the simulations are found inside the canopy (see Figure 4.37a), where a significant higher concentration is found in the experiments. Separate tests on the spanwise homogeneity of the experimental line source reveal a slightly non-uniform flow rate distribution. As a result of the turbulent mixing in the downstream direction, this lateral inhomogeneity decreases further downstream, resulting in a closer match between both methods in the eighth street canyon. Despite this small difference, the shape of the concentration profiles is similar for both methods. The vertical concentration profiles are largely controlled by δ_i [96]. For C10 and C15 (see Figure 4.37c,d) the concentration profile at $x/h = -0.5$ depicts a peak in concentration just above the fence. In downstream direction this peak quickly disappears and the maximum concentration is again found inside the canopy region (i.e. $z/h < 1$), similar to the C00 case (Figure 4.37a). Due to the strong mixing associated with the shear layer emanating from the fence, the concentration above the urban canopy almost linearly decreases to zero above the IBL. However, the recirculation zone downstream the fence induces a well-mixed region of nearly uniform concentration above the street canyon. This behaviour is particularly visible in the C15 case (Figure 4.37d). Furthermore, the mean concentration inside the urban canopy reduces considerably with increasing fence height. Figure 4.38 shows the streamwise development of the mean canyon concentration and the root-mean-square of the concentration fluctuations. Since the street canyon is not completely visible in the experimental results, the average street canyon concentration is determined only in the upper part of the street canyon. This is a good approximation, as the canyon concentration is quite uniform [96]. For the C00 case the mean canyon concentration increases for the first two streets and reaches its maximum in the third street canyon. This is because the passive scalar is advected with high velocity through the streamwise streets, thereby passing the first two street canyons. After a few streets the flow velocity is decreased, which results in an increased canyon concentration. The behavior of the concentration curve is distinctly different once a fence is introduced. Already for C05, the streamwise development of the mean canyon concentrationreveals a continuous decrease whereas the C00 case shows an initial increase followed by a decrease in concentration, despite the fact that the flow fields are quite similar (Figure 4.32a,b and Figure 4.33a,b). The reason is that a fence prohibits the transport of pollutants along streamwise streets. The maximum canyon concentration for cases C05, C10, and C15 is found in the first street canyon. Please note that the fence should be at least $1h$ high to be beneficial in terms of lower pollutant concentration levels in the first street canyon downstream of the fence. Furthermore, with increasing fence height, the maximum $\langle \overline{c} \rangle$ decreases. Finally, the RMS profiles of $\langle \overline{c} \rangle$, depicted in Figure 4.38b, indicate a similar streamwise trend as $\langle \overline{c} \rangle$. The difference between LES and experiments is attributed to the higher Schmidt number in the experiments, resulting in distinct layers, that significantly increase the concentration fluctuations in the experiments.

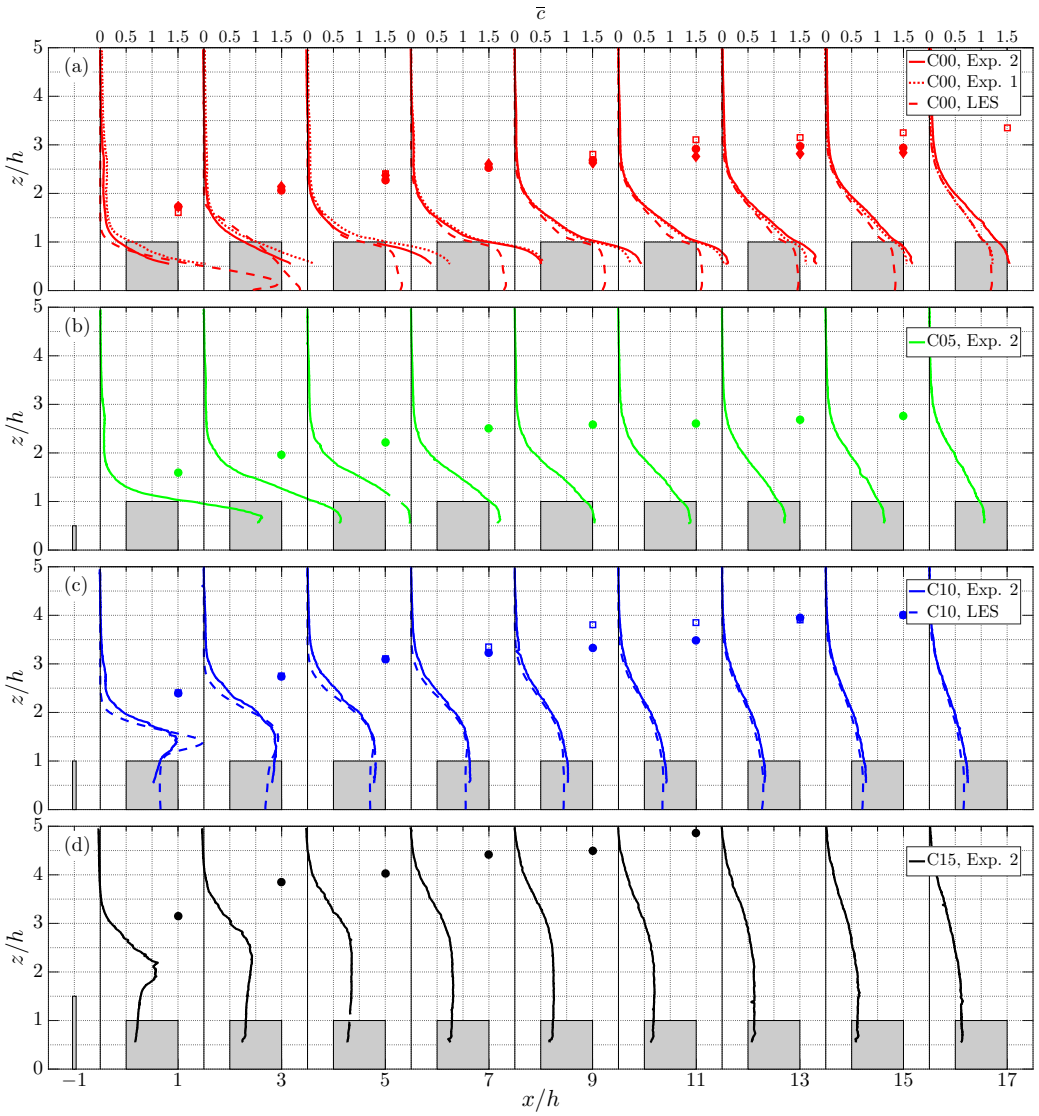

Figure 4.37: Profiles of mean concentration $\overline{c}$ in the middle of each street canyon for cases $0h$ (a), $0.5h$ (b), $1h$ (c) and $1.5h$ (d). Additionally for the $0h$ case (a) the profiles of $\overline{u}/U_h$ at $h^+ = 209$ in the experiments is shown as the dotted line. The internal boundary-layer depth, δ_i, is shown by solid markers for the experiments and by open markers for the LES (if available).

4.7.3.2 *Pollutant Removal due to Sweeps/Ejections*

As mentioned by Reynolds and Castro [141] sweeps are the dominant contributors to the Reynolds shear stress around the top of the canopy region, which is confirmed in Section 4.7.2. Furthermore, they hypothesize that sweeps must play an important role in the behavior of pollutant dispersion at this level. The simultaneous measurements of velocity and concentration fields enables to elucidate the role of sweeps and ejections, as defined in Section 4.7.2, on the pollutant dispersion. Tomas *et al.* [107] investigated the

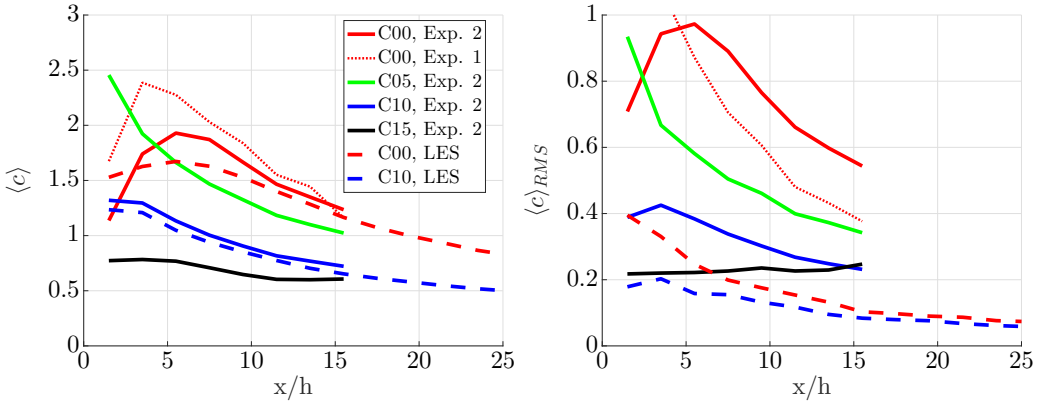

Figure 4.38: Profiles of the mean canyon concentration $\langle \overline{c} \rangle$ (a) and the RMS of the canyon concentration for $\langle \overline{c} \rangle_{\text{rms}}$ (b) for different fence heights.

joint probability density function (JPDF) of the streamwise velocity fluctuation u' and the instantaneous total vertical pollutant flux wc at roof level. They concluded that ventilation of street canyons is associated with low-momentum regions passing the street canyons. Furthermore, the pollutant removal mechanism did not change significantly after three streets.

To investigate the influence of the different quadrants of the u' and w' on the pollutant dispersion at roof level, the JPDF of u' and w' (denoted by $P(u', w')$) is computed in each street canyon in the region ($0.05 < x'/h < 0.95$, $0.95 < z/h < 1.05$), where $x' = 0$ represents the location of the upstream wall of the street canyon. Furthermore, the contribution of the u' and the w' to the instantaneous vertical pollutant flux wc, i.e. $wc\, P(u', w')$, is computed. Figure 4.39 shows $wc\, P(u', w')$, normalized with the mean concentration at roof level, for street 6 for cases C00, C05, C10 and C15. The contour shapes in Figure 4.39 closely resemble the JPDFs of u' and wc found in Tomas *et al.* [107], indicating that wc is dominated by w' in this region. The results reveal that low-momentum fluid (with $u' < 0$) is mainly responsible for pollutant removal from the street canyon ($wc > 0$). For cases C00, C05 and C10, ejections are the dominant cause of pollutant removal from street canyons. Similarly, sweeps contribute to the negative concentration flux. This confirms the suggestion of Reynolds and Castro [141], that sweeps will play a significant role in the dispersion of scalar pollutants. An exception is the C15 case (see Figure 4.39d). Neither sweeps nor ejections are the dominant contributors to wc at this position. This is because the sixth street canyon in the C15 case is still in the recirculation region of the fence (see Figure 4.32d). As a result, the flow is more isotropic in this region.

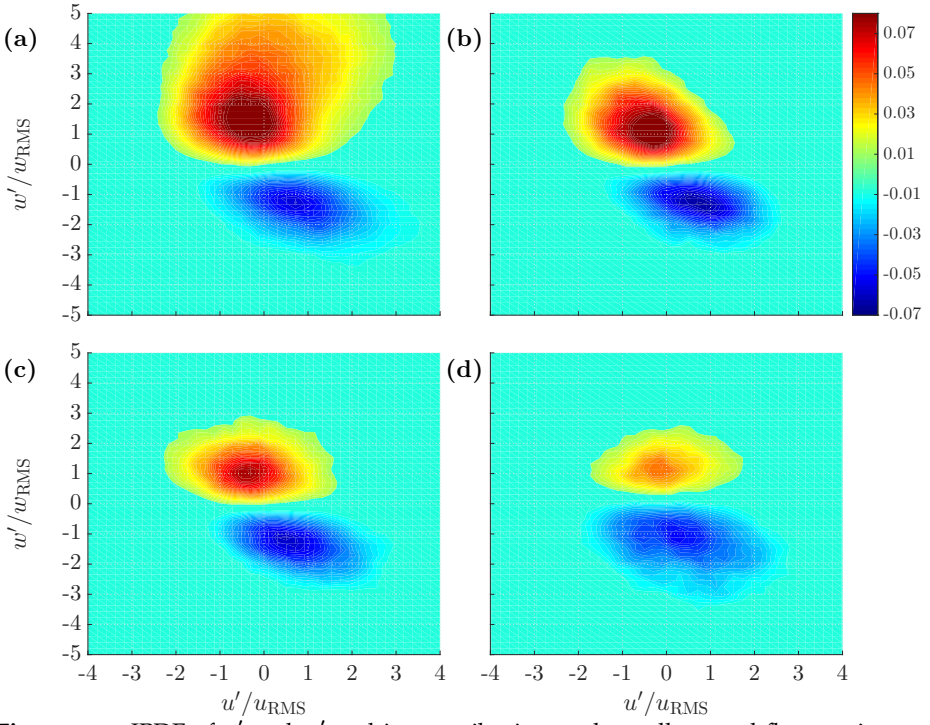

Figure 4.39: JPDF of u' and w' and its contribution to the wall-normal flux wc, i.e. $wc\,P(u', w')$, for C00 (a), C05 (b), C10 (c) and C15 (d) at street six. Only experimental results are shown. The contours are normalized with the mean canyon concentration $\langle \overline{c} \rangle$ and U_h.

4.7.4 MODELLING CONSIDERATIONS

4.7.4.1 *The Mixing Length Model*

Flows over and inside the urban canopies are commonly simulated using models based on the Reynolds-averaged Navier-Stokes equations. However, adequate closure relations are needed to model the Reynolds stresses. One of the most basic closure models of the Reynolds stresses, relating the time averaged Reynolds shear stress to the gradients of the mean flow, was introduced by Boussinesq [152] as:

$$-\overline{u'w'} = \nu_T \left(\frac{\partial \overline{u}}{\partial z} + \frac{\partial \overline{w}}{\partial x} \right), \tag{4.16}$$

where the turbulent viscosity ν_T can be written according to Prandtl [153] as:

$$\nu_T = l_m^2 \left| \frac{\partial \overline{u}}{\partial z} \right|, \tag{4.17}$$

where l_m is the unknown mixing length. This mixing length model is also commonly used in 1D models of urban canopy flows [25, 154]. The model of Coceal and Belcher [25] is basically the non-linear extension of the quasi-linear model that Belcher *et al.* [155] proposed to model the adjustment of a rural boundary layer to an urban canopy. Macdonald [154] proposed the use of a uniform mixing length inside the urban canopy, and a value that increases linearly with height above the canopy, i.e. $l_m \propto z$. An alternative formulation of the mixing length inside the canopy is proposed by Coceal and Belcher [25] as:

$$\frac{1}{l_m(z)} = \frac{1}{\kappa z} + \frac{1}{l_c}, \tag{4.18}$$

where the spatially averaged mixing length in the canopy, l_c is constant and depends on the thickness of the shear layer emanating from the top of the obstacles, i.e. $h - d$. It is computed as $l_m(z = h) = \kappa(h - d)$ to assure a continuous profile. Here κ denotes the von Kármán constant. The zero-plane displacement height d is found by fitting the streamwise velocity profile to the law of the wall which reads:

$$\frac{\overline{u}}{u_\tau} = \frac{1}{\kappa} \ln \left(\frac{z - d}{z_0} \right) \tag{4.19}$$

where z_0 is the roughness length. The proposed form of the mixing length by Coceal and Belcher [25] is motivated by, on the one hand, the sparse canopy case, in which the turbulent eddies scale with the distance from the ground, and on the other hand, the dense canopy limit in which eddies are blocked by the strong shear layer near roof level of the roughness elements. In the latter case the mixing length above the canopy scales with $l_m(z) = \kappa(z - d)$, i.e. the displaced mixing length model [156]. Both Macdonald [154] and Belcher *et al.* [155] note that their models are valid for a relatively low packing density (i.e. $\lambda_f \leq 0.25$). Especially at higher packing densities these models are inadequate in predicting the velocity statistics due to the recirculation regions inside the street canyons. Because a similar simple model for dense urban canopies is not available, in the current study the possibility to use a mixing length model for these cases will be assessed. Cheng and Porté-Agel [102] present the mixing length profiles

for different λ_f for staggered and aligned arrays of cubical obstacles, for $\lambda_f \leq 0.25$. In the current research λ_f is 0.25 for the C00 case, which is the upper limit that Cheng and Porté-Agel [102] considered.

In Figure 4.40 the mixing length profiles for the cases C00 and C10, calculated according to Eqs. 4.16 and 4.17, are shown $0.5h$ in front of the first obstacle row and in the middle of each subsequent street canyons. The gradients of the mean flow are calculated using second-order spatial regression filter with a filter length of $0.3h$ [85]. Additionally, Figure 4.40 shows the models given by Equation 4.18 and the updated model given by Equation 4.20, which will be derived further on in this section.

First, the C00 case is discussed. The agreement between the LES and the experimental results is satisfactory within the internal boundary layer, i.e. $z < \delta_i$. For the C00 case shown in Figure 4.40a it is clear that after a few streets the shape of the mixing length profile does not change significantly. This observation is in line with the observations made by Cheng and Porté-Agel [102]. Inside the canopy, the model of Coceal and Belcher [25] does not capture the correct trend of l_m, as is expected for dense canopies. Figure 4.40a shows a local peak in the profiles for l_m at roughly $z/h = 0.5$, in accordance with Cheng and Porté-Agel [102] and Coceal *et al.* [99]. The profiles of l_m have a local minimum at roof level. This is a result of the strong shear layer at roof level, resulting in a small mixing length at that location. In the region just above the street canyons, i.e. $1 < z/h < 1.5$, l_m increases approximately linearly with height, which is most clearly visible for $x/h \geq 5.5$. This behaviour is indicative for the presence of a log-law in the internal boundary layer in which the mixing length scales linearly with $z - d$ [25]. In the region $1.5 < z/h < \delta_i/h$ the mixing length increases about linear, but distinctly slower compared to the model prediction by Coceal and Belcher [25]. Finally, the mixing length in the outer region of the flow ($z > \delta_i$) again shows a linear increase, indicating the remnants of the log-law region of the original approaching smooth-wall boundary layer. The most important difference between the C00 and the C10 is found in the region $1.5 < z/h < \delta_i/h$. For case C10 (Figure 4.40b) l_m reaches an approximately constant value. Furthermore, the mixing length in this region increases in size when moving downstream.

As a result of the roughness transition a strong shear layer is present above the canopy region that defines the IBL and appears as a well-mixed region, that shows close resemblance to a plane mixing layer which is characterized by a mixing length that is constant with height and that is proportional to the mixing layer width. It is interesting to note that Belcher *et al.* [155] mention the concept of the growth of a new internal boundary layer at a roughness transition. However, this concept is not taken into account into the model description. This is likely because relatively sparse canopies are considered for which the strength of the shear layer at the start of the urban canopy does not dominate the flow, and hence the mixing length.

The linear behaviour of l_m, that is indicative for a log-law behaviour of the mean flow, in the regions $1 < z/h < 1.5$ and $z > \delta_i$ is persistent up to the streamwise extent of the LES domain. Figure 4.41a shows the mixing length in the 23rd street of the LES domain, while Figure 4.41b shows the linear-log plot of the streamwise velocity profile at the same location. Both C00 and C10 indicate the presence of a so-called double log-layer structure. The bottom log-layer in the range $1 < z/h < 1.7$ belongs to the internal boundary layer over the roughness elements, whereas the upper log-layer

($z/h > 4.2$) belongs to the remainder of the approaching flow boundary layer. These regions are the regions in Figure 4.41a in which l_m is found to increase linearly with height according to $l_m = \kappa z$. As the approaching flow boundary layer has a relatively limited depth of approximately $10h$, the remainder of the original log-law from the approaching flow boundary layer is only present in the region $3.5 < z/h < 4$. Above $z/h > 4$ l_m becomes approximately constant, which is the outer layer of the approaching smooth-wall boundary layer in which the scaling $l_m \propto \kappa(z-d)$ does not hold anymore.

The mixing length profiles shown in Figure 4.40 and Figure 4.41a suggest the presence of different regimes, that are schematically visualized in Figure 4.42. Instead of modelling the mixing length above the urban canopy as $l_m = \kappa(z-d)$ [25], an additional region is present inside the internal boundary layer that is governed by a combination of both a linear increase (according to $l_m = \kappa(z-d)$) just above the canopy and plane mixing layer like behaviour in the upper part of the internal boundary layer ($l_m \approx$ constant in z, but increasing with x). Analogous to Equation 4.18, the mixing length in this region (regions IIa and IIb in Figure 4.42) can be described by taking the harmonic mean of these two behaviours:

$$\frac{1}{l_{m_{II}} - \kappa(h-d)} = \frac{1}{\kappa(z-h)} + \frac{1}{l_i}, \tag{4.20}$$

where l_i is a length scale that is proportional to the internal boundary layer depth, i.e. $l_i = \alpha(\delta_i - h)$. A constant $\alpha = 0.2$ gave the best match between the measured profiles and the proposed model. Furthermore, this mixing length formulation was found to give the best match in the region $1 < z/h < 0.75\delta_i/h$. The additional term in the denominator on the left hand side of Equation 4.20 originates from the closure relation $l_{m_{\mathrm{II}}} = l_{m_{\mathrm{I}}}$ at $z = h$. As $\delta_i \to \infty$, the mixing length is dominated by the first term on the right hand side (RHS) of Equation 4.20 and the mixing length returns to $l_m = \kappa(z-d)$, which is the same expression as proposed by Coceal and Belcher [25] and others to use above the canopy. Furthermore, for small z, l_m is also dominated by the first term on the RHS of Equation 4.20 and l_m behaves again linearly, which is in accordance with the linear behaviour of l_m in region IIa. Finally, in region III, above the mixing layer, a linear increase of the mixing length with height is applied. From Figure 4.40, it is clear that the mixing length according to Equation 4.20 provides an accurate description of the mixing length in the region $1 < z/h < 0.75\delta_i/h$. Especially in the C10 case (Figure 4.40b) the match in the streets further downstream is better compared to the form proposed by Coceal and Belcher [25]. As noted before, the current models do not provide accurate results for dense canopies due to the recirculation regions inside the street canyons, which is not discussed at present. However it is shown that the presence of the IBL should be taken into account to properly model the flow over dense urban canopies.

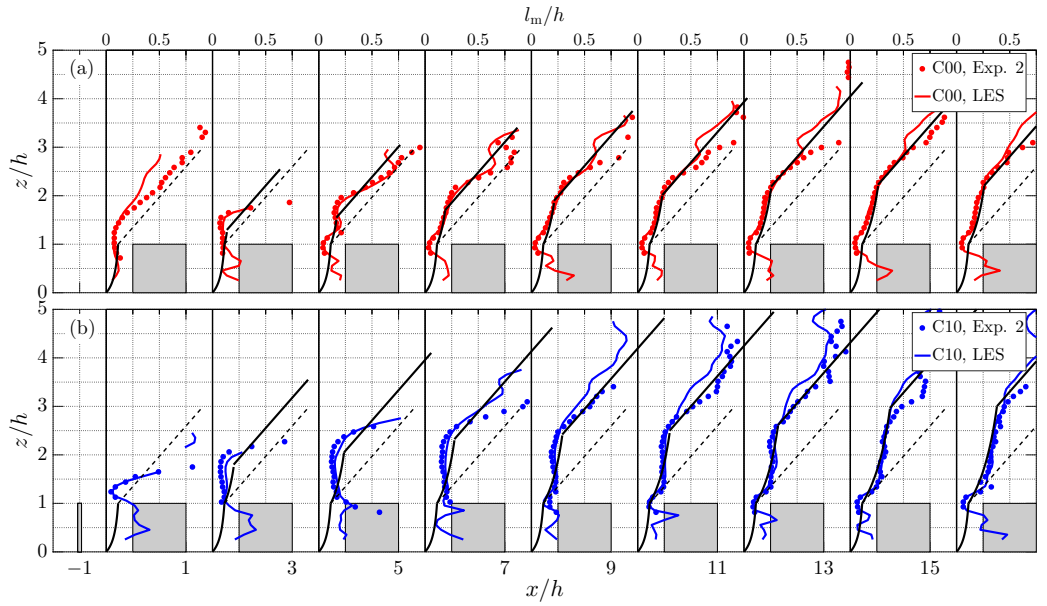

Figure 4.40: Profiles of mixing length l_m in the middle of each street canyon for cases C00 (a) and C10 (b). The dashed black line is the model of Coceal and Belcher [25] expressed in Equation 4.18, while the adjusted mixing length model expressed in Equation 4.20 is given by the solid black line.

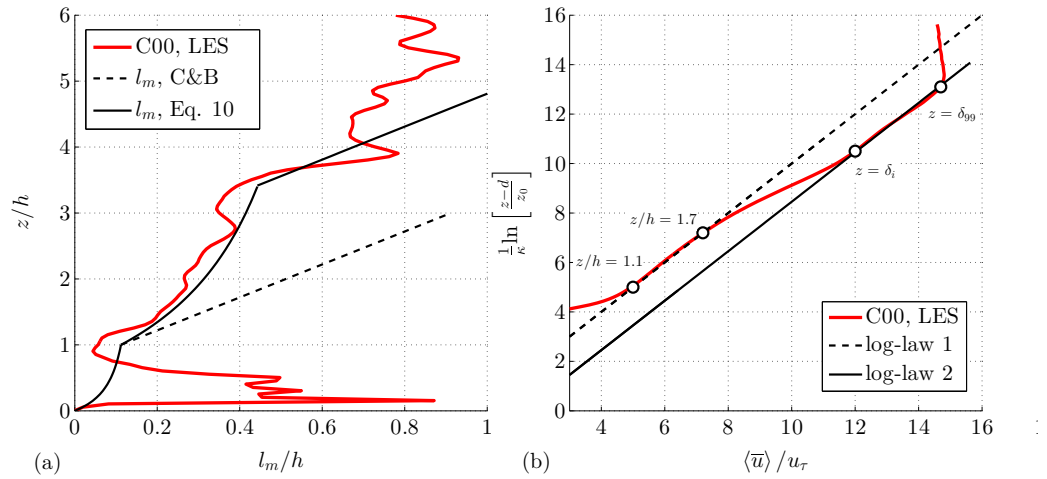

Figure 4.41: (a) Profile of the mixing length at the 23rd street in the LES data. The dashed black line depicts the model of Coceal and Belcher [25] expressed in Equation 4.18, while the adjusted model according to Equation 4.20 is given by the solid black line. (b) The streamwise velocity profile in inner scaling.

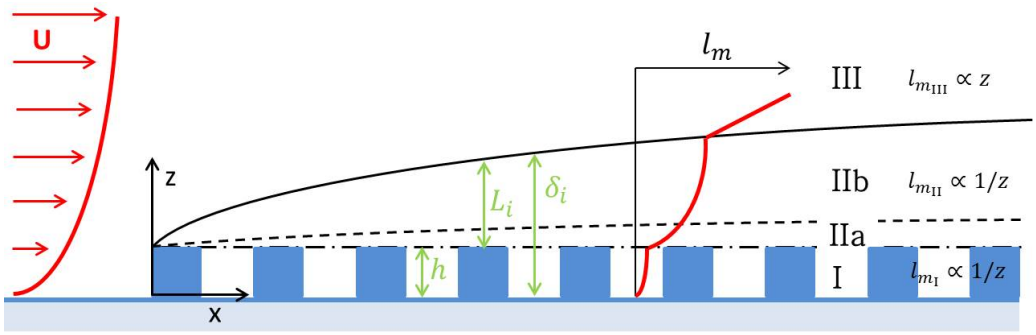

Figure 4.42: Schematic overview of the different regimes of l_m in the transition region. The obstacles are shown in blue, the canopy region is denoted by I, the roughness sublayer by II, the mixing layer region III and the outer region by IV. The edge of the canopy region is denoted by the black dash-dotted line, the roughness sublayer is shown by the black dashed line, and the internal boundary layer by the solid black line.

4.7.4.2 *Scaling of the Mean Concentration Field*

The rural-to-urban roughness transition is characterized by a region where the flow is mainly governed by the strong shear layer emanating from the first row of obstacles. In the first few streets the flow quickly adapts to the new surface roughness. Coceal and Belcher [25] propose a 'rule of thumb' to calculate the length of the adjustment region (x_0) as:

$$x_0 = 3L_c \ln K, \tag{4.21}$$

where $K = (U_h/u_\tau)/(h/L_c)$, and the length scale L_c is given as:

$$L_c = \frac{1-\lambda_p}{\lambda_f} h, \tag{4.22}$$

For the current set-up the adjustment region according to Equation 4.21 is approximately $17h$, i.e. after eight streets.

The initial pollutant dispersion is governed by the local flow, which is mainly determined by the (local) geometry of the obstacles. However, further downstream the (mean) vertical dispersion is bounded by the (mean) shear layer that characterizes the IBL. The vertical extent of the region that bounds the mean concentration field is approximately $L_i = \delta_i - h$ (see Figure 4.42). Because δ_i increases with x, L_i also depends on x. In addition, the mean advection of pollutants released inside the IBL is governed by the mean streamwise velocity in the internal boundary layer, which can be described by the bulk velocity of the IBL. Here, the streamwise development of the bulk velocity is estimated by the mean streamwise velocity at half the IBL depth; $U_i(x) \equiv \overline{u}(x, z = \frac{1}{2}\delta_i)$. With the length scale L_i and velocity scale U_i the development of the mean concentration field can be described by:

$$\overline{c}\,(x,z) = \frac{Q}{L_y U_i\,(x)\,L_i\,(x)} f\,(z/\delta_i)\,, \tag{4.23}$$

where L_y is the width of the domain, and Q is the constant mass flow rate of the source. Figure 4.43 shows the vertical profiles of the mean concentration, where the vertical coordinate is scaled with the local δ_i and the concentration is scaled with the local L_i and U_i. The results are shown for cases C00, C10, and 2D. Although, U_i and δ_i (and consequently L_i) differ for each case, the results collapse onto a single profile using the proposed scaling. A fit for the vertical distribution profile $f\,(z/\delta_i)$ is shown by the thick continuous line. As expected, the profiles start to differ near the surface roughness, where the specific geometry governs the concentration distribution. This scaling means that the spanwise-averaged concentration field can be described by the flow parameters L_i and U_i that depend solely on x, while the dependence of z is accounted for in the universal function $f\,(z/\delta_i)$. In addition, the flow parameters L_i and U_i are most likely related to each other, and they can be found from measurements, simulations, or self-similarity considerations for the flow over roughness transitions.

Using the fitted profile for $f\,(z/\delta_i)$ the prediction of $\overline{c}\,(x,z)$ is given in Figure 4.44, where for cases C00 (red lines) and C10 (blue lines) the LES results are shown by the thin continuous lines, and the model results from Equation 4.23 are shown by the thick dashed lines. Close to the start of the urban canopy the model results do not match the

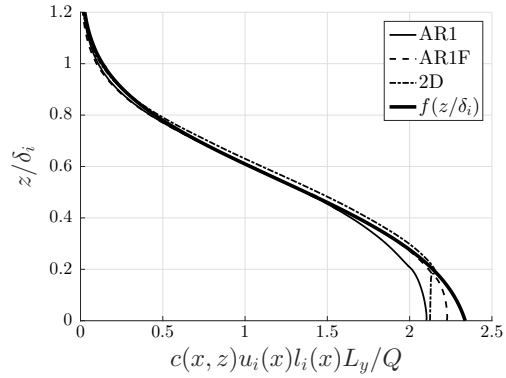

Figure 4.43: Vertical profiles of mean concentration scaled according to Equation 4.23 for street 24

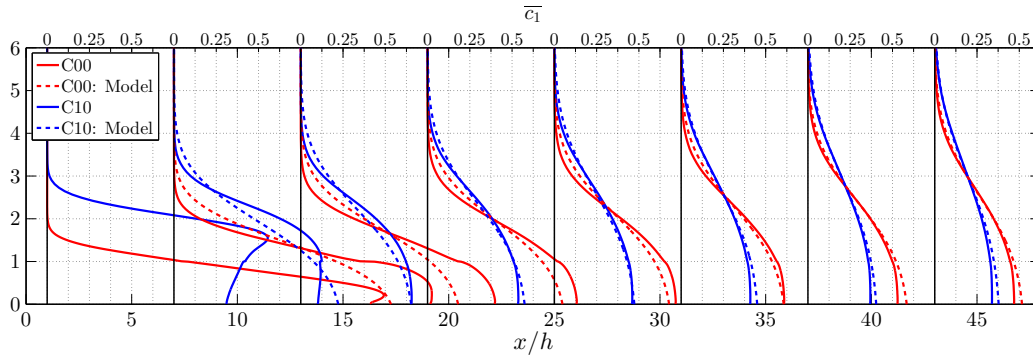

Figure 4.44: Vertical profiles of mean concentration for cases AR1 and AR1F at several downstream locations including model prediction from Equation 4.23.

LES results. This is expected, because the local velocity field has not yet reached a self-similar state. However, from around street 8 ($x = 15h$) and onwards the model results agree well the LES results, which indicates the mean pollutant dispersion is indeed governed by the properties of the IBL.

4.8 CONCLUSIONS

This section summarizes the main conclusions this chapter.

Varying Spanwise Length Scale of the Roughness

Simultaneous PIV and LIF measurements were employed to investigate flow and pollutant dispersion behaviour in regions where the surface topology changes from rural to urban type roughness. The results were compared with LES simulations. The approaching rural boundary layer was modeled by a smooth wall boundary layer, while the urban area consisted of obstacles of constant height h, where roughness Reynolds number h^+ was 194 for the simulations and 209 for the experiments. The aspect ratio of the obstacles was varied between 1 and 8 in the different experiments. The results show that the two methods independently predict similar velocity statistics. However, minor differences in the region of the first row of obstacles were observed, which were attributed to the accuracy of both methods and differences in the generated approaching smooth-wall boundary layers. The pollution concentration statistics showed some differences in the region due to a slight non-uniformity in the emission source in the experiment. Nevertheless, qualitatively there was a good agreement between the methods, and the same dispersion mechanisms were identified.

The effect of the roughness transition on pollutant dispersion is that the mean vertical pollutant flux at the top of the street canyons is dominated by the advective pollutant flux $\overline{w}\,\overline{c}$ in the first three streets, after which the profiles of $\overline{w}\,\overline{c}$ and $\overline{w'c'}$ along the streamwise extent of the street canyons become similar to those for the fully-developed cases described by Michioka *et al.* [24]. Likewise, the JPDFs of streamwise velocity fluctuation u' and instantaneous vertical pollutant flux wc have a similar shape from the fourth street onwards. In addition, it is found that, in agreement with Michioka *et al.* [24], the JPDFs are qualitatively similar for all considered aspect ratios, showing that street canyon ventilation of pollutant is mostly associated with $u' < 0$.

Subsequently, the flow structure that is associated with street canyon ventilation was identified by means of linear stochastic estimation. It was found that for larger l/h street canyon ventilation is associated with larger regions of $u' < 0$, and that their vertical length scale increases linearly with increasing l/h. However, the result for the 2D case does not result in the largest structure. In addition, during such a ventilation event the flow structure inside the urban canopy shows more variation in the horizontal plane for $l/h = 1$ and $l/h = 2$ than for larger aspect ratios, for which the variation is confined mostly to the considered street canyon.

Reynolds Number Variation

Next, the roughness Reynolds number h^+ was varied from 209 up to 598. The influence of the Reynolds number variation on both velocity statistics as well as concentration statistics in this range is limited. None of the presented statistics shows a clear trend with Reynolds number, consistent with observations by Castro [118] and Cheng and Castro [98].

Influence of a Fence

The influence of an additional fence was investigated for various fence heights at a roughness Reynolds number, h^+, of 194 for the simulations and 307 and 209 for the experiments. Again, both methods predict practically the same velocity and concentration statistics. A strong shear layer is present starting from the top of fence, which characterizes the IBL. With increasing fence height (and thus an increased blockage), a stronger shear layer is formed, resulting in a higher IBL. The initial disturbance generated by this shear layer determines the downstream development of the IBL and therefore also the concentration statistics in and above the canopy.

A quadrant analysis indicates that sweeps are the predominant flow features near roof level, while ejections only become important farther away from the canopy. As hypothesized by Reynolds and Castro [141] sweeps and ejections are important for dispersion at roof level. Sweeps are mainly found to lower the total pollutant flux $\overline{wc}$ out of the street canyon, whereas pollutant removal is mainly associated with ejections. These results are in line with the conclusions by Michioka *et al.* [24] and Tomas *et al.* [96].

The flow in a rural-to-urban transition for dense canopies, i.e. $\lambda_f \geq 0.25$, can be modelled with a mixing length model by considering (1) the roughness geometry and (2) the internal boundary-layer development. The effect of the IBL is persistent farther downstream than the streamwise extent of the presently considered domain. An improved mixing length model is proposed that is applicable to rural-to-urban transitions for dense urban canopies. Moreover, when δ_i increases (as $x/h \to \infty$) this model exhibits similar characteristics as the model proposed by Coceal and Belcher [25]. In addition, the average mean concentration field is found to attain a self-similar profile when scaled with the characteristic velocity and length scale of the IBL, i.e. the IBL bulk velocity and the IBL height. This means that, after an initial adjustment region, the mean concentration field can be described by the characteristics of the IBL solely. Hence, this result emphasizes the conclusion that accurate modelling of the flow and dispersion over rural-to-urban transitions for dense urban canopies requires taking into account the characteristics of the IBL.

5

CONCLUSIONS AND PERSPECTIVES

This chapter provides the conclusions that are drawn from the different chapters. Each chapter is based upon one or more publications, hence these chapters are self-contained. Therefore, only the main conclusions are presented here. Moreover, perspectives on future research and developments are given in this chapter.

5.1 CONCLUSIONS

The main research objectives, as stated in Section 1.2, were twofold. Firstly, aspects of the regions of high shear were studied including the relation with the dispersion of a passive scalar. Secondly, the dispersion of a passive scalar in an idealized urban geometry was studied.

SHEAR LAYERS, UNIFORM MOMENTUM ZONES AND DISPERSION

Thin layered structures of high shear were observed in a TBL. A conditional sampling approach was employed to determine the conditional statistics across these layers. Next, a first order jump model was derived based on these conditional statistics, from which entrainment velocities of the layers could be derived. These entrainment velocities are indicative of the growth rates of large scale regions bounded by the shear layers. This model was validated by performing the same analysis on the T/NT interface for which a theoretical prediction was available. This research revealed that internal shear layers exhibit qualitatively the same statistical characteristics as the external T/NT interface. Furthermore, the regions of high shear on average move very slowly outwards, with an increasing wall-normal velocity away from the wall. This implies that on average large scale regions grow very slowly.

A follow up study considered the role of these large-scale regions of nearly uniform momentum, also referred to as UMZs, and their accompanying shear layers, on the dispersion of a passive scalar. This research revealed for the first time the existence of distinct UCZs. Furthermore, the conditional sampling approach illustrates the blocking behaviour of the regions of high shear as the wall-normal concentration flux is reduced over the edges of UMZs and UCZs. These results indicate that UMZs are important for pollutant dispersion as observed before by Michioka *et al.* [24].

DISPERSION IN AN IDEALIZED URBAN GEOMETRY

Dispersion of a passive scalar in an idealized urban geometry was studied in the second part of this thesis. Simultaneous PIV and LIF yielded similar the same velocity and concentration statistics compared to the LES, despite the different methods to generate the inflow boundary layer. The mean vertical pollutant flux at the top of the street canyons is dominated by the advective flux in the first few streets after the roughness transition. The profiles of the advective and turbulent fluxes become similar to previous results by Michioka *et al.* [24] further downstream. Similarly, the JPDF of the vertical concentration flux and the streamwise velocity fluctuations indicate that low-momentum fluid is mainly responsible for a pollutant flux out of the street canyon. A linear stochastic estimate is used to show that a large scale low-momentum region above the canyon is associated with this outward flux. The present investigation reveals that with increasing aspect ratio the length scales of these large scale structures increase. The influence of the Reynolds number on the different statistics is shown to be limited, i.e. the flow inside the canopy region is dominated by the turbulence generated off the sharp-edged obstacles, which is in line with previous observations by Cheng and Castro [98]. Next, a fence was introduced in between the line source and the urban geometry. A strong shear layer is formed at the edge of this fence, which determines the characteristics of the IBL. Increasing the fence height also increases the height of the IBL. The concentration profiles indicate that the pollutants are predominantly kept inside this newly formed IBL. A quadrant analysis reveals that sweeps and ejections are the main contributors to the concentration flux at roof level. The results from this study reveal that the rural-to-urban transition in case of dense urban canopies can be modelled with a modified mixing length model. The strong shear layer that appears at the edge of the fence resemblances a plane-mixing layer, as observed above vegetation canopies by Raupach *et al.* [157]. Furthermore, the mean concentration field is shown to be self-similar after the initial adjustment region and is described solely by the IBL characteristics. Hence, the results indicate that it is crucial to take the characteristics of the IBL into account to properly model flow and dispersion characteristics in dense urban canopies in case of rural-to-urban transitions.

5.2 PERSPECTIVES ON FUTURE RESEARCH

As indicated in the previous section, important insights were gained in the understanding of dispersion in both flat plate TBLs as well as over idealized urban geometries. Nevertheless, there are remaining questions and issues. Some of these remaining issues and recommendations on how to address these are provided in this section.

A GUIDE FOR FUTURE DISPERSION EXPERIMENTS

In this thesis PIV and LIF are the main experimental techniques. Both techniques produce instantaneous quantitative velocity or concentration fields in a single plane. The combination of these methods provides a very powerful tool to study dispersion in turbulent flows. However, there are a number of limitations accompanying this tech-

nique. Optical access to the measurement domain is essential to succesfully perform PIV and LIF. Unfortunately, the difference in refractive index of the obstacles made from PMMA and water causes reflections and shadows (see Chapter 4), thereby limiting the optical access inside the urban canopy. Weitzman *et al.* [158] shows a promising approach to produce refractive-index-matched hydrogels models, which largely eliminate these shadows and refractions, i.e. full optical access is maintained. Experiments in our laboratory revealed that careful selection of the hydrogel ingredients is necessary to match the refractive index and to obtain the required material stiffness. Nevertheless, the approach is encouraging for future dispersion experiments in more complex urban geometries.

Furthermore, the PIV and LIF experiments in Chapter 4 were performed in the symmetry plane of the urban geometry. In experiments, an estimation for the friction velocity u_τ is commonly based on the peak values in Reynolds stress near the roof level of the urban canopy. As shown by Tomas *et al.* [96] the spanwise variation of the Reynolds stress for an aspect ratio of 2 is significant and cannot be neglected. Hence, an accurate estimation of u_τ should be based upon the spanwise averaged velocity field, and thus spanwise velocity fields are required.

A scaled ABL was generated by means of Irwin type spires [120]; a very easy and straightforward method. However, some clear differences between the simulations and the experiments were observed, which might become noticeable in case of fully developed conditions [119]. Nevertheless, for the present purpose these spires generated satisfactory results, because the flow and concentration statistics inside the urban canopy appear to be rather insensitive to the approach flow conditions when a sudden and distinct roughness transition is encountered. More flexibility and better control of the approach flow conditions can be achieved by installing an active grid. Cekli and Water [122] showed the benefits of such a grid for generating a properly scaled ABL. By varying the average angle and the rotation speeds of horizontally and vertically rotating axes with attached vanes, different approach flow conditions could easily be obtained. One of the advantages of active grids is that more realistic integral turbulent length scales and turbulence intensities can be reproduced [159], something that is difficult to get right with passive spires [160].

In the current thesis the approach flow boundary layer is perpendicular to the line source and the urban geometry. Obviously, this is a very specific example, and the experiments should be repeated for different flow angles. In the current setup, mean advective transport along streets is absent by definition as measurements were performed in the symmetry plane of the obstacles. However, the advective transport along streets becomes important once non-perpendicular approach flow conditions are considered. The current experimental setup has been prepared to perform these experiments, although the angle is limited to 30°.

As mentioned by Tomas *et al.* [107] the effects of buoyancy on pollutant dispersion in a generic urban environment cannot be neglected. In this thesis only neutral conditions are considered, due to the complexity of generating an (un)stable approach flow boundary layer in the current experimental facility. It should be noted that (near) neutral conditions are commonly encountered in countries like The Netherlands in case of moderate wind speeds and (partly) cloudy days. Furthermore, around sunrise and sunset the boundary layer reaches near neutral conditions as it turns from unstable

to a stable nocturnal boundary layer or vice-verse [161]. Moreover, these hours generally coincide with rush hour traffic. Stable conditions are frequently encountered during sunset and nights whereas unstable conditions are commonly encountered during calm sunny days. It is certainly worthwhile to study the influence of atmospheric stability in a controlled laboratory setting.

RELATION TO FULL-SCALE APPLICATION

In Chapter 4 of this thesis an idealized urban geometry was considered in a scaled version of the ABL. The ratio between the obstacle height and the boundary layer thickness was set to 0.1. As such, the obstacles are fully submerged into the logarithmic region of the ABL. However, the new IBL that develops over the canopy quickly reaches three to four obstacle heights, i.e. the edge of the logarithmic region of the ABL is reached. In real life applications this ratio can be of the order of 0.01. This can be achieved by either increasing the boundary layer thickness and the Reynolds number or by decreasing the obstacle height. The first option is not feasible as the boundary layer height is already half of the water tunnel depth and the Reynolds number can only be increased by a factor of two. The second option, that is to decrease the building height, appears to be the most promising approach, although one should take care of the achievable spatial resolution in the PIV and LIF experiments and assure that the flow remains in the fully rough regime [126]. Furthermore, experiments at different Reynolds numbers confirmed the observation that Reynolds number influences on the flow over sharp edged obstacles are small if $\mathrm{Re} = U_\infty h/\nu \geq 5 \times 10^3$ [98, 118, 162]. It is recommended to verify this also for more realistic building geometries.

FUTURE URBAN DISPERSION MODELS

This thesis presents detailed measurements on both concentration fields as well as velocity fields in turbulent flows. However, these results are by no means exhaustive in terms of geometry, wind angles, and numerous other parameters. It is clearly unfeasible to perform these type of experiments for every specific situation. This motivates the use of more low-order models that capture the essential physics, deduced from the presented high quality experiments.

As mentioned in Chapter 1, Gaussian plume models are not suitable to predict dispersion characteristics in urban areas. Instead of relying on (semi) empirical or analytical models, there is a growing interest in the use of computational fluid dynamics (CFD) methods like LES and Reynolds Averaged Navier-Stokes (RANS) methods. With the continuously increasing computing capabilities, LES simulations became feasible for dispersion studies on realistic urban geometries [163–166]. Still, the computational domain is usually limited to a few kilometers in size with a resolution of typically one meter, and the required computational power is still significant. Though this is a promising approach there remains a need for simplified dispersion models. Based on the results presented in this thesis two lines of thought are presented which may be found useful for the development of future urban dispersion models.

First of all, the results presented in Chapter 4 emphasize the importance of the IBL formed at the roughness transition, i.e. the pollutants are mainly kept inside this IBL. Actual urban areas are heterogeneous and continuously change in space, forming multiple IBLs in urban areas [20]. Therefore, an accurate prediction of pollutant concentrations in transitional regions relies firmly upon the correct prediction of the IBL depth as well as its streamwise development.

A second (and definitely a more sophisticated) approach is the use of coherent structures in the development of dispersion models. Reduced order modelling, such as proper orthogonal decomposition, linear stochastic estimation, and conditional averaging, are promising approaches to build models that capture the correct physics while only a fraction of the computational power of a full simulation or experiment is required [167]. In Chapter 4, a linear stochastic estimate results in a large scale region of low-momentum associated with street canyon ventilation. However, stronger evidence of the importance of large scale structures lies in the fact that these structures are also observed in instantaneous realizations of a TBL (see Chapter 2,3) and not only in a statistical average sense, i.e. from a POD or an LSE analysis. The presence of these large scale structures has been observed by other researchers above idealized urban geometries [24, 75, 149], and also in full-scale atmospheric flows [23, 73, 168, 169]. Moreover, the simultaneous PIV and LIF experiment in Chapter 3 revealed the existence of UCZs. A conditional sampling approach shows that the edges of these zones act as barriers for scalar transport. A possibility for a practical dispersion model is to extent the first order jump model (developed in Chapter 2) with a similar approach for the scalar concentration field. As a result, the turbulent flow can be divided in multiple regions with uniform momentum and concentration, while the momentum and scalar transport among the different zones is governed by a simple jump model. It is recommended to study the performance of such a model for real-life conditions.

A

THEORETICAL DERIVATION OF FIRST ORDER JUMP MODEL

In this appendix the theoretical derivation of the first order jump model as proposed by VanZanten *et al.* [62] and Pino *et al.* [63] is given with modifications for the internal shear layers. It starts by integrating the mean streamwise momentum equation (Equation 2.3) over the distinct regions shown in Figure 2.5.

A.1 INTEGRATE OVER REGION A

First, we integrate the conditional momentum equation 2.3 over the region A which extends from $(y_1 - \epsilon)$ to y_1 below the layer.

$$\int_{y_1-\epsilon}^{y_1} \frac{\partial \langle \overline{u} \rangle}{\partial t} \, \mathrm{d}y = - \int_{y_1-\epsilon}^{y_1} \langle \overline{v} \rangle \frac{\partial \langle \overline{u} \rangle}{\partial y} \, \mathrm{d}y - \int_{y_1-\epsilon}^{y_1} \frac{\partial \left\langle \overline{u'v'} \right\rangle}{\partial y} \, \mathrm{d}y \tag{A.1}$$

Then we apply the Leibniz integral rule to the left hand side (LHS):

$$\begin{aligned} \int_{y_1-\epsilon}^{y_1} \frac{\partial \langle \overline{u} \rangle}{\partial t} \, \mathrm{d}y &= \frac{\partial}{\partial t} \int_{y_1-\epsilon}^{y_1} \langle \overline{u} \rangle \, \mathrm{d}y - \langle \overline{u} \rangle_{y_1} \frac{\partial y_1}{\partial t} + \left[\langle \overline{u} \rangle_{y_1} - \gamma_1 \epsilon \right] \frac{\partial (y_1 - \epsilon)}{\partial t} \\ &= \frac{\partial}{\partial t} \left[\epsilon \langle \overline{u} \rangle_{y_1} - \frac{1}{2} \epsilon^2 \gamma_1 \right] - \epsilon \gamma_1 \frac{\partial y_1}{\partial t} \end{aligned} \tag{A.2}$$

where it is assumed that the gradient of the streamwise conditional velocity $\gamma_1 = \frac{\partial \langle \overline{u} \rangle}{\partial y}\Big|_{y<y_1}$ is constant in this region and $\frac{\partial (y_1 - \epsilon)}{\partial t} = \frac{\partial (y_1)}{\partial t}$, because ϵ is constant. The first term on the right hand side (RHS) of Equation A.1 can be written as:

$$\begin{aligned} - \int_{y_1-\epsilon}^{y_1} \langle \overline{v} \rangle \frac{\partial \langle \overline{u} \rangle}{\partial y} \, \mathrm{d}y &= -\gamma_1 \int_{y_1-\epsilon}^{y_1} \langle \overline{v} \rangle \, \mathrm{d}y \\ &= -\epsilon \gamma_1 \langle \overline{v} \rangle_{y_1}, \end{aligned} \tag{A.3}$$

where again it is assumed that the gradient of the conditional streamwise velocity profile is constant (i.e. γ_1). The last term on the RHS of Equation A.1 can be written as:

$$- \int_{y_1-\epsilon}^{y_1} \frac{\partial \left\langle \overline{u'v'} \right\rangle}{\partial y} \, \mathrm{d}y = -\epsilon \gamma_4, \tag{A.4}$$

where $\gamma_4 = \frac{\partial \langle \overline{u'v'} \rangle}{\partial y}\big|_{y<y_1}$ is the gradient in the Reynolds stress in the turbulent region below the interface. Combining these results yields:

$$\frac{\partial}{\partial t}\left[\epsilon \langle \overline{u} \rangle_{y_1} - \frac{1}{2}\epsilon^2 \gamma_1\right] - \epsilon\gamma_1 \frac{\partial y_1}{\partial t} = -\epsilon\gamma_1 \langle \overline{v} \rangle_{y_1} - \epsilon\gamma_4 \tag{A.5}$$

Rearranging Equation A.5, dividing by ϵ and taking the limit of $\epsilon \to 0$ yields:

$$\frac{\partial \langle \overline{u} \rangle_{y_1}}{\partial t} = \gamma_1 \left(\frac{\partial y_1}{\partial t} - \langle \overline{v} \rangle_{y_1}\right) - \gamma_4 \tag{A.6}$$

A.2 INTEGRATE OVER REGION B

Next, we integrate Equation 2.3 over the jump region B (i.e. $y_1 < y < y_2$):

$$\int_{y_1}^{y_2} \frac{\partial \langle \overline{u} \rangle}{\partial t} \, \mathrm{d}y = -\int_{y_1}^{y_2} \langle \overline{v} \rangle \frac{\partial \langle \overline{u} \rangle}{\partial y} \, \mathrm{d}y - \int_{y_1}^{y_2} \frac{\partial \left\langle \overline{u'v'} \right\rangle}{\partial y} \, \mathrm{d}y \tag{A.7}$$

Now, Leibniz rule is applied to move the partial derivative of the left hand side (LHS) out of the integral. For the LHS of Equation A.7 this yields:

$$\begin{aligned}\int_{y_1}^{y_2} \frac{\partial \langle \overline{u} \rangle}{\partial t} \, \mathrm{d}y &= \frac{\partial}{\partial t} \int_{y_1}^{y_2} \langle \overline{u} \rangle \, \mathrm{d}y - \langle \overline{u} \rangle_{y_2} \frac{\partial y_2}{\partial t} + \langle \overline{u} \rangle_{y_1} \frac{\partial y_1}{\partial t} \\ &= \frac{\partial}{\partial t}\left[\langle \overline{u} \rangle_{y_1} \delta_w + \frac{\delta_w}{2} \Delta \langle \overline{u} \rangle\right] - \Delta \langle \overline{u} \rangle \frac{\partial y_2}{\partial t}\end{aligned} \tag{A.8}$$

where the assumption $\frac{\partial y_2}{\partial t} \approx \frac{\partial y_1}{\partial t}$ has been made. The first term on the RHS of Equation A.7 is rewritten by using integration by parts and assuming that $\langle \overline{v} \rangle$ is linear inside the jump region. In this region $\langle \overline{v} \rangle$ is approximated as $\left\langle \overline{v(y)} \right\rangle = \langle \overline{v} \rangle_{y_1} + \gamma_3(y - y_1)$, where $\gamma_3 = \frac{\partial \langle \overline{v} \rangle}{\partial y}\big|_{y_1<y<y_2}$. Substituting this relation yields:

$$\begin{aligned}-\int_{y_1}^{y_2} \langle \overline{v} \rangle \frac{\partial \langle \overline{u} \rangle}{\partial y} \, \mathrm{d}y &= -\int_{y_1}^{y_2} \left(\langle \overline{v} \rangle_{y_1} + \gamma_3(y - y_1)\right) \frac{\partial \langle \overline{u} \rangle}{\partial y} \, \mathrm{d}y \\ &= -\left[\left(\langle \overline{v} \rangle_{y_1} + \gamma_3(y - y_1)\right) \langle \overline{u} \rangle\right]_{y_1}^{y_2} + \int_{y_1}^{y_2} \langle \overline{u} \rangle \frac{\partial \langle \overline{v} \rangle}{\partial y} \, \mathrm{d}y \\ &= -\Delta \langle \overline{u} \rangle \langle \overline{v} \rangle_{y_1} - \frac{1}{2}\gamma_3 \delta_w \Delta \langle \overline{u} \rangle\end{aligned} \tag{A.9}$$

where $\Delta \langle \overline{u} \rangle$ is the jump in streamwise velocity over the layer and δ_w is the thickness of the jump region. The second term on the RHS of Equation A.7 yields:

$$-\int_{y_1}^{y_2} \frac{\partial \left\langle \overline{u'v'} \right\rangle}{\partial y} \, \mathrm{d}y = -\left\langle \overline{u'v'} \right\rangle_{y_2} + \left\langle \overline{u'v'} \right\rangle_{y_1} \tag{A.10}$$

Combining the results from Equation A.8 - A.10 into Equation A.7 yields:

$$\delta_w \frac{\partial}{\partial t}\left[\langle \overline{u} \rangle_{y_1} + \frac{1}{2}\Delta \langle \overline{u} \rangle\right] = \left\langle \overline{u'v'} \right\rangle_{y_1} - \left\langle \overline{u'v'} \right\rangle_{y_2} - \Delta \langle \overline{u} \rangle \langle \overline{v} \rangle_{y_1} - \frac{1}{2}\gamma_3 \delta_w \Delta \langle \overline{u} \rangle + \Delta \langle \overline{u} \rangle \frac{\partial y_2}{\partial t} \tag{A.11}$$

A.3 INTEGRATE OVER REGION C

The last integration step is performed on the non-turbulent side over region C, between y_2 and $y_2 + \epsilon$:

$$\int_{y_2}^{y_2+\epsilon} \frac{\partial \langle \overline{u} \rangle}{\partial t} \, \mathrm{d}y = -\int_{y_2}^{y_2+\epsilon} \langle \overline{v} \rangle \frac{\partial \langle \overline{u} \rangle}{\partial y} \, \mathrm{d}y - \int_{y_2}^{y_2+\epsilon} \frac{\partial \left\langle \overline{u'v'} \right\rangle}{\partial y} \, \mathrm{d}y \tag{A.12}$$

Using Leibniz once more for the LHS of Equation A.12 yields:

$$\int_{y_2}^{y_2+\epsilon} \frac{\partial \langle \overline{u} \rangle}{\partial t} \, \mathrm{d}y = \frac{\partial}{\partial t} \left[\langle \overline{u} \rangle_{\delta_i} \epsilon + \Delta \langle \overline{u} \rangle \epsilon + \frac{\epsilon^2}{2} \gamma_2 \right] - \epsilon \gamma_2 \frac{\partial h}{\partial t}, \tag{A.13}$$

where the gradient of the conditional streamwise velocity is given as $\gamma_2 = \frac{\partial \langle \overline{u} \rangle}{\partial y}\big|_{y>y_2}$. Assuming additionally that $\gamma_5 = \frac{\partial \langle \overline{u'v'} \rangle}{\partial y}\big|_{y>y_2}$ is constant in the non-turbulent region, the RHS of Equation A.12 is evaluated as:

$$-\int_{y_2}^{y_2+\epsilon} \langle \overline{v} \rangle \frac{\partial \langle \overline{u} \rangle}{\partial y} \, \mathrm{d}y - \int_{y_2}^{y_2+\epsilon} \frac{\partial \left\langle \overline{u'v'} \right\rangle}{\partial y} \, \mathrm{d}y = -\epsilon \gamma_2 \langle \overline{v} \rangle_{y_2} - \epsilon \gamma_5 \tag{A.14}$$

Substituting A.13 and A.14 into Equation A.12, dividing by ϵ and taking the limit $\epsilon \to 0$ finally yields:

$$\frac{\partial}{\partial t} \left[\langle \overline{u} \rangle_{y_1} + \Delta \langle \overline{u} \rangle \right] = \gamma_2 \left(\frac{\partial y_2}{\partial t} - \langle \overline{v} \rangle_h \right) - \gamma_5 \tag{A.15}$$

A.4 CALCULATING THE GROWTH RATE OF THE BOUNDARY LAYER

In order to determine the growth rate of the boundary layer (BL) different equations derived in the previous sections will be combined. First of all, the LHS of Equation A.11 is rewritten as:

$$\delta_w \frac{\partial}{\partial t} \left[\langle \overline{u} \rangle_{y_1} + \frac{1}{2} \Delta \langle \overline{u} \rangle \right] = \frac{\delta_w}{2} \left[\frac{\partial \langle \overline{u} \rangle_{y_1}}{\partial t} + \frac{\partial \left(\langle \overline{u} \rangle_{y_1} + \Delta \langle \overline{u} \rangle \right)}{\partial t} \right] \tag{A.16}$$

Now Equation A.5 and A.15 can be substituted into Equation A.11 yielding:

$$\frac{\delta_w}{2} \left[\gamma_1 \left(\frac{\partial y_1}{\partial t} - \langle \overline{v} \rangle_{y_1} \right) - \gamma_4 + \gamma_2 \left(\frac{\partial y_2}{\partial t} - \langle \overline{v} \rangle_{y_2} \right) - \gamma_5 \right] = \ldots$$

$$\left\langle \overline{u'v'} \right\rangle_{y_1} - \left\langle \overline{u'v'} \right\rangle_{y_2} - \Delta \langle \overline{u} \rangle \langle \overline{v} \rangle_{y_1} - \frac{1}{2} \gamma_3 \delta_w \Delta \langle \overline{u} \rangle + \Delta \langle \overline{u} \rangle \frac{\partial y_2}{\partial t}, \tag{A.17}$$

rewriting this equation to solve for $\frac{\partial y_2}{\partial t}$ yields:

$$E_b = \frac{1}{\Delta \langle \overline{u} \rangle - \frac{\delta_w}{2}(\gamma_1 + \gamma_2)} \left[-\frac{\delta_w}{2} \left(\gamma_1 \langle \overline{v} \rangle_{y_1} + \gamma_2 \langle \overline{v} \rangle_{y_2} + \gamma_4 + \gamma_5 - \gamma_3 \Delta \langle \overline{u} \rangle \right) - \left\langle \overline{u'v'} \right\rangle_{y_1} + \left\langle \overline{u'v'} \right\rangle_{y_2} + \Delta \langle \overline{u} \rangle \langle \overline{v} \rangle_{y_1} \right], \tag{A.18}$$

where it is assumed that $E_b = \frac{\partial y_2}{\partial t} \approx \frac{\partial y_1}{\partial t}$, i.e. the jump thickness does not change with time. It is good to realize that once the jump thickness decreases to zero, the standard 0^{th} order jump model is retrieved that was originally derived by Lilly [64].

REFERENCES

[1] N. Osseiran and K. Chriscaden, *Air pollution levels rising in many of the world's poorest cities*, 2016. [Online]. Available: http://www.who.int/mediacentre/news/releases/2016/air-pollution-rising/en/ (visited on 07/04/2016).

[2] World Health Organisation, *Air Quality Guidelines, Global Update 2005*. Druckpartner Moser, 2005, p. 496. [Online]. Available: http://www.euro.who.int/en/publications/abstracts/air-quality-guidelines.-global-update-2005.-particulate-matter,-ozone,-nitrogen-dioxide-and-sulfur-dioxide.

[3] T. Jasarevic, G. Thomas, and N. Osseiran, *7 million premature deaths annualy linked to air pollution*, 2014. [Online]. Available: http://www.who.int/mediacentre/news/releases/2014/air-pollution/en/ (visited on 07/04/2016).

[4] Council of the European Union, "Council Directive 1999/30/EC relating to limit values for sulphur dioxide, nitrogen dioxide and oxides of nitrogen, particulate matter and lead in ambient air," *Off. J. Eur. Comm.*, vol. 163, no. 9, pp. 41–60, 1999.

[5] J. Cramer, *Nationaal Samenwerkingsprogramma Luchtkwaliteit (NSL)*. 2009. [Online]. Available: https://www.rijksoverheid.nl/onderwerpen/luchtkwaliteit/documenten/brochures/2011/01/03/nationaal-samenwerkingsprogramma-luchtkwaliteit.

[6] N. S. Holmes and L. Morawska, "A review of dispersion modelling and its application to the dispersion of particles: An overview of different dispersion models available," *Atmos. Environ.*, vol. 40, no. 30, pp. 5902–5928, 2006.

[7] S. Vardoulakis, B. E. Fisher, K. Pericleous, and N. Gonzalez-Flesca, "Modelling air quality in street canyons: a review," *Atmos. Environ.*, vol. 37, no. 2, pp. 155–182, 2003.

[8] Projectgroep Revisie Nationaal Model, *Het Nieuwe Nationaal Model*, 2002nd ed., InfoMil, Ed. Den Haag: TNO Milieu, Energie en Procesinnovatie, 1998.

[9] R. E. Britter and S. R. Hanna, "Flow and Dispersion in Urban Areas," *Annu. Rev. Fluid Mech.*, vol. 35, pp. 469–496, 2003.

[10] R. Berkowicz, "OSPM - a parameterised street pollution model," *Environ. Monit. Assess.*, vol. 65, pp. 323–331, 2000.

[11] L. Soulhac, P. Salizzoni, F.-X. Cierco, and R. Perkins, "The model SIRANE for atmospheric urban pollutant dispersion; part I, presentation of the model," *Atmos. Environ.*, vol. 45, no. 39, pp. 7379–7395, 2011.

[12] M. J. Barnes, T. K. Brade, A. R. Mackenzie, J. D. Whyatt, D. J. Carruthers, J. Stocker, X. Cai, and C. N. Hewitt, "Spatially-varying surface roughness and ground-level air quality in an operational dispersion model," *Environ. Pollut.*, vol. 185, pp. 44–51, 2014.

[13] S. E. Belcher, "Mixing and transport in urban areas.," *Philos. Trans. A. Math. Phys. Eng. Sci.*, vol. 363, no. 1837, pp. 2947–68, 2005.

[14] X. I. A. Yang, J. Sadique, R. Mittal, and C. Meneveau, "Exponential roughness layer and analytical model for turbulent boundary layer flow over rectangular-prism roughness elements," *J. Fluid Mech.*, vol. 789, pp. 127–165, 2016.

[15] M. Gordon, R. M. Staebler, J. Liggio, S.-M. Li, J. Wentzell, G. Lu, P. Lee, and J. R. Brook, "Measured and modeled variation in pollutant concentration near roadways," *Atmos. Environ.*, vol. 57, pp. 138–145, 2012.

[16] P. M. Klein and J. M. Galvez, "Flow and turbulence characteristics in a suburban street canyon," *Environ. Fluid Mech.*, 2014.

[17] M. W. Rotach, "Profiles of turbulence statistics in and above an urban street canyon," *Atmos. Environ.*, vol. 29, no. 13, pp. 1473–1486, 1995.

[18] R. E. Britter, S. Di Sabatino, F. Caton, K. M. Cooke, P. G. Simmonds, and G. Nickless, "Results from three field tracer experiments on the neighbourhood scale in the city of Birmingham UK," *Urban Air Qual. - Recent Adv. Proc.*, pp. 79–90, 2002.

[19] I. Marusic, R. Mathis, and N. Hutchins, "Predictive model for wall-bounded turbulent flow.," *Science (80-.).*, vol. 329, no. 5988, pp. 193–196, 2010.

[20] J. F. Barlow, "Progress in observing and modelling the urban boundary layer," *Urban Clim.*, vol. 10, no. P2, pp. 216–240, 2014.

[21] I. Marusic, B. J. McKeon, P. A. Monkewitz, H. M. Nagib, A. J. Smits, and K. R. Sreenivasan, "Wall-bounded turbulent flows at high Reynolds numbers: Recent advances and key issues," *Phys. Fluids*, vol. 22, no. 065103, 2010.

[22] C. D. Meinhart and R. J. Adrian, "On the existence boundary layer of uniform momentum zones in a turbulent boundary layer," *Phys. Fluids*, vol. 7, no. 4, pp. 694–696, 1995.

[23] S. C. Morris, S. R. Stolpa, P. E. Slaboch, and J. C. Klewicki, "Near-surface particle image velocimetry measurements in a transitionally rough-wall atmospheric boundary layer," *J. Fluid Mech.*, vol. 580, pp. 319–338, 2007.

[24] T. Michioka, H. Takimoto, and A. Sato, "Large-Eddy Simulation of Pollutant Removal from a Three-Dimensional Street Canyon," *Boundary-Layer Meteorol.*, vol. 150, no. 2, pp. 259–275, 2014.

[25] O. Coceal and S. E. Belcher, "A canopy model of mean winds through urban areas," *Q. J. R. Meteorol. Soc.*, vol. 130, no. 599, pp. 1349–1372, 2004.

[26] J. Eisma, J. Westerweel, G. Ooms, and G. E. Elsinga, "Interfaces and internal layers in a turbulent boundary layer," *Phys. Fluids*, vol. 27, no. 055103, 2015.

[27] S. Corssin and A. L. Kistler, "Free-stream boundaries of turbulent flows," *NACA Tech. Note*, vol. 1244, pp. 1033–1064, 1955.

[28] J. C. R. Hunt, I. Eames, C. B. da Silva, and J. Westerweel, "Interfaces and inhomogeneous turbulence.," *Phil. Trans. R. Soc. A*, vol. 369, no. 1937, pp. 811–832, 2011.

[29] J. Westerweel, C. Fukushima, J. M. Pedersen, and J. C. R. Hunt, "Momentum and scalar transport at the turbulent/non-turbulent interface of a jet," *J. Fluid Mech.*, vol. 631, no. 2009, pp. 199–229, 2009.

[30] T. Ishihara, T. Gotoh, and Y. Kaneda, "Study of high Reynolds number isotropic turbulence by direct numerical simulation," *Annu. Rev. Fluid Mech.*, vol. 41, no. 1, pp. 165–180, 2009.

[31] J. Westerweel, C. Fukushima, J. M. Pedersen, and J. C. R. Hunt, "Mechanics of the Turbulent-Nonturbulent Interface of a Jet," *Phys. Rev. Lett.*, vol. 95, no. 174501, 2005.

[32] T. Ishihara, Y. Kaneda, and J. Hunt, "Thin shear layers in high Reynolds number turbulence - DNS results," *Flow, Turbul. and Combust.*, vol. 91, no. 4, pp. 895–929, 2013.

[33] C. B. da Silva and R. R. Taveira, "The thickness of the turbulent / nonturbulent interface is equal to the radius of the large vorticity structures near the edge of the shear layer," *Phys. Fluids*, vol. 22, no. 121702, pp. 1–4, 2010.

[34] M. Holzner, A. Liberzon, M. Guala, A. Tsinober, and W. Kinzelbach, "Generalized detection of a turbulent front generated by an oscillating grid," *Exp. Fluids*, vol. 41, no. 5, pp. 711–719, 2006.

[35] M. Holzner, A. Liberzon, N. Nikitin, W. Kinzelbach, and A. Tsinober, "Small-scale aspects of flows in proximity of the turbulent/nonturbulent interface," *Phys. Fluids*, vol. 19, no. 071702, 2007.

[36] C. B. da Silva, J. C. R. Hunt, I. Eames, and J. Westerweel, "Interfacial layers between regions of different turbulence intensity," *Annu. Rev. Fluid Mech.*, vol. 46, no. 1, pp. 567–590, 2014.

[37] M. van Reeuwijk and M. Holzner, "The turbulence boundary of a temporal jet," *J. Fluid Mech.*, vol. 739, pp. 254–275, 2013.

[38] K. Chauhan, J. Philip, C. M. de Silva, N. Hutchins, and I. Marusic, "The turbulent/non-turbulent interface and entrainment in a boundary layer," *J. Fluid Mech.*, vol. 742, pp. 119–151, 2014.

[39] T. Ishihara, H. Ogasawara, and J. C. Hunt, "Analysis of conditional statistics obtained near the turbulent/non-turbulent interface of turbulent boundary layers," *J. Fluid Struct.*, vol. 53, no. February 2015, pp. 50–57, 2014.

[40] M. Iovieno, S. Di Savino, L. Gallana, and D. Tordella, "Mixing of a passive scalar across a thin shearless layer: concentration of intermittency on the sides of the turbulent interface," *J. Turb.*, vol. 15, no. 5, pp. 311–334, 2014.

[41] S. K. Robinson, "Coherent motions in the turbulent boundary layer," *Annu. Rev. Fluid Mech.*, vol. 23, no. 1, pp. 601–639, 1991.

[42] R. F. Blackwelder and L. S. G. Kovasznay, "Time scales and correlations in a turbulent boundary layer," *Phys. Fluids*, vol. 15, no. 9, pp. 1545–1554, 1972.

[43] R. J. Adrian, C. D. Meinhart, and C. D. Tomkins, "Vortex organization in the outer region of the turbulent boundary layer," *J. Fluid Mech.*, vol. 422, pp. 1–54, 2000.

[44] N. Hutchins and I. Marusic, "Evidence of very long meandering features in the logarithmic region of turbulent boundary layers," *J. Fluid Mech.*, vol. 579, pp. 1–28, 2007.

[45] W. T. Hambleton, N. Hutchins, and I. Marusic, "Simultaneous orthogonal-plane particle image velocimetry measurements in a turbulent boundary layer," *J. Fluid Mech.*, vol. 560, no. 2006, pp. 53–64, 2006.

[46] B. Ganapathisubramani, E. K. Longmire, and I. Marusic, "Characteristics of vortex packets in turbulent boundary layers," *J. Fluid Mech.*, vol. 478, pp. 35–46, 2003.

[47] K. T. Christensen and R. J. Adrian, "Statistical evidence of hairpin vortex packets in wall turbulence," *J. Fluid Mech.*, vol. 431, pp. 433–443, 2001.

[48] G. E. Elsinga and I. Marusic, "Universal aspects of small-scale motions in turbulence," *J. Fluid Mech.*, vol. 662, pp. 514–539, 2010.

[49] L. Wei, G. E. Elsinga, G. Brethouwer, P. Schlatter, and A. V. Johansson, "Universality and scaling phenomenology of small-scale turbulence in wall-bounded flows," *Phys. Fluids*, vol. 26, no. 035107, 2014.

[50] M. Stanislas, L. Perret, and J. Foucaut, "Vortical structures in the turbulent boundary layer: a possible route to a universal representation," *J. Fluid Mech.*, vol. 602, pp. 327–382, 2008.

[51] J. Westerweel and F. Scarano, "Universal outlier detection for PIV data," *Exp. Fluids*, vol. 39, no. 6, pp. 1096–1100, 2005.

[52] C. Poelma, J. Westerweel, and G. Ooms, "Turbulence statistics from optical whole-field measurements in particle-laden turbulence," *Exp. Fluids*, vol. 40, no. 3, pp. 347–363, 2005.

[53] P. S. Klebanoff, "Characteristics of Turbulence in a Boundary Layer with Zero Pressure Gradient," *NACA Tech. notes*, vol. 1247, pp. 1135–1153, 1954.

[54] A. Schröder, R. Geisler, K. Staack, G. E. Elsinga, F. Scarano, B. Wieneke, A. Henning, C. Poelma, and J. Westerweel, "Eulerian and Lagrangian views of a turbulent boundary layer flow using time-resolved tomographic PIV," *Exp. Fluids*, vol. 50, no. 4, pp. 1071–1091, 2010.

[55] P. Joshi, X. Liu, and J. Katz, "Effect of mean and fluctuating pressure gradients on boundary layer turbulence," *J. Fluid Mech.*, vol. 748, pp. 36–84, 2014.

[56] D. B. DeGraaff and J. K. Eaton, "Reynolds-number scaling of the flat-plate turbulent boundary layer," *J. Fluid Mech.*, vol. 422, pp. 319–346, 2000.

[57] D. K. Bisset, J. C. R. Hunt, and M. M. Rogers, "The turbulent/non-turbulent interface bounding a far wake," *J. Fluid Mech.*, vol. 451, pp. 383–410, 2002.

[58] J. M. Foucaut and M. Stanislas, "Some considerations on the accuracy and frequency response of some derivative filters applied to particle image velocimetry vector fields," *Meas. Sci. Technol.*, vol. 13, pp. 1058–1071, 2002.

[59] V. Kolár, "Vortex identification: New requirements and limitations," *Int. J. Heat Fluid Flow*, vol. 28, no. 4, pp. 638–652, 2007.

[60] Y. Maciel, M. Robitaille, and S. Rahgozar, "A method for characterizing cross-sections of vortices in turbulent flows," *Int. J. Heat Fluid Flow*, vol. 37, pp. 177–188, 2012.

[61] J. S. Turner, "Turbulent entrainment: the development of the entrainment assumption, and its application to geophysical flows," *J. Fluid Mech.*, vol. 173, pp. 431–471, 1986.

[62] M. C. VanZanten, P. G. Duynkerke, and J. W. M. Cuijpers, "Entrainment parameterization in convective boundary layers," *J. Atmos. Sci.*, vol. 56, no. 6, pp. 813–828, 1999.

[63] D. Pino, J. Vila-Guerau de Arellano, and S. Kim, "Representing sheared convective boundary layer by zeroth- and first-order-jump mixed-layer models : large-eddy simulation verification," *J. Appl. Met. Clim.*, vol. 45, pp. 1224–1243, 2006.

[64] D. K. Lilly, "Cloud-topped mixed layers under a strong inversion," *Q. J. Roy. Meteor. Soc.*, vol. 94, no. 401, pp. 292–309, 1968.

[65] O. M. Phillips, "The irrotational motion outside a free turbulent boundary," *Math. Proc. Camb. Phil. Soc.*, vol. 51, no. 01, pp. 220–229, 1954.

[66] F. M. White, *Viscous fluid flow*. McGraw-Hill Higher Education, 2006.

[67] G. Borrell, J. A. Sillero, and J. Jiménez, "A code for direct numerical simulation of turbulent boundary layers at high Reynolds numbers in BG/P supercomputers," *Comput. Fluids*, vol. 80, pp. 37–43, 2013.

[68] G. E. Elsinga, C. Poelma, A. Schröder, R. Geisler, F. Scarano, and J. Westerweel, "Tracking of vortices in a turbulent boundary layer," *J. Fluid Mech.*, vol. 697, pp. 273–295, 2012.

[69] S. Zheng and E. K. Longmire, "Perturbing vortex packets in a turbulent boundary layer," *J. Fluid Mech.*, vol. 748, pp. 368–398, 2014.

[70] D. J. C. Dennis and T. B. Nickels, "On the limitations of Taylor's hypothesis in constructing long structures in a turbulent boundary layer," *J. Fluid Mech.*, vol. 614, pp. 197–206, 2008.

[71] M. R. Head and P. Bandyopadhyay, "New aspects of turbulent boundary-layer structure," *J. Fluid Mech.*, vol. 107, pp. 297–338, 1981.

[72] J. Eisma, J. Westerweel, and G. E. Elsinga, "Simultaneous scanning tomo-PIV and LIF in a turbulent boundary layer: The role of internal shear layers in the dispersion of a passive scalar," in *11th Int. Symp. Part. Image Velocim.*, Santa Barbara, 2015, pp. 1–10.

[73] N. Hutchins, K. Chauhan, I. Marusic, J. Monty, and J. Klewicki, "Towards Reconciling the Large-Scale Structure of Turbulent Boundary Layers in the Atmosphere and Laboratory," *Boundary-Layer Meteorol.*, vol. 145, pp. 273–306, 2012.

[74] T. Michioka and A. Sato, "Effect of Incoming Turbulent Structure on Pollutant Removal from Two-Dimensional Street Canyon," *Boundary-Layer Meteorol.*, vol. 145, no. 3, pp. 469–484, 2012.

[75] L. Perret and E. Savory, "Large-Scale Structures over a Single Street Canyon Immersed in an Urban-Type Boundary Layer," *Boundary-Layer Meteorol.*, vol. 148, no. 1, pp. 111–131, 2013.

[76] C. Brücker, D. Hess, and J. Kitzhofer, "Single-view volumetric PIV via high-resolution scanning, isotropic voxel restructuring and 3D least-squares matching (3D-LSM)," *Meas. Sci. Technol.*, vol. 24, no. 024001, 2013.

[77] T. A. Casey, J. Sakakibara, and S. T. Thoroddsen, "Scanning tomographic particle image velocimetry applied to a turbulent jet," *Phys. Fluids*, vol. 25, no. 025102, 2013.

[78] B. R. Halls, D. J. Thul, D. Michaelis, S. Roy, T. R. Meyer, and J. R. Gord, "Single-shot, volumetrically illuminated, three-dimensional, tomographic laser-induced-fluorescence imaging in a gaseous free jet," *Opt. Express*, vol. 24, no. 9, pp. 10 040–10 049, 2016.

[79] J. Westerweel, T. Hofmann, C. Fukushima, and J. C. R. Hunt, "Experimental investigation of the turbulent/non-turbulent interface at the outer boundary of a self-similar turbulent jet," *Exp. Fluids*, vol. 33, pp. 873–878, 2002.

[80] K. Hishida and J. Sakakibara, "Combined planar laser-induced fluorescence-particle image velocimetry technique for velocity and temperature fields," *Exp. Fluids*, vol. 29, no. 7, S129–S140, 2000.

[81] C. Vanderwel and S. Tavoularis, "Scalar dispersion by coherent structures in uniformly sheared flow generated in a water tunnel," *J. Turbul.*, vol. 17, no. 7, pp. 633–650, 2016.

[82] J. Westerweel, G. E. Elsinga, and R. J. Adrian, "Particle Image Velocimetry for Complex and Turbulent Flows," *Annu. Rev. Fluid Mech.*, vol. 45, no. 1, pp. 409–436, 2013.

[83] B. Wieneke, "Stereo-PIV using self-calibration on particle images," *Exp. Fluids*, vol. 39, no. 2, pp. 267–280, 2005.

[84] G. E. Elsinga, F. Scarano, B. Wieneke, and B. W. Oudheusden, "Tomographic particle image velocimetry," *Exp. Fluids*, vol. 41, no. 6, pp. 933–947, 2006.

[85] G. E. Elsinga, R. J. Adrian, B. W. Van Oudheusden, and F. Scarano, "Three-dimensional vortex organization in a high-Reynolds-number supersonic turbulent boundary layer," *J. Fluid Mech.*, vol. 644, pp. 35–60, 2010.

[86] J. P. Crimaldi, "Planar laser induced fluorescence in aqueous flows," *Exp. Fluids*, vol. 44, no. 6, pp. 851–863, 2008.

[87] G. Eitel-Amor, R. Örlü, and P. Schlatter, "Simulation and validation of a spatially evolving turbulent boundary layer up to," *Int. J. Heat Fluid Flow*, vol. 47, pp. 57–69, 2014.

[88] F. H. Clauser, "The Turbulent Boundary Layer," *Adv. Appl. Mech.*, vol. 4, pp. 1–51, 1956.

[89] A. Schröder, R. Geisler, K. Staack, B. Wieneke, G. E. Elsinga, F. Scarano, and A. Henning, "Lagrangian and Eulerian views into a turbulent boundary layer flow using time-resolved tomographic PIV," in *14th Int. Symp. Appl. Laser Tech. to Fluid Mech.*, Lisbon, 2008, pp. 1–14.

[90] Y. Jodai and G. E. Elsinga, "Experimental observation of hairpin auto-generation events in a turbulent boundary layer," *J. Fluid Mech.*, vol. 795, pp. 611–633, 2016.

[91] M. Khashehchi, G. E. Elsinga, A. Ooi, J. Soria, and I. Marusic, "Studying invariants of the velocity gradient tensor of a round turbulent jet across the turbulent / nonturbulent interface using Tomo-PIV," in *15th Int. Symp. Appl. Laser Tech. to Fluid Mech.*, Lisbon, 2010, pp. 1–12.

[92] J. Zhang, B. Tao, and J. Katz, "Turbulent flow measurement in a square duct with hybrid holographic PIV," *Exp. Fluids*, vol. 23, no. 5, pp. 373–381, 1997.

[93] D. Krug, M. Holzner, B. Lüthi, M. Wolf, A. Tsinober, and W. Kinzelbach, "A combined scanning PTV/LIF technique to simultaneously measure the full velocity gradient tensor and the 3D density field," *Meas. Sci. Technol.*, vol. 25, no. 065301, 2014.

[94] B. Münch, P. Trtik, F. Marone, and M. Stampanoni, "Stripe and ring artifact removal with combined wavelet–Fourier filtering.," *Opt. Express*, vol. 17, no. 10, pp. 8567–91, 2009.

[95] C. M. de Silva, N. Hutchins, and I. Marusic, "Uniform momentum zones in turbulent boundary layers," *J. Fluid Mech.*, vol. 786, pp. 309–331, 2016.

[96] J. M. Tomas, H. Eisma, M. J. B. M. Pourquie, G. E. Elsinga, H. J. J. Jonker, and J. Westerweel, "Pollutant Dispersion in Boundary Layers Exposed to Rural-to-Urban Transitions : Varying the Spanwise Length Scale of the Roughness," *Boundary-Layer Meteorol.*, vol. submitted, 2016.

[97] H. E. Eisma, J. M. Tomas, M. B. J. M. Pourquie, G. E. Elsinga, H. J. J. Jonker, and J. Westerweel, "Effects of a 2D fence on Pollutant Dispersion in Boundary Layers Exposed to Rural-to-Urban Transitions," *(in Prep.*,

[98] H. Cheng and I. P. Castro, "Near wall flow over urban-like roughness," *Boundary-Layer Meteorol.*, vol. 104, pp. 229–259, 2002.

[99] O. Coceal, T. G. Thomas, I. P. Castro, and S. E. Belcher, "Mean Flow and Turbulence Statistics Over Groups of Urban-like Cubical Obstacles," *Boundary-Layer Meteorol.*, vol. 121, no. 3, pp. 491–519, 2006.

[100] V. B. L. Boppana, Z.-T. Xie, and I. P. Castro, "Thermal Stratification Effects on Flow Over a Generic Urban Canopy," *Boundary-Layer Meteorol.*, vol. 153, pp. 141–162, 2014.

[101] J. H. Lee, H. J. Sung, and P. Å. Krogstad, "Direct numerical simulation of the turbulent boundary layer over a cube-roughened wall," *J. Fluid Mech.*, vol. 669, pp. 397–431, 2011.

[102] W.-C. Cheng and F. Porté-Agel, "Adjustment of Turbulent Boundary-Layer Flow to Idealized Urban Surfaces: A Large-Eddy Simulation Study," *Boundary-Layer Meteorol.*, vol. 155, no. 2, pp. 249–270, 2015.

[103] H. Cheng and I. P. Castro, "Near-wall flow development after a step change in surface roughness," *Boundary-Layer Meteorol.*, vol. 105, pp. 411–432, 2002.

[104] J. M. Tomas, M. J. B. M. Pourquie, and H. J. J. Jonker, "The influence of an obstacle on flow and pollutant dispersion in neutral and stable boundary layers," *Atmos. Environ.*, vol. 113, pp. 236–246, 2015.

[105] T. Michioka, A. Sato, and K. Sada, "Wind-Tunnel Experiments for Gas Dispersion in an Atmospheric Boundary Layer with Large-Scale Turbulent Motion," *Boundary-Layer Meteorol.*, vol. 141, pp. 35–51, 2011.

[106] J.-Y. Vinçont, S. Simoëns, M. Ayrault, and J. M. Wallace, "Passive scalar dispersion in a turbulent boundary layer from a line source at the wall and downstream of an obstacle," *J. Fluid Mech.*, vol. 424, pp. 127–167, 2000.

[107] J. M. Tomas, M. J. B. M. Pourquie, and H. J. J. Jonker, "Stable Stratification Effects on Flow and Pollutant Dispersion in Boundary Layers Entering a Generic Urban Environment," *Boundary-Layer Meteorol.*, vol. 159, no. 2, pp. 221–239, 2016.

[108] T. R. Oke, "Street design and urban canopy layer climate," *Energy Build.*, vol. 11, pp. 103–113, 1988.

[109] T. Heus, C. C. Van Heerwaarden, H. J. J. Jonker, *et al.*, "Formulation of the Dutch Atmospheric Large-Eddy Simulation (DALES) and overview of its applications," *Geosci. Model Dev.*, vol. 3, no. 2, pp. 415–444, 2010.

[110] M. Pourquie, W. P. Breugem, and B. J. Boersma, "Some Issues Related to the Use of Immersed Boundary Methods to Represent Square Obstacles," *Int. J. Multiscale Comput. Eng.*, vol. 7, no. 6, pp. 509–522, 2009.

[111] A. W. Vreman, "An eddy-viscosity subgrid-scale model for turbulent shear flow: Algebraic theory and applications," *Phys. Fluids*, vol. 16, no. 10, pp. 3670–3681, 2004.

[112] J. Smagorinsky, "General Circulation Experiments With the Primitive Equations," *Mon. Weather Rev.*, vol. 91, no. 3, pp. 99–164, 1963.

[113] D. K. Lilly, "On the numerical simulation of buoyant convection," *Tellus*, vol. 14, no. 2, pp. 148–172, 1962.

[114] W. Hundsdorfer, B. Koren, M. van Loon, and J. G. Verwer, "A positive finite-difference advection scheme," *J. Comput. Phys.*, vol. 117, pp. 35–46, 1995.

[115] H. J. J. Jonker, M. van Reeuwijk, P. P. Sullivan, and E. G. Patton, "On the scaling of shear-driven entrainment: a DNS study," *J. Fluid Mech.*, vol. 732, pp. 150–165, 2013.

[116] J. M. Tomas, M. J. B. M. Pourquie, H. Eisma, G. E. Elsinga, H. J. J. Jonker, and J. Westerweel, "Pollutant Dispersion in the Urban Boundary Layer," in *Direct Large-Eddy Simul. IX*, J. Frohlich, H. Kuerten, B. Geurts, and V. Armenio, Eds., vol. 1, Springer, 2015, pp. 435–441.

[117] T. S. Lund, X. Wu, and K. D. Squires, "On the Generation of Turbulent Inflow Conditions for Boundary Layer Simulations," *J. Comput. Phys.*, vol. 140, no. 2, pp. 233–258, 1998.

[118] I. P. Castro, "Relaxing wakes behind surface-mounted obstacles in rough wall boundary layers," *J. Fluid Mech.*, vol. 93, no. 04, pp. 631–659, 1979.

[119] K. Blackman, L. Perret, and E. Savory, "Effect of upstream flow regime on street canyon flow mean turbulence statistics," *Environ. Fluid Mech.*, vol. 15, no. 4, pp. 823–849, 2015.

[120] H. P. A. H. Irwin, "The design of spires for wind simulation," *J. Wind Eng. Ind. Aerodyn.*, vol. 7, pp. 361–366, 1981.

[121] J. Counihan, "An improved method of simulating an atmospheric boundary layer in a wind tunnel," *Atmos. Environ.*, vol. 3, pp. 197–214, 1969.

[122] H. E. Cekli and W. V. D. Water, "Tailoring turbulence with an active grid," *Exp. Fluids*, vol. 49, pp. 409–416, 2010.

[123] N. Cook, "Wind-tunnel simulation of the adiabatic atmospheric boundary layer by roughness, barrier and mixing-device methods," *J. Wind Eng. Ind. Aerodyn.*, vol. 3, pp. 157–176, 1978.

[124] J. E. Cermak and S. P. S. Arya, "Problems of atmospheric shear flows and their laboratory simulation," *Boundary-Layer Meteorol.*, vol. 1, pp. 40–60, 1970.

[125] J. M. Osterlund, "Experimental Studies of Zero Pressure-Gradient Turbulent Boundary Layer Flow," PhD thesis, Royal Institute of Technology Stockholm, 1999.

[126] M. R. Raupach, R. a. Antonia, and S. Rajagopalan, "Rough-Wall Turbulent Boundary Layers," *Appl. Mech. Rev.*, vol. 44, no. 1, p. 1, 1991.

[127] R. N. Meroney, M. Pavageau, S. Rafailidis, and M. Schatzmann, "Study of line source characteristics for 2-D physical modelling of pollutant dispersion in street canyons," *J. Wind Eng. Ind. Aerodyn.*, vol. 62, pp. 37–56, 1996.

[128] C. W. H. van Doorne, "Stereoscopic PIV on transition in pipe flow," PhD Thesis, Delft University of Technology, 2004. [Online]. Available: www.ahd.tudelft.nl.

[129] A. K. Prasad and K. Jensen, "Scheimpflug stereocamera for particle image velocimetry in liquid flows.," *Appl. Opt.*, vol. 34, no. 30, pp. 7092–9, 1995.

[130] O. Reynolds, "An Experimental Investigation of the Circumstances Which Determine Whether the Motion of Water Shall Be Direct or Sinuous, and of the Law of Resistance in Parallel Channels," *Philos. Trans. R. Soc. London*, vol. 174, pp. 935–982, 1883.

[131] L. A. Melton and C. W. Lipp, "Criteria for quantitative PLIF experiments using high-power lasers," *Exp. Fluids*, vol. 35, no. 4, pp. 310–316, 2003.

[132] C. Vanderwel and S. Tavoularis, "On the accuracy of PLIF measurements in slender plumes," *Exp. Fluids*, vol. 55, no. 1801, pp. 1–18, 2014.

[133] P. L. Smart and I. M. S. Laidlaw, "An evaluation of some fluorescent dyes for water tracing," *Water Resour. Res.*, vol. 13, no. 1, pp. 15–33, 1977.

[134] D. A. Donzis, K. R. Sreenivasan, and P. K. Yeung, "The batchelor spectrum for mixing of passive scalars in isotropic turbulence: Submitted for the special issue dedicated to S. B. Pope," *Flow, Turbul. Combust.*, vol. 85, pp. 549–566, 2010.

[135] A. Obukhov, "Structure of the temperature field in a turbulent flow," *Dokl. Akad. Nauk. SSSR*, vol. 13, no. 1, pp. 58–69, 1949.

[136] S. Corrsin, "On the spectrum of isotropic temperature fluctuations in an isotropic turbulence," *J. Appl. Phys.*, vol. 22, no. 4, pp. 469–473, 1951.

[137] G. K. Batchelor, "Small-scale variation of convected quantities like temperature in turbulent fluid Part 1. General discussion and the case of small conductivity," *J. Fluid Mech.*, vol. 5, pp. 113–133, 1959.

[138] Z. Warhaft, "Passive Scalars in Turbulent Flows," *Annu. Rev. Fluid Mech.*, vol. 32, pp. 203–240, 2000.

[139] D. A. Walker, "A fluorescence technique for measurement of concentration in mixing liquids," *J. Phys. E.*, vol. 20, pp. 217–224, 1987.

[140] F. Scarano, "Theory of non-isotropic spatial resolution in PIV," *Exp. Fluids*, vol. 35, no. 3, pp. 268–277, 2003.

[141] R. T. Reynolds and I. P. Castro, "Measurements in an urban-type boundary layer," *Exp. Fluids*, vol. 45, no. 1, pp. 141–156, 2008.

[142] T. Michioka, A. Sato, H. Takimoto, and M. Kanda, "Large-Eddy Simulation for the Mechanism of Pollutant Removal from a Two-Dimensional Street Canyon," *Boundary-Layer Meteorol.*, vol. 138, no. 2, pp. 195–213, 2010.

[143] R. J. Adrian and P. Moin, "Stochastic estimation of organized turbulent structure: homogeneous shear flow," *J. Fluid Mech.*, vol. 190, pp. 531–559, 1988.

[144] W. H. Snyder and I. P. Castro, "The critical Reynolds number for rough-wall boundary layers," *J. Wind Eng. Ind. Aerodyn.*, vol. 90, no. 1, pp. 41–54, 2002.

[145] J. Counihan, J. C. R. Hunt, and P. S. Jackson, "Wakes behind two-dimensional surface obstacles in turbulent boundary layers," *J. Fluid Mech.*, vol. 64, no. 3, pp. 529–563, 1974.

[146] J. M. Wallace, "Quadrant Analysis in Turbulence Research: History and Evolution," *Annu. Rev. Fluid Mech.*, vol. 48, no. 1, pp. 131–158, 2016.

[147] S. S. Lu and W. W. Willmarth, "Measurements of the structure of the Reynolds stress in a turbulent boundary layer," *J. Fluid Mech.*, vol. 60, p. 481, 1973.

[148] I. P. Castro, H. Cheng, and R. Reynolds, "Turbulence Over Urban-type Roughness: Deductions from Wind-tunnel Measurements," *Boundary-Layer Meteorol.*, vol. 118, no. 1, pp. 109–131, 2006.

[149] O. Coceal, A. Dobre, T. G. Thomas, and S. E. Belcher, "Structure of turbulent flow over regular arrays of cubical roughness," *J. Fluid Mech.*, vol. 589, pp. 375–409, 2007.

[150] P.-Å. Krogstad, H. I. Andersson, O. M. Bakken, and A. Ashrafian, "An experimental and numerical study of channel flow with rough walls," *J. Fluid Mech.*, vol. 530, no. 2005, pp. 327–52, 2005.

[151] P. Krogstadt and R. Antonia, "Surface roughness effects in turbulent boundary layers," *Exp. Fluids*, vol. 27, no. 5, pp. 450–460, 1999.

[152] J. Boussinesq, "Essai sur la théorie des eaux courantes, Mémoires présentés par divers savants à l'Académie des Sciences," *Impremerie Natl.*, vol. XXIII, no. 1, I. Nationale, Ed., pp. 1–680, 1877.

[153] L. Prandtl, "Bericht über Untersuchungen zur ausgebildeten Turbulenz," *Z. Angew. Math. Mech.*, vol. 5, pp. 136–139, 1925.

[154] R. W. Macdonald, "Modelling the mean velocity profile in the urban canopy layer," *Boundary-Layer Meteorol.*, vol. 97, pp. 25–45, 2000.

[155] S. Belcher, N. Jerram, and J. Hunt, "Adjustment of a turbulent boundary layer to a 'canopy' of roughness elements," *J. Fluid Mech.*, vol. 488, pp. 369–398, 2003.

[156] S. E. Belcher, N. Jerram, and J. C. R. Hunt, "Adjustment of a turbulent boundary layer to a canopy of roughness elements," *J. Fluid Mech.*, vol. 488, pp. 369–398, 2003.

[157] M. R. Raupach, J. J. Finnigan, and Y. Brunei, "Coherent eddies and turbulence in vegetation canopies: The mixing-layer analogy," *Boundary-Layer Meteorol.*, vol. 78, no. 3-4, pp. 351–382, 1996.

[158] J. S. Weitzman, L. C. Samuel, A. E. Craig, R. B. Zeller, S. G. Monismith, and J. R. Koseff, "On the use of refractive-index-matched hydrogel for fluid velocity measurement within and around geometrically complex solid obstructions," *Exp. Fluids*, vol. 55, no. 1862, pp. 1–12, 2014.

[159] P. Knebel, A. Kittel, and J. Peinke, "Atmospheric wind field conditions generated by active grids," *Exp. Fluids*, vol. 51, no. 2, pp. 471–481, 2011.

[160] E. Savory, L. Perret, and C. Rivet, "Modelling considerations for examining the mean and unsteady flow in a simple urban-type street canyon," *Meteorol. Atmos. Phys.*, vol. 121, no. 1-2, pp. 1–16, 2013.

[161] R. B. Stull, *An Introduction to Boundary Layer Meteorology*, 1st ed. Kluwer Academic Publishers, 1988, pp. XIV, 670.

[162] Z. Xie and I. P. Castro, "LES and RANS for turbulent flow over arrays of wall-mounted obstacles," *Flow, Turbul. Combust.*, vol. 76, no. 3, pp. 291–312, 2006.

[163] Z.-T. Xie and I. P. Castro, "Large-eddy simulation for flow and dispersion in urban streets," *Atmos. Environ.*, vol. 43, no. 13, pp. 2174–2185, 2009.

[164] P. Gousseau, B. Blocken, T. Stathopoulos, and G. J. F. van Heijst, "CFD simulation of near-field pollutant dispersion on a high-resolution grid: A case study by LES and RANS for a building group in downtown Montreal," *Atmos. Environ.*, vol. 45, no. 2, pp. 428–438, 2011.

[165] B. Blocken, "Computational Fluid Dynamics for urban physics: Importance, scales, possibilities, limitations and ten tips and tricks towards accurate and reliable simulations," *Build. Environ.*, vol. 91, pp. 219–245, 2015.

[166] M. G. Giometto, A. Christen, C. Meneveau, J. Fang, M. Krafczyk, and M. B. Parlange, "Spatial Characteristics of Roughness Sublayer Mean Flow and Turbulence Over a Realistic Urban Surface," *Boundary-Layer Meteorol.*, 2016.

[167] G. Berkooz, P. Holmes, and J. L. Lumley, "The Proper Orthogonal Decomposition in the Analysis of Turbulent Flows," *Annu. Rev. Fluid Mech.*, vol. 25, pp. 539–575, 1993.

[168] S. E. Hommema and R. J. Adrian, "Packet Structure of Surface Eddies in the Atmospheric Boundary Layer," *Boundary-Layer Meteorol.*, vol. 106, pp. 147–170, 2003.

[169] A. Inagaki and M. Kanda, "Organized Structure of Active Turbulence Over an Array of Cubes within the Logarithmic Layer of Atmospheric Flow," *Boundary-Layer Meteorol.*, vol. 135, no. 2, pp. 209–228, 2010.

ACKNOWLEDGEMENTS

Deze thesis markeert het einde van vier jaar onderzoek in het Laboratory for Aero- and Hydrodynamics op de Technische Universiteit Delft. De droge tekst in wetenschappelijke artikelen (en ook in deze thesis) verbergt op vakkundige wijze de vele inspanningen die er geleverd zijn om dit werk tot stand te brengen. Ik wil dit nawoord dan ook graag gebruiken om mijn dank uit te spreken aan verschillende mensen die in belangrijke mate hebben bijgedragen aan de totstandkoming van dit proefschrift, zonder hen was dit werk er niet geweest.

Allereerst, en ik denk ook allermeest, een hartelijk dank aan mijn promotor Jerry Westerweel en mijn dagelijkse begeleider Gerrit Elsinga. Beiden hebben ontzettend veel betekend voor dit proefschrift en daarmee ook voor mijn eigen ontwikkeling. Ik ben beiden erkentelijk dat ze me de gelegenheid hebben geboden om mijn PhD uit te voeren. Ik kijk met veel genoegen terug op de vele discussies die we hebben gehad over de meest uiteenlopende zaken. Ook wanneer een publicatie voor de tweede keer werd afgewezen praatten jullie mij moed in om toch door te gaan. Hartelijk dank voor dat vertrouwen! Ik kreeg veel vrijheid om mijn eigen onderzoeksplannen te realiseren, maar jullie waren altijd bereid mee te denken over de exacte invulling en uitwerkingen van de experimenten. Door jullie ben ik gevormd tot de wetenschapper die ik nu ben.

Een experimentalist kan nooit zonder goede technici, het is echt teamwerk. In het bijzonder wil ik Edwin, Jasper en Jan bedanken. Jullie hulp is onmisbaar gebleken in het realiseren van de experimenten die ik tijdens mijn promotie heb gedaan. Ik realiseer me dat ik soms niet de meest geduldige experimentator ben geweest, daarom is een bedankje hier extra op z'n plaats. Het is altijd mijn passie geweest om vanuit het 'niks' een experiment te realiseren. Jullie hebben mij daar altijd ontzettend goed in bij gestaan! Edwin: hartelijk dank voor de vele keren waarbij jij je expertise inzette om de uitlijning van camera's, laservlak e.d. goed te krijgen. Ik bewonder je pragmatische aanpak; gaat het niet linksom, dan doen we het maar rechtsom! Jasper: in sommige gevallen moet ik wel op je zenuwen gewerkt hebben. Ik wil je heel hartelijk danken voor de vele, vele keren dat je 'even' (ik denk typerende woorden voor mij) iets maakte. Jan: je ondersteuning bij LabVIEW uitdagingen hebben het mogelijk gemaakt om een complex experiment te realiseren, het resultaat mag er wezen!

Wetenschap doe je nooit alleen. Ik heb het voorrecht gehad met een numerieke tegenhanger samen te werken. Jasper, ik wil je hartelijk bedanken voor de constructieve en productieve samenwerking gedurende het laatste jaar. Het heeft geresulteerd in twee prachtige papers, waarbij de overlap tussen de experimenten en simulaties verbazingwekkend goed was! Daarmee alleen doe ik je echter tekort. Ik heb deze periode als de meest prettige tijd van mijn PhD ervaren, ook op persoonlijk vlak. Henk, Greta, Gosse, en Hyuongsoo zijn mijn roommates geweest de afgelopen vier jaar. In het bijzonder een woord van dank aan Henk: bedankt voor je grondige adviezen m.b.t. mijn onderzoek en ook de vele waardevolle gesprekken die we hadden, die ga ik zeker missen. Veel succes met je promotie!

Administratieve zaken werden altijd zeer vakkundig en vlot opgelost door Caroline, Ria en Rob, waarvoor dank. Verder wil ik ook mijn vroegere en huidige collega's van het lab bedanken voor hun hulp, adviezen en ondersteuning in alle omstandigheden; Andries, Aris, Willem, Gijs, Wim-Paul, Rene, Rene van Hout, Joshi, Ruud, Gosse, Christian, Florian, Pedro, Manu, Arnoud, Ernst Jan, Melika, Maurice, Saad, Mark, Daniel, Valentina, Sören, Likun, Chem, Dirk, Mathieu, Marieke. Ik vergeet er vast een paar, en dat ligt niet aan jullie inspanningen, maar aan mijn vergeetachtigheid. Dus wees ervan verzekerd dat ik je bijdrage op prijs heb gesteld.

Uiteraard mag familie ook niet ontbreken in dit dankwoord. Heit en mem: de liefde en ondersteuning die jullie mij gegeven hebben, van o to nu, zijn voor mij heel belangrijk. Het is teveel om op te noemen wat ik van jullie heb ontvangen; alleen al het luisterend oor wat jullie bieden. Dank daarvoor! Yke, we hebben zo'n anderhalf jaar een kamer gedeeld, ik kijk met plezier terug op die tijd en ik koester de goede broederband die alleen maar versterkt is geworden! Ook de rest van mijn broers en zussen, schoonouders, zwagers, schoonzussen wil ik hier danken voor hun interesse en ondersteuning, iedereen op zijn eigen manier.

In de laatste plaats, maar zeker niet in de minste, wil ik mijn dank uitspreken aan mijn lieve vrouw Salomé. Woorden kunnen niet uitdrukken hoeveel ondersteuning en liefde ik van jou heb gehad de afgelopen vier jaar. Ik waardeer je op alle gebieden, maar in het bijzonder wel hoe je elke dag weer klaar staat voor onze lieve kinderen Martha en Elnathan. Het was altijd prachtig om na een dag je beziggehouden te hebben met één enkel grafiekje vervolgens waardevolle momenten mee te maken met jullie. Dat plaatst alle zorgen op het werk weer in het juiste perspectief.

Bovenal dank ik God voor Zijn talloze zegeningen, in het bijzonder dat Hij mij in staat stelde dit proefschrift te voltooien. Ik geloof dat Hij deze wereld heel wonderlijk gemaakt heeft en nog steeds onderhoudt en regeert. Ik heb de afgelopen vier jaar iets van Zijn schepping bestudeerd, en dat heeft mijn verwondering en ontzag voor Hem alleen maar groter gemaakt.

Jerke Eisma
Rijnsburg, December 2016

CURRICULUM VITÆ

Heerke Eelke EISMA

03-11-1986 Born in Wouterswoude, The Netherlands.

EDUCATION

1990–1999	Primary education CNS, Wouterswoude, The Netherlands
1999–2002	Secondary education Mavo de Saad, Damwoude, The Netherlands
2002–2004	Secondary education Havo, Dockinga College, Dokkum, The Netherlands
2004–2006	Secondary education VWO, Dockinga College, Dokkum, The Netherlands
2006–2009	Bachelor Aerospace Engineering Delft University of Technology, Delft, The Netherlands
2009-2012	Master Aerodynamics Delft University of Technology, Delft, The Netherlands Thesis: *Flow visualization and force measurements on a flapping-wing MAV DelFly II in forward flight configuration*
2012–2016	PhD researcher Delft University of Technology, Delft, The Netherlands Thesis: *Pollutant Dispersion in Wall-Bounded Turbulent Flows* Promotor: Prof. dr. J. Westerweel Copromotor: Dr. ir. G. E. Elsinga
2016–...	Consultant Analytics and Information Management Deloitte Consulting, Amsterdam, The Netherlands

LIST OF PUBLICATIONS

JOURNAL PUBLICATIONS

[1] H.E. Eisma, J. M. Tomas, M. B. J. M. Pourguie, G. E. Elsinga, H. J. J. Jonker, and J. Westerweel, "Effects of a Fence on Pollutant Dispersion in Boundary Layers Exposed to a Rural-to-Urban Transition." *(submitted to Boundary-Layer Meteorol.)*, 2016.

[2] J. M. Tomas, J. E. Eisma, M. J. B. M. Pourquie, G. E. Elsinga, H. J. J. Jonker, and J. Westerweel, "Pollutant Dispersion in Boundary Layers Exposed to Rural-to-Urban Transitions: Varying the Spanwise Length Scale of the Roughness.", *(accepted for publication in Boundary-Layer. Meteorol.)*, 2016.

[3] J. Eisma, J. Westerweel, G. Ooms, and G. E. Elsinga, "Interfaces and internal layers in a turbulent boundary layer.", *Phys. Fluids*, vol. 27:055103, 2015.

[4] M. Percin, B. W. van Oudheusden, H. E. Eisma, and B. D. W. Remes, "Three-dimensional vortex wake structure of a flapping-wing micro aerial vehicle in forward flight configuration.", *Exp. Fluids*, vol. 55, pp. 1-16, 2014.

CONFERENCE PUBLICATIONS AND CONTRIBUTIONS

[1] H. E. Eisma, J. M. Tomas, M. J. B. M. Pourquie, G. E. Elsinga, H. J. J. Jonker, and J. Westerweel, "Pollutant Dispersion in Boundary Layers Exposed to Rural-to-Urban transitions.", *Burgers Symposium*, 16-17 June 2016, Lunteren, The Netherlands.

[2] R. van Hout, J. Eisma, E. Overmars, G. Elsinga, and J. Westerweel, "Experimental investigation of the interaction between a stationary rigid sphere and a turbulent boundary layer.", *9th International Conference on Multiphase Flow*, 22-27 May 2016, Firenze, Italy.

[3] R. van Hout, J. Eisma, E. Overmars, G. Elsinga, and J. Westerweel, "Time-resolved Tomo-PIV measurements of the interaction between a stationary held sphere and a turbulent boundary layer.", *68th American Physical Society Division of Fluid Dynamics Conference*, 22-24 November 2015, Boston, Massachusetts.

[4] J. Eisma, J. Westerweel, and G. E. Elsinga, "Simultaneous scanning Tomo-PIV and LIF in a turbulent boundary layer.", *11th International Symposium on Particle Image Velocimetry*, 14-16 September 2015, Santa Barbara, California.

[5] J. Hunt, T. Ishihara, J. Eisma, W. P. Breugem, J. Westerweel, and M. Braza, "External and Internal interfacial turbulent shear layers.", *15th European Turbulence Conference*, 25-28 August 2015, Delft, The Netherlands.

[6] J. Eisma, J. Westerweel, and G. E. Elsinga, "Predicting growth rates of interfaces and internal layers in a turbulent boundary layer using a first order jump model.", *15th European Turbulence Conference*, 25-28 August 2015, Delft, The Netherlands.

[7] J. M. Tomas, M. J. B. M. Pourquie, H. E. Eisma, and H. J. J. Jonker, "Pollutant Dispersion in Neutral and Stable Boundary Layers Enering an Urban Environment.", in *Proc. TSFP-9*, vol. 3, pp. 1-6, Melbourne, Australia.

[8] J. M. Tomas, M. J. B. M. Pourquie, H. E. Eisma, G. E. Elsinga, H. J. J. Jonker, and J. Westerweel, "Pollutant dispersion in the urban boundary layer." In Frölich, J., Kuerten, H., Geurts, B. J., and Armenio, V., editors, *Direct and Large-Eddy Simulation 9 Workshop*, pp. 435-441. Springer.

[9] J. Eisma, J. Westerweel, and G. E. Elsinga, "Interfaces and Internal layers in a TBL.", *Burgers Dag 2015*, 13 January 2015, Delft, The Netherlands.

[10] J. Eisma, G. Elsinga, and J. Westerweel, "Characteristics of Interfaces in a Turbulent Boundary Layer.", *14th European Turbulent Conference*, 1-4 September 2013, Lyon, France.

[11] M. Percin, J. Eisma, B. van Oudheusden, B. Remes, R. Ruijsink, and C. de Wagter, "Wake reconstruction of Flapping-Wing MAV 'DelFly II' in Forward Flight.", *International Micro Air Vehicle conference and competitions*, 3-6 July 2012, Braunschweig, Germany.

[12] M. Percin, J. Eisma, B. van Oudheusden, B. Remes, R. Ruijsink, and C. de Wagter, "Flow Visualization in the Wake of the Flapping-Wing MAV 'DelFly II' in Forward Flight.", *30th AIAA Applied Aerodynamics Conference*, AIAA-2012-2664, New Orleans, United States.

OTHER SCIENTIFIC CONTRIBUTIONS

[1] J. M. Tomas, M. J. B. M. Pourquie, H. E. Eisma,, and H. J. J. Jonker, "The effect of stable stratification on boundary-layer development and pollutant dispersion behind an obstacle.", Poster at *EUROMECH Colloquium 567: Turbulent mixing in stratified flows*, 22-25 March 2015, Cambridge, UK.

[2] J. Eisma, G. E. Elsinga, and J. Westerweel, "Detection criterion for interfaces in a Turbulent Boundary Layer measured with planar-PIV.", Poster at *10th International Symposium on Particle Image Velocimetry*, 1-3 July 2013, Delft, The Netherlands.